

Detection of Rare Earth Elements and Rare Earth Oxides with Hyperspectral Spectroscopy

Near-field and Spaceborne Investigations in Preparation of the EnMAP Mission

Dissertation
zur Erlangung des akademischen Grades
"doctor rerum naturalium"
(Dr. rer. nat.)
in der Wissenschaftsdisziplin Geologie

eingereicht an der
Mathematisch-Naturwissenschaftlichen Fakultät
der Universität Potsdam

von
Nina Kristine Bösche

Potsdam, den 24.06.2015

Published online at the
Institutional Repository of the University of Potsdam:
URN urn:nbn:de:kobv:517-opus4-85363
<http://nbn-resolving.de/urn:nbn:de:kobv:517-opus4-85363>

**Für meine Familie – Kristine, Leff, Katrin und meinen Neffen,
der in wenigen Tagen in diese wundervolle Welt geboren wird**

Eidesstattliche Erklärung

Ich erkläre an Eides statt, dass ich die beiliegende Doktorarbeit selbstständig und ohne fremde Hilfe verfasst, andere als die angegebenen Quellen nicht benutzt und die den benutzten Quellen wörtlich oder inhaltlich entnommenen Stellen als solche kenntlich gemacht habe.

Die Doktorarbeit hat keiner anderen Prüfungsbehörde vorgelegen.

Berlin, den 21.06.2015

Content

Abstract.....	6
Zusammenfassung	7
1. Chapter Introduction.....	8
1.1 Rare Earth Elements – Classification and Usage	9
1.2 Objectives of the Thesis	11
1.3 Thesis Outline.....	12
1.4 The absorption band producing processes	14
1.4.1 Electronic Processes	14
1.4.2 Vibrational Processes	15
1.4.3 Absorption Bands of REEs.....	16
1.5 Geological Origin of REE Deposits	17
1.6 Standard Procedures for Mineral Exploration Using Remote Sensing Data.....	19
1.7 EnMAP – A Future Hyperspectral Satellite Mission.....	20
1.8 Literature.....	21
2. Chapter Development of the REE Detection Routine (REEMAP) and Comprehensive Spectroscopic Investigation of REO, REM, REE Bearing Minerals and Synthetic Samples.....	22
2.1 Hyperspectral REE (Rare Earth Element) Mapping of Outcrops—Applications for Neodymium Detection (published: Remote Sens. 2015, 7(5), 5160-5186; doi:10.3390/rs70505160).....	23
2.1.1 Introduction.....	24
2.1.2 Geological Setting.....	27
2.1.3 Methods	28
2.1.4 Results	35
2.1.5 Discussion.....	41
2.1.6 Conclusions.....	48
2.1.7 Acknowledgments	49
2.1.8 Author Contributions.....	49
2.1.9 References.....	50
2.2 Supplement: Reflectance Spectra of REM, REO and REE-bearing minerals	52
2.2.1 Materials and Methods	52
2.2.2 Results and Evaluation of the Results	53
3. Chapter Re-calibration of REEMAP on Dysprosium and Holmium and Spectroscopic Study of Proxy and Associated Minerals	59
3.1 Hyperspectral Rare Earth Element Mapping of three Outcrops at the Fen Complex, Norway – Calcitic, Dolomitic and Ankeritic Carbonatites (submitted, accepted for publication, publication planned in august 2015 - ISBN-13: 978-0128023280)	60
3.1.1 Introduction.....	61
3.1.2 Geological Setting	65
3.1.3 Materials and Methods	66
3.1.4 Results	78
3.1.5 Discussion.....	87
3.1.6 Conclusion	89
3.1.7 Acknowledgements	90
3.1.8 References.....	90
3.2 Supplement: Proxy Minerals for Fenites	92
3.2.1 Materials and Methods	92
3.2.2 Results and Evaluation of the Results.....	92
4. Chapter Adaption of REEMAP on thulium and erbium and for satellite image data and investigation of the most important limiting factor (signal to noise ratio).....	95
4.1 Spaceborne Rare Earth Element Mapping (Neodymium, Thulium and Erbium) - Capabilities and Limitations of Hyperspectral Imaging Sensors (EO-1 Hyperion and EnMAP) (submitted to mdpi, “The Environmental Mapping and Analysis Program (EnMAP) Mission: Preparing for Its Scientific Exploitation”, in June 2015).....	96
4.1.1. Introduction.....	97

4.1.2. Experimental Setup	100
4.1.3. Results and Discussion.....	106
4.1.4. Conclusions.....	113
4.1.5 Acknowledgments	114
4.1.6 Author Contributions.....	114
4.1.7 Conflicts of Interest	114
4.1.8 References.....	115
4.1.9 Appendix	117
5. Chapter Discussion and Conclusion	120
5.1 Discussion of the Results.....	121
5.1.1 REE Related Spectra and their Special Optical Characteristics	121
5.1.2 REEMAP Methodology	122
5.1.3 Capabilities and Limitations of the REE Detection Using Spectroscopy	124
5.2 Summarizing Remarks and Outlook	128
5.3 Conclusion	130
6. References	131
7. Acknowledgments	133
8. Appendix.....	135
8.1 Appendix of the supplementary Chapter 2.1 and 3.1	135

Abstract

The continuously increasing demand for rare earth elements in technical components of modern technologies, brings the detection of new deposits closer into the focus of global exploration. One promising method to globally map important deposits might be remote sensing, since it has been used for a wide range of mineral mapping in the past. This doctoral thesis investigates the capacity of hyperspectral remote sensing for the detection of rare earth element deposits. The definition and the realization of a fundamental database on the spectral characteristics of rare earth oxides, rare earth metals and rare earth element bearing materials formed the basis of this thesis. To investigate these characteristics in the field, hyperspectral images of four outcrops in Fen Complex, Norway, were collected in the near-field. A new methodology (named REEMAP) was developed to delineate rare earth element enriched zones. The main steps of REEMAP are: 1) multitemporal weighted averaging of multiple images covering the sample area; 2) sharpening the rare earth related signals using a Gaussian high pass deconvolution technique that is calibrated on the standard deviation of a Gaussian-bell shaped curve that represents by the full width of half maxima of the target absorption band; 3) mathematical modeling of the target absorption band and highlighting of rare earth elements. REEMAP was further adapted to different hyperspectral sensors (EO-1 Hyperion and EnMAP) and a new test site (Lofdal, Namibia). Additionally, the hyperspectral signatures of associated minerals were investigated to serve as proxy for the host rocks. Finally, the capacity and limitations of spectroscopic rare earth element detection approaches in general and of the REEMAP approach specifically were investigated and discussed. One result of this doctoral thesis is that eight rare earth oxides show robust absorption bands and, therefore, can be used for hyperspectral detection methods. Additionally, the spectral signatures of iron oxides, iron-bearing sulfates, calcite and kaolinite can be used to detect metasomatic alteration zones and highlight the ore zone. One of the key results of this doctoral work is the developed REEMAP approach, which can be applied from near-field to space. The REEMAP approach enables rare earth element mapping especially for noisy images. Limiting factors are a low signal to noise ratio, a reduced spectral resolution, overlaying materials, atmospheric absorption residuals and non-optimal illumination conditions. Another key result of this doctoral thesis is the finding that the future hyperspectral EnMAP satellite (with its currently published specifications, June 2015) will be theoretically capable to detect absorption bands of erbium, dysprosium, holmium, neodymium and europium, thulium and samarium. This thesis presents a new methodology REEMAP that enables a spatially wide and rapid hyperspectral detection of rare earth elements in order to meet the demand for fast, extensive and efficient rare earth exploration (from near-field to space).

Zusammenfassung

Die weltweit steigende Nachfrage nach seltenen Erden für technische Komponenten in modernen Technologien, rückt die Erkundung neuer Lagerstätten näher in den Fokus der globalen Exploration. Die Erkundung und Beschreibung neuer Lagerstätten mittels hyperspektraler Fernerkundung findet basierend auf Mineralkartierung bereits eine breite Anwendung. Diese Doktorarbeit befasst sich mit der Machbarkeit hyperspektraler Fernerkundung zur Detektion von Seltenerdelement-Vorkommen. Um dieser Fragestellung nachzukommen, wird eine grundlegende Datenbank der spektralen Eigenschaften von Seltenerdoxiden, Seltenerdmetallen und Seltenerdelement-haltigen Materialien hergestellt. Diese Eigenschaften wurden an vier Aufschlüssen des Fen Complexes in Norwegen hyperspektral analysiert. Auf dieser Grundlage wurde eine neue Methodik (REEMAP) entwickelt, die Seltenerdelement angereicherte Zonen im Aufschluss auffindet und kartiert. Die wichtigsten Schritte dieser Methode sind wie folgt: 1) multi-temporal gewichtete Mittelung mehrerer hyperspektraler Bilder des gleichen Ausschnittes; 2) Verstärkung des charakteristischen spektralen Merkmals unter Verwendung eines Hochpassfilterverfahrens, das auf der Standardabweichung einer Gaußkurve basiert die der gesuchten Absorptionsbande entspricht; 3) die mathematische Modellierung der gesuchten Absorptionsbande und thematische Klassifikation der Bildpixel. REEMAP wurde auf verschiedene Sensoren (EO-1 Hyperion und EnMAP) und ein neues Testgebiet (Lofdal, Namibia) re-kalibriert. Weiterhin wurde untersucht, inwiefern hyperspektrale Methoden zum Detektieren von Proxymaterialien verwendet werden können. Die Limitationen der Seltenerd-Detektion mittels Spektroskopie im Allgemeinen und der Detektion unter Anwendung von REEMAP wurden erforscht und diskutiert. Ein Ergebnis dieser Arbeit ist, dass acht Seltenerdoxid Spektren eindeutig detektierbare Absorptionsbanden zeigen, die für eine Seltenerddetektion verwendet werden können. Zusätzlich können die spektralen Merkmale von Eisenoxiden, eisenhaltigen Sulfaten, Kalzit und Kaolinit verwendet werden, um metasomatische Alterationszonen und die Erzgänge zu erkennen. Eines der wichtigsten Ergebnisse dieser Doktorarbeit ist die Entwicklung der REEMAP Methode. Vor allem für verrauschte hyperspektrale Bilder zeigten die Ergebnisse unter der Verwendung von REEMAP eine höhere Detektionswahrscheinlichkeit. Neben dem Signal-zu-Rausch-Verhältnis des Bildes, sind die davon abhängige spektrale Auflösung, überdeckende Materialien, atmosphärische Effekte und Aufnahmen unter suboptimalen Lichtverhältnissen als weitere wichtige Limitation der Seltenerd-Detektion zu nennen. Ein weiteres wichtiges Ergebnis dieser Doktorarbeit ist, dass der zukünftige EnMAP Satellit (mit seinem aktuell veröffentlichten Spezifikationen, Juni 2015) theoretisch in der Lage sein wird die Absorptionsbanden von Erbium, Dysprosium, Holmium, Neodym, Europium, Thulium und Samarium zu detektieren. Meine Dissertation stellt eine neue fernerkundliche Methode (REEMAP) vor, die zur weiträumigen und schnellen hyperspektralen Detektion von seltenen Erden verwendet werden kann und somit hilfreich bei der Exploration seltener Erden sein kann.

1. Chapter

Introduction

This chapter describes rare earth elements (REEs), rare earth oxides (REOs), rare earth metals (REMs), their global importance, and their geological origin. It introduces the spectroscopic fundamental principles (absorption processes), the future EnMAP satellite, and how remote sensing techniques can contribute to geological field exploration. Finally, this chapter deals with the objectives and the outline of this thesis and presents the most important literature.

1.1 Rare Earth Elements – Classification and Usage

This chapter is based on the comprehensive publication of Brüning and Böhmer, 2011 [1]. The REEs, or Lanthanides, are subdivided into light REEs (LREEs: lanthanum, cerium, praseodymium, neodymium, promethium, samarium) and heavy REE (HREE: europium, gadolinium, terbium, dysprosium, holmium, erbium, thulium, ytterbium, lutetium). In addition, yttrium and scandium are often grouped with the REEs due to their similar chemical properties. The worldwide demand for REEs is steadily increasing due to the wide range of applications in which these elements are used. REEs are classified as critical raw materials by the European Union because supply disruptions would have a significant impact on the production chains of sensitive modern technologies. So far, a substitution of REEs with other materials often fails and recycling does not yet deliver the expected outcome.

REEs are used for a wide range of applications in modern technologies. Several optical, magnetic, and chemical properties make REEs increasingly important for future technologies (Table 1.1).

Table 1.1: Chemical properties and applications of REEs [1].

Element Atomic number	Oxidation number	Crustal abundances	Electronic configuration	Application
Yttrium (Y) 39	III	0.003 %	[Kr]4d15s2	Automobiles (catalysts, spark plug), electronic (red color in monitors, LEDs), medicine (cancer treatment, ceramic in prostheses), jewelry (diamond substitute)
Lanthanum (La) 57	III	0.003 %	[Xe]5d16s2	Glass/ceramic (polishing, quality improvement of glasses), energy (NiMH batteries), alloys (HSLA steel)
Cerium (Ce) 58	III, IV	0.004 %	[Xe]4f 15d16s1	Glass/ceramic (polishing, dental filling), electronic (LEDs), alloys (increases heat residency), automobile (catalysts, diesel addition), medicine (contrast enhancement in magnetic resonance imaging)
Praseodymium (Pr) 59	III, IV	0.005 %	[Xe]4f 36s2	alloys (aerial engines, magnets), glass/ceramic (UV protection glass)
Neodymium (Nd) 60	III	0.002 %	[Xe]4f 46s2	Alloys (neo-magnets, high temp resistant magnets), glass (rear-view mirrors)

Element Atomic number	Oxidation number	Crustal abundances	Electronic configuration	Application
Promethium (Pm)	61	III	0.00000000 000000000 01 %	[Xe]4f 56s2 Energy (radionuclide batteries, thermoelectric generators), jewelry (luminescence of numbers)
Samarium (Sm)	62	III, II	0.0006 %	[Xe]4f 66s2 Electronic (permanent magnets), medicine (pain treatment), glass (absorbs infrared light)
Europium (Eu)	63	III, II	0.00006 %	[Xe]4f 76s2 Electronic (red color in lamps and TV), energy (part in atomic reactors), marker in Euro bank notes
Gadolinium (Gd)	64	III	0.0006 %	[Xe]4f 75d16s2 Electronic (microwaves, green color in radar-monitors, re-writable CDs), medicine (contrast enhancement in MRTs, X-rays, PETs), glass (magneto-optic films), energy (nuclear fuels)
Terbium (Tb)	65	III, IV	0.00009 %	[Xe]4f 96s2 Electronic (green color in lamps and TV), alloys (semiconductors, terfenol-D alloys)
Dysprosium (Dy)	66	III	0.0004 %	[Xe]4f 106s2 Automobiles (neo-magnets, hybrid cars), electronic (terfenol-D alloys used in converters, resonators, injectors), energy (part in nuclear reactors, dose-meter), glass (lasers)
Holmium (Ho)	67	III	0.0001 %	[Xe]4f 116s2 Glass/ceramic (yellow/red glass color), electronic (magnets, semiconductors, spectrophotometers), energy (part in nuclear reactors)
Erbium (Er)	68	III	0.0002 %	[Xe]4f 126s2 Glass/ceramic (optical glass fiber, pink color in glass and porcelain), alloys (vanadium alloys, nickel alloys), medicine (dermatology and odontology)
Thulium (Tm)	69	III, II	0.00002 %	[Xe]4f 136s2 Electronic (superconductors, microwaves), medicine (handheld X-ray devices)
Ytterbium (Yb)	70	III, II	0.0003 %	[Xe]4f 146s2 Alloys (stainless steel, dental fillings), glass/ceramic (semiconductor lasers), energy (solar panels), medicine (X-rays)
Lutetium (Lu)	71	III	0.00007 %	[Xe]4f 145d16s2 Electronic (bubble memory, OLED), medicine (PETs, cancer treatment), energy (catalyst in oil refinery)

1.2 Objectives of the Thesis

The globally increasing demand for REEs and the associated research of new and existing deposits lead to a tremendous need of new methods for fast and effective exploration. Digital remote sensing image analysis is one of those effective methods to analyze and map geological deposits. Spaceborne imaging spectroscopy, provided e.g. by the future hyperspectral satellite mission EnMAP, will enable spatially wide and rapid exploration of deposits across country borders. Nowadays hyperspectral remote sensing (from all scales) is common for base metal ore deposits, but it is barely used for the detection of REE deposits. On the other hand, in the field of coordination chemistry REE solutions are investigated in a multitude of ways using the methods of laboratory spectroscopy. This doctoral study is performed to address and remedy the lack of knowledge exchange between these two disciplines. More specifically it states that new remote sensing approaches are necessary in order to utilize REE related spectral signatures and existing methods need to be adapted for an improved analysis of indicating minerals.

The primary objective of this work is to characterize the capacity of hyperspectral remote sensing for the detection of REE deposits. This includes:

1. Selection of robustly detectable absorption bands for REEs using state of the art spectrometers
2. Development of an automated REE detection algorithm (REEMAP).
3. Adaption of REEMAP to different sensors and scales (near-field to space)
4. Capacity and limitations for the REE detection (sensors and geology)
5. Aggregation of REEMAP for EnMAP.

Finally, the findings are discussed in the context of geological exploration.

1.3 Thesis Outline

The introduction deals with the fundamentals of spectroscopy from near-field to space and their contribution to exploration geology. In remote sensing spectroscopy mostly relates to the characteristic interaction between incident electromagnetic light and surface materials. Those interactions can be observed as small indentations in the reflectance spectrum [2], which are named absorption bands or absorption features (features are composed of several absorption bands). This is described in more detail in Chapter 1.4 that also deals with the different physical and chemical processes that lead to characteristic absorptions. Spectroscopy can be applied from near-field to space. This doctoral thesis starts with an investigation on a near-field scale (geological outcrop mapping). The related fieldwork, which was performed in order to calibrate and validate the spectroscopic results, concentrated on carbonatitic REE deposits. General information on the mineralogy and geological origin of carbonatite deposits are described in Chapter 1.5. In Chapter 1.6 an overview of the link between spectroscopy and geological exploration is given. It highlights fields of geological exploration to which remote sensing techniques can contribute. Spaceborne REE detection is discussed in Chapter 4. Here, REE detection methods are aggregated to the future EnMAP and the operating EO-1 satellite. The question whether EnMAP is capable of detecting REEs is one of the key questions in this thesis. Therefore, Chapter 1.7 of the introduction covers the EnMAP hyperspectral satellite mission. The last chapter of the introduction deals with the historic and actual literature about spectroscopic techniques and remote sensing digital image analysis used for REE exploration.

Chapter 2 presents neodymium as a first exemplary REE and it introduces a new methodology (REEMAP) that can be used to sharpen absorption bands in a spectroscopic dataset of an outcrop survey. Such an algorithm must include the parameters of robustly recognizable features and it must respect the narrow Gaussian-bell shape of the absorption bands. Thus it will surface that a differentiation between the target REE absorption and other external factors must be made. The study, on which the Chapter 2.1 is based on, is performed and the paper written by Nina Bösch. The supplementary chapter (Chapter 2.2) gives an overview of the spectra of almost all REEs, REOs, REMs and REE bearing ores (6 minerals). Particular attention is given to the economically important (neodymium and dysprosium) and spectroscopically well recognizable REEs (thulium, erbium and holmium). Well recognizable features can be defined through absorption bands not overlapped by atmospheric absorptions or other materials, and/or can be discriminated from noise. Moreover, mathematical dependency between concentration and intensity of diagnostic absorption bands will be discussed.

Chapter 3 deals with a shift of the 800 nm neodymium absorption band and adapts the methodology developed in Chapter 2 to two more REEs. These two elements belong to the HREEs (dysprosium and holmium) and are known to have diagnostic absorption bands in the VNIR and SWIR region of the electromagnetic spectrum. Additionally, a spectral adaption process will be implemented in the REE detection routine, called albedo normalization. This is necessary, because the rotational scanning mode, applied at outcrops in northern latitudes, requires a reduction of varying illumination conditions in the image. Furthermore, Chapter 3 deals with associated ferro-minerals as factors that hamper REE detection. The influence of iron as a hampering factor in the detection of REEs in carbonatites is analyzed quantitatively with synthetic mixtures of neodymium, calcite and hematite. In order to detect local trends in the spatial distribution other associated minerals are additionally mapped in three studied outcrops. These proxy maps play an important role whenever REE deposits have to be found in an area that is smaller than the average pixel size of the data set. The study, on which the Chapter 3.1 is based on, is performed and the paper written by Nina Bösch (Chapter 3.1.3.2.2 and 3.1.3.2.3 have been written with the help of Friederike Körting and Christian Mielke). The supplementary chapter (Chapter 3.2) includes the spectra of fenites from the Fen Complex, Norway. Fenites often mark a wide area around carbonatite deposits. Although, the spectra of the important minerals in fenites can be considered as neutral spectra (convex spectra, whose continuum equals the albedo), a proxy map of their weathering products (kaolinite, etc.) could provide additional information.

Chapter 4 shows the adaption of the REE sharpening methodology developed in Chapter 2 and 3 to spaceborne sensors. It also focuses on the limiting factors of REE detection from space. The limitations are discussed considering two hyperspectral imagers - the operating system EO-1 Hyperion and the future satellite EnMAP. Additionally, this chapter includes a calibration of the REEMAP methodology for thulium and erbium. The limiting factors addressed here are the signal-to-noise-ratio (SNR) and the spectral resolution of the two sensors. The study, on which the Chapter 4.1 is based on, is performed and the paper written by Nina Bösche.

The concluding chapter (Chapter 5) discusses the results of this thesis. The capacity and limitations of remote sensing for REE detection are outlined in more detail. It will address the question to what extent operating and future hyperspectral sensors are and will be able to detect REEs. Moreover, it will show perspectives for new investigations on the detectability of REEs using remote sensing techniques.

1.4 The absorption band producing processes

Spectroscopy integrates the measurement and interpretation of the physical interaction between electromagnetic light and elements, minerals, and rocks causing energy absorptions (bands and slopes), e.g. in the visible and infrared range (350 to 2500 nm). These absorptions can be caused by 1) crystal field effects, 2) charge-transfer, 3) color centers, 4) transitions to conduction bands, and 5) vibrational transitions (overtone and combination tone) [3]. Every material reacts differently to incident electromagnetic radiation. Depending on their chemical composition, the environmental ions, valence electrons, the energy, and the spectral range of the incident light material characteristic absorption features can occur. It can be assumed that the form of the absorption feature follows a Gaussian-bell shaped curve. Multiple features can therefore be described as superimposing Gaussian functions. The Gaussian assumption for features was published by Sunshine et al. 1990, 1993 [4,5]. The Gaussian-bell shaped superimpositions were assumed to be caused by the normal distribution of the orbital probabilities and the normal distribution for the bond lengths in the crystal. Generally, it can be assumed that electronic field transitions mainly absorb in the visible and near infrared range (350-1000 nm). Vibrational effects can mainly be observed in the short wave infrared and in the thermal infrared wavelength range (1-12 μm). Besides the shape of the absorption bands the wavelength position of material characteristic absorption bands is discriminative. The absorption depth is related to the spatial surface abundance, texture, and density of a certain material (concentration of the material per sample and percentage of the material per pixel). In summary, a reflectance spectrum collected from a rock sample can be considered as a superimposition of the emitted light from the light source, the material characteristic absorption features, and material induced changes of slopes. Electromagnetic emissions of thermal energy plays a marginal role in the visible to short wave infrared region and will find no attention in this work.

1.4.1 Electronic Processes

This section is based on the publication of Hunt, 1977 [3] and was summarized to provide an overview on absorption band producing electronic processes.

1. Crystal field transitions: It is described as the transition of the "outer" orbital electrons from one energy state to another. The energy that is required for the electron to change the energy level is discrete and follows quantum mechanical rules. For minerals and rocks that are not pure, the outer electrons are not associated with a certain atom anymore. In this case, the energy levels are widened (energy bands) and the absorption features in the spectrum appear of a great width as well (e.g. iron oxides). In contrast to iron oxides, the REE atomic structure includes partially filled f-orbitals. Those orbitals are shielded by the surrounding d-orbitals. Hence, the energy levels remain mostly unchanged. The absorption bands that are caused by crystal field transitions in the f-orbitals of the REEs are therefore very pronounced and of a low width.
2. Charge transfer: Charge transfer is the transition of an electron from its excited state to a neighboring ion or to a neighboring ligand. Absorption features that are caused by charge transfer appear more intense than features caused by crystal field transitions. Those features can be observed e.g. for iron oxides (F-O charge transfer band and ferric-ferrous ion charge transfer) and vegetation (chlorophyll band).
3. Color centers: Color centers can be described as excited electrons that would not return into their positively charged holes. Instead they fill a discrete energy level that exist due to crystal lattice defects. The most common mineral that shows color centers is fluorite.

4. Conduction band transitions: Conduction band transitions occur between energy bands in which the electrons of the lattice composing ions are not bound to the atom anymore. The conduction band represents a higher energy level. In this band the electrons are released from the hosting atom and are free to move through the crystal lattice. The valence band electrons are attached to ions or bonds. Only few materials show conduction band transitions. Generally, the effect of conduction band transitions appear as a slope in the spectrum, e.g. sulfur and arsenopyrite show a reduced reflection over the visible range and a slope to higher reflection towards the near infrared range of the spectrum (absorption edge).

1.4.2 Vibrational Processes

This section is based on the comprehensive publication of Hunt, 1977 [3] and was summarized to provide an overview on the absorption band that occur due to vibrations.

Normal modes and fundamentals: Solid matter can vibrate/oscillate in three dimensions (x, y, z). A number of n atoms have $3n-6$ degrees of freedom or normal modes/fundamentals. The motions include symmetrical and asymmetrical stretching and bending. The number and form of vibrations is dependent on the chemical composition, the crystal lattice geometry, and the binding forces of the atoms. All motions can be triggered by electromagnetic energy. The most known vibrational energy absorption of electromagnetic light is water (symmetric O-H stretch, H-O-H bend, and asymmetric O-H stretch). Their fundamentals appear in the thermal infrared region. However, their overtones can be observed in the short wave infrared region. Another important material that vibrates when exposed to electromagnetic light is carbonate. It has four fundamentals in the planar CO_3^{2-} ion (C-O symmetric stretch, doubly degenerated asymmetric stretch, and two bending modes). All fundamentals occur in the thermal infrared region and their overtones can be observed in the short wave infrared region. Other geologically important minerals, such as quartz and feldspars, show vibrational absorptions in the thermal infrared region. Overtones of these minerals are not observable in the visible to short wave infrared region. These minerals are therefore spectrally homogeneous and direct hyperspectral detection in the solar optical range is not possible.

1.4.3 Absorption Bands of REEs

This section is based on the comprehensive publication of Kumar et al., 2007 [6], citations from other literature are mentioned in the corresponding sentence.

The absorption bands of REEs represent the crystal field transitions that are allowed in the REE ions. Hence, the spectral features are distinct, pronounced, and sharp. Most REEs have a high number of features. As described in section “Electronic Processes” (Chapter 1.4.1) the f-orbitals are sheltered by the d-orbitals. A valence binding of the d-orbitals to the neighboring atoms is therefore supposed to have no effect to the f-orbitals. However, at least two REEs (neodymium and europium) are known to show shifted positions of their absorption bands in different minerals. In case the REE is bond to ligands of a high electronegativity the ligand field can overlap the f-orbital, which then leads to a higher degree of covalency between rare earth ion and the ligand. An increased ion-ligand bond covalency causes a shift of the absorption band towards the longer wavelength. The unusual sensitivity of neodymium and europium for neighboring ions is named “ligand mediated pseudohypersensitivity” [7]. Figure 1.1 shows the spectrum of neodymium oxide as a representative for a typical reflectance spectrum for REEs.

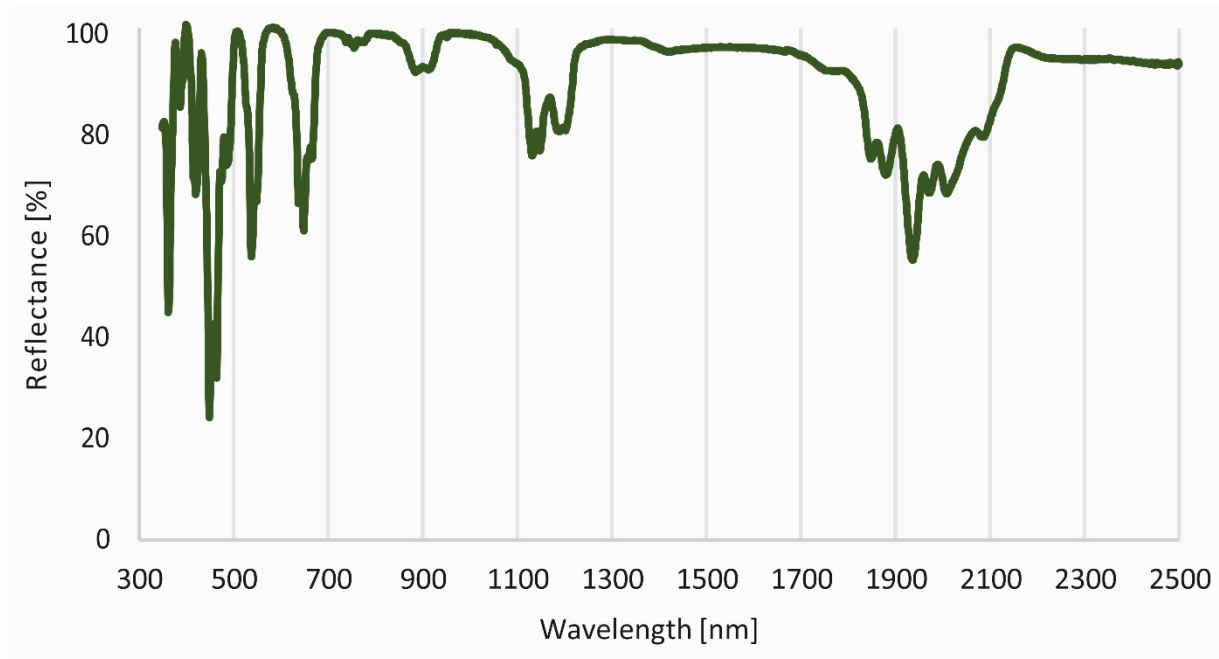


Figure 1.1: Reflectance spectrum of neodymium, showing its representative absorption bands in the VNIR and SWIR region.

1.5 Geological Origin of REE Deposits

This work concentrates on carbonatites because most of the economically important REE deposits are directly or indirectly associated with carbonatites and alkaline magmatic complexes. Alkaline intrusives are relatively rare in comparison to felsic and mafic igneous rocks. Generally, the bulk of the documented alkaline deposits are geologically “old” [8]. They can be found in regions of stable crust that underwent thinning and extension [8]. The generation of alkaline melts usually occurs in early phases of rifting and a direct link to mantle plumes is assumed [9]. Intra-oceanic carbonatites are rarely found [10]. The composition of alkaline magmatic associations is transitional between three alkaline series endmembers: Carbonatites (nepheline dominated), kimberlites (leucite dominated) and dunites (olivine dominated) [8]. Thus, in their pure form alkalis are not contained in the rocks [8]. However, fractionating processes in the silica-undersaturated magma lead to varying vertical and radial compositions of the igneous rock body. The typical form of alkaline deposits are central volcanos or volcano-plutonic ring complexes (Figure 1.2) [9]. Additionally, they can occur as hypabyssal plugs, isolated in clusters, as small dykes, breccias or vein/stockwork hosted [8,9]. The composition of the alkaline rock body and the concentration of ores primarily depends on the original magma composition, the nature of its source region, and the interactions with the country rocks [9]. The carbonatite endmember is understood as the latest fractionation product of concentrically zoned alkaline ultramafic complexes [8]. Carbonatites are usually H₂O poor and contain non-hydrous volatiles (CO₂, B, F). Further, they are generally enriched in REEs and other high field strength elements (Zr, Nb, U, Th, Hf, Ta) [9]. Usually, they are surrounded with ijolite-urtite melts, alkali pyroxenites and fenites (from inside to outside; Figure 1.2). Fenites are produced in the late stage of differentiation and can be characterized as metasomatized wallrocks of the country rock [9]. Their composition changes from orthoclase feldspatites (breccia) close to the intrusion to metasomatic albite, nepheline syenites and Na-amphiboles and Na-pyroxenes, which occur farther away from the intrusion [8]. The spatial extension of the fenitized zone depends on the permeability of the country rocks (porosity, fractures, faults or shear zones) and can reach up to several kilometers [9]. Although most carbonatite-hosted REE deposits belong to the ring shaped carbonatite complexes, recent literature discusses an alternative theory of the origin [8]. For example in Bayan Obo, China, the deposit that produces most of the world’s LREEs, is likely a metasomatically carbonatized meta-sedimentary marble [8]. However, different suits of carbonatites are known:

1. Calcite carbonatites (*søvites*)
2. Dolomite carbonatites (*rauhaugites*, dolomitic carbonatites)
3. Ferro carbonatites (*rødbergites*, ankeritic carbonatites)
4. Sodium carbonatites (Na, K carbonatites)

This doctoral thesis focusses on a ring shape carbonatite complex, the Fen complex in Norway, and a carbonatite-phonolite dyke-swarm at Lofdal, Namibia. The Fen complex is defined as a type locality of carbonatite REE deposits and is the origin of several associated rock type names (*fenites*, *rødbergites*, *søvites*, *rauhaugites*).

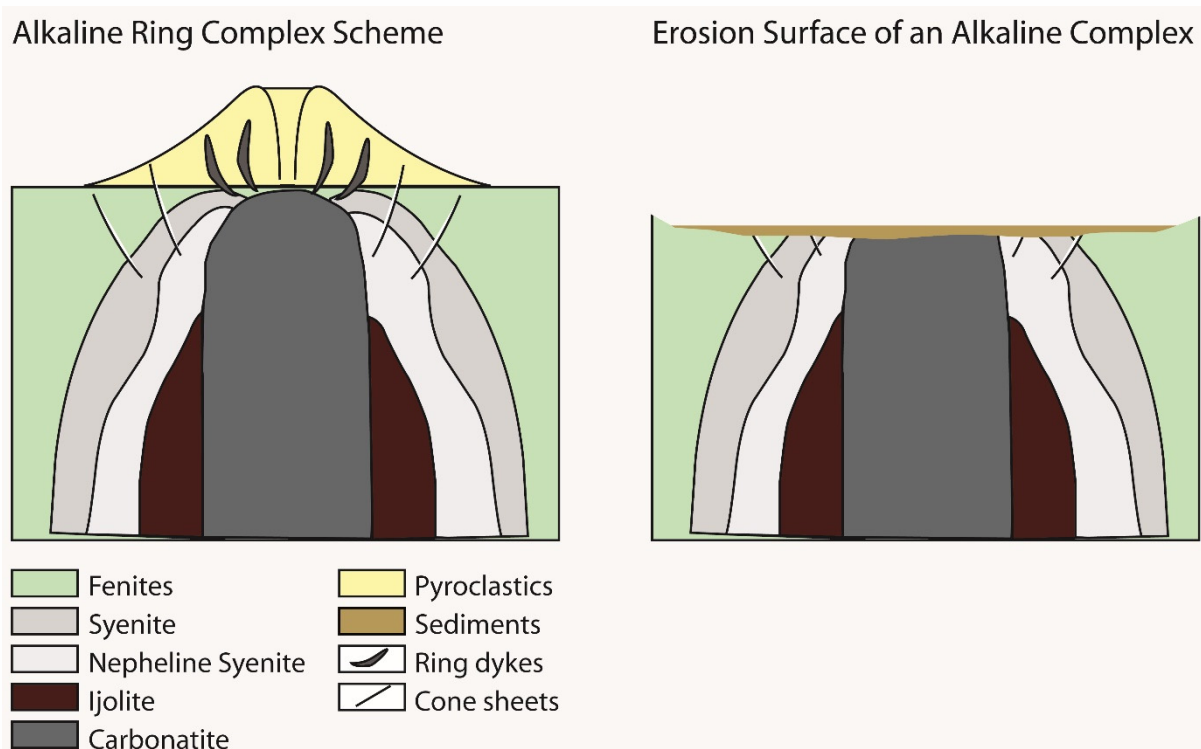


Figure 1.2 : Schematic cross section of alkaline ring complexes, modified after [9].

Table 1.2: Common REE-minerals in carbonatites [11].

Mineral	Chemical formula
Monazite	$(\text{Ce,La,Nd,Th})\text{PO}_4$
Bastnaesite	$\text{Ce}(\text{CO}_3)\text{F}$
Synchesite	$\text{CaCe}(\text{CO}_3)_2\text{F}$
Parisite	$\text{Ca}(\text{Ce,La})_2(\text{CO}_3)_3\text{F}_2$
Allanite	$(\text{Ce,Ca,Y})_2(\text{Al,Fe}^{3+})_3(\text{SiO}_4)_3(\text{OH})$
Xenotime	$(\text{Yb,Y})\text{PO}_4$

1.6 Standard Procedures for Mineral Exploration Using Remote Sensing Data

The geological exploration utilizes many physical and geochemical methods for discovering and evaluating new deposits. Depending on the geological situation, environmental conditions, and expected mineralization, different methods are preferred. In the initial phase airborne and spaceborne overflights (solar optical and thermal remote sensing, radiometric surveys, laser altimetry) and first geological field surveys are carried out. In this phase first field samples are geochemically analyzed and areas of prospectivity defined. The geological origin and evolution are explored and a spatial distribution pattern is identified. In the next phase of exploration the shape of the orebodies and their homogeneity is determined. Geophysical techniques - such as seismic and geoelectric surveys and gravimetric analysis - are applied. Drill cores are collected and a high number of samples are geochemically analyzed to set up a comprehensive database. Besides geochemical sampling the ore distribution is also mapped with RGB-scanners (the use of hyperspectral core scanning is becoming more frequent) and with UV induced fluorescence mapping. Moreover, micro-XRF scans along the core can be used in order to analyze gradual changes in the mineralization. Due to low penetration depths remote sensing techniques play a minor role in this phase. After this phase the grade of the deposit is determined and the metallurgical evaluation of the deposit is completed. In the following phase mineral extraction and ore processing is performed, a local infrastructure is set up, and the ore processing machines are installed. Remote sensing techniques are increasingly important to monitor possible environmental pollution and to track local enrichment zones. 3D hyperspectral pit mappings are in development and might play a bigger role in the future.

1.7 EnMAP – A Future Hyperspectral Satellite Mission

This chapter is based on the comprehensive publication of Guanter et al. 2015 [12]. The hyperspectral EnMAP imager is a dual-spectrometer sensor that utilizes the push broom principle. It covers the spectral range between 420 and 2450 nm. The mean spectral sampling distance is 6.5 nm in the VNIR region and 10 nm in the SWIR region. The ground sampling distance is 30 x 30 m and the swath width 30 km. The temporal resolution is 4 days with 30° across-track pointing and 27 days with nadir pointing. Its orbit is sun synchronous and the revisiting time is 11:00 h local time. The publicly available data products of the EnMAP are first, the radiometrically-corrected, spectrally- and geometrically-characterized radiance images (Level 1B); second, the orthorectified level 1B data product (Level 1C); and third, the atmospherically-corrected level 1C (Level 2a). Especially the level 2a data are of high value for the application in geological remote sensing, because most geological applications require a ready-to-use data product, including for example the radiometric corrections, rectification, and atmospheric correction. The level 2a data will be therefore the basis for most cases of future geological and mineralogical classifications of certain areas. Mineralogical classifications and the mapping of mineral deposits are amongst the key applications of the EnMAP mission. The hyperspectral analysis of sedimentation processes, or erosion processes and environmental monitoring in general - in the pre- and post-phase of geological exploration - are focused by the EnMAP science team. Other important application fields are agriculture, forests, natural ecosystems, soil science, coastal and inland waters, and urban development. The application-based algorithms will be collectively provided in the open-source tool box named "EnMAP-Box".

1.8 Literature

In this section the most important and relevant literature on the hyperspectral REE detection is listed and discussed to some extent.

A fundamentally important essay about the physical and chemical structure of rare earth ions and their emission spectra was published by Dieke and Crosswhite, 1963 [13]. Comprehensive reflectance spectral measurements on REOs, trivalent rare earth chlorides, and tungstates were published by White, 1967, and Jassie, 1964 [14,15]. In 1986, Rowan et al. describe hyperspectral measurements on REE bearing minerals and rocks [16]. They referred to Hunt, 1977, and proclaimed crystal field transitions as the physical interaction that is responsible for the observed absorption bands [3].

In the following years a multitude of studies on spaceborne multi- and hyperspectral REE detection were carried out. Some important investigations will be mentioned here, as they are relevant for this study and represent milestones in the field. 1995, Rowan et al. used an airborne hyperspectral survey to map a carbonatite-alkalic igneous complex [17]. Although they found neodymium absorptions in their field spectra, the maps were generated with the proxy minerals of the hostrocks. Ten years later, reflectance spectra of REEs were studied in greater detail. Kumar et al., 2007, measured the absorptions of chalcogenides-bound trivalent neodymium molecules [6]. They found out that ions of high electronegativity (fluorine) cause shifts of the absorption bands. Bedini, 2009, and Bedini and Tukiainen, 2009, used hyperspectral remote sensing data to map a carbonatite complex in West Greenland [18, 19]. They mapped proxy minerals and discovered that the mapping of REEs fails due to their low concentration and their narrow absorption depths. In 2011, Momose et al. mapped the proxy minerals of a pegmatite Li-REE deposit in an airborne hyperspectral dataset in southern Namibia and Hernandez and Filho, 2013, defined characteristic endmember spectra for carbonatite mapping in Brazil, using ASTER data [20, 21].

In 2013, Dai et al. presented hyperspectral measurements of dissolved REEs [22]. They correlated the intensity of REE diagnostic absorption features with the abundance of total dissolved REEs. Thus, they found a linear relationship between feature intensity and abundance, which was discovered for low concentrations (80-48 000 $\mu\text{g/L}$). One year later, in 2014, Turner et al. published a comprehensive study, which deals with hyperspectral analysis of fluorocarbonates [23]. They generated a detailed classification of distinct absorption bands and ascribed the probable origin of LREEs (Nd, Sm, Pr) to their responding wavelength positions. They reported a shift of REE absorption bands of a few nm and mentioned the sensitivity of the f-orbitals as one possible reason for the shifts.

2. Chapter

Development of the REE Detection Routine (REEMAP) and Comprehensive Spectroscopic Investigation of REO, REM, REE Bearing Minerals and Synthetic Samples

2.1 Hyperspectral REE (Rare Earth Element) Mapping of Outcrops—Applications for Neodymium Detection

(published: *Remote Sens.* 2015, 7(5), 5160-5186; doi:10.3390/rs70505160)

Nina Kristine Boesche ^{1,2,*}, Christian Rogass ¹, Christin Lubitz ¹, Maximilian Brell ¹, Sabrina Herrmann ¹, Christian Mielke ^{1,2}, Sabine Tonn ¹, Oona Appelt ¹, Uwe Altenberger ² and Hermann Kaufmann ¹

¹ GeoForschungsZentrum Potsdam, Helmholtz Zentrum, Telegrafenberg, 14473 Potsdam, Germany; E-Mails: rogass@gfz-potsdam.de (C.R.); christin.lubitz@gfz-potsdam.de (C.L.); brell@gfz-potsdam.de (M.B.); saherrma@gfz-potsdam.de (S.H.); chmielke@gfz-potsdam.de (C.M.); sabine.tonn@gfz-potsdam.de (S.T.); oona.appelt@gfz-potsdam.de (O.A.); charly.kaufmann@web.de (H.K.)

² Universität Potsdam, Karl-Liebknecht Str. 24-25, 14476 Potsdam-Golm, Germany; E-Mail: altenber@uni-potsdam.de

* Author to whom correspondence should be addressed; E-Mail: nina.boesche@gfz-potsdam.de; Tel.: +49-331-288-28775; Fax: +49-331-288-1192.

Academic Editors: Richard Gloaguen and Prasad S. Thenkabail

Received: 9 October 2014 / Accepted: 20 April 2015 / Published: 24 April 2015

Abstract: In this study, an in situ application for identifying neodymium (Nd) enriched surface materials that uses multitemporal hyperspectral images is presented (HySpex sensor). Because of the narrow shape and shallow absorption depth of the neodymium absorption feature, a method was developed for enhancing and extracting the necessary information for neodymium from image spectra, even under illumination conditions that are not optimal. For this purpose, the two following approaches were developed: (1) reducing noise and analyzing changing illumination conditions by averaging multitemporal image scenes and (2) enhancing the depth of the desired absorption band by deconvolving every image spectrum with a Gaussian curve while the rest of the spectrum remains unchanged (Richardson-Lucy deconvolution). To evaluate these findings, nine field samples from the Fen complex in Norway were analyzed using handheld X-ray fluorescence devices and by conducting detailed laboratory-based geochemical rare earth element determinations. The result is a qualitative outcrop map that highlights zones that are enriched in neodymium. To reduce the influences of non-optimal illumination, particularly at the studied site, a minimum of seven single acquisitions is required. Sharpening the neodymium absorption band allows for robust mapping, even at the outer zones of enrichment. From the geochemical investigations, we found that iron oxides decrease the applicability of the method. However, iron-related absorption bands can be used as secondary indicators for sulfidic ore zones that are mainly enriched with rare earth elements. In summary, we found that hyperspectral spectroscopy is a noninvasive, fast and cost-saving method for determining neodymium at outcrop surfaces.

Keywords: rare earth elements; imaging spectroscopy; neodymium; hyperspectral; HySpex; remote sensing; Fen complex

2.1.1 Introduction

Today, rare earth elements (REE) are of special interest for the global economy. Particularly, REEs are important in modern technologies, such as batteries, LCD displays, catalytic converters, and in green technologies, such as wind turbines. Rare earth metals include the chemical elements of lanthanides. Scandium and yttrium are often grouped together with the rare earth metals because both elements have similar chemical properties and frequently occur in the same deposits. Detecting possible future deposits and determining the concentrations and relative enrichment of REEs in carbonatites, silicocarbonatites, peralkaline granites and pegmatites are of interest for mineral exploration and mining processes. The world's largest REE deposits are mostly bound to carbonatites or their altered equivalents [1]. The geochemical investigation of REE distributions within outcrops and the characterization of parental melts are currently debated and are usually performed by conducting laboratory analyses or by collecting handheld X-ray fluorescence measurements at a single spot [2]. Here, we present a new method that uses a hyperspectral imaging spectrometer (HySpex camera) for mapping the distribution of neodymium at the surface of a carbonatite outcrop in southern Norway. Generally, hyperspectral imagers can be applied from micro (laboratory) to macro (airborne or spaceborne systems) scales. Moreover, hyperspectral imaging is an ideal technology for monitoring exploration, particularly for reducing the environmental impacts of mining and decreasing costs. This study focuses on characterizing the REE distribution at one outcrop from one type of carbonatitic REE deposit by using the HySpex imaging spectrometer system.

2.1.1.1 Introduction to Hyperspectral Data Acquisition

A hyperspectral sensor uses the photoelectric effect by collecting pairs of free electron holes in the detector element. The number of collected electrons is a function of the incident photons. Thus, the function of illumination is determined in the radiometric calibration process for each detector element [3]. Hyperspectral sensors can be classified as either imaging spectrometers (e.g., HySpex) or point spectrometers (e.g., ASD field spectrometer). Single point spectrometers measure the incident electromagnetic radiation within a solid angle, whereas imaging spectrometers (in this case, a push broom line scanner) consist of at least one detector array and detectors that are contemporarily illuminated by spectrally and spatially dispersed incident electromagnetic radiation. Hence, each detector element 'counts' photons from a solid angle across a specific wavelength range and the system is configured to enable continuous spatial and spectral acquisition. If the detector array or the scanning object is moved over time and space, each scan line of a hyperspectral image represents one time step with a certain integration time, which can be used to successively collect the hyperspectral data cube. The x-axis of a hyperspectral data cube represents the number of detectors (across-track), the y-axis represents the number of frames or time steps (along-track) and the z-axis represents the wavelengths (spectrum). Thus, each pixel represents a single spectrum that can be analyzed to retrieve information regarding geochemical properties. Depending on the sensor, between 100 and 10,000 different wavelength ranges (bands) can be recorded on the z-axis. Minerals, metals and organic materials absorb electromagnetic radiation differently according to their inner structure and chemical composition. This absorption is detected as concave indentations within the spectrum that are referred to as absorption features. The position of the peak is referred to as the absorption band. Technically, different ranges of the electromagnetic spectrum represent different materials. Most absorption in the visible, near infrared (VNIR: 350 nm–1000 nm) and shortwave infrared (SWIR: 1000 nm–2500 nm) ranges can be explained by vibrational overtones, electronic transitions, charge transfer and/or conduction processes [4].

2.1.1.2 Introduction to Imaging Spectroscopy Principles for the Classification of Rare Earth Element Bearing Minerals and Rocks

In addition to the public spectral library of the USGS [4], the reflectance spectra of different minerals and rocks and spectroscopic investigations of carbonatite rocks have been published [5–11]. Generally, classification applications utilize spectrum-matching techniques that compare unknown spectra with known spectra from spectral libraries (Cross-correlations, spectral angle mapper, support vector machines, spectral feature fitting, etc.) [12,13] and spectral unmixing algorithms (linear spectral unmixing, pixel purity index) [12,13]. All of these methods are usually applied across the entire spectrum. Absorption features that are widely used to characterize mineral deposits include clay minerals (approximately 2.2 μm), calcite (approximately 2.33 μm), dolomite (approximately 2.34 μm) and iron oxides (approximately 900 nm, 650 nm and 540 nm) [4,12–15]. All of these absorption features are considerably broad, and the most mineralogically important bands are located in the SWIR. Exceptions include the characteristic absorption bands of metal oxides, such as iron oxides, and most of the REEs. According to Rowan et al. 1986 [5] and White 1967 [16], the absorption bands of REEs can be physically and chemically explained by electronic field transitions. This goes back to the fact that the 4f orbitals are partially occupied in nearly all lanthanides [17]. Overall, two electrons can occupy 7f orbitals, resulting in 14 different electron configurations. Except for lanthanum and lutetium, which have f orbitals that are completely occupied or empty, incident electromagnetic radiation will be absorbed at the appropriate energy, which results in electron excitations. This absorption is mainly detectable in the ultraviolet, visible, and near infrared ranges [5,16,17]. For example, the peak positions of the key spectral characteristic absorption bands for neodymium are ~ 580 nm, ~ 740 nm, ~ 800 nm, and ~ 870 nm [5,6,8,16]. In the 1960s, various rare earth oxide and rare earth chloride spectra were published that show absorption features in the visible and near infrared ranges [16,17]. Moreover, less abundant and less pronounced absorptions occur in the SWIR, which are usually explained by vibrations in the crystal lattice or chemical bond lengths. It is unknown if this observation holds for absorptions in the SWIR range of REE bearing minerals. Another special property of REE-related absorption bands is their narrow shape, with the concave feature having a width of approximately 60–80 nm [5] (Figure 2.1.1). Two example spectra are shown in Figure 2.1.1. The first spectrum is from a hyperspectral integration of sand sized monazite crystals. The second spectrum integrates the fresh surface of a rock sample from the studied test site (see Chapter 2). The monazite sand was provided by Dan Harlov (REE percentage: La_2O_3 : 12.49, Ce_2O_3 : 28.77, Pr_2O_3 : 3.058, Nd_2O_3 : 12.28, Sm_2O_3 : 1.694, HREE < 1.6%) [18]. Due to the multiple absorption shapes of neodymium related absorption features when a high percentage of neodymium is present in the sample, we used a natural sample with a medium-high concentration to generate an example spectrum. In this study, the monazite sand provides a good basis for defining the peak positions of the features because multiple absorptions are not resolved with the used spectrometer. The spectra were measured using an Analytical Spectral Device (ASD) spectrometer [19] and by integrating a circular area with a diameter of approximately 2 cm. Each of the collected spectra represents a mean of 200 averaged ASD spectra. In both example spectra, the absorption bands at ~ 580 nm, ~ 740 nm, ~ 800 nm, and ~ 870 are resolved. These bands are attributed to neodymium based on the publications of [5,16,17,20–22].

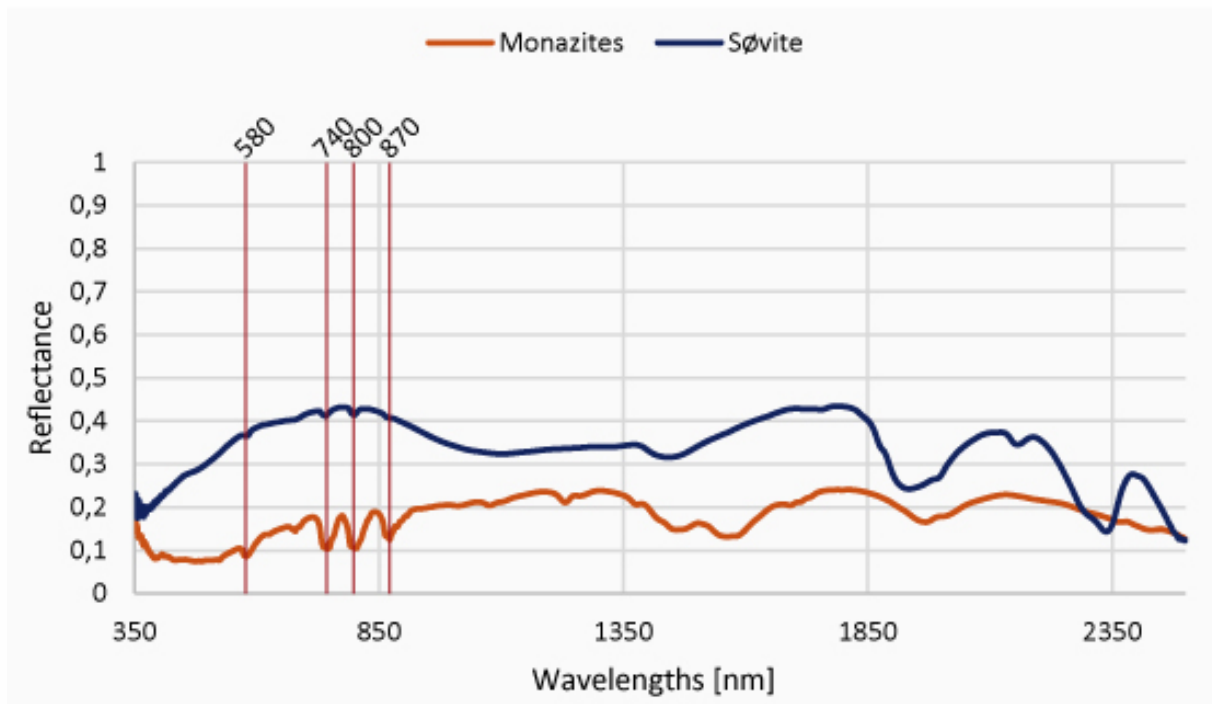


Figure 2.1.1. Two reference spectra for monazite (a neodymium-bearing mineral) and a monazite-rich rock sample (a calcitic carbonatite from the Fen complex). The key spectral characteristic absorption bands in the VNIR range that are associated with neodymium [5,16,17,20–22]. The graph is modified after Boesche et al. 2014 [23].

2.1.2 Geological Setting

The studied outcrop is located in an open cut natural mine located along Grønvoldvegen Road in Ulefoss, Nome, Norway (Figure 2.1.2) (location lat 59.282636°, lon 9.285511°). The outcrop consists of søvite type carbonatite rocks that are part of the Fen complex. This area was selected as the investigation area because it is widely recognized for its REE bearing igneous carbonate rocks. The Fen complex is formed from a Cambrian intrusion of alkaline and carbonatite melts that represent the volatile end fraction of a larger magma chamber, which probably lies beneath the surface [24–28]. Mitchell and Brunfeld [25] describe the søvites as a cap that lies on top of a urtite-ijolite-series (nepheline- and alkali-pyroxene-rich intrusions). The final liquids represent the less abundant silicocarbonites. During this sequence of intrusion, fenitization of the country rocks occurred [25,27]. The silica-undersaturated magma provided a source of fenitizing fluids that altered the gneissic wall rocks, mainly to the west of the oval-shaped complex [27]. A second phase of intrusion occurred of damtjernite (ultramafic) composition that was later altered and metasomatized to alkaline magnesio-calcite carbonatites (rauhaugite) and ferro-carbonatites (rødbergite) [25].

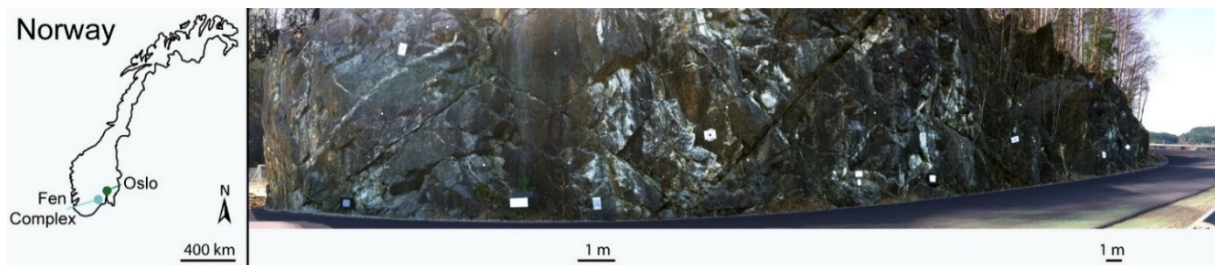


Figure 2.1.2. Map of Norway showing the location of the study area and a ~180 degree image that was collected as part of the HySpex data acquisition. The two scale bars below the outcrop image indicate a distance of one meter horizontally and represent their exact vertical locations. The image is compressed towards the edges because the rotational acquisition mode was used. The overview map is modified after Boesche et al. 2014 [23].

2.1.3 Methods

2.1.3.1 Remote Sensing Analyses

2.1.3.1.1 Instruments and Fieldwork Procedure

The studied søvite outcrop (calcite carbonatites and silico-carbonatites) is located along a two-lane coastal road at lake Norsjø and strikes from the southeast to northwest. The surface normal to the outcrop points east. Therefore, solar illumination that is spectroscopically beneficial only occurs during the early morning hours. However, due to cloud formation in the early morning hours and because of the highest sun elevation (peak position was at ca. 1.30 p.m. in April), the best recording time was at ~2.00 p.m. The outcrop is approximately 50 m long with a height of approximately 6 m. The HySpex hyperspectral imager used in this study consists of two sensors (HySpex VNIR 1600/SWIR320 m-e), one operating in the visible and near infrared (VNIR: 350 nm–1000 nm) and the other operating in the shortwave infrared (SWIR: 1000 nm–2500 nm) [29]. These sensors were mounted on a tripod with a rotation stage and the entire system was installed ca. 10 m in front of the outcrop and perpendicular to the assumed REE enriched zones (Figure 2.1.3).

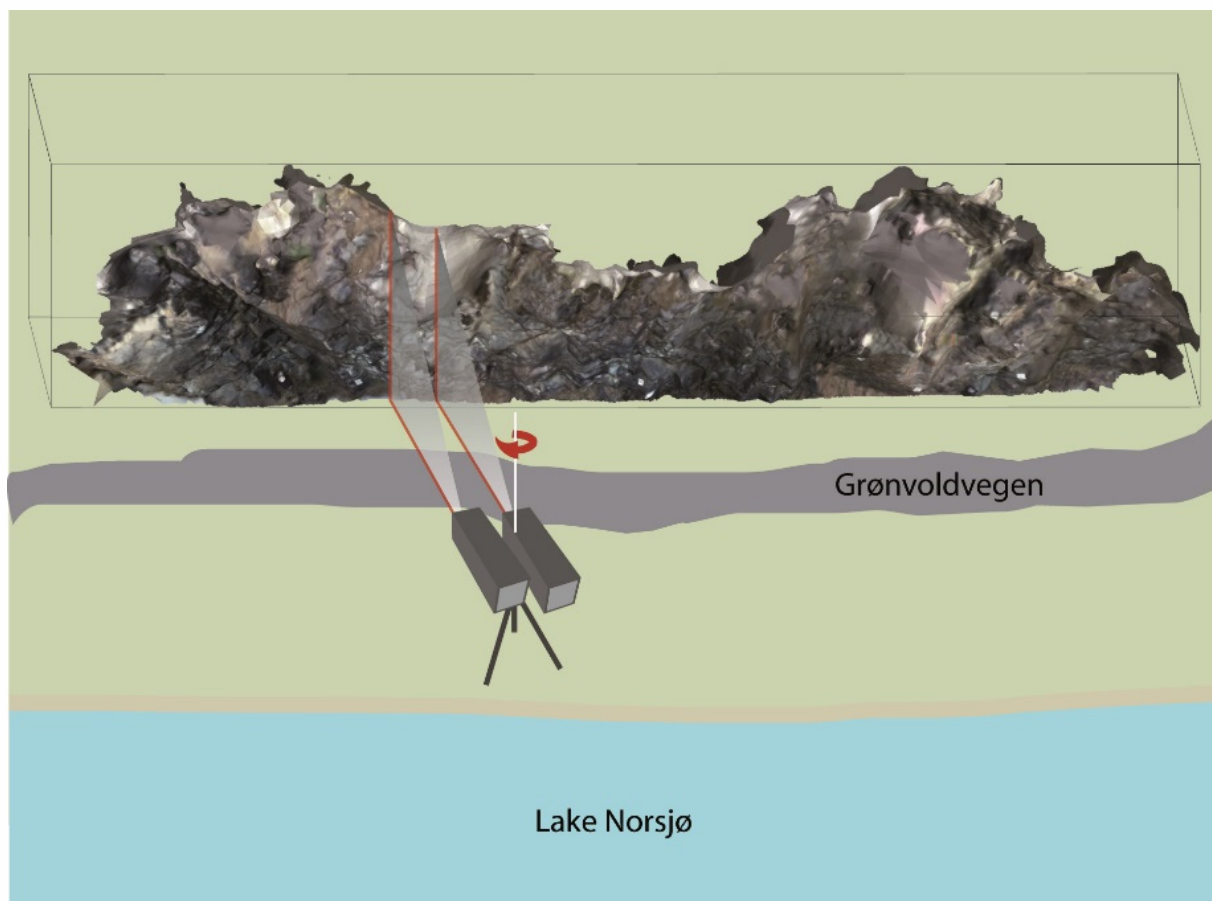


Figure 2.1.3. Experimental setup. The two HySpex cameras are located ca. 10 m in front of the outcrop. The measurement mode consisted of a clockwise rotation.

High spatial resolution (pixel size) and low geometric distortion were achieved at the position of the REE enriched zone. The edges of the acquired images were always more distorted due to the rotational scanning process of the system, particularly because a field-of-view expander was used. The rotational acquisition was performed clockwise (from left to right), and a single acquisition period lasted for approximately two minutes, depending on the number of frames and the frame period. In this study, we only analyzed the VNIR image scene because most of the REE related absorption bands occurred within this specific range. The overall system settings are provided in Table 2.1.1. The ground truth reflectance spectra of nine field samples (ground to a particle size < 63 μm) were obtained using an ASD Field spectrometer. We used a contact probe that was directly applied to the powdered samples to prevent stray light from superimposing the direct sample illumination and creating bias. Ground samples were used for these measurements because the ASD spectra were later compared with the chemical analyses results for the same sample powders.

Table 2.1.1. Campaign settings for the two HySpex cameras. A high integration time was used because direct illumination was not present and due to the low reflectance targets.

Camera	VNIR	SWIR
Integration time (ms)	30	30
Frame period (ms)	31	61.753
Frames (#)	4000	1110
Field of view ($^{\circ}$)	34 ¹	27 ¹
Spectral sampling interval (nm)	3.7	6
Radiometric resolution (bit)	12	14
Bands (#)	160	256
Detectors (pixel)	1600	320

¹ FOV is the Field Of View of the expander used to enable acquisition of nearly the full outcrop (height ~6 m in the VNIR, from a distance of 10 m).

2.1.3.1.2 Brief Description of the Proposed Approach

As shown in Figure 2.1.1, the REE related absorption features are so sharp that the spectral input of the entire spectrum would hamper the detection of small features within the matching algorithms due to the overestimation of the albedo and broad spectral signals (e.g., iron oxides). This result indicates the necessity of methods based on absorption bands, such as feature extraction [4] or modified Gaussian modeling [30]. These methods produce robust and reliable results for mineral mapping when the Signal-to-Noise Ratio (SNR) is high, when only minor topographical variations exist, and when atmospheric scattering is low. Under fieldwork conditions, these criteria are unrealistic. In addition, other hampering factors must be considered. The identification of REE bearing minerals is, for example, aggravated when surfaces are partly covered (e.g., by vegetation and/or surface weathering) [31]. Additionally, atmospheric absorptions are spectrally adjacent to REE related absorptions, or even superimpose them. Absorption bands of atmospheric molecules have an unpredictable shape that depends on the atmospheric pressure and temperature and on different isotopes within the molecules and aerosols [32]. Consequently, the detection of small REE related absorption bands is complex. To overcome these difficulties, we combined two detection methods. First, a multitemporal approach is used to reduce noise and varying illumination due to the positions of clouds and the sun. The integration time used for image acquisition was determined by compromising between the duration of image acquisition and the signal-to-noise ratio. If the signal-to-noise ratio had increased when a longer integration time was used, the time difference between the first and last frame would have been longer than two minutes. Having an acquisition window of more than two minutes, effects such as sun azimuth changes, cloud movement and the movement of cars passing through the image potentially resulted in variations in the image quality. However, every nearly full-frame image was assigned for its homogeneity, and the best recording times at this particular location were determined. Next, the homogeneity parameters were used to obtain a weighted average of all

scenes. Second (and afterwards), Richardson-Lucy deconvolution (R-L deconvolution), which is widely used to sharpen signals, was applied [33]. R-L deconvolution is performed according to the following principle. If absorptions are characterized by means of the albedo, all small but sharp absorption bands can be considered as high frequency contributions to the low frequency albedo signal according to signal processing theory. Thus, the wavelength dependent impulse noise would have a high frequency, and spectrally broad iron oxide absorptions would have a low frequency. Although a single absorption band only represents one oscillation, it is associated with a certain frequency. Hence, a full spectrum represents superimpositions of different frequencies that are located in certain ranges of the electromagnetic spectrum. Mathematically, R-L deconvolution is applied to enhance the spectral contrast for the frequencies that are related to REE absorptions. This specific high pass technique mainly sharpens absorptions, such as those from rare earth bearing minerals, and simultaneously preserves the shape of broader absorptions or the albedo. The absorption features have a shape that is similar to a Gaussian curve; thus, a Gaussian function was selected as a filter for R-L deconvolution. This function also addresses the assumption that the absorption bands represent a Gaussian distribution, regardless of the type of absorption (electronic field transitions or molecular motions) [34]. The definition of sigma for the Gaussian filter is a function of the desired REE absorption bands and must be selected beforehand. Here, the frequency of the Gaussian-shaped filter is twice the frequency of the smallest REE feature to avoid aliasing following the Nyquist Shannon theorem. The 70 nm wide neodymium feature that is the focus of this work can be observed in 18 VNIR HySpex channels. When the positive and negative 3σ interval (including 99.7% of the integral area) is equivalent to the filter width (here: 9 channels), sigma is calculated with a standard deviation of $\sigma = 1.5$.

2.1.3.1.3 Proposed Approach

Step 1 (Figure 2.1.4) is to collect multitemporal image scenes that must be transformed to reflectance data. For this study, five different reference panels are used for reflectance retrieval. These reference panels contain 5%, 20%, 50%, 90% and 95% calibrated reflectance standards and approximate the optimal Lambertian reflectance targets. Regarding the spatial shape of the outcrop, the 20% panel was mounted near the left edge of the outcrop, the 90% panel was mounted near the right edge of the outcrop and the 5%, 50% and 95% panels were mounted in the center with the normal surface of each panel oriented to the rotating sensor. The panels are measured during each acquisition to enable reflectance retrieval for each image. After measuring the raw Digital Number (DN), the data were radiometrically scaled to radiance ($W \cdot sr^{-1} \cdot m^{-2}$) by using radiometric calibration coefficients. Reflectance retrieval was performed by incorporating the panel-specific spectral and spatial averages. All panels were spatially delineated in each image set (an image set has the same acquisition properties). All pixel spectra for each panel were averaged to obtain mean panel spectra (as radiance) and successively normalized based on their reflectance level (e.g., 5%). A second order or greater order polynomial model was estimated for each image and band integrating all of the averaged and normalized panel spectra as gray values per band and image and their respective spatial position (pixel). Next, the polynomial model was inverted and applied pixel-wise to the image to retrieve the portion of incident radiation per image, band and pixel (irradiance). Next, this hyperspectral irradiance cube was used to normalize previously derived radiance values. Hence, reflectance retrieval was performed by rationing radiance to irradiance. After reflectance retrieval for each individual scene, a multitemporal average was generated by calculating a weighted mean of all single images. For this purpose, individual reflectance data cubes were evaluated with respect to the quality of each scene by analyzing the reference panels for spectral homogeneity. Spectral homogeneity was determined by calculating the standard deviations of all pixel spectra at the panel locations within the wavelength range where neodymium absorption features occur. The average for all scenes was calculated using a normalized weighting factor according to the spectral homogeneity as follows:

$$\bar{im} = \sum_i \frac{|\overline{WR} - WR_i|}{\sum_i |\overline{WR} - WR_i|} \cdot im_i \quad (1)$$

where WR represents all image pixels of the white references within the image scenes, im is the image scene and i is the running number of all collected images that are to be averaged.

In step 2 of this approach, each spectrum of the averaged image scene was smoothed using a Gaussian filter with the same sigma used for the R-L deconvolution to suppress the remaining noise. In addition, the spectrum was further transformed into relative absorption by using the following equation:

$$S = S(x, y, \lambda) = \log \frac{1}{\bar{im}(x, y, \lambda)} \quad (2)$$

where $S(x, y, \lambda)$ represents the smoothed absorption spectra of the averaged image scene (im). R-L deconvolution was conducted for every absorption spectrum $S(x, y, \lambda)$ following the principle that the Hadamard product of the Fourier transforms in the frequency domain equals convolution in the local domain. Here, the Hadamard product is the product of the initial image spectrum $S(x, y, \lambda)$ and the filter function (H), which provides the deconvolution term as follows:

$$S^{i+1} = S^i \circ H(x, y, \lambda) \quad (3)$$

$$H = H(x, y, \lambda) = \frac{\mathcal{F}\{S^0\}}{\mathcal{F}\{S^i * f\}} f \quad (4)$$

The input spectrum S^i is the spectrum of a single pixel (x, y) and is flipped upside down due to Equation (2). In addition, f is the filter function for R-L deconvolution and is the Gaussian distribution with a standard deviation $\sigma = 1.5$.

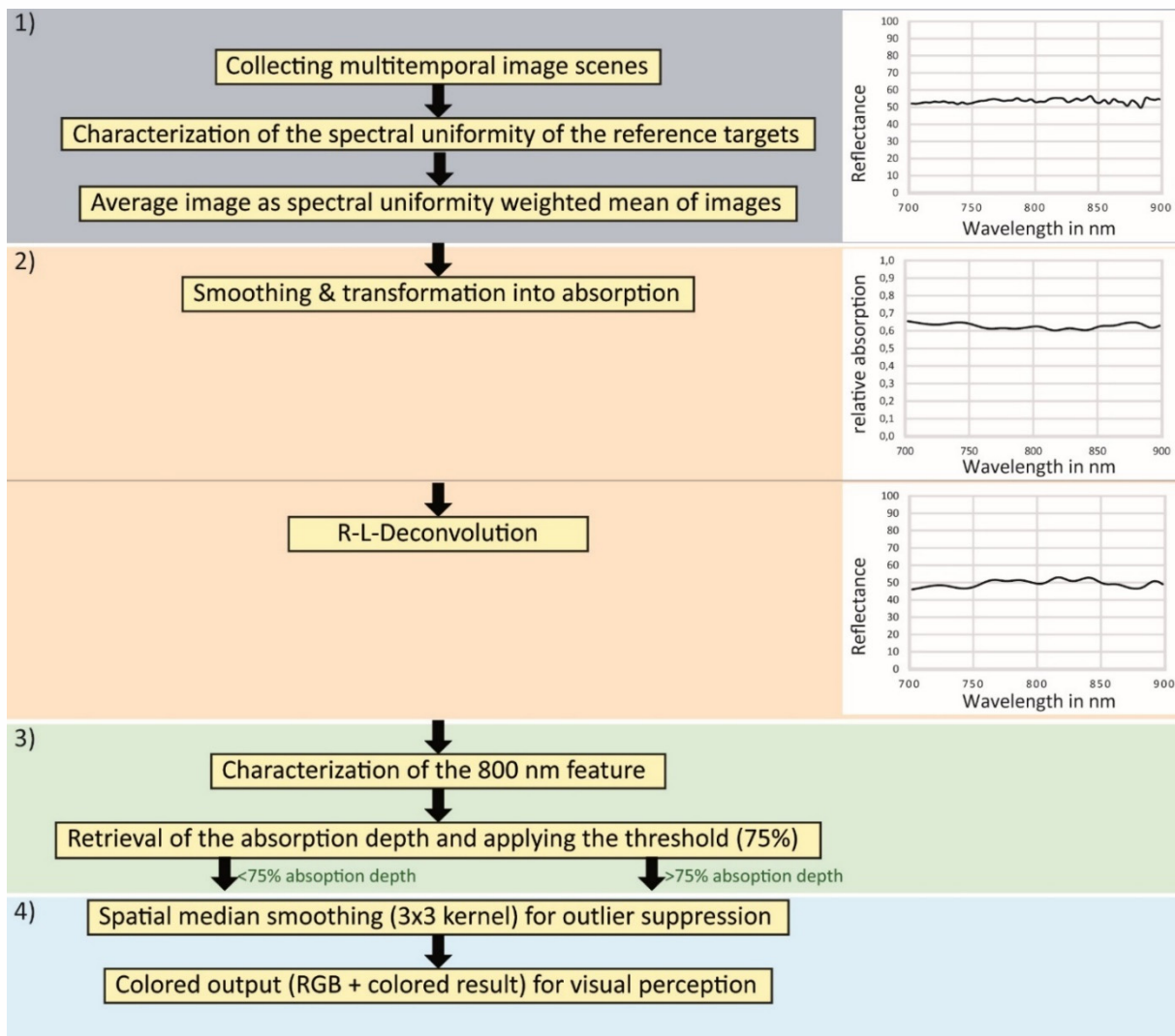


Figure 2.1.4. Flow Chart of the REE mapping approach showing the four main steps of its application. The first step is the collection of the multitemporal data cube and preprocessing. The second step is the application of Richardson-Lucy deconvolution. The third step is the identification and characterization of indicative and discriminative absorption bands and image pixel clustering. The fourth step describes the post-processing of the data and visualization.

In step 3, the spectra were exponentially transformed back to reflectance and the resulting spectra were directly used in the following steps to detect pixels that did or did not indicate REEs. The bands that were spectrally closest to the shoulders of the 800 nm neodymium feature were selected, and the spectra between the shoulders were normalized using a straight line between the shoulders in a procedure known as continuum removal for features. After continuum normalization, the differences between the continuum and the peak of the absorption band were computed to retrieve the absorption depth. The peak of the absorption feature was determined precisely by resampling the reference spectrum from Figure 2.1.2 to the spectral channels of the HySpex imager (the 800 nm peak appeared at 803 nm). The positions of the two shoulders were determined using a continuum removal method (convex hull) for the down-sampled reference spectra. The left shoulder is at 778 nm and the right shoulder is at 840 nm. If the absorption depth of a pixel spectrum was higher than the three sigma of the noise (according to the averaged SNR) it was flagged as a REE indicative pixel. Step 4 includes outlier suppression using median filtering (here: 3×3 kernel) and coloring of the results.

2.1.3.2 Geochemical Analysis Tools for Retrieving Complimentary Information

2.1.3.2.1 Brief Theoretical Background of the Geochemical Methods and Sampling Design

The imaging spectroscopy methods delivered a high-resolution synopsis of the enriched and non-enriched areas of the surface of the outcrop. In addition, geochemical methods contribute to the exact quantitative compositional analyses of certain points. To obtain an overview of the REE distribution and further indications of the carbonatite-forming processes, several rock samples were collected along the outcrop. Their chemical and mineralogical compositions were analyzed from pulverized samples and thin sections thereby using three different methods. The first method was inductively coupled plasma atomic emission spectroscopy (ICP-AES), which was used to determine the REE concentrations of the pulverized samples. The second method was handheld X-ray fluorescence analysis of the same pulverized samples. The third method used an electron microprobe (EMPA) to characterize the composition of the REE-mineral monazite within thin sections. When validating the performance of the REE mapping method by geochemical analysis, it must be remembered that remote sensing techniques only penetrate the upper nm of the material. The surface penetration depth is wavelength dependent, and is half that of the center wavelength. Thus, remote sensing techniques can only determine the amounts of REEs within the weathered surface. Thus, it is important to sample thin chips (a few millimeters to one centimeter thick). In addition, if the samples contain too much fresh rock material, they must be cut parallel to the weathering surface and the fresh rock must be discarded. Because both positive and negative spectroscopic indications must be evaluated, rock samples were collected based on a preliminary image analysis using the 2.3 nm calcite feature and geologic field observations at the outcrop. These findings and the macroscopic analysis of the outcrop were used to identify sample locations (Figure 2.1.5). Generally, the outcrop was macroscopically divided into three rock units. The first unit consists of the carbonatite surrounding rocks of fenite, which mainly consist of silicate minerals (albite, potassic feldspar, quartz). The second and third rock units were established in schlieren and consist of melano-carbonatites (melanocrate minerals: biotite, iron oxides, pyrite, hornblende) and leuco-carbonatites (leucocrate minerals: carbonates, mica). Samples of these types of rocks were collected and were macroscopically determined to include REE-enriched carbonatites (HREE), medium REE-enriched carbonatites (MREE) and of less REE-enriched carbonatites (LREE). The geochemical results showed that samples 7L and 8L were not macroscopically classified in the field and actually were highly enriched samples.

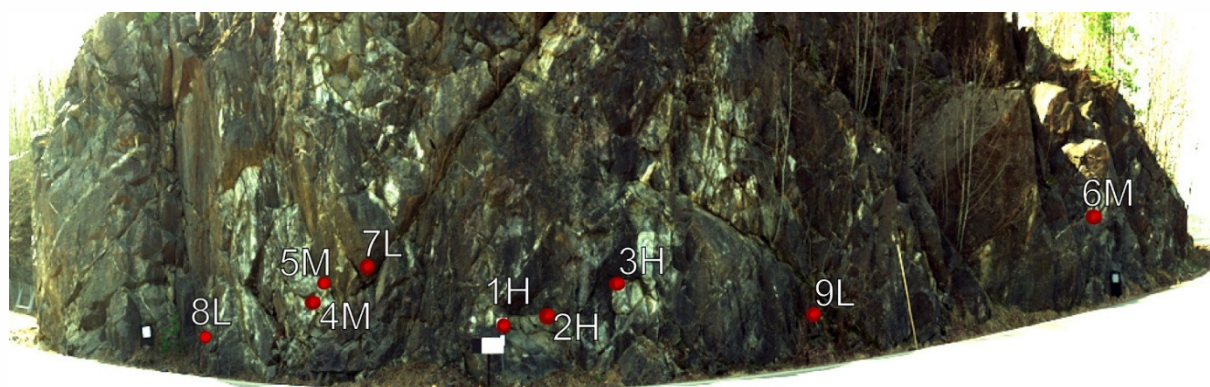


Figure 2.1.5. Sampling positions of the nine collected field samples. The letters within the descriptions of the sample locations represent the in situ interpretations of the relative sample enrichment (H-high, M-middle, L-low).

2.1.3.2.2 Realization and Instrumentation for Chemical Analysis

To validate the spectroscopic results, four geochemical analyses were conducted. Three methods were used to determine the elemental compositions of the field samples (see Section 3.2.1). The fourth method involved an analysis of the spectral behaviors of different artificial mixtures of neodymium and calcite carbonate. When used on the field samples, the first method was helpful for determining the REE concentration. Nine rock samples were ground to a particle size of less than 63 μm . After sample preparation, chromatographic separation was applied using a Na_2O_2 sinter dissolution procedure before ion-exchange separation [35]. Then, geochemical analyses were performed using ICP-AES [35]. All results were normalized to C1-chondrite [36]. The second method was used to determine the major elemental abundances of rock samples and all other elements that could not be detected using ICP-AES. To accomplish this, the powder from the first method was further analyzed by using a handheld XRF instrument (Thermo Niton XL3) [37]. The third method included the mineral analysis of thin sections by using an electron microprobe (EMPA). The rock samples were cut into slabs to produce polished thin sections with a thickness of 30 μm that were coated with a layer of carbon. The thin sections were analyzed to determine the elemental compositions of the different monazite crystals by using a stationary electron microprobe (SuperProbe Jeol JXA-8230) [38]. The fourth method was used to estimate the extent at which the collection of hyperspectral images from the outcrop could be used to quantitatively determine the REE contents. Therefore, a series of artificial mixtures was measured in the laboratory and compared with the hyperspectral field recordings. For this purpose, certain amounts of neodymium oxide were mixed with calcium carbonate. The neodymium and calcium carbonate powders both had grain sizes of less than 63 μm . The investigated neodymium oxide percentages were approximately 0.1%, 0.5%, 1.0%, 2.0% and 5.0%. The exact concentrations were achieved using a precision digital scale. All mixtures were spectroscopically measured using the HySpex hyperspectral imager in the laboratory and their absorption depths at 803 nm were determined. As described in the chapter regarding the proposed method, the absorption depth was achieved by subtracting the reflectance value of the absorption band from the corresponding value at the feature-based continuum.

2.1.4 Results

2.1.4.1 Spectroscopy

The results of the proposed method include a thematic map that highlights the positively identified neodymium pixels in red (Figure 2.1.6). The reference panels and ground control points are covered in black. From the first in situ macroscopic descriptions and discrete spectroscopic measurements (ASD field spectrometer), areas of potentially high and low neodymium concentrations were identified. These zones are visible as whitish zones that were identified as leuco-carbonatites, bluish to light-brown zones of silico-carbonatites and silicate rocks (fenites) and brownish zones of melano-carbonatites according to geochemical testing. The hyperspectral mapping results from the introduced approach successively confirmed the presence of neodymium-enriched carbonatites (Figure 2.1.6). Particularly, one important finding is that the outer regions of the neodymium-enriched zones (transition zones from highly enriched rocks to less concentrated ore zones) are still recognized. Thus, the zones with different compositions can be mapped better, including their gradual decrease in the direction of the outer contact zone (Figure 2.1.6a). In addition, REE containing pixels could still be identified when covered with a very small weathering layer or thin, small-scale vegetation layer (e.g., tiny lichens). At points with dense vegetation cover, soil forming on the top of the protruding morphology or a dense weathering surface, continuous positive detection was not possible because iron coatings hamper the detection of any underlying materials [15]. In addition, the remaining individual positive findings (1 to 4 adjacent pixels) were mostly deleted by the median filter. Melano-carbonatites are one example of a weathered rock and are brownish in color due to iron oxide coatings. The upper right corner in Figure 2.1.6 shows false positive identifications. The most plausible explanation for these false positives is the presence of transmissions from the leaves of small plants (moss, young plants and grass) growing on the outcrop.

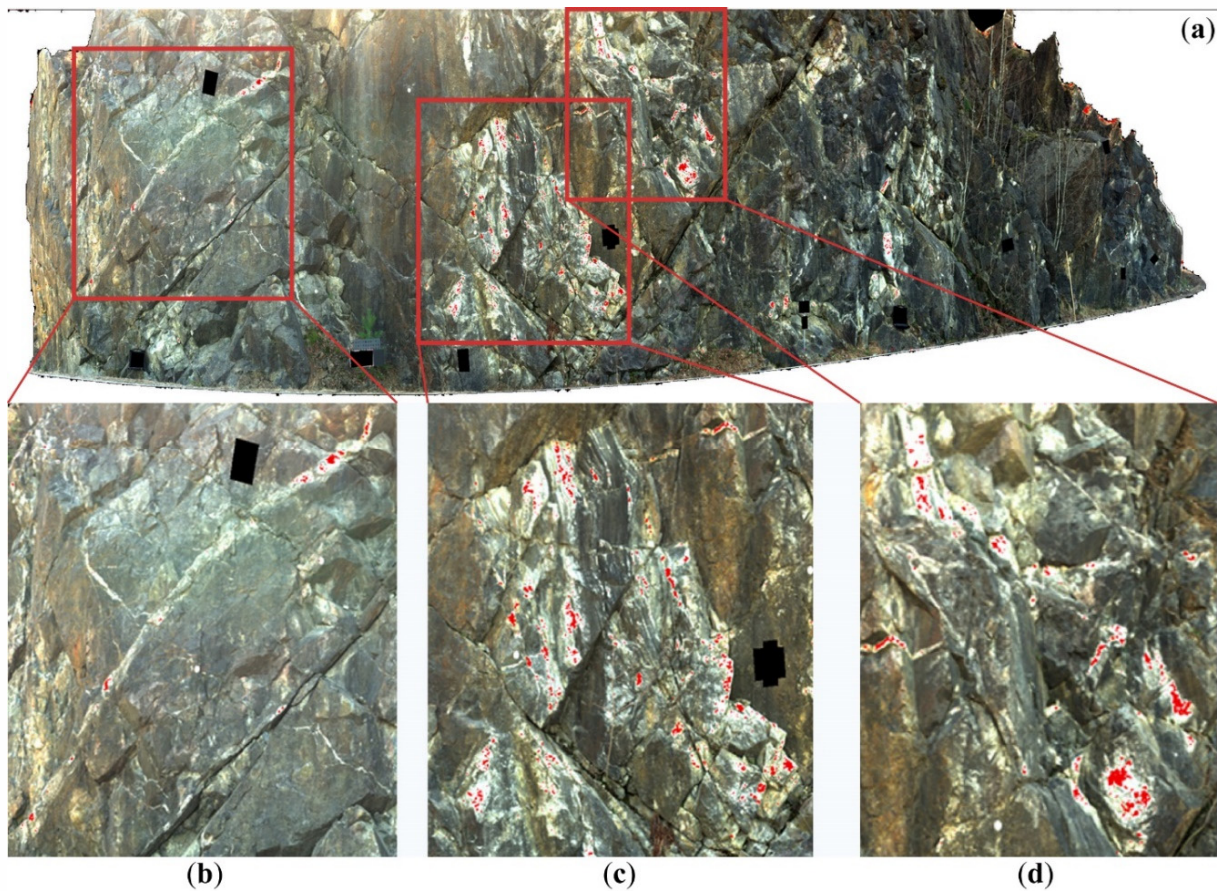


Figure 2.1.6. (a) REE thematic map of the søvite outcrop based on R-L deconvolution and combined with absorption depth determination. Red pixels indicate the enriched portion of the outcrop; (b–d) are the zoom images of the most important zones. Reference panels and the ground control points (for georeferencing) are colored black. The image highlights the local neodymium distribution as an indicator for LREE. The center area (c,d) is especially enriched in neodymium within the surface material that spatially follows the structured bands of alternating white and bluish weathering surfaces. Moreover, a ca. 4 m long band can be observed on the left portion of the outcrop (b) that is partly identified as containing neodymium oxide. Modified after Boesche et al. 2014 [23].

2.1.4.2 Chemistry and Mineralogy

Compared with the REE distribution pattern published in [39], the distribution diagrams that were obtained for the ground truth samples (ICP-AES) show two different types of REE distributions (Figure 2.1.7). Although one distribution type represents rock types that consist of pure calcite-carbonatites (Figure 2.1.7a,b), the second type consists of siderite-bearing carbonatites (Figure 2.1.7c). The first type of distribution is represented by samples 1H, 2H, 3H, 4M, 5M, 6M and 9L and corresponds with the REE distributions published in Hornig-Kjarsgaard 1998 [39]. The second type of distribution is represented by samples 7L and 8L and shows a trend for the LREE that has been published for sulfide bearing søvites in Phalaborwa, South Africa [39]. In contrast with the steep slope towards the HREE in the Phalaborwa samples [39], the analyzed Fen samples plateau towards the HREE. All samples show a positive $(La/Lu)_{(n)}$ ratio that ranges from 30 in the first group to 170 in the second group (i.e., siderite-bearing carbonatites) (Figure 2.1.7, Table 2.1.2). The highest LREE concentrations (La, Ce, Pr, Nd, Sm) within the first type (calcite-carbonatite) were obtained for sample 6M, with a concentration of approximately 860 ppm, and for sample 5M, with a concentration of approximately 1270 ppm. The second type (siderite-bearing carbonatite) shows high concentrations of the middle REEs (Eu, Gd, Tb, Dy). Compared with the first rock type (ca. 40 ppm MREE in total), the second rock type contains up

to 290 ppm MREE with a total LREE of up to 1900 ppm. The handheld XRF measurements show the main differences between the two types of iron and the sulfur contents (see Table 2.1.3). In addition, pyrite was also visible in the hand specimen and on the outcrop surfaces.

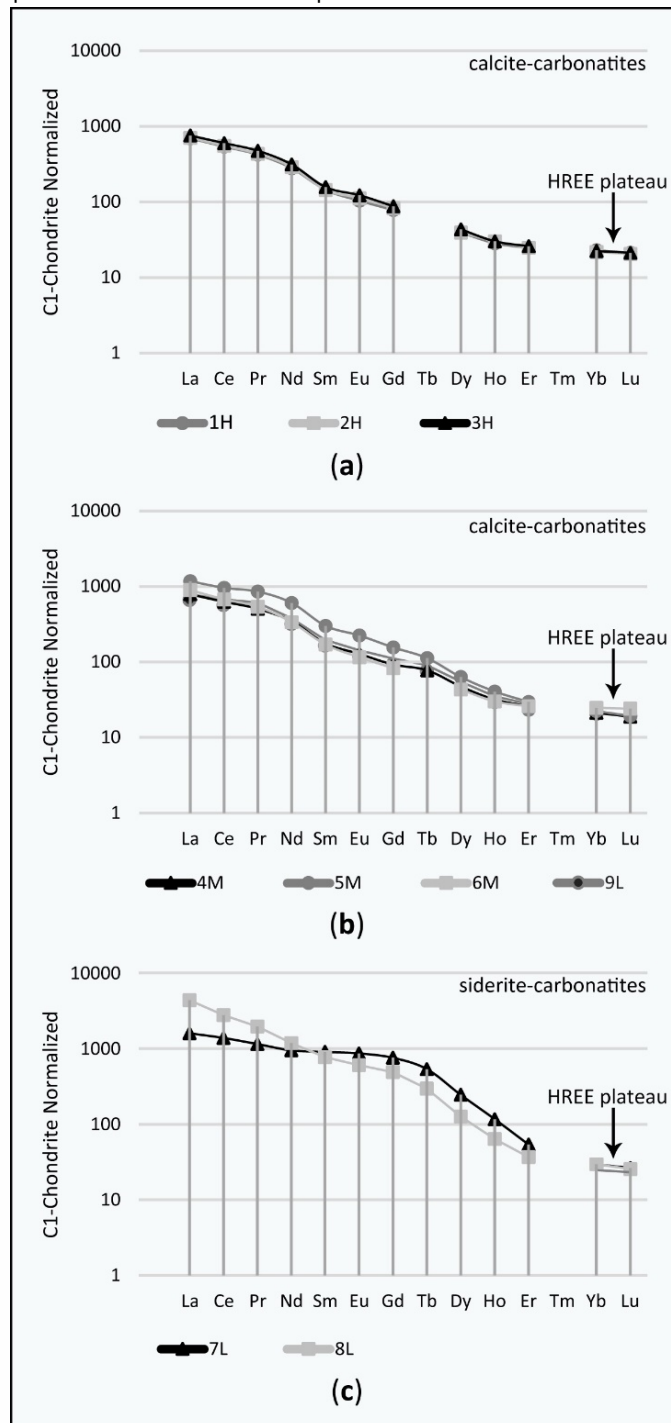


Figure 2.1.7. REE distribution patterns of nine collected field samples. The values are normalized to C1-chondrite [36]. Graph (a) shows the REE distribution patterns of samples 1H, 2H and 3H that were expected for the søvite outcrop, as published by [39]; Graph (b) shows four REE distributions of samples 4M, 5M, 6M, and 9L that mainly belong to the calcite-carbonatite rocks shown in graph (a). Sample 5M shows a slightly higher enrichment of light REE (LREE_(n)) and middle REE (MREE_(n)), but with the same distribution patterns as those for the samples in graph (a); Graph (c) shows different distributions that represent siderite-bearing carbonatites (7L and 8L) and indicates higher LREE_(n) and MREE_(n) concentrations. However, the MREE_(n) indicates a positive anomaly. The curves plateau towards the heavy REEs (HREE_(n)) in all three graphs.

The microscale analyses for both rock types showed evenly distributed rare earth minerals (mainly Ce-monazites and parisites; Table 2.1.4) within a matrix of calcite and some allanite. The monazites and parisites appear to represent different stages of fractionation evolution or epigenetic hydrothermal overprint. Few Ti-rich Fe-columbites occur. The ore rocks are sporadically veined. Some parisites include thorite or uraninite. Minor mineral occurrences of hematite needles, apatites, pyrites, ilmenites and barytes are present. The average composition of the monazites is provided in Table 2.1.4.

Table 2.1.2. Concentrations of REEs in the nine ground samples (ppm) and the C1-chondrite normalizing factors. Cerium (Ce) and gadolinium (Gd) show the differences between the two classes of rocks. Cerium represents the distribution of the LREE and gadolinium represents enrichment within the MREEs in samples 7L and 8L. N/A are either values that are not provided in the cited literature or are erroneous ICP-AES measurements.

	C1-Chondrite	1H	2H	3H	4M	5M	6M	7L	8L	9L
Y	N/A	48	49	51	53	61	50	168	89	58
La	0.237	164	167	179	186	278	212	377	1032	186
Ce	0.612	330	338	367	383	587	413	845	1699	413
Pr	0.095	40	41	45	48	81	51	109	185	58
Nd	0.467	130	135	146	161	282	157	442	550	178
Sm	0.153	22	22	24	27	46	26	138	118	30
Eu	0.058	6	6.5	7.1	7.4	13	6.7	50	35	8.3
Gd	0.2055	16	17	18	19	32	17	155	100	23
Tb	0.0374	N/A	N/A	N/A	2.9	4.2	N/A	20	11	3.4
Dy	0.254	10	10	11	12	16	11	62	32	14
Ho	0.0566	1.6	1.7	1.7	1.8	2.3	1.7	6.6	3.6	2.0
Er	0.1655	4.1	4.1	4.3	4.3	4.9	4.3	8.9	6.1	4.6
Tm	0.0255	N/A								
Yb	0.17	3.9	3.7	3.8	3.6	3.8	4.2	5.0	5.0	4.2
Lu	0.0254	0.54	0.52	0.54	0.48	0.49	0.61	0.67	0.65	0.59
Sc	N/A	2.2	2	3.6	2.1	2.9	3.7	74	33	5.3

Table 2.1.3. Elemental compositions of nine ground field samples analyzed using the handheld XRF. All samples had calcium concentrations of between ca. 35% and 45%. The lower calcium concentrations were observed in samples 7L and 8L. These two samples also had higher concentrations of iron, yttrium, thorium and uranium. However, all samples can be subdivided into pure calcium carbonatites (1H, 2H, 3H, 4M, 5M, 6M and 9L) and the two siderite bearing carbonatite samples enriched with Th, U, Y and REEs (7L and 8L). LOD represents the limit of detection.

Reading No.	1H	2H	3H	4M	5M	6M	7L	8L	9L
Duration of measurement (s)	122.79	124.86	132.57	123.58	121.99	120.58	124.35	123.32	123.38
Units	ppm								
Nb	2493.48	1155.47	1694.60	2094.15	2963.61	521.13	4748.08	1578.00	1447.73
Y	62.31	59.15	58.60	63.69	71.98	58.74	176.11	111.74	64.98
Th	<LOD	480.00	<LOD						
U	<LOD	<LOD	<LOD	<LOD	<LOD	<LOD	121.81	<LOD	<LOD
Units	percent								
Fe	0.64	0.26	0.38	0.29	0.67	0.38	3.87	4.50	0.84
Ca	43.35	43.24	43.33	43.69	41.39	43.29	32.32	36.23	42.56
K	0.16	0.06	0.12	<LOD	0.09	<LOD	0.13	0.09	0.06
S	0.13	<LOD	<LOD	<LOD	0.08	<LOD	0.44	1.05	0.23
P	0.24	0.34	0.55	0.70	2.46	0.20	1.03	0.41	0.44
Si	1.03	0.66	1.25	0.44	1.03	0.43	1.17	0.81	0.77
Cl	0.01	0.01	0.01	<LOD	0.01	0.01	0.01	0.01	0.02
Mn	0.31	0.24	0.35	0.26	0.43	0.47	0.54	0.42	0.36
Al	<LOD								
Mg	<LOD								
Not detectable	52.91	53.99	52.72	53.53	52.67	54.28	57.42	54.99	53.98
Total	99.21	99.10	99.04	99.33	99.40	99.29	97.75	99.12	99.52

Table 2.1.4. Averaged elemental concentrations of 19 individual monazite crystals. All monazites are pure calcium carbonatite rocks, and due to the high amounts of cerium, all monazites are Ce-monazites. The presented values were determined by using electron microprobe analyses.

Element Oxide	Average Weight Percent of 19 Monazite Measurements
P ₂ O ₅	30.05
CaO	0.79
SiO ₂	0.35
Al ₂ O ₃	0.04
FeO	0.36
Y ₂ O ₃	0.12
La ₂ O ₃	12.98
Ce ₂ O ₃	31.83
Nd ₂ O ₃	15.61
Pr ₂ O ₃	4.00
Sm ₂ O ₃	1.81
Gd ₂ O ₃	0.60
Tb ₂ O ₃	0.03
Dy ₂ O ₃	0.08
Ho ₂ O ₃	0.01
Er ₂ O ₃	0.03
Yb ₂ O ₃	0.01
Lu ₂ O ₃	<LOD
ThO ₂	0.22
UO ₂	<LOD
PbO	0.02
Total	98.94

2.1.5 Discussion

2.1.5.1 Validation of the Proposed Method, the Richardson Lucy Deconvolution and the Multitemporal Approach.

To discuss the benefits of R-L deconvolution, the results from only using the absorption band depth determination method and the results from after applying R-L deconvolution were compared. Many absorption bands were not identified until deconvolution strengthened them and made them detectable. Figures 2.1.8 and 2.1.9 show that detection using R-L deconvolution was beneficial, especially for transitional zones with less prominent features. The graphs in Figure 2.1.8 show four different spectra of pixels that are good examples for different neodymium concentrations at the outcrop and are verified by geochemical sample analysis (sample position 1H, Figure 2.1.5). The straight line in each spectrum shows the continuum of the feature that was anchored at the shoulders of the 803 nm feature. The value in the legend indicates the absorption depth (which is the difference between the absorption band at 803 nm and the corresponding value of the continuum). Negative values represent non-enriched pixels because no defined absorption bands are mathematically describable. The yellow spectrum is extracted at the center of the ore zone and the red spectrum is extracted at the wall rocks of the carbonatite. The pixels that mark the transition between the ore zone and the wall rocks of the carbonatite are represented by orange and green spectra. The difference between the simple absorption depth determination and the determination of absorption depth is especially visible for those pixels after applying the introduced deconvolution approach. While the orange and yellow spectra can still be described with an absorption feature at 803 nm in both graphs, the green spectrum of the simple approach did not show any absorption features until after R-L deconvolution was applied. Thus, the introduced approach was helpful for more accurately delineating the borders of enriched zones. Figure 2.1.9 shows the final mapping results of the outcrop without using the introduced approach and compares the zoom images with those shown in Figure 2.1.6.

Regarding the low image SNR, several image collections were taken using a multitemporal approach. Ten images were necessary for obtaining a good quality average. To determine the minimum number of images required for the first, quick REE detection and the number of images required for a high-quality product, all scenes were sorted with respect to reflectance panel homogeneity. Then, for each run of the introduced approach, each of the sorted images was added individually in descending order of their homogeneity. After every run, a REE thematic map was generated. After ten runs, all of the resulting maps were classified. To classify all of the indicative pixels for each resulting image into statistically significant quantiles (here four classes), the absorption depths of all spectra were scaled to values of 0 to 255, which is a broadly accepted 8-Bit image quantization technique for suppressing noisy outliers. Consequently, every image had the same maximum absorption value and scaling. To establish the four classes as quantiles of the abundance distribution, percentage values were used to improve the interpretability. The first class or 10-quantile comprises all pixels with spectra showing absorption depths of between 100% and 90% (255–230 absorption depth value). In addition, the second class or 10-quantile encompasses between 90% and 80% (230–204 absorption depth value), the third class or 5-quantile encompasses between 80% and 75% (204–190 absorption depth value), and the last class or 4-quantile represents the pixels that are below 75% (190 absorption depth value) or do not show a significant absorption band (0 to negative absorption depths). To compare the ten classification results with each other, we extracted a predefined region of interest that only covers the pixel that were flagged as neodymium enriched in the ten-fold weighted average image (11,343 pixel). Because the ten-fold average likely provides the most reliable result, we assumed that all neodymium rich flagged pixels were correctly classified. Hence, the following comparison is restricted to the relative omission classification error when less than ten images were used. The commission error and the absolute omission error are not testable in this case because a dense grid of ground truth sampling (several hundred to be statistically accurate) was not possible in terms of the laboratory analysis periods for geochemical REE analysis. The results (Figure 2.1.10) show that the accuracy of the classification is not increasing linearly for all quantiles. Regarding the pixels that show strong features within the spectrum (absorption depths of between 90% and 100%), the number of correctly classified pixels does not change significantly as the

number of averaged scenes increases (Figure 2.1.10). The same independence of the number of averaged scenes can be observed for non-indicative pixels. However, for pixels that mark the transition zone between carbonatite surrounding rocks and the ore zone (90% to 80%), the average number of scenes is very relevant. In this study, seven scenes were required to observe an increase in the neodymium detection accuracy within these transition zones. With each additional scene, a noticeable increase in accuracy was observed. Finally, the noise depends on many factors (weather, instrument characteristics, multiple reflections of surrounding objects (trees, buildings, cars, lakes, etc.)) that noise estimations would always count under specific measurement conditions. However, the question of how many scenes one would need under similar conditions to obtain an improved classification result could be answered.

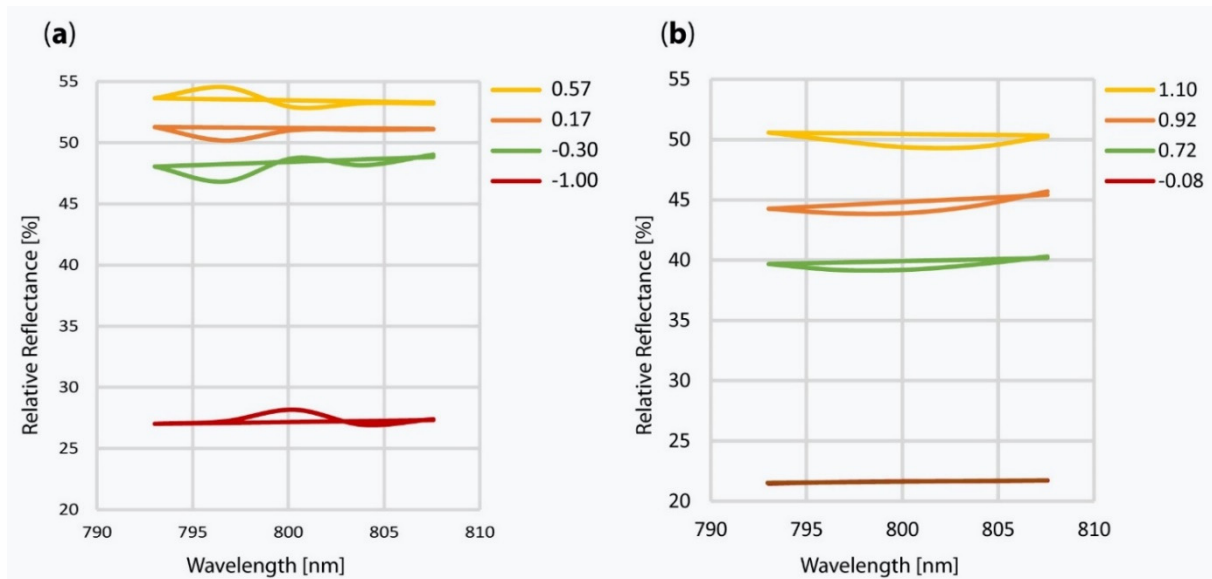


Figure 2.1.8. A comparison between four image spectra with and without applying R-L deconvolution. (a) Image spectra from the simple run (without R-L deconvolution); and (b) image spectra from the full approach (including R-L deconvolution). The legend values represent the absorption depth (difference between the absorption band at 803 nm and its corresponding value in the continuum). Deconvolution has a high potential for mapping the exact borders of these zones, especially for transition pixels at the outer zones of the REE-enriched parts. Modified after Boesche et al. 2014 [23].

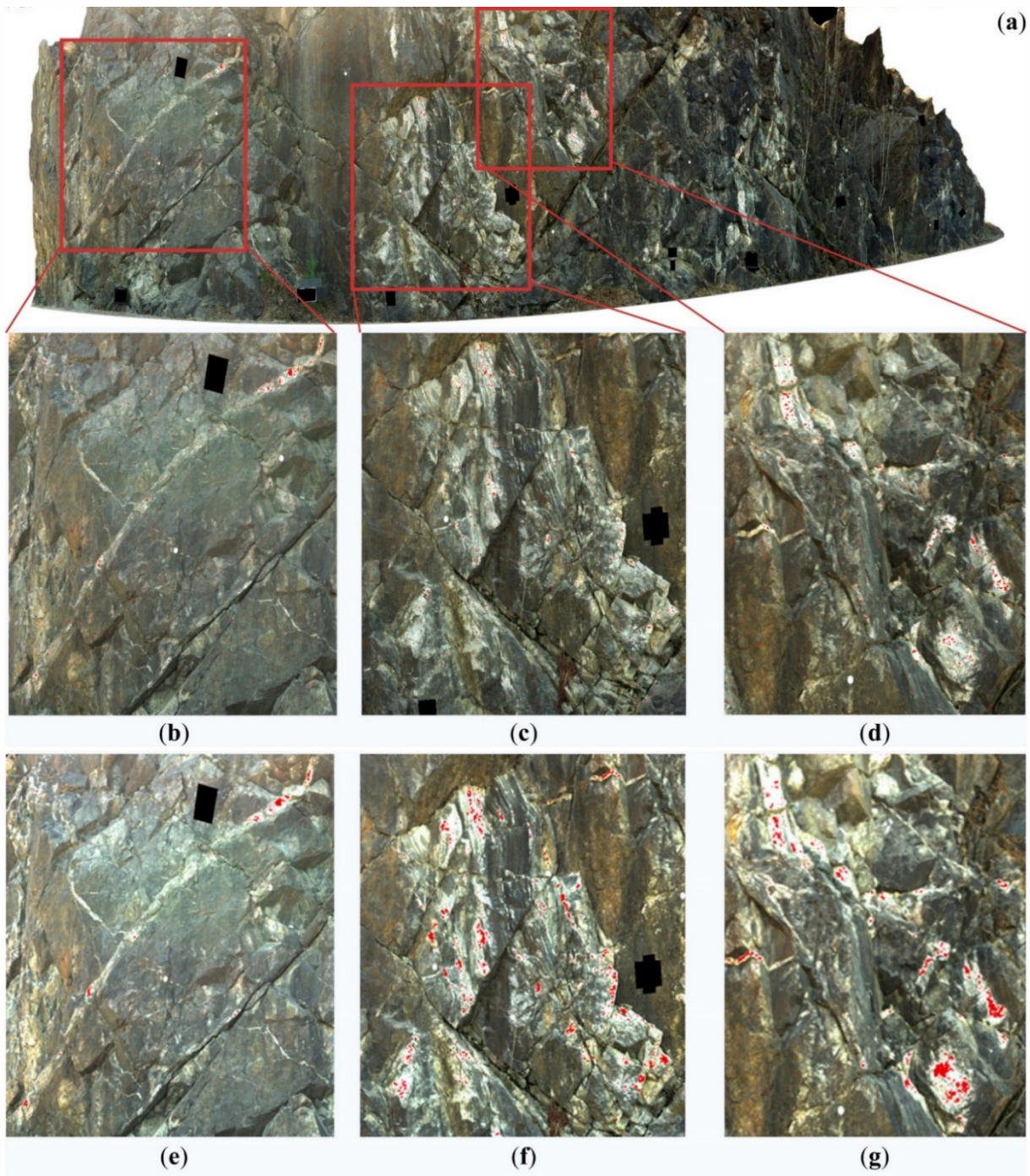


Figure 2.1.9. REE thematic map based on the simple algorithm (without R-L deconvolution). Enriched zones cannot be identified at their full spatial extent. (a) Shows the full extent of the map; (b–d) are zoom images at where the original approach shows the most positive findings. Here, only some pixels could be identified correctly. For comparison, the results of the full approach shown in Figure 2.1.6b–d are shown in the zoom images (e–g). Modified after Boesche et al. 2014 [23].

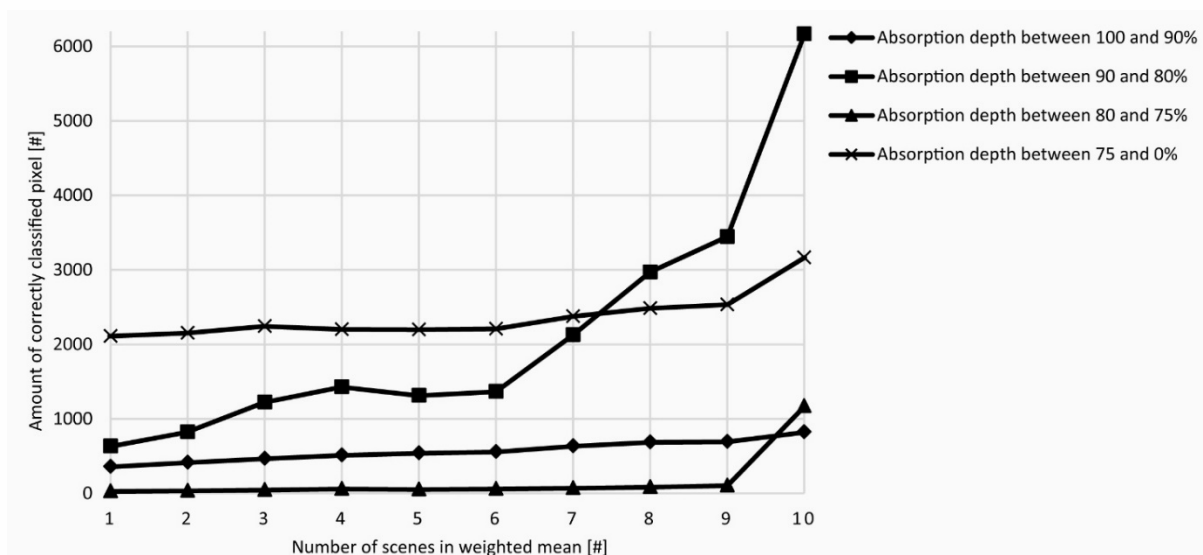


Figure 2.1.10. The impacts of using multiple image scenes for a weighted mean in the first step of the approach. Each run was performed using one more of the collected image scenes. The first run was accomplished using the image scene with the highest homogeneity for the white references. The SNR was calculated using the reference panels that were placed in front of the outcrop. Run after run, one image scene was added to the weighted mean according to its descending SNR. After using the best seven scenes, an increase in the number of correctly classified pixels was observed for the transition pixels between the enriched zones and the unenriched areas. From then on, every run that included one additional scene had a better result.

2.1.5.2 Discussion of the Results from the Introduced New Method and their Chemical Evaluation

As described in the chemical analysis results, outcrop rock types can be divided into two different rock classes. Although both of the classes are carbonatites, one class contains more ore minerals (such as REE minerals, iron ores and pyrites). Figure 2.1.11 shows the laboratory reflectance spectra for all collected and powdered field samples that were measured using the ASD spectrometer. The pyrite bearing carbonatites are represented by the 7L and 8L spectra in orange and yellow (Figure 2.1.11). Both spectra show strong iron oxide features (that would superimpose the neodymium feature [15]) and a very small calcite absorption band. By contrast, the spectra of samples 4M and 6M, which contain medium enrichments of sulfates and REEs, show low iron absorption at 530 nm and 910 nm. However, the 670 nm feature is missing. These two features would not superimpose the 800 nm neodymium feature. Hence, these spectra provide robust results for spectral neodymium analysis. The zoom image in the lower right corner of Figure 2.1.11 shows a continuum-removed subset of the spectra that points towards the neodymium oxide absorption band at approximately 800 nm. The samples with the highest neodymium absorption are 5M, 2H and 6M. The absorption band at approximately 800 nm of sample 6M shows a shift towards shorter wavelength/higher energy. This shift may be explained by the higher amounts of bastnaesites or parisites in the ore rocks. In spectra from bastnaesite and parasite, the peak absorptions occur at 797 and 798 nm [22]. However, in monazites, the peak position occurs at 800 nm (Figure 2.1.1). The main differences between the chemical bonds of the Nd^{3+} in monazite and in the bastnaesite solid solution series is the presence of a fluorine atom in the bastnaesites series. It is broadly assumed that the absorption features for REEs can be explained by electronic field transitions [5,21,22] in the 4f-orbitals. The 4f-orbitals are shielded by the $5s^2$ and $5p^6$ orbitals. The inner location of the 4f-orbitals is believed to prevent 4f orbitals from influencing the orbitals of the host mineral [20]. However, shifts towards shorter wavelengths were observed and explained by Kumar et al. [21], who analyzed two different chalcogen bound Nd^{3+} compounds, and by Misra et al. [40], who compared the absorption spectra of trifluoroacetate and trichloroacetate. Kumar et al. described the occurrence of a blue shift for the 800 nm feature ($4I_{9/2} \rightarrow 4F_{5/2}$ shift: 801 nm to 797 nm [21]) for a material in which neodymium is surrounded by SC_6F_5 . Misra et al. 2006 described the $4F_{5/2}$ shift as ligand mediated pseudohypersensitive. Kumar et al. explained the hypersensitive transition shifts of absorption bands with changes in the covalency of the bond [21]. Whether

this decrease results from fluorine atoms was not answered directly. However, the decrease in the polarizability (due to the high electronegativity) of the ligands (F) around Nd^{3+} is provided as an explanation for the decreased overlap of the ligand (F) and Nd^{3+} orbitals [21,40]. Further, Kumar et al. [21] explain the occurrence of an inverse proportionality between the shifts in peak-wavelength and the 4f–5d energy difference.

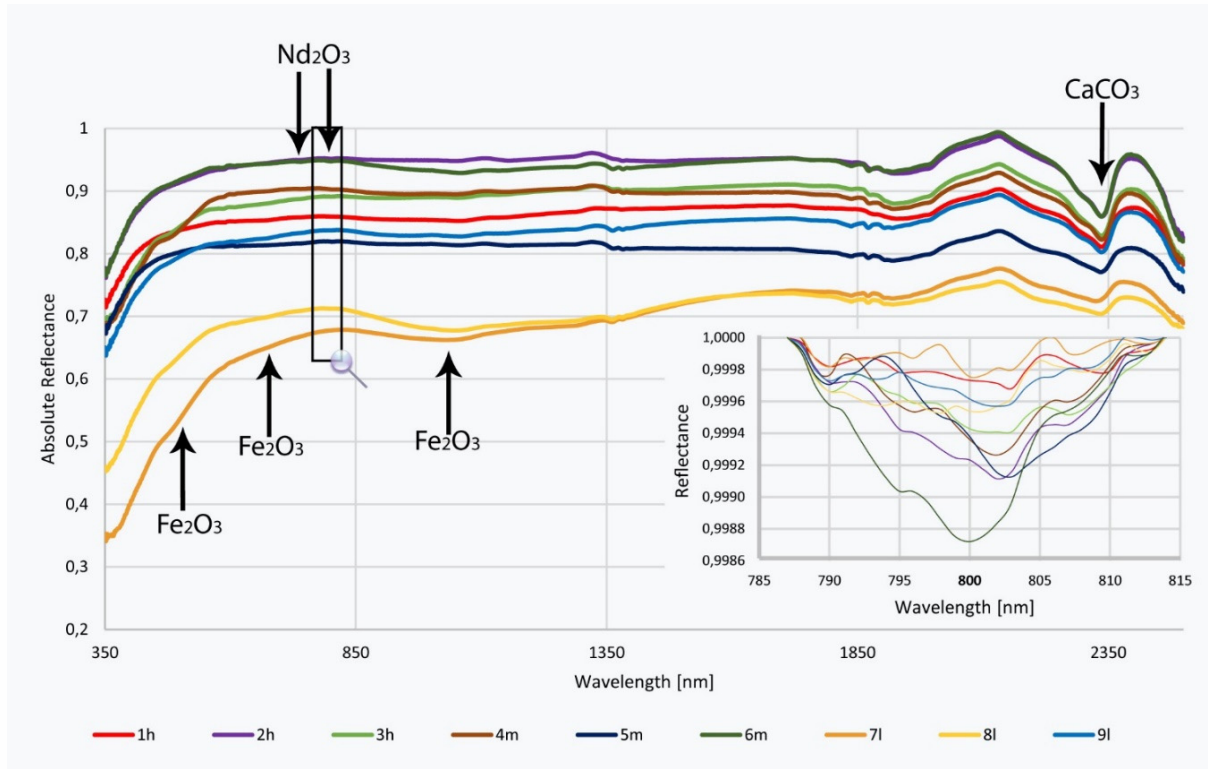


Figure 2.1.11. Resulting ASD spectra of the ground truth measurements. The zoom image shows (feature based) continuum-removed subsets of the ground truth measurements. The spectra of samples 1H, 2H, 3H, 4M, 5M, 6M and 9L show a nicely resolved calcium carbonate absorption band at 2.3 μm and a small superimposition of neodymium oxides. The spectra of samples 7L and 8L show less absorption for the calcium carbonate band. The two spectra clearly show three iron oxide absorption bands. Hence, the spectra are correlated with the chemical results in Tables 2.1.2 and 2.1.3. The 800 nm absorption band is the most diagnostic feature for neodymium detection. A correlation between the absorption depth and neodymium content is visible (especially for the spectra of samples 5M, 2H, 6M, 4M and 3H), if they contain no iron oxide.

A second explanation for this shift may be the higher amount of thulium, which absorbs at 801 nm and superimposes the neodymium absorption band [16]. Based on the geochemical analysis used in this study, it was not possible to validate the shift of the 800 nm feature with the exact concentrations of thulium in the rock samples. However, the distribution patterns shown in Figure 2.1.7 can be used as indicators for the values of thulium when analyzing general trends of the HREE plateau. Hence, Figure 2.1.7b,c show higher HREE values in sample 6M compared with samples 1H, 2H, 3H, 4M, 5M and 9L, and lower values than samples 7L and 8L. The spectra of samples 7L and 8L would not show thulium absorption because of the iron content. Thus, sample 6M is the only spectrum that shows the superimposed and widened feature of neodymium and thulium.

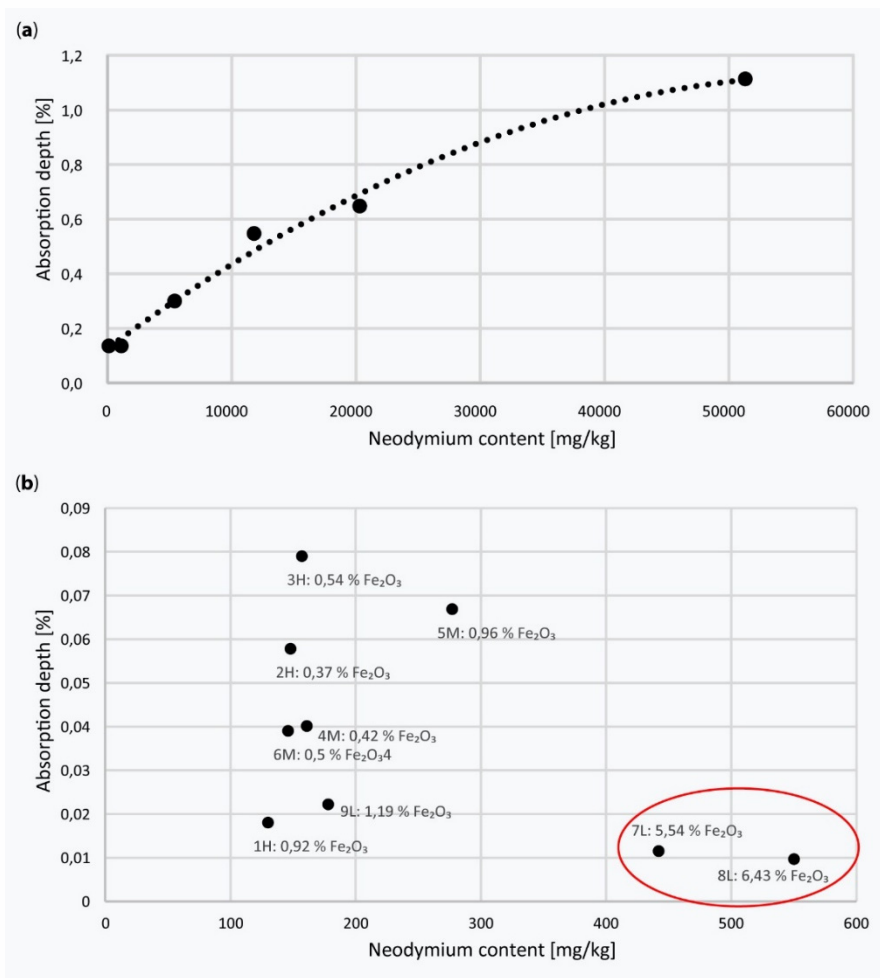


Figure 2.1.12. Quantitative comparison between the neodymium concentrations of mixture samples and field samples and the corresponding hyperspectral recordings. (a) Correlation between the amount of neodymium oxide within a calcium carbonate powder and the absorption depth of the 803 nm absorption band measured with the HySpex spectrometer in the laboratory. The trend line is a second-degree polynomial fit. (b) Correlation of the REE content of the field-samples with the depths of the neodymium absorption band measured with the ASD field spectrometer in the laboratory. Only samples 7L and 8L occur as outliers. This result is due to the iron oxide content, which is shown for all field samples as index numbers next to the plotted points in graph (b).

The quantitative concentration determination results of a series of laboratory measurements of artificial sample mixtures (CaCO₃ and Nd₂O₃) that were compared with hyperspectral recordings revealed an algebraic dependence between the 800 nm absorption band (Figure 2.1.12: y-axis) and the neodymium concentration (Figure 2.1.12: x-axis). Figure 2.1.12a shows that for the laboratory mixtures with minor neodymium concentrations less than 5%, the two parameters are multiplicatively dependent with a polynomial grade of two. Figure 2.1.12b shows the neodymium concentration of the powdered field samples plotted on the x-axis and the absorption depths of the hyperspectral ASD measurements on the y-axis. In addition, Figure 2.1.12b shows that an algebraic dependency between the neodymium concentration and absorption depth may only be visible for samples with low pyrite. This observation occurs because the very small amount of iron oxide (less than 10%) dramatically hampers the identification of REE related absorption bands (Figure 2.1.12b: values in the red circle). In addition, this observation can be explained by the fact that the presence of only minor concentrations of iron oxides (approximately 5%–6% FeO or Fe₂O₃) within the weathered surfaces of the rocks inhibits any reflection of the subsurface material. Additionally, [31] stated that a thin reddish film resulting from rubification processes (e.g., free iron oxides that were released from the rock and coat the surface of an outcrop) already exists and significantly affects the spectrum. Therefore, spectral muting in the presence of iron oxides makes identification of the small REE absorption bands impossible. A new study

on how carbonatites erode and weather under Scandinavian climate conditions (rain, frost, snow, etc.) and on how mobile rare earth elements behave in the weathering surface is necessary for quantifying weathering as a hampering factor. Besides the pyrite rich samples, the algebraic dependency shows that spectroscopy has a large potential to semi-quantify low REE concentrations. However, superimpositions with other materials hamper direct quantitative estimations. To quantify the influences of vegetation coverage, the exact species, leaf thickness, the ability of the plant to store REEs in the fabrics of the roots or leaves and the multiple reflections and transmittance of the incident radiation at the vegetation pixel must be considered.

2.1.6 Conclusions

The results of our study provide valuable information regarding the concentrations and distributions of rare earth elements in carbonatites. The proposed approach is a first and robust tool for spectroscopically identifying rare earth elements. This approach allows for spatial mapping of distribution patterns at different enrichment levels and provides further insights regarding the signatures of the parental magma.

- Spectroscopy has been identified as a powerful tool for mapping outcrops for rare earth elements, even under non-optimal illumination conditions (e.g., dark materials, shadowed outcrops, low sun elevation angles). Remarkable hyperspectral mapping of neodymium-enriched zones is achievable if data acquisition conditions are good or if multitemporal scenes are collected and the outcrop has little or no weathered surface.
- The R-L-deconvolution method has a high potential for resolving neodymium related absorption bands, even when the noise is considerably high.
- The weighted mean of a minimum of seven scenes already allows for good mapping of transition zones. To locate the highly enriched zones of the outcrop, only one scene taken under good illumination conditions is required.
- Our approach is suitable for analyzing outcrops that are located short distances from the sensor (30 m to 5 m). The presented approach provides results within a short period of ~10–30 min, including field measurements, and can be readily used in the field as an additional tool for mineral prospecting processes. We suggest applying this approach in a two-step procedure. The first step involves a run with a fast integration time and low multi-temporal average. This quick-result serves as a basis for setting up the ideal acquisition conditions in the field (e.g., the position of the sensor, position of the white references, illumination angles). The second step includes the full approach with the best integration time and a high number of acquisitions.
- The spectroscopic results show a direct relationship between low-pyrite carbonatites and the geochemical results. Therefore, this approach produces accurate results when the iron content is low. Nevertheless, iron and other ore minerals can be used to detect enriched zones within the carbonatite body because higher amounts of iron ore minerals represent a secondary indicator of sulfidic conditions during melt intrusion and can highlight particularly enriched zones.
- The geochemical results show two classes of rock types within the investigated sövite outcrop. The first type (carbonatite) shows the expected rare earth element distribution, and the second type (siderite-carbonatite) contains surprisingly high amounts of the middle rare earth elements.

Future studies should focus on the key spectral characteristics of the remaining 15 rare earth elements. In addition, we recommend investigating the potential of iron oxide spectroscopy as a secondary indicator of sulfidic melts in carbonatitic rocks. Quantifying the applicability in the presence of spectroscopical hampering materials, such as vegetation or iron coatings, would be very interesting. Additional hampering factors, such as incidence angles, illumination angles, non-optimal acquisition conditions (lack of white references in the images, shifts of pixel due to the unstable underground of the tripod) and dust should be focused on in the future. Moreover, the proposed technique could be tested at different scales (e.g., microscopical image collections on thin sections and remote sensing of the whole ore body from airborne and space borne). Finally, the geological interpretation of carbonatitic outcrops might be enhanced by incorporating LiDAR or from photogrammetrically retrieved three-dimensional surface models to conduct more complex spatial analyses of the mineral phases in the outcrop. This method would be especially useful when using the REE mapping technique for vertical 3D monitoring of vertical open pit mining surfaces.

2.1.7 Acknowledgments

This study was financed and scientifically supported by the German National EnMAP framework program (Department of Economics and Technology BMWi No. 50EE1256) and the GeoForschungsZentrum (GFZ) of the Helmholtz Foundation. We would like to thank BERGFALD Miljørådgivere for significantly supporting our work and for allowing us to work at the Fen complex. Many thanks are extended to the editors and the reviewers for their valuable comments, which have helped improve the quality of this paper.

2.1.8 Author Contributions

Nina Kristine Bösche initiated and carried out this study and wrote the manuscript. Christian Rogaß helped with the preprocessing of the collected field data, including radiometric calibration and reflectance retrieval. Christin Lubitz, Christian Rogaß and Maximilian Brell belonged to the field excursion team and made successful image collections possible. Sabrina Herrmann conducted the laboratory measurements of the powdered samples and neodymium mixtures with the HySpex and handheld XRF instruments. Christian Mielke, Sabine Tonn and Oona Appelt monitored the geochemical analyses at the GFZ laboratories. Uwe Altenberger and Hermann Kaufmann supervised this work and helped with the interpretation of the mineral analyses.

Conflicts of Interest

The authors declare no conflict of interest.

2.1.9 References

1. Laznicka, P. *Giant Metallic Deposits*; Springer Berlin Heidelberg: Berlin, Heidelberg, 2010.
2. Xu, C.; Wang, L.; Song, W.; Wu, M. Carbonatites in China: A review for genesis and mineralization. *Geosci. Front.* **2010**, *1*, 105–114.
3. Rogass, C.; Spengler, D.; Bochow, M.; Segl, K.; Lausch, A.; Doktor, D.; Roessner, S.; Behling, R.; Wetzel, H.U.; Kaufmann, H. Reduction of radiometric miscalibration—Applications to pushbroom sensors. *Sensors* **2011**, *11*, 6370–6395.
4. Clark, R.N.; Swayze, G.A.; Livo, K.E.; Kokaly, R.F.; Sutley, S.J.; Dalton, J.B.; McDougal, R.R.; Gent, C.A. Imaging spectroscopy: Earth and planetary remote sensing with the USGS Tetracorder and expert systems. *J. Geophys. Res.* **2003**, doi:10.1029/2002JE001847.
5. Rowan, L.C.; Kingston, M.J.; Crowley, J.K. Spectral reflectance of carbonatites and related alkalic igneous rocks; selected samples from four North American localities. *Econ. Geol.* **1986**, *81*, 857–871.
6. Rowan, L.C.; Mars, J.C. Lithologic mapping in the Mountain Pass, California area using advanced spaceborne thermal emission and reflection radiometer (ASTER) data. *Remote Sens. Environ.* **2003**, *84*, 350–366.
7. Momose, A.; Miyatake, S.; Arvelyna, Y.; Nguno, A.; Mhopjeni, K.; Sibeso, M.; Muyongo, A.; Muvangua, E. Mapping pegmatite using HyMap data in southern Namibia. In *Proceedings of the 2011 IEEE International Geoscience and Remote Sensing Symposium (IGARSS)*, Vancouver, BC, Canada, 2011; pp. 2216–2217.
8. Hernandez, E.A.; Filho, C.R. Spectral reflectance and emissivity features of PO₄-bearing carbonatitic rocks from the Catalão I and Tapira complexes: New constraints for detection of igneous phosphates with remote sensing data. In *Anais XVI Simpósio Brasileiro de Sensoriamento Remoto-SBSR*; Publisher: Foz do Iguaçu, Brasil, 2013.
9. Bedini, E. Mapping lithology of the Sarfartoq carbonatite complex, southern West Greenland, using HyMap imaging spectrometer data. *Remote Sens. Environ.* **2009**, *113*, 1208–1219.
10. Dai, J.; Wang, D.; Wang, R.; Chen, Z. Quantitative estimation of concentrations of dissolved rare earth elements using reflectance spectroscopy. *J. Appl. Remote Sens.* **2013**, *7*, doi:10.1117/1.JRS.7.073513 .
11. Bedini, E.; Tukiainen, T. Using spectral mixture analysis of hyperspectral remote sensing data to map lithology of the Sarfartoq carbonatite complex, southern West Greenland. *Geological Survey of Denmark and Greenland Bulletin* **2009**, *17*, 69-72
12. Van der Meer, F.D.; van der Werff, H.M.A.; van Ruitenbeek, F.J.A.; Hecker, C.A.; Bakker, W.H.; Noomen, M.F.; van der Meijde, M.; Carranza, E.J.M.; de Smeth, J.B.; Woldai, T. Multi- and hyperspectral geologic remote sensing: A review. *Int. J. Appl. Earth Obs. Geoinf.* **2012**, *14*, 112–128.
13. Cloutis, E.A. Hyperspectral geological remote sensing: Evaluation of analytical techniques. *Int. J. Remote Sens.* **1996**, *17*, 2215–2242.
14. Mielke, C.; Boesche, N.K.; Rogass, C.; Kaufmann, H.; Gauert, C.; de Wit, M. Spaceborne mine waste mineralogy monitoring in South Africa, applications for modern push-broom missions: Hyperion/OLI and EnMAP/Sentinel-2. *Remote Sens.* **2014**, *6*, 6790–6816.
15. Townsend, T.E. Discrimination of iron alteration minerals in visible and near-infrared reflectance data. *Journal of geophysical research* **1987**, *92*, 1441–1454.
16. White, W.B. Diffuse-reflectance spectra of rare-earth oxides. *Appl. Spectrosc.* **1967**, *21*, 167–171.
17. Dieke, G.H.; Crosswhite, H.M. The spectra of the doubly and triply ionized rare earths. *Appl. Opt.* **1963**, *2*, 675–686.
18. Williams, M.L.; Jercinovic, M.J.; Harlov, D.E.; Budzyń, B.; Hetherington, C.J. Resetting monazite ages during fluid-related alteration. *Chem. Geol.* **2011**, *283*, 218–225.
19. ASD Inc Field Spec 3 HR (Build in 2010). Available online: <http://www.sphereoptics.de/en/spectrometers/docs/Field%20Spec%203%20HR%202010.pdf> (accessed on 1 April 2015).
20. Leonard, J.P.; Nolan, C.B.; Stomeo, F.; Gunnlaugsson, T. Photochemistry and photophysics of coordination compounds: Lanthanides. *Top. Curr. Chem.* **2007**, *281*, 1–43.

21. Kumar, G.A.; Riman, R.E.; Diaz Torres, L.A.; Banerjee, S.; Romanelli, M.D.; Emge, T.J.; Brennan, J.G. Near-infrared optical characteristics of chalcogenide-bound Nd³⁺ molecules and clusters. *Chem. Mater.* **2007**, *19*, 1610–1620.
22. Turner, D.J.; Rivard, B.; Groat, L.A. Visible and short-wave infrared reflectance spectroscopy of REE fluorocarbonates. *Am. Mineral.* **2014**, *99*, 1335–1346.
23. Boesche, N.K.; Rogaß, C.; Mielke, C.; Kaufmann, H. Hyperspectral digital image analysis and geochemical analysis of a rare earth elements mineralized intrusive complex (fen carbonatite complex in Telemark region, Norway). In Proceedings of 34th EARSel Symposium; Warsaw, Poland, 16-20 June 2014.
24. Ramberg, D.I.B. Gravity studies of the Fen complex, Norway, and their petrological significance. *Contrib. Mineral. Petrol.* **1973**, *38*, 115–134.
25. Mitchell, R.H.; Brunfelt, A.O. Rare earth element geochemistry of the Fen alkaline complex, Norway. *Contrib. Mineral. Petrol.* **1975**, *52*, 247–259.
26. Andersen, T. Evolution of peralkaline calcite carbonatite magma in the Fen complex, southeast Norway. *Lithos* **1988**, *22*, 99–112.
27. Andersen, T. Magmatic fluids in the Fen carbonatite complex, S.E. Norway. *Contrib. Mineral. Petrol.* **1986**, *93*, 491–503.
28. Lie, A.; Ostergaard, C. The Fen carbonatite complex, Ulefoss, Norway. 21st NORTH, Svendborg 12, Denmark 2011
29. Norsk Elektro Optikk. HySpex VNIR 1600/SWIR320 m-e. Available online: <http://www.sphereoptics.de/de/spektrometer/docs/HySpex-GenerellMail.pdf> (accessed on 1 April 2015).
30. Sunshine, J.M.; Pieters, C.M.; Pratt, S.F. Deconvolution of mineral absorption bands: An improved approach. *J. Geophys. Res.: Solid Earth* **1990**, *95*, 6955–6966.
31. Ben-Dor, E.; Chabrilat, S.; Demattê, J.A.M.; Taylor, G.R.; Hill, J.; Whiting, M.L.; Sommer, S. Using imaging spectroscopy to study soil properties. *Remote Sens. Environ.* **2009**, *113*, S38–S55.
32. Guanter, L.; Richter, R.; Moreno, J. Spectral calibration of hyperspectral imagery using atmospheric absorption features. *Appl. Opt.* **2006**, *45*, 2360–2370.
33. Harsdorf, S.; Reuter, R. Stable deconvolution of noisy lidar signals. In Proceedings of 2000 EARSel-SIG-Workshop, Dresden, Germany, 16–17 June 2000.
34. Sunshine, J.M.; Pieters, C.M. Estimating modal abundances from the spectra of natural and laboratory pyroxene mixtures using the modified Gaussian model. *J. Geophys. Res.: Planets* **1993**, *98*, 9075–9087.
35. Zuleger, E.; Erzinger, J. Determination of the REE and Y in silicate materials with ICP-AES. *Fresenius' Z. Anal. Chem.* **1988**, *332*, 140–143.
36. Sun, S.-S.; McDonough, W.F. Chemical and isotopic systematics of oceanic basalts: Implications for mantle composition and processes. *Geol. Soc. Lond. Spec. Publ.* **1989**, *42*, 313–345.
37. Thermo Scientific Niton_XL3t_GOLDD. Available online: http://www.niton.com/docs/literature/Niton_XL3t_GOLDD_Spec_Sheet.pdf?sfvrsn=2 (accessed on 1 April 2015).
38. Jeol USA Inc. JEOL USA JXA-8230 SuperProbe Electron Probe Microanalyzer (EPMA). Available online <http://www.jeolusa.com/PRODUCTS/MicroprobeandAuger/JXA-8230/tabid/223/Default.aspx> (accessed on 1 April 2015).
39. Hornig-Kjarsgaard, I. Rare earth elements in sövitic carbonatites and their mineral phases. *J. Petrol.* **1998**, *39*, 2105–2121.
40. Misra, S.N.; Mehta, S.B.; Balar, B.M.; John, K. Absorption difference and comparative absorption spectrophotometry of neodymium(III) haloacetates in non-aqueous media and in Crystalline State. *Synth. React. Inorg. Met.-Org. Chem.* **2006**, *22*, 729–757.

2.2 Supplement: Reflectance Spectra of REM, REO and REE-bearing minerals

In order to produce a comprehensive dataset of the REMs, REOs and REE-bearing minerals, these materials were purchased and spectroscopically analyzed [24]. Particular importance was placed on a sensor independent analysis of all materials. Therefore, all materials were measured with at least three different instruments. The resulting dataset was used to define the peak and shoulder wavelength positions that were used in the following chapters (Chapters 3, 4 and 5). This supplementary chapter briefly explains the methods used and summarizes the findings of the hyperspectral REE-analysis. New discoveries, which are not published by Herrmann, 2015, are explained in greater detail [24].

2.2.1 Materials and Methods

In order to investigate their spectral response a set of REMs, REOs, REE bearing minerals and synthetic mixtures of REOs with calcite were spectroscopically analyzed (the spectra of the REOs, REO mixtures and REE bearing minerals (except monazite) are provided by Herrmann, 2015,[24]). The REOs were produced by Alfa Aesar and belong to a series of rare earth metals (REacton). The rare earth oxide powders can be considered as pure because they comprise of at least 99.9 %. With this REO powders and a calcite powder 8 to 12 synthetic mixtures were produced per REO. The amount of mixtures per element oxide depends on the price of the raw REO powder. Mixtures with a higher concentration of 30% could not be established for expensive REOs (thulium and lutetium). The calcite powder (product number: 31208) was produced by the Riedel-de Haen AG. The REMs were provided by Seltenerdmetalle24, an online distributor of REMs for personal use. The samples have a weight of at least 1 gr. In order to prevent the REMs from oxidizing all REM were conserved in argon. Seltenerdmetalle24 provided an empty glass filled with argon, which could be used as a reference for the evaluation of the measured spectra. The REE bearing minerals (except of monazite) were purchased via mail-order from Gunnar Färber Minerals. The monazite-sand sample was provided by Dan Harlov (REE percentage: La_2O_3 : 12.49, Ce_2O_3 : 28.77, Pr_2O_3 : 3.058, Nd_2O_3 : 12.28, Sm_2O_3 : 1.694, HREE < 1.6%) [25]. The rare earth bearing minerals were measured with different spectrometers. Which spectrometer was used for which sample was re-decided case by case. The REO synthetic mixtures, the monazite sand, the bastnaesite mineral sample, and the REMs provided in glass tubes could be measured best with the imaging spectrometer (Hypex) [26]. The advantage of the Hypex is the imaging measurement mode with a translation stage and the pushbroom scanning technique. For these materials it is crucial to select pixel that fully covers the sample material. Thus, regions of interest in the image were defined and the median spectrum extracted. Minerals with a grain size of more than 1 cm could be measured with an integrative measurement spot (direct and diffuse light portions) in the Perkin Elmer Lambda 950 spectrometer [27]. The advantage of the Perkin Elmer is the spectral resolution of 1 nm. Neodymium oxide was additionally measured with the Analytical Spectral Device Fieldspec 3 Spectrometer [28]. This additional measurement was applied in order to analyze the spectral response to varying illuminations. This goes back to anomalous shifts that were published by Herrmann, 2015 [24]. The instrument specifications and the sample specifications are listed in the appendix 8.

2.2.2 Results and Evaluation of the Results

Except for neodymium, gadolinium, lanthanum, and europium the resulting reflectance spectra of the REMs are spectrally neutral (Figure 2.2.1). Thus their spectra do not show any absorptions in the VNIR and SWIR range. Gadolinium and lanthanum show at least four absorption bands at the wavelength position of water, which are most probably due to water [24]. Neodymium and europium show several absorptions. Those absorptions are known to be produced by crystal field transitions. Most of those crystal field transitions are also known to be hypersensitive [6, 29, 30]. Since it is broadly assumed that most REE related absorptions are produced by crystal field transitions [3, 16] the neutral character of the reflectance spectra of the remaining REMs is an unexpected result. Although it is known that some absorptions are sensitive to surrounding ions, it is expected that the crystal field transitions in the REMs would at least be visible for some absorptions. All absorption bands that can be observed in the REM reflectance spectra are shown in Figure 2.2.2.

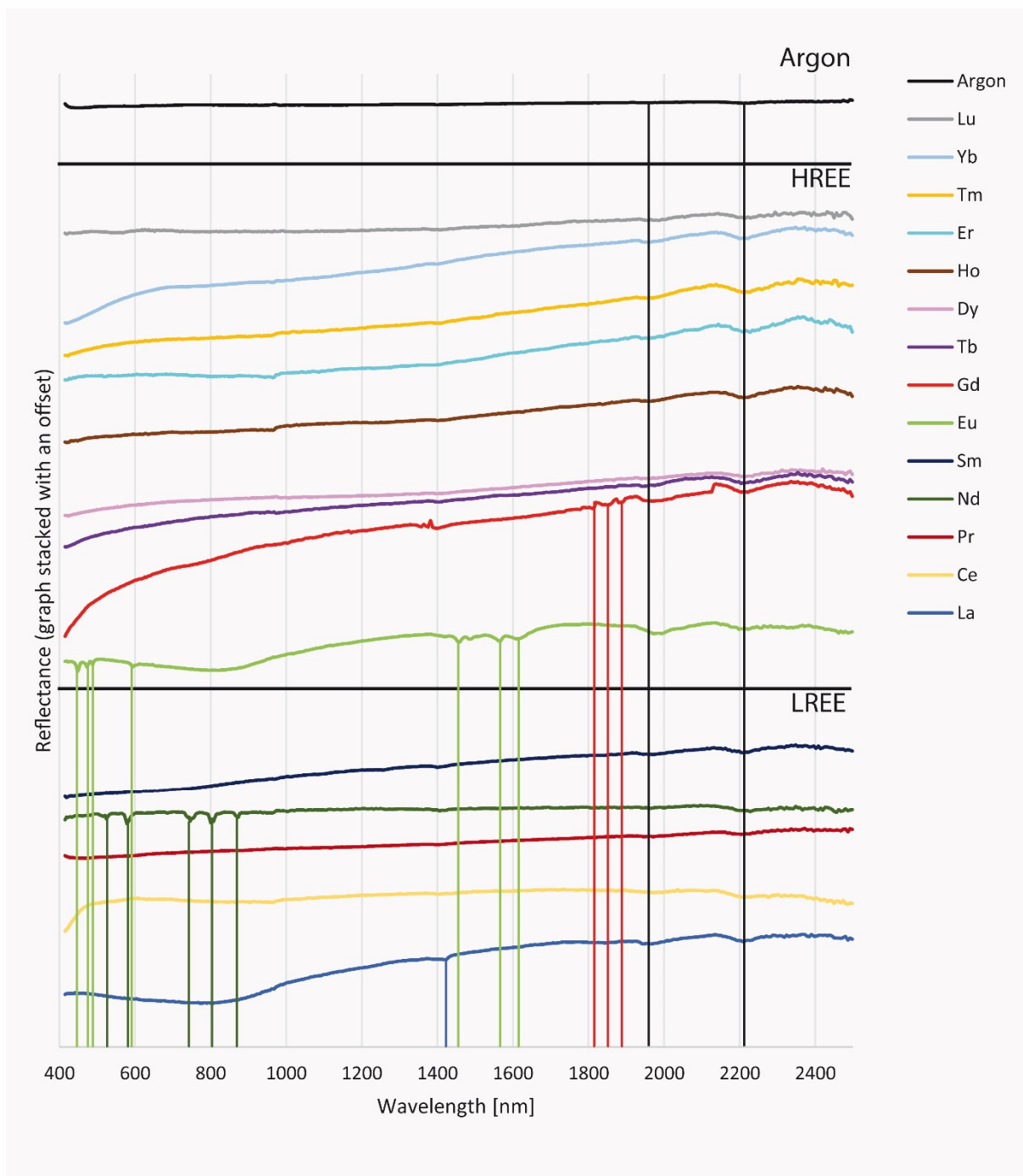


Figure 2.2.1: The REMs had a diameter of approximately one centimeter and were conserved in argon in order to prevent oxidation. Therefore an empty sample glass, filled with argon, is plotted as a reference as well. Note the absorption bands of neodymium and europium can be distinguished in the REM related spectra. The neodymium and europium absorptions are known to be produced by hypersensitive crystal field transitions [6, 30]. The absorptions in the spectra of lanthanum and gadolinium are most probably due to water [24].

The reflectance spectra of the REO powders (Chapter 3, Figure 3) show a high number of absorption bands for lanthanum, neodymium, samarium, europium, dysprosium, holmium, erbium, thulium and ytterbium. The absorption bands are distributed over the VNIR and SWIR range of the spectrum. Most absorption bands are narrow and their minimum reflectance can be observed at distinct wavelength positions (Appendix: Table 8.1 and Figure 8.1 to 8.5). In total, 287 absorption bands were observed (49 x Er, 42 x Dy, 45 x Ho, 39 x Nd, 38 x Sm, 35 x Tm, 27 x Eu, 10 x Yb, 2 x La). Several of those determined bands are described as 4f electron transition absorptions in the respective literature [6, 30, 31]. In the Appendix Table 8.1 these absorption bands are marked '+'. Absorption bands, which are shown as bold numbers are classified as diagnostic absorption bands in this thesis. Most spectra show overlapping absorption bands that are merged to doublet or triplet features. The criteria for diagnostic absorption bands are either one selected high absorption depth per range of multiple features or a single distinct feature. The resulting spectral plots of the REO-CaCO₃ mixtures are shown in the Appendix (Figure 8.1 to 8.5). Figure 2.2.2 shows the mathematical relationship of the spectral response (absorption depth) at varying neodymium concentrations. As an example the absorption depth of four diagnostic absorption bands of neodymium oxide in a mixture with a predefined weight percent neodymium (0.1 to 10%) to calcite powder are shown. The maximum concentration of 10% is chosen because it represents the highest natural amount of neodymium in a solid material. The relationship that can be observed for the plotted data points is a polynomial trend with 2nd degree. This copes with the observations in Chapter 2.1, in which the relationship between the absorption depth at 803 nm and concentration of neodymium in synthetic mixtures is analyzed. In Herrmann, 2015, the mathematical relationship between feature depth and concentration is given for most REOs [24]. Herrmann considers the whole spectral range (up to 2500 nm) and finds a logarithmic trend to describe the dependency. The logarithmic trend is assumed because a plateau can be observed towards the high concentrations (<10%). Nevertheless, based on the naturally occurring percentages, the polynomial trend is preferred. A comparatively low increase in the absorption depth towards higher abundances (<10%) as it is described in Herrmann, 2015, is rather explainable with saturation effect.

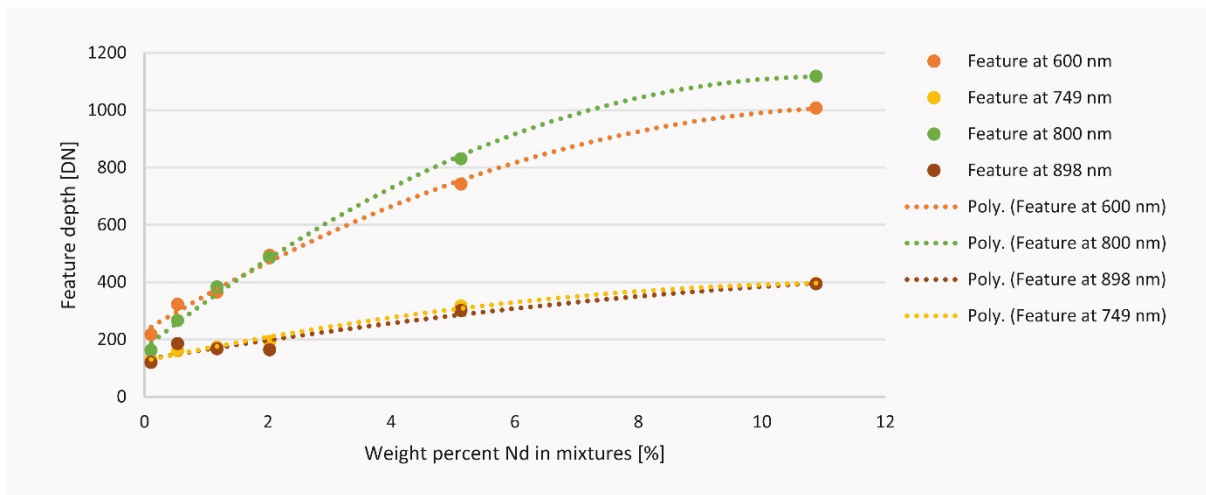


Figure 2.2.2: The mathematical relationship of the spectral response (absorption depth) and the neodymium concentration. A polynomial dependency of 2nd degree can be observed here. It represents the best fit of the measurements. The plotted concentrations represent natural concentration levels of neodymium.

The reflectance spectra of six common ores in carbonatites are shown in Figure 2.2.3. Several absorption bands can be observed in their spectra. Ore minerals that represent the LREEs, mainly show absorption bands similar to those of neodymium and samarium. The shift that is caused by the fluorine ion in the fluorocarbonates (bastnaesite, synchesite, parisite) can be observed in comparison to the LREE-phosphate (monazite). The HREE-phosphates (xenotime a and b) show a high number of REE related absorption bands. Most of the absorption bands can be attributed to holmium, erbium, dysprosium, samarium and europium.

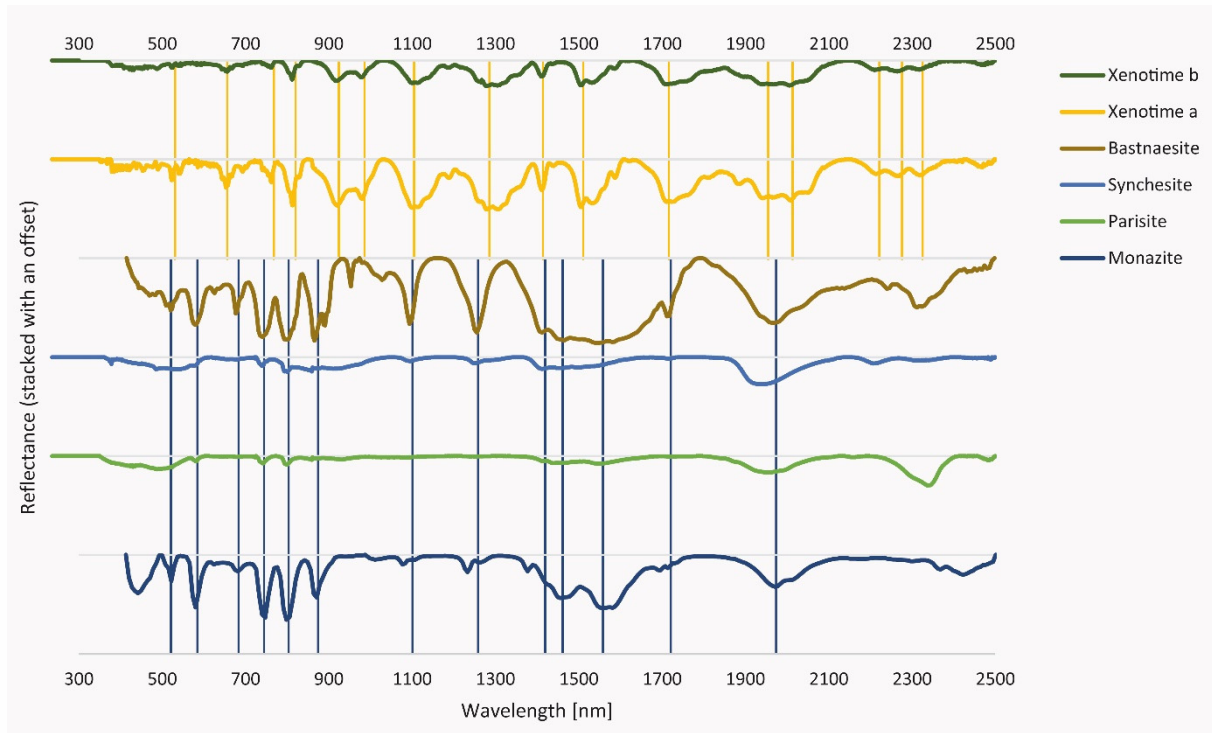


Figure 2.2.3: Reflectance spectra of the analyzed REE-ore minerals. Note the similar absorption that can be observed for LREE incorporating minerals and the similar spectra for HREE incorporating minerals. The LREE ore minerals mainly show the absorptions that are related to neodymium and samarium. The HREE related spectra show absorptions that are related to holmium, erbium, dysprosium, samarium and europium.

In the work of Herrmann, 2015, some differences between three reflectance spectra, measured on the same material (neodymium oxide), could be observed [24]. These differences have been further investigated in this doctoral thesis. The results are explained in the following section. In Figure 2.2.4, additionally to the three measurements of the neodymium oxide from Herrmann, 2015, the neodymium metal and LREE bearing minerals are shown. The differences between all spectra can be classified into three observations:

1. The three measurement modes show peak positions at two different wavelength positions. The spectra, measured with the ASD and Perkin Elmer devices, differ from the spectra measured with the Hypsax sensor. The shift between the absorption band peak positions between the measurement modes is not equal for every feature.
2. A shift of some absorption bands peak positions between different materials that were measured with the same sensor can be observed.
3. Varying absorption depths of several individual absorption bands are visible.

The reasons for this observations are not related to device failures or post-processing steps, because the measurements of the other REOs (which do not show the shifts and changes in feature depths) were recorded contemporaneously and all measurements were processed with the same post-processing steps [24]. In Figure 2.2.4 absorption features that are shifted due to the chemical composition (influences of the 5d-orbitals on the 4f-orbitals) are marked in red. Those shifts can be observed in any measurement mode and, as expected, are stronger in minerals that incorporate fluorine (spectra highlighted in blue). Changes in the individual absorption depth can be observed in multiple (triplet or higher) absorption bands. It is particularly noticeable that the absorption depths of multiple features seem to vary in the depths of the individual narrow bands that make up the multiple features. The overall depth / area of the multiple features does not seem to vary significantly. However, the absorption depth changes of individual features would also change the peak position that might be defined for the multiple feature. The shift between the absorption bands, recorded with the Hypsax sensor and the two point spectrometer, is probably due to a combination of hypersensitive transitions in the f-orbitals, different illuminations or other sensor specific properties (e.g. point spread function, percentages of diffuse and direct light, etc.).

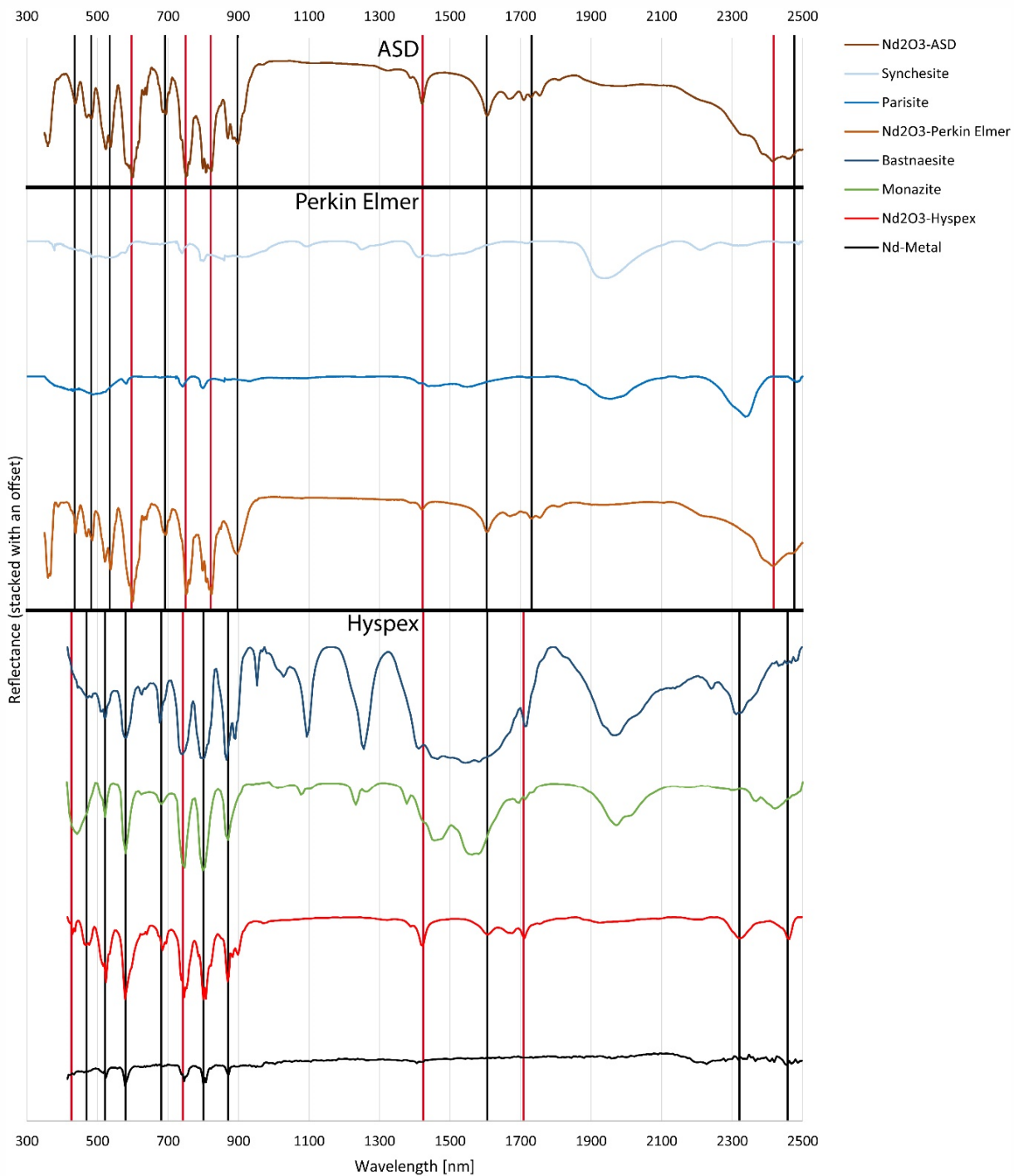


Figure 2.2.4: The figure highlights the differences of individual absorption bands that could be observed between different measurement modes, and the differences that could be observed between different materials within the same measurement mode. Note, the shift of the peak positions between ASD/Perkin Elmer and Hypspec measurements. Also note the shift between the Nd_2O_3 Perkin Elmer spectrum and the Nd-incorporating fluorocarbonates parasite and synchesite.

3. Chapter

Re-calibration of REEMAP on Dysprosium and Holmium and Spectroscopic Study of Proxy and Associated Minerals

3.1 Hyperspectral Rare Earth Element Mapping of three Outcrops at the Fen Complex, Norway – Calcitic, Dolomitic and Ankeritic Carbonatites (submitted, accepted for publication, publication planned in august 2015 - ISBN-13: 978-0128023280)

Nina Kristine Boesche ^{1,2,*}, Christian Rogass ¹, Christian Mielke^{1,2}, Sabrina Herrmann^{1,2}, Friederike Körting^{1,2}, Anne Papenfuß^{1,2}, Christin Lubitz ¹, Maximilian Brell¹, Sabine Tonn¹, Uwe Altenberger²

¹ Helmholtz Centre Potsdam - GFZ German Research Centre for Geosciences, Telegrafenberg, 14473 Potsdam

E-Mails: rogass@gfz-potsdam.de; chmielke@gfz-potsdam.de; saherrma@gfz-potsdam.de; koerting@gfz-potsdam.de; apapenfu@uni-potsdam.de; christin.lubitz@gfz-potsdam.de; brell@gfz-potsdam.de; tonn@gfz-potsdam.de

² University of Potsdam, Karl-Liebknecht Str. 24-25, 14476 Potsdam-Golm; E-Mail: altenber@uni-potsdam.de

* Author to whom correspondence should be addressed; E-Mail: nina.boesche@gfz-potsdam.de; Tel.: +49-331-28828775; Fax: +49-331-2881192.

Abstract: Imaging spectroscopy is widely used to identify the spatial distribution of surface cover materials via characteristic absorption features. The present study proposes a new approach to map calcitic, dolomitic and ankeritic carbonatite outcrops in the Fen complex in Norway. Our method allows the characterization of the outcrop mineralogy in a rapid and robust manner thanks to new spatio-temporal hyperspectral methods. In order to spectrally differentiate between the three different rocktypes and to characterize their geochemical composition and rare earth element concentration, multi-temporal series of hyperspectral images were collected and analyzed according to their spectral homogeneity. The mineral analysis was achieved using the iron feature depth indicator and the dolomite-carbonate feature depth estimation in accordance with the USGS Tetracorder expert rule-set. Spectroscopic identification of rare earth element enriched zones consisted of a two-step-approach: 1) Spectral sharpening using a Richardson Lucy deconvolution and 2) knowledge-based retrieval of the rare earth element indicative absorption depth. The resulting outcrop maps were evaluated using reference measurements from a handheld X-ray fluorescence device. Additionally, rock samples were taken for further geochemical and petrographic work, which includes the elemental analysis of selected samples in the inductively coupled plasma optical emission spectrometry. Our results show that hyperspectral remote sensing is a rapid and robust technique to map the spatial distribution of the mineral and rare earth element content of carbonatite outcrops of calcitic, dolomitic or ankeritic composition.

Keywords: hyperspectral imaging spectroscopy; neodymium; holmium; dysprosium; HySpex; Fen complex

3.1.1 Introduction

The worldwide demand for rare earth elements is increasing and the detection and characterization of new deposits is an ongoing process. Mineable concentrations of ore minerals (such as bastnaesite, pyrochlore and zircon) occur in rare alkaline rocks and carbonatites (a rare variation of igneous rocks) and rare earth element-containing pegmatites and placer deposits. The worldwide and economic most important rare earth element deposit types are the carbonatites, which occur in alkaline rocks, such as in the Fen complex in Ulefoss, Norway, Mountain Pass, USA and Bayan Obo, China. Recent development in the world's economics for mineral resources (Yap, 2015) (drastic change in the export quotas for rare earth elements) again showed that new mineable deposits are required to stabilize the rare earth element export market. Field exploration techniques, which are widely used for the detection of new deposits, include geophysical methods (such as radiometric, gravity or magnetism surveys) and geochemical methods (such as chemical analysis on field samples, drill cores or trench-materials and in situ handheld X-ray fluorescence). These exploration techniques are spatially limited and time and cost intensive. Therefore, it is necessary to develop and integrate new technologies that perform the analysis on large areas, time saving and in detail. For this purpose, remote sensing techniques are of more frequent use. Especially to map hardly accessible terrains or large surface areas, for target detection, prospection mapping and mining monitoring they bear an enormous potential. This study focusses on the development of new technologies to establish a link between classic exploration tools and the hyperspectral mapping. The potential to classify the surface of an outcrop and therefore give valuable information on locally concentrated ore zones is investigated. More precisely, the fusion of rare earth elements detection using sharpened absorption bands, spectral segregation of iron oxides and spatial mapping of major carbonatite forming minerals is investigated. In addition, the capacity of remote sensing techniques to sharpen the geological exploration is studied. In order to validate the accomplished results, a geological investigation including geochemical and hyperspectral laboratory analysis of field samples was performed for every outcrop of the test site.

Compared to a digital photo camera that collects the reflected photons in the wavelength ranges equivalent to red, green and blue light, a hyperspectral data cube consists of about 100 to 1000 different wavelength ranges (channels). As shown in figure 3.1.1, the reflectance values of every pixel can be plotted along the wavelength axis, forming one spectrum per pixel. Hence, the spectrum is the visualization of the reflectance characteristics of different materials at different wavelengths. In order to interpret such a spectrum, the concave indentations (absorption features) that occur at specific wavelength ranges are analyzed. The position of an absorption feature is characteristic for a certain material and the absorption depth correlates with the abundance of this material. Important absorption features of carbonatites are shown in the example spectra of figure 3.1.2.

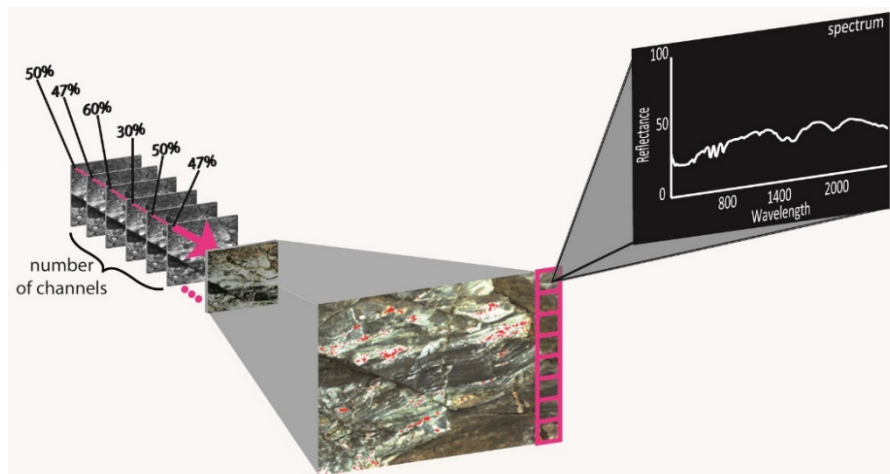


Figure 3.1.1: Example of hyperspectral image acquisition.

In order to map the local distribution and relative concentration of rare earth elements in the outcrop, a detailed knowledge of the distribution of the ores (calcitic, dolomitic and ankeritic carbonatites) is required.

Therefore, the analysis of the absorption bands of Ca-calcite, Mg-calcite and iron oxides is necessary. After Clark et al., 2003, and Clark and Swayze, 1995, the absorption band for Ca-calcite is located at 2330 nm and for Mg-calcite at 2340 nm. The solid solution series for calcitic-dolomitic calcites would absorb between 2330 and 2340 nm depending on the amount of Ca and Mg. Iron oxides show their characteristic absorptions at 940 nm, 650 nm and 540 nm (Ben-Dor et al., 2009; Clark and Swayze, 1995; Townsend, 1987).

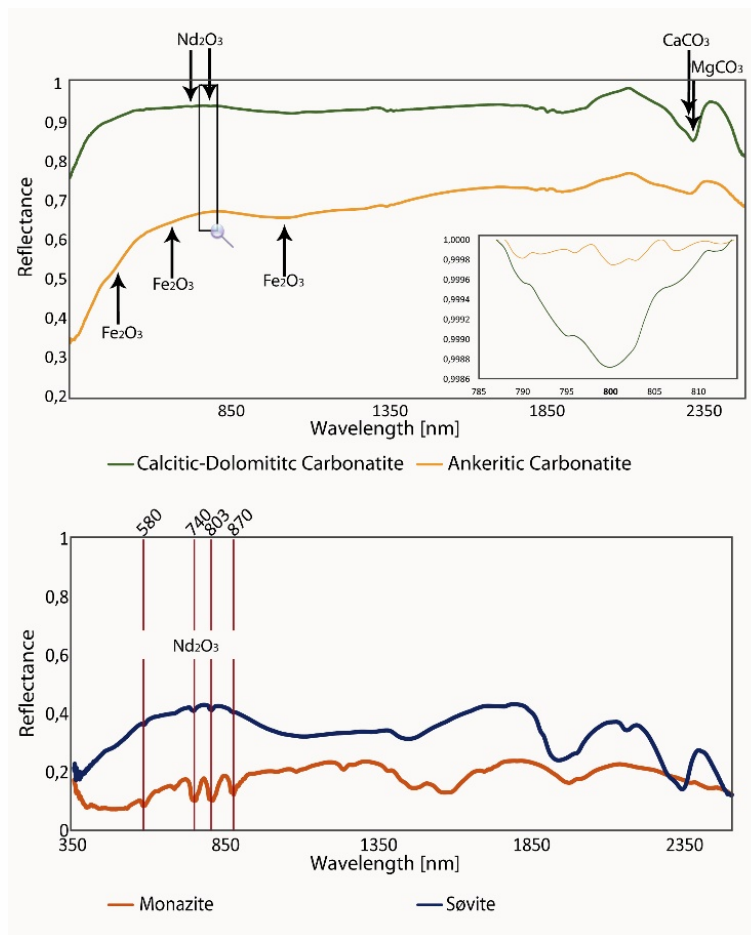


Figure 3.1.2: Example spectra of rare earth elements bearing rocks and minerals (measured with the ASD-analytical spectral device Fieldspec3 Hi-Res). Upper graph: carbonatite rocks from Fen complex. Lower graph: Monazite-mineral and monazite bearing carbonatite rock (søvite). Graph is modified after Boesche et al., (2015).

Compared to the considerably broad absorption bands of calcites and iron oxides, rare earth elements have narrow and distinct absorption bands. As shown in figure 3.1.3, the strongest absorptions are at 870 nm, 803 nm, 740 nm and 580 nm for neodymium, at 1260 nm, 887 nm, 800 nm and 745 nm for dysprosium and at 649 nm, 538 nm, 464 nm, 421 nm and 363 nm for holmium. The spectrum of neodymium can be representatively used for the detection of Light Rare Earth Elements (LREE: La, Ce, Pr, Nd) and dysprosium and holmium can be representatively used for the detection of Heavy Rare Earth Elements (HREE: Tb, Dy, Ho, Er, Tm, Yb, Lu). In addition, due to their direct correlation they can also be used for Medium Rare Earth Elements (MREE: Sm, Eu, Gd). Those three elements (neodymium, dysprosium and holmium) are used because they are less affected by absorption bands of other materials.

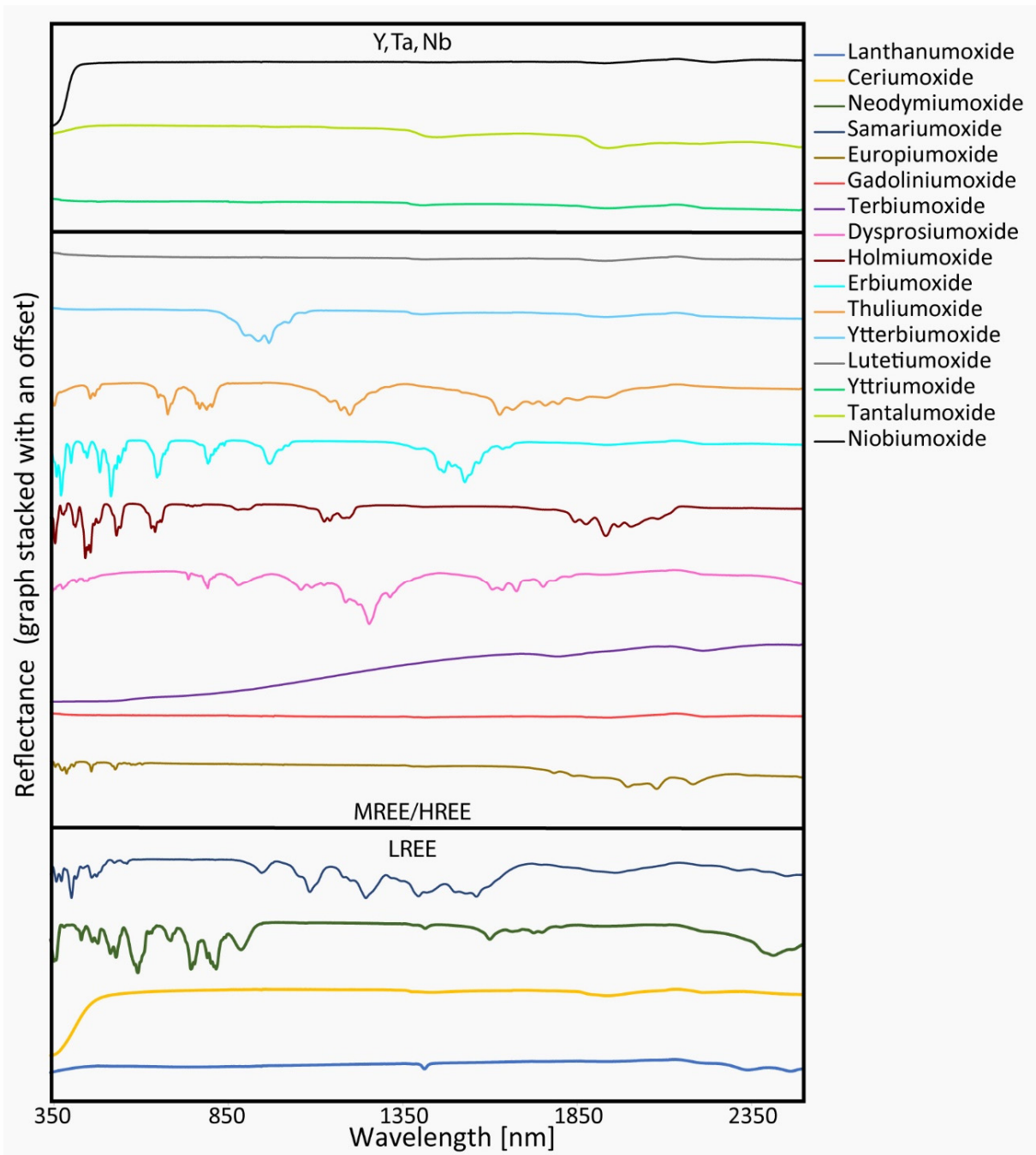


Figure 3.1.3: Spectra of 13 rare earth elements and 3 associated elements of rare earth element deposits.

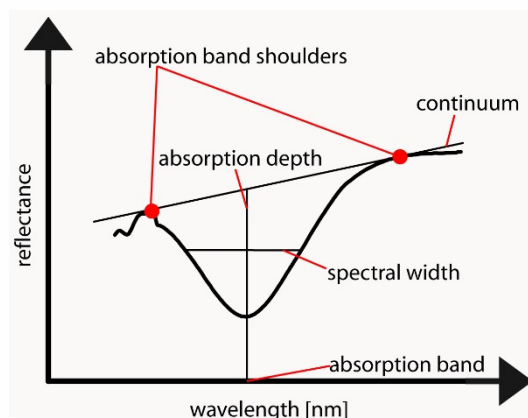


Figure 3.1.4: Important terms for the description of absorption features.

The most diagnostic rare earth element absorption bands, which were mentioned before, and the absorption bands for calcite, dolomite and iron oxide provide the information needed for a classification of the hyperspectral images. All used absorption features can be described by their minimum peak positions (absorption band), their local maxima (absorption band shoulders), their relative depth (absorption depth), their width (spectral width) and their continuum (straight line between the two band shoulders representing the spectrum without a given absorption) (figure 3.1.4). Metals mainly absorb in the VNIR range (350-1000 nm) due to electronic field transitions and minerals mainly absorb in the SWIR range (1000-3000 nm) due to molecular dynamics. In literature it is commonly assumed that all absorption features can be mathematically described as a Gaussian curve, because the electronic field transitions and molecular vibrations originating absorption features follow a Gaussian probability function (Sunshine and Pieters, 1993). Therefore doublet (or triplet-) features might be modeled as a superimposition of two (or three) Gaussian curves that are spectrally close to each other. The interpretation of reflectance spectra is based on the diagnostic absorption features and is usually performed using spectral expert knowledge and/or library comparison. Broadly applied methods are spectrum matching techniques (cross-correlations, spectral angle mapper and spectral feature fitting) (Cloutis, 1996; van der Meer et al., 2012) and spectral unmixing algorithms (linear spectral unmixing, pixel purity index) (CLOUTIS, 1996; van der Meer et al., 2012). These methods were also considered in the first publications for rare earth element mapping by Bedini (2009) and Rowan et al., (2003, 1986). However, an extended method for detection of rare earth elements is required, because the absorption features of rare earth element bearing rocks are narrow and flat as shown in figure 3.1.2. Therefore, they may have a similar shape than sensor characteristic noise and random background noise. Additionally, rare earth element absorption bands are superimposed with broad absorptions of other materials, such as iron oxides.

3.1.2 Geological Setting

The Fen complex is an oval shaped intrusion of magmatic limestones, that was first described by Brøgger, (1894). The comprehensive work of Brøgger, (1894), about the magmatic intrusion of alkaline melts formed the base for today's carbonatite research. Consequently, Fen complex is the most well-known alkali province of the world and has established as standard type locality for the following rock types: fenites (alkali-metasomatized rocks), damtjernites (phlogopite bearing ultramafic alkaline lamprophyre), rødbergites (hydrothermally altered Fe-rich carbonatites) rauhaugites (dolomite-ankerite carbonatites) and søvites (calcite carbonatites). In literature it is broadly assumed that the rocks of the Fen complex were formed in a two-step intrusion, which occurred in the late Ediacaran to early Cambrian (around 580 Ma before 1950) period (Andersen, 1988, 1986; Lie and Ostergaard, 2011).

After Mitchell and Brunfelt (1975), the first event was the intrusion of the søvites, highly fractionated silicocarbonatites that lie on top of a nepheline- and alkali-pyroxene-rich magma chamber. Contemporarily, the intrusion of the alkali-rich magma caused an alteration of the surrounding gneisses - the fenites. The fenites include several rock types and rock's fabrics that are formed by hydrothermal alkaline metasomatism (Andersen, 1986; Brøgger, 1894; Lie and Ostergaard, 2011). The fenites in the Fen complex are represented by an overprint of the foliated neighboring gneiss, the formation of new minerals (fluorite, aegirin, augite and epidote), partially occurring monomineralic rocks of few meters diameter (epidotite and albitite) and rocks with syenitic composition. The fenite rocks form a ring shape around three different carbonatite units (søvites, rauhaugites and rødbergites) and few outcrops of the ultramafic, mantle derived damtjernite rocks (Mitchell and Brunfelt, 1975). The magma of the second intrusion was a magnesium rich carbonatite magma, which caused a metamorphose and metasomatism of ankerite carbonatites into hematite-rich rødbergites .

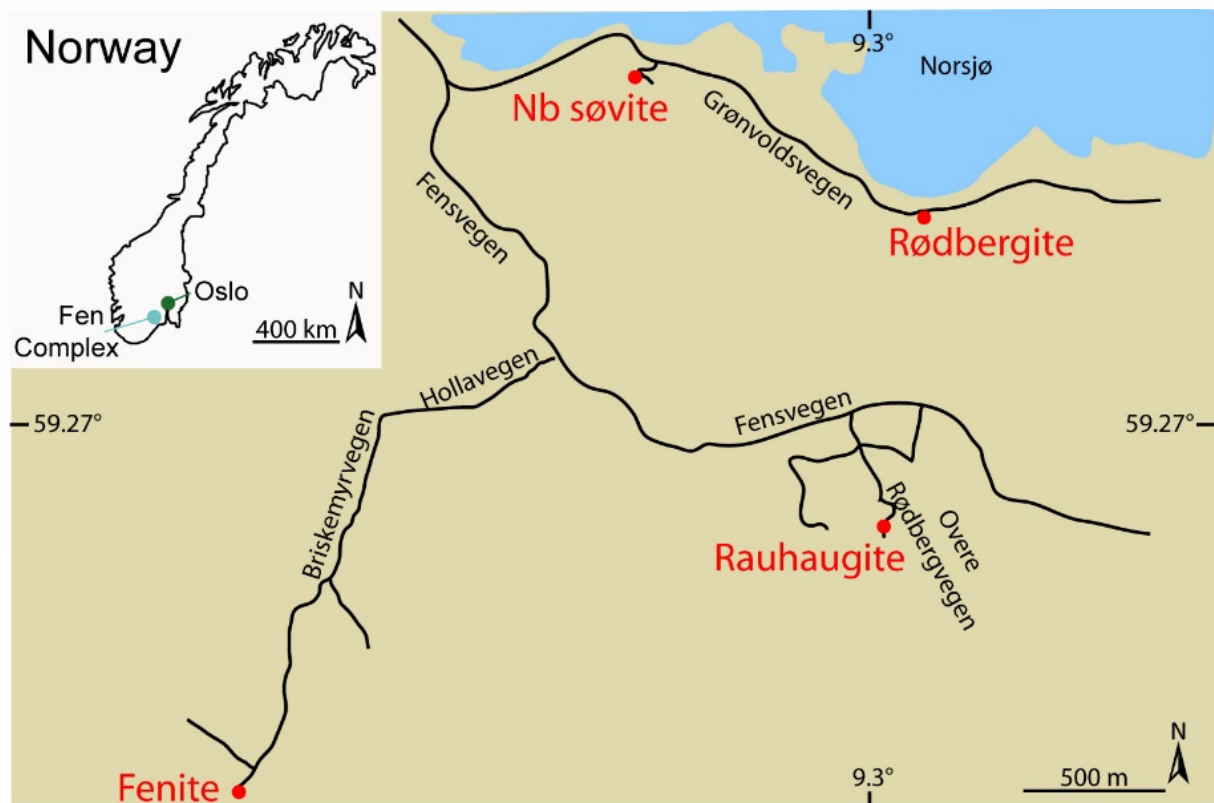


Figure 3.1.5: Overview map of the Fen complex region. The map of Norway in the upper left corner is modified after Boesche et al. (2015).

This study focusses on three outcrops of the Fen complex (figure 3.1.5): One of the søvites (59.28120°N, 9.28628°E), one of the rauhaugites (59.26670°N, 9.30068°E) and one of the rødbergites (59.27676°N,

9.30513°E). All three outcrops are open cuts along a road. The outcrop surfaces have a thin weathering surface. Some horizontal parts of the outcrop are covered with moss and lichen that appear to be non-indicative neither for specific minerals or rocks. The mineral composition of those three carbonatite rocks is (Sieg, 2014):

- Søvites: apatite, baryte, calcite, hematite, columbite, monazite, uraninit, pyrite
- Rauhaugites: allanite, baryte, celsian, calcite, dolomite, hematite, ilmenite, columbite, parasite, pyrite, (Dy-) pyrochlore, quartz, rutil
- Rødbergites: allanite, ankerite, calcite, hematite, ilmenite, pyrite, quartz, thorite, bastnaesite

3.1.3 Materials and Methods

A bundle of different hyperspectral and geochemical methods were used to describe the three outcrops at Fen complex.

- Hyperspectral methods: The hyperspectral methods include a general mineral analysis based on the MICA algorithm (Kokaly, 2011), a detailed mapping of iron oxides and iron containing minerals and a detection of the spectral signatures of neodymium, dysprosium and holmium. Additionally, the influence of iron oxides on the neodymium detection is investigated.
- Geochemical methods: The geochemical methods include in situ detection of chemical elements using a handheld XRF device and laboratory ICP-OES measurements of the rare earth element concentrations on field rock samples. The results of the geochemical part also include the validation of the hyperspectral results.

3.1.3.1 Materials

3.1.3.1.1 Field Work Procedure to Collect the Hyperspectral Data Cube

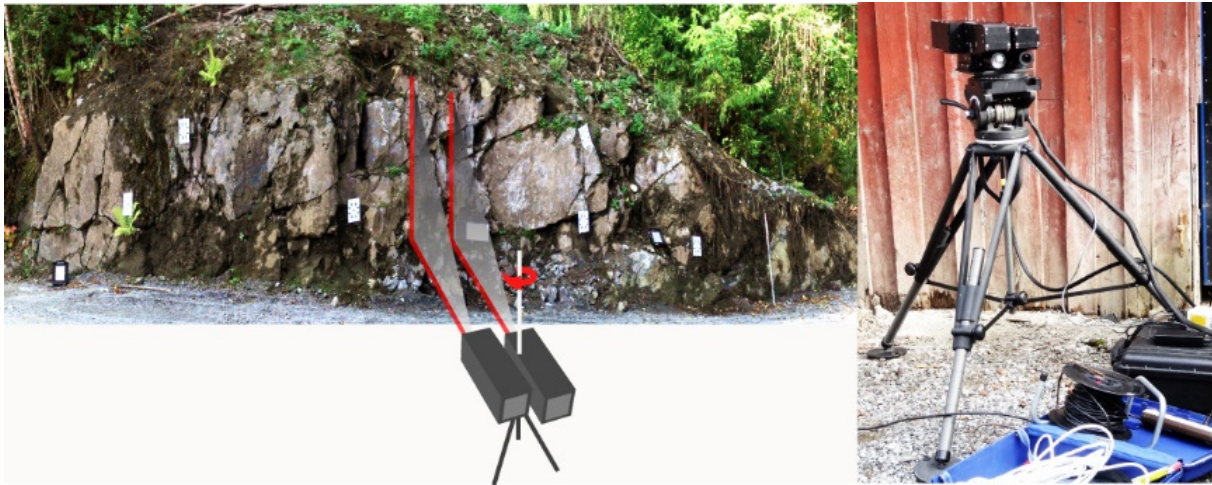


Figure 3.1.6: Descriptive map of hyperspectral image acquisition with the HySpex imager in the field.

A map of the local distribution and relative concentration of rare earth elements in the outcrop surface and a detailed knowledge of the distribution of the ore rocks is a result of the spectral analysis of the images provided by an outcrop-covering hyperspectral imager. In this work, the hyperspectral image cube is collected with a HySpex hyperspectral imager consisting of two cameras covering the VNIR and SWIR ranges, respectively (HySpex VNIR 1600, HySpex SWIR 320-me specifications). The HySpex imager outperforms other hyperspectral ground imager in particular through its capability of collecting the full spectral range (VNIR and SWIR). Additionally, its high spectral and spatio-temporal resolution and its ease of image acquisition in the field are beneficial. The two separate HySpex cameras were mounted in parallel on a tripod and placed 8-11 m distant to the target outcrop (figure 3.1.6) for a full coverage of the outcrop. The number of pixels per line for the HySpex system was 1600 for the VNIR and 320 for the SWIR. Field-Of-View expanders were used for both cameras to double the Field-Of-View (FOV) and therefore enable the acquisition of the full outcrop height. After outcrop related selection of frames (number of lines) and integration time (integration time as an function of the mean outcrop brightness; the brighter the shorter) clockwise scanning was performed using both sensors. The scan lines or frames successively formed a hyperspectral data cube in which each pixel represents the reflectance spectrum of a small surface area. The number of channels (spectral sampling interval) for the VNIR was 160 (3.6 nm band pass) and for the SWIR 256 (6 nm band pass). The integration time, frame period and frames per image collection were defined differently for every outcrop scan (table 3.1.1). The limitations of the HySpex system are the requirement of an external energy supply or generator and that acquisition type is push broom (e.g. full-frame acquisition would decrease illumination variations and acquisition time). Additionally, a limitation for hyperspectral analyses in general is the low penetration depth, which is wavelength and material dependent (for geological applications it is less than 1 mm).

Table 3.1.1: Camera settings and preferences for the image acquisition with the HySpex imager.

	Camera settings	VNIR	SWIR
Søvite	Integration time [ms]	30	18
	Frame period [ms]	31	61.753
	Frames [#]	3000	830
	Rotation angle [degree]	97°	
	Average distance to outcrop [m]	8	
Rauhaugite	Integration time [ms]	7	5
	Frame period [ms]	8.1	16.135
	Frames [#]	2100	520
	Rotation angle [degree]	68°	
	Average distance to outcrop [m]	10	
Rødbergite	Integration time [ms]	50	30
	Frame period [ms]	51	101.594
	Frames [#]	4500	1140
	Rotation angle [degree]	145.5°	
	Average distance to outcrop [m]	10.5	

3.1.3.1.2 Field Sampling

The field work comprises the collection of rock samples for the geochemical analyses and an in situ X-ray fluorescence (XRF) analysis. It also forms the basis for the validation of the hyperspectral results. Representative rock samples for rare earth element analysis were extracted from visually homogeneous and mineral gradient free regions of the outcrop, as marked with red squares in figure 3.1.7. Those rock samples are the basis for the following geochemical analysis. In addition, in situ XRF analysis using a Thermo Niton XL3t were performed at the positions of the red circles in figure 3.1.7. The Thermo Niton XL3t performs a nondestructive testing of chemical element concentrations with fast but accurate results. The limitation for this device is that the excitation voltage is too low for a testing of the MREE and HREE. The XRF sampling positions were chosen based on the physical accessibility for the field team and on eventual occurring vertical material gradients.

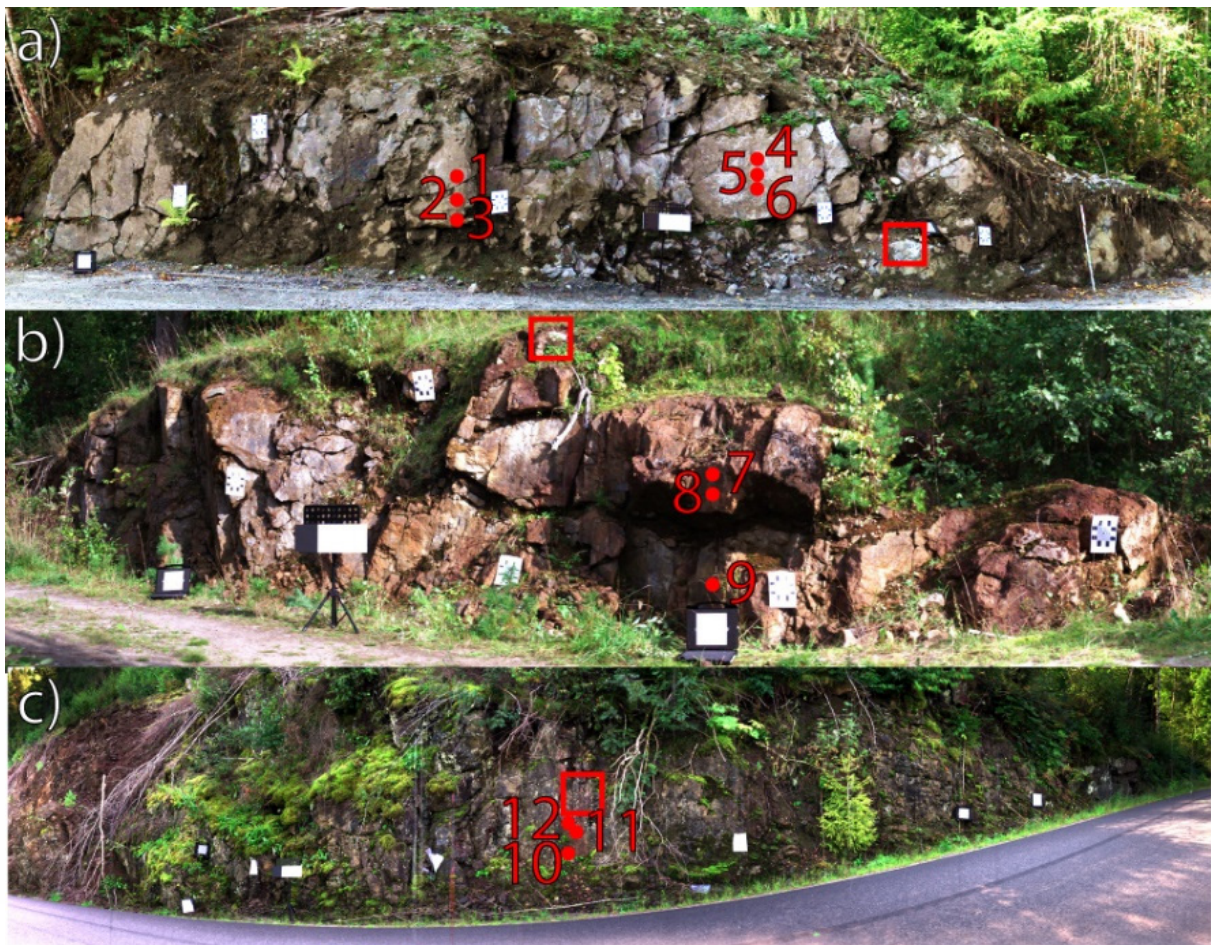


Figure 3.1.7: Sampling positions in the field. a) shows the søvite outcrop, b) shows the rauhaugite outcrop and c) shows the rødbergit outcrop. The images were acquired with the HySpex imager (R, G, B color composite).

3.1.3.2 Hyperspectral Methods

In this study, a synthesis of three different hyperspectral analysis methodologies is presented. Those methodologies have been validated with the results of geochemical analysis in the laboratory. The first method was the MICA mineral determination after Kokaly (2011). It was applied on both the VNIR and SWIR spectrum of each pixel to characterize the outcrop surfaces to spatially delineate material gradients (dykes, schlieren, etc.). MICA detected calcite, dolomite and siderite. Here, only the søvite and rauhaugite outcrops were classified for these carbonatite typical minerals. The rødbergite outcrop was erroneously characterized due to its high amount of iron. MICA was chosen because it represents the further development of the well-established USGS Tetracorder expert system, which is the reference method for mineral mapping from imaging spectroscopy data. The second method was the detection of iron indicative pixel. The benefit of the Iron Feature Depth (IFD) of Mielke et al. (2014) was the concentration of the analyses on the VNIR in a fast and robust manner (the SWIR was impacted by low image signal-to-noise-ratio (SNR)). This method was performed for all three outcrops in the indicative VNIR range. The third method was the rare earth element detection after Boesche et al., 2015, and was also applied on all outcrops. This method is introduced to determine the spatial distribution of neodymium (VNIR range), holmium (VNIR range) and dysprosium (SWIR range).

3.1.3.2.1 Hyperspectral Preprocessing

For every outcrop a minimum of ten images were acquired and each of them transformed into reflectance data. Before transforming the data cube into reflectance, a normalization of the image albedo (reflection coefficient) was applied to account for varying illumination and surface shadowing. Here, a rationing between a reconstructed pan image and hyperspectral data cube was used. The pan image was retrieved as a spectral integral of all VNIR channels, smoothed using a broad Boxcar filter and then mean normalized. After illumination normalization by dividing each channel with the normalized pan image, the raw Digital Number (DN) was radiometrically scaled to radiance ($W \cdot sr^{-1} \cdot m^{-2} \cdot nm^{-1}$) using predefined sensor characteristic radiometric calibration coefficients. Therefore five calibrated reflectance standards (reference panels) were placed in front of every outcrop (5%, 20%, 50%, 90% and a 95%) and the mean radiance spectrum of every panel was calculated and normalized according to their relative reflectance level. Then, a polynomial modeling of the incident direct and diffuse irradiance was performed for every spatial position (pixel) of the image and for all channels using all five panel spectra. The irradiance model was then applied on each pixel for reflectance retrieval. Afterwards a weighted average of all three data cubes according to their spectral homogeneity was calculated (figure 3.1.8a). For every image the spectral homogeneity of the five calibrated reflectance standards was determined using the standard deviation of all pixel spectra at the reflectance standard locations (Boesche et al. 2015). The resulting data cube was then used for the analysis of the surface mineralogy.

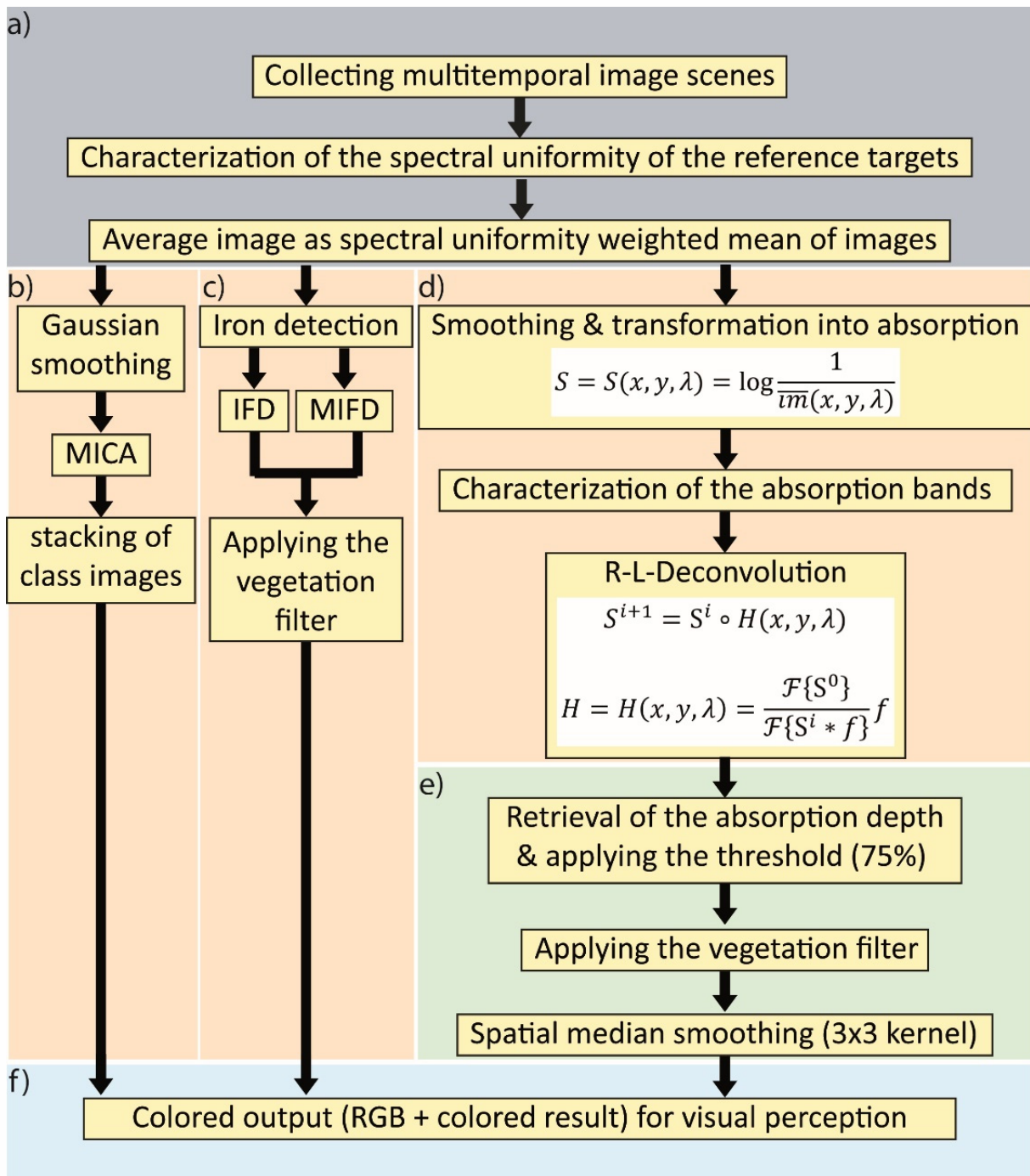


Figure 3.1.8: Processing flow chart of the applied imaging spectroscopy methodologies. Modified after Boesche et al. (2015).

3.1.3.2.2 MICA (written with the help of Friederike Körting)

In order to map the calcite and dolomite concentration, all spectra of the hyperspectral image cube from section 3.2.1 (figure 3.1.8a) had to be smoothed using a convolution of each spectrum with a Gaussian curve ($\sigma = 2$). The smoothed hyperspectral image cube was then analyzed with the ENVI-software associated U.S. Geological Survey "Processing Routines in IDL for Spectroscopic Measurements" PRISM program (Kokaly, 2011). The "Material Identification and Characterization Algorithm" MICA algorithm (figure 3.1.8b) focuses on detecting and differentiating minerals and mineral-phase-mixtures (Kokaly, 2011). The reference spectra included in MICA are from materials of known composition from the USGS's spectral library splib06 (Clark et al., 2003). Those spectra are the base for a comparison with an image spectrum of unknown material. To be comparable both spectra have to have the same spectral properties. Thus the HySpex data were resampled to HyMap reflectance data (MICA is originally adapted for the HyMAP sensor (Cocks et al., 1998) characteristics) and a continuum removal was applied. The following description of the MICA software is based on Kokaly (2011). To get hold of the most diagnostic absorption bands, strong and unique absorption bands are extracted automatically at their continuum endpoints from the library. MICA then uses a linear regression for the comparison of those features, whereas the merit function is the coefficient of determination (r^2) from the linear regression. In addition, MICA matches the depth value of the unknown and known absorption bands. Positive depth values are termed absorption feature, negative depth values emission features. For every absorption band found, an associated weight factor is defined (here the area of absorption). Therefore a weighted fit value for every absorption band of each material can be calculated by multiplying the fit values by the associated weighting factors which are then summed up for every material. The reference material with the highest fit value is then assigned to the unknown material ("best match"). To avoid wrong decision making, feature and continuum constraints are defined for every material. If a spectrum does not pass these thresholds (e.g. minimal albedo, minimal absorption etc.) the material is not assigned to it. To analyze the carbonatites the MICA command file "mica_cmds_group2_hymap2007.mcf" was used, it contains mainly information to detect mica, clay minerals and carbonates. The MICA -algorithm is able to analyze the image cubes pixel based and gives out classification maps for the detected mineral phases. After using the MICA software, a mineral map of the detected dolomite and calcite was created. Therefore the classification images of the MICA analysis were stacked in the ENVI-software and a mask was applied to show their distribution in the outcrop. The limitations of the MICA method are that always the VNIR and SWIR have to be analyzed together, the image cube has to be down sampled to HyMAP spectral resolution, the input library is restricted to one predefined input set and a continuum removal has to be applied prior to analysis. Hence, superimpositions of different absorption bands would not necessarily be recognized separately. This is especially the case for the small absorption bands of the rare earth elements that may be superimposed by wide absorptions of iron oxides or vegetation.

3.1.3.2.3 Hyperspectral Iron Oxides Detection (written with the help of Christian Mielke)

The Iron Feature Depth (IFD) of Mielke et al. (2014) was used in a modified way (HySpex VNIR) to map the spatial distribution of iron bearing minerals on the outcrop surface (figure 3.1.8c). Originally the IFD has been defined as a three-point band-depth at 900 nm. This concept of the IFD was transferred to the 650 nm iron absorption band because the original IFD definition would include the usage of data from both HySpex detectors (VNIR and SWIR). This adaption avoids problems from a potential imperfect data calibration and has the advantage that it may also be used under unfavorable light conditions that would especially reduce the SNR in the SWIR sensor. For the 650 nm (± 20 nm) iron absorption feature, these modifications are a redefinition of the left shoulder at 603 nm, the maximum absorption at 658 nm and the right shoulder at 778 nm. The difference between the reflectance value at 658 nm and the linear interpolated reflectance value between the left and the right shoulder of the feature represents this IFD at this position. A modified version of the IFD (MIFD) was additionally defined using first order univariate spline interpolation (figure 3.1.8c). This modified version was used to construct an interpolated version of the input spectrum that estimates the

albedo of the VNIR data with the node points for the spline interpolation spanning three ranges, shown in table 3.1.2. However, it is not possible to construct the IFD at 940 nm as original defined in Mielke et al. (2014) because the spectral range of the HySpex VNIR sensor would be exceeded. A low root-mean-square error between the classical three-point band-depth IFD at 658 nm and the spline version was detected in case of data from the rauhaugite example. Therefore, the result may also be used as a proxy for iron bearing minerals, such as goethite or hematite. That fact may now be exploited to define the MIFD at 940 nm in a similar fashion to the MIFD at 658 nm, as the difference between the spline interpolated reflectance value at 940 nm and the measured reflectance value at 940 nm. This is especially useful if only a VNIR spectrometer is available for fieldwork or if the SWIR capabilities are seriously hampered due to unfavorable illumination and scanning conditions. All iron feature depth and modified iron feature depth maps are filtered with the normalized difference vegetation index (NDVI (red=670nm, infrared=770nm) < 0.1). In order to reduce the false positive rate caused by superimpositions of reflected or transmitted vegetation spectra. The limitations of the IFD and MIFD are that they cannot distinguish between Fe-minerals and Fe-oxides and they are have to be manually adapted for every sensor.

Table 3.1.2: Wavelength ranges used for the spline interpolation of a smoothed representative of the VNIR input spectrum for a retrieval of the modified interpolated IFD at 658 nm and 940 nm.

Range	Wavelength Range (nm)
A (5 HySpex Channels)	414-436
B (4 HySpex Channels)	578-592
C (2 HySpex Channels)	771-781

3.1.3.2.4 Rare Earth Element Detection

For the detection of the rare earth elements indicative pixel a knowledge based algorithm was used. It mainly sharpens the diagnostic absorption bands and it is able to detect visually non perceptible absorption bands. The limitations of this method clearly are that it is only tested for a detection of neodymium and that the presence of spectroscopic hampering materials, such as vegetation or iron coatings is not fully understood. In this study, the method that was firstly published by Boesche et al., 2015, was adapted in two ways. 1) it was calibrated for two more rare earth elements indicating MREE and HREE and 2) the results are filtered for vegetation coverage using the NDVI ratio (Julien et al., 2011). Additionally the impact of iron oxides was investigated.

Integrating proposed adaptations, the hybrid method can be described as follows:

As shown in figure 3.1.8d) the first algorithm step is a smoothing of every spectrum of the hyperspectral data cube (equation (1) and a transformation into absorption spectra is performed).

$$S = S(x, y, \lambda) = \log \frac{1}{\overline{im}(x, y, \lambda)} \quad (1)$$

$S(\lambda)^i$ are the resulting smoothed absorption spectra (\overline{im}) from chapter 3.2.1 and i is a running index representing all image pixel. Now the absorption bands are assigned to a spectral library (figure 3.1.3) and their widths are determined. Those parameters are then used to set up the filter function for the Richardson Lucy deconvolution (equation (3)). The filter function f is a Gaussian bell shaped curve, because as described in the introduction the diagnostic absorption bands are similar shaped. The sigma of the Gaussian curve directly is a function of the width of the diagnostic absorption band. It is twice the frequency equivalent of the rare earth element-absorption band to avoid aliasing due to the Nyquist Shannon theorem. Here the absorption band for neodymium has a width in the VNIR region of about 70 nm (here: sigma = 1.5), the

absorption band for holmium has a width in the VNIR region of about 40 nm (here: sigma = 0.75) and the absorption band for dysprosium has a width in the SWIR region of about 70 nm (here: sigma = 0.75). The Richardson Lucy deconvolution can be described as follows:

$$S^{i+1} = S^i \circ H(x, y, \lambda) \quad (2)$$

$$H = H(x, y, \lambda) = \frac{\mathcal{F}\{S^0\}}{\mathcal{F}\{S^i * f\}} f \quad (3)$$

where H is the Filter Matrix, \circ is the Hadamard product, i is the iteration index, \mathcal{F} denotes the Fourier transform, f is the Fourier transformed filter function for the R-L deconvolution and $*$ the convolution operator. After applying the Richardson Lucy deconvolution, the absorption depth has to be determined. Therefore a linear continuum from the shoulders of the absorption feature is estimated and then removed. In this study we slightly changed the positions of the shoulders and absorption bands compared to Boesche et al. (2015). The recently measured spectra that are shown in figure 3.1.3, showed that the absorption band have a triplet shape, hence, the absolute feature peak is at 818 nm instead of 803 nm. The diagnostic absorption bands are listed in table 3.1.3.

Table 3.1.3: Wavelength positions for the shoulders and peaks of the diagnostic absorption bands (the values are defined with a HySpex image).

Rare Earth Element	Left shoulder position	Peak position	Right shoulder position
Neodymium	778 nm	818 nm	840 nm
Dysprosium	1237 nm	1261 nm	1303 nm
Holmium	433 nm	449 nm	473 nm

Only pixel with an absorption depth of more than three sigma of the noise (according to averaged SNR) are then flagged as rare earth element indicative pixel. A vegetation mask (VNIR: NDVI (red=670, infrared=770) < 0.3 and SWIR: NDVI (red=1207, infrared=1555) < 2.5) and a median-kernel of 3x3 pixel was applied in order to reduce outliers, such as multiple reflections, transmittance or positively identified random noise.

In Boesche et al. (2015) spectral abundances of iron oxides are considered as hampering factors for the detection of neodymium. A series of laboratory measurements was conducted to find an answer of how strong iron influences the rare earth element detection and to find a way how neodymium detection can be realized even if iron is occurring (like in the rauhaugite and rødbergite rock unit). Therefore several CaCO₃, FeO/Fe₂O₃ and Nd₂O₃ concentrations were realized by artificial mixing (see table 3.1.4 and 3.1.5). In total two mixtures were realized: 1) a carbonate powder with a neodymium concentration of 0.1% and 2) a carbonate powder with a neodymium concentration of 0.5%. Natural deposits are often enriched with around 0.1% (1000 ppm) neodymium while highly enriched parts of outcrops can reach a concentration of 0.5% (5000 ppm) or higher (Hornig-Kjarsgaard, 1998). These mixtures are the two input powder that were then mixed with ten different concentrations of iron oxide. The exact concentrations were realized using a digital precision scale. The mixtures were then measured with the hyperspectral HySpex imager and the relative absorption depths of the neodymium feature were determined. The relative absorption depth was calculated using the difference between the feature related continuum and the reflectance value of the absorption band. Finally, a comparison between the previously set concentrations and the actual absorption depth could be accomplished.

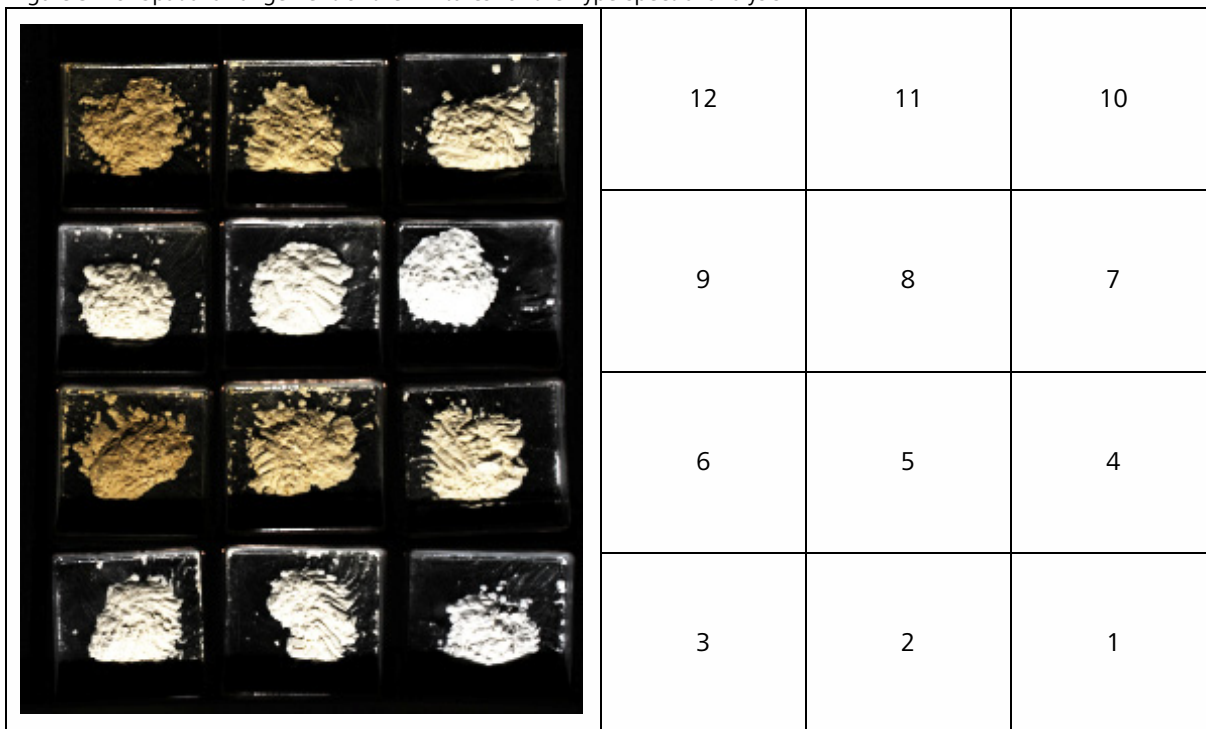
Table 3.1.4: Concentrations in % of neodymium oxide, iron oxide and carbonate powder for the artificial mixture 1.

Mixture 1: 0,1% Nd ₂ O ₃ + 99,9% CaCO ₃					
Nr	Iron Oxide	CaCO ₃ +Nd ₂ O ₃	(CaCO ₃	+	Nd ₂ O ₃)
1	0.12	99.9	(99.8001	+	0.0999)
2	0.58	99.5	(99.4005	+	0.0995)
3	1.07	99	(98.901	+	0.099)
4	2.08	98	(97.902	+	0.098)
5	5.23	95	(94.905	+	0.095)
6	10.37	90	(89.91	+	0.09)

Table 3.1.5: Concentrations in % of neodymium oxide, iron oxide and carbonate powder for the artificial mixture 2.

Mixture 2: 0,5% Nd ₂ O ₃ + 99,5% CaCO ₃					
Nr	Iron Oxide	CaCO ₃ +Nd ₂ O ₃	(CaCO ₃	+	Nd ₂ O ₃)
7	0.11	99.9	(99.4005	+	0.4995)
8	0.57	99.5	(99.0025	+	0.4975)
9	1.22	99	(98.505	+	0.495)
10	2.22	98	(97.51	+	0.49)
11	5.01	95	(94.525	+	0.475)
12	10.09	90	(89.55	+	0.45)

Figure 3.1.9: Spatial arrangement of the mixtures for the hyperspectral analysis



3.1.3.3 Geochemical Methods

3.1.3.3.1 In situ Analysis with a Handheld XRF

The in situ validation of the data set was performed using a mobile X-ray fluorescence device (Thermo Scientific Niton XRF Analyzer: Niton XL3t specifications). For every outcrop, a measurement series has been conducted at the red dot positions in figure 3.1.7. The measuring spot has a diameter of around one cm and the penetration depths for carbonatite material is approximately a few centimeters. The instrument has a 50 kV X-ray tube and can measure most of the investigated elements (except of HREE, Pm and Sm, which would require a higher excitation voltage). The elements are measured by applying four analysis filter: Main, Light, High and Low. The time per measurement was at least 120 sec (30 sec per analysis filter). The error is given as two-sigma of the data distribution. The benefit of the in situ XRF analysis is the direct and iterative knowledge contribution for the field team. The triple test per outcrop allows a detection and reduction of erroneous measurements and increases the precision of the results.

3.1.3.3.2 Geochemical Analysis of the Rare Earth Element Concentrations

In order to prepare the collected field samples for the rare earth elements and yttrium determination, the collected field samples were ground to powder of a particle size of $<63 \mu\text{m}$. After Zuleger and Erzinger, 1988, the first step of the approach is a Na_2O_2 -sinter dissolution of the carbonate material. Afterwards, the rare earth elements and yttrium are separated from the sample using the ion-exchange chromatography (Zuleger and Erzinger, 1988). The inductively coupled plasma atomic emission spectroscopy (Agilent technologies ICP-OES Vista MPX axial specifications) is then used to determine rare earth elements and yttrium concentrations by analyzing the characteristic electromagnetic signatures that are emitted by excited atoms and ions (Zuleger and Erzinger, 1988). In order to plot the resulting rare earth element concentrations, all values were normalized using the C1-chondrite factors of Sun and McDonough (1989). The limitations of the method is the extensive and time consuming preprocessing of the sample and the time consuming ion-exchange chromatography procedure. However, unless only three samples were processed, the precision of this methodology is considerably high.

3.1.4 Results

3.1.4.1 The hyperspectral results

Figure 3.1.10 shows the spatial distribution of the spectral signature of calcite, dolomite and siderite on two outcrops (*søvite* and *rauhaugite*). In figure 3.1.10a) it is shown that the spectral signature of calcite at the *søvite* outcrop is evenly distributed, while the spectral signatures of dolomite and siderite mineral phases are barely occurring. In figure 3.1.10b) two spatial gradients in the spectral signature of the carbonates are perceptible. The first gradient ranges from the left part that mainly shows calcite signatures to the right where calcite and dolomite signatures are visible. The gradient between the left and right units is sharp and follows a vertical geological structure that separates the outcrop into two parts. The other trend is more gradual and extends from the top to the bottom. The top unit shows a higher amount of dolomite indicating pixel than the bottom unit of the image. In addition to these two trends a local enrichment of siderite bearing carbonatites is spectroscopically indicated in the middle of the image.

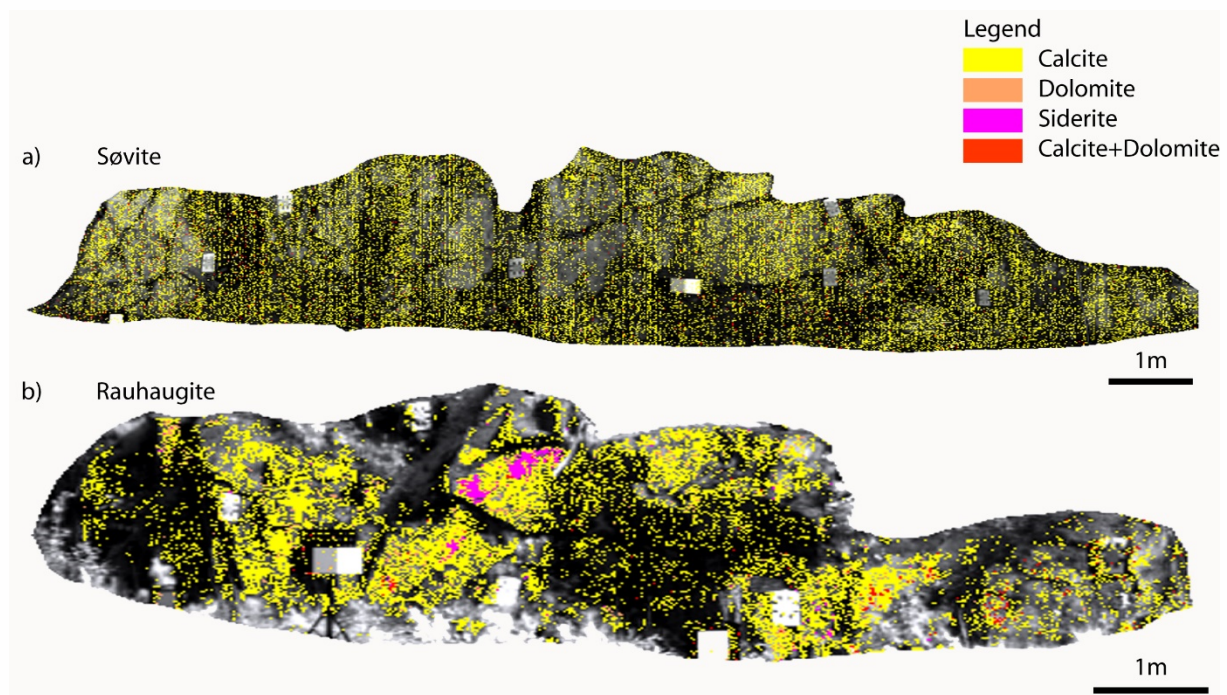


Figure 3.1.10: Lithological classification map of carbonates using the MICA algorithm. a) shows the *søvite* and b) shows the *rauhaugite*.

Figure 3.1.11, 3.1.12 and 3.1.13 show the spatial distribution of iron oxides, whereas the a) images represent the spline interpolated MIFD at the 650 nm iron absorption feature. The b) images show the 940 nm MIFD. In contrast to the 650 nm feature, the 940 nm MIFD is noisier and, hence, cannot resolve gradients between high and low enriched rock units. This is explainable because it represents a wavelength band, which is close to the VNIR sensitivity edge of the detector. Therefore, MIFD is here biased and of limited usage because of insufficient illumination. Figure 3.1.11 shows the iron distributions for the *søvite* outcrop. In image 11a) a trend from the left to the right is perceptible. The left part of the image shows relatively higher amounts of iron oxides. Additionally, structures of weaker material (cracks, weathering surfaces) seem to have higher concentrations of iron oxide. In the distribution pattern of the *rauhaugite* outcrop shown in figure 3.1.12b) one can see the same trends that are visible in the carbonate distributions (higher iron oxide concentrations to the top and to the left of the image). Figure 3.1.13b) shows the iron oxide distribution of the *rødbergite* outcrop. There is an increase of the spectral signature of iron oxide in the center of the image. Here, a thick, vertically extending iron-bearing vein in the center of both of the 650 and 940 nm MIFD results occurs.

Additionally, a trend from the left to the right is perceptible. Especially to the left the spectral signature of iron oxide is of increasing abundance.



Figure 3.1.11: Thematic map of iron oxide showing the søvite outcrop. The classification was done using the MIFD. The underlying images were acquired with the HySpex imager (R, G, B color composite).



Figure 3.1.12: Thematic map of iron oxide showing the rauhaugite outcrop. The classification was done using the MIFD. The underlying images were acquired with the HySpex imager (R, G, B color composite).

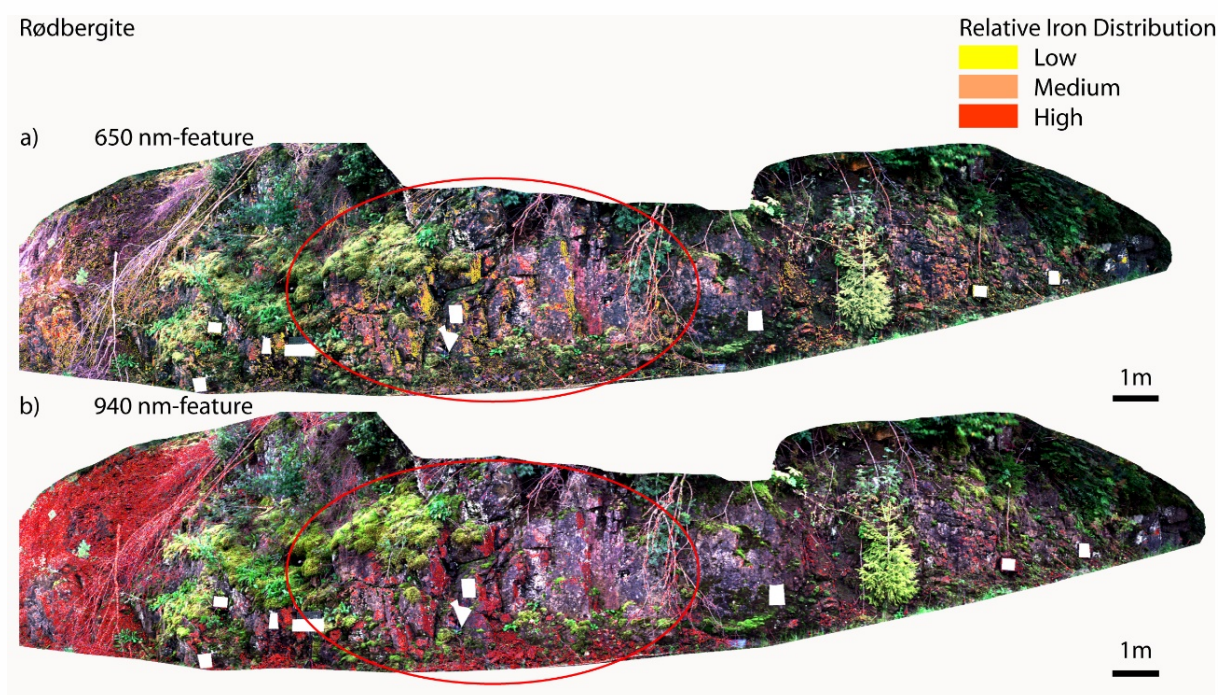


Figure 3.1.13: Thematic map of iron oxide showing the rødbergite outcrop. The classification was done using the MIFD. The underlying images were acquired with the HySpex imager (R, G, B color composite).

Figure 3.1.14, 3.1.15 and 3.1.16 show the spatial distribution of dysprosium, holmium and neodymium. Figure 3.1.14 shows the distribution pattern for the søvite outcrop. In this image there is a trend from the left to the right perceptible for all three rare earth elements. On the left side of the image the amount of rare earth elements increases. This copes with the result of the iron oxide analysis. In addition, there is no difference between the HREE and the LREE perceptible. Figure 3.1.15 shows the spatial distribution of the rare earth elements of the rauhaugite outcrop. As described for the iron oxide and carbonate classification image, the distribution of the rare earth elements shows two trends for this outcrop (higher values at the top and to the lower left of the image). In contrast to the iron oxide maps, the spectral signature for rare earth elements is different for the top unit from the lower-right unit. The lower-right unit shows more pixel with the spectral signature for dysprosium and holmium. In the upper unit one can see an increase in neodymium indicating pixel. Figure 3.1.16 shows the distribution of the rødbergite outcrop. In the center on the image there is a higher amount of dysprosium indicating pixel. It seems that the middle part of the outcrop is enriched in dysprosium over a wider area. However, neodymium seems to be enriched in the center as well, but it is more concentrated to the vertical dyke that is also perceptible in the iron oxide distribution pattern. To the left of the image the amount of holmium and neodymium indicative pixel increases. This copes with the observations of the iron oxide distribution.

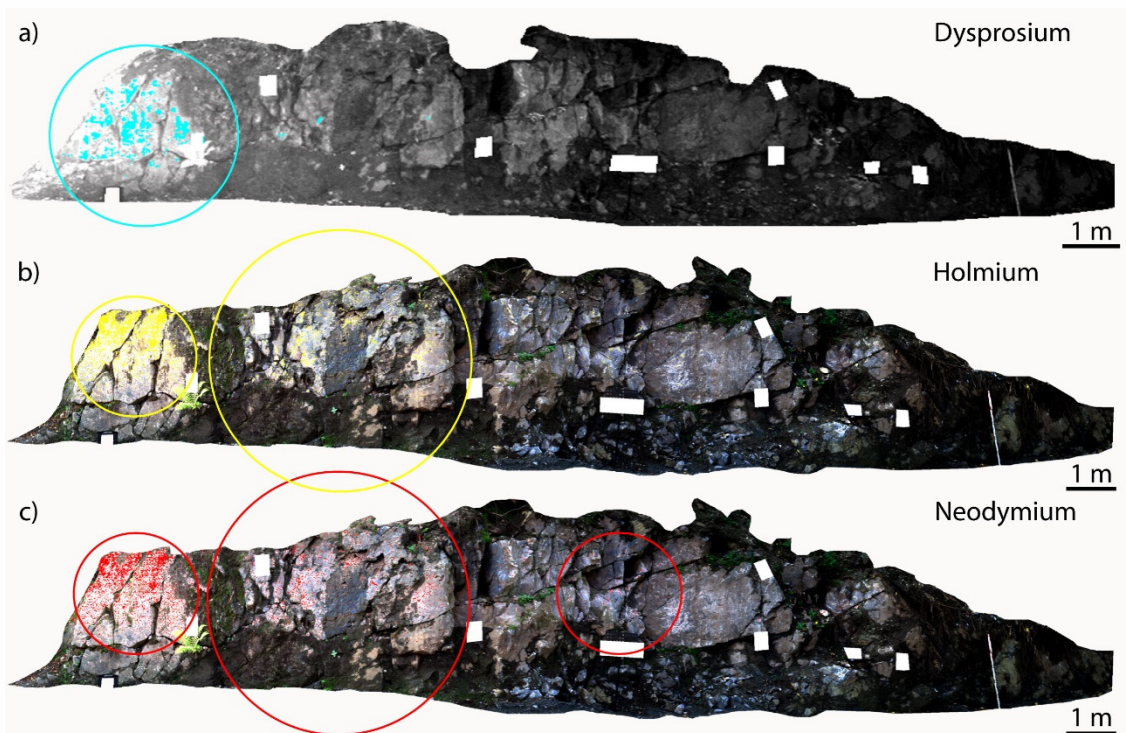


Figure 3.1.14: Thematic map of rare earth element distribution showing the søvite outcrop. The classification was done using the proposed approach of this paper. a) shows the dysprosium distribution, b) shows the holmium distribution and c) shows the neodymium distribution.

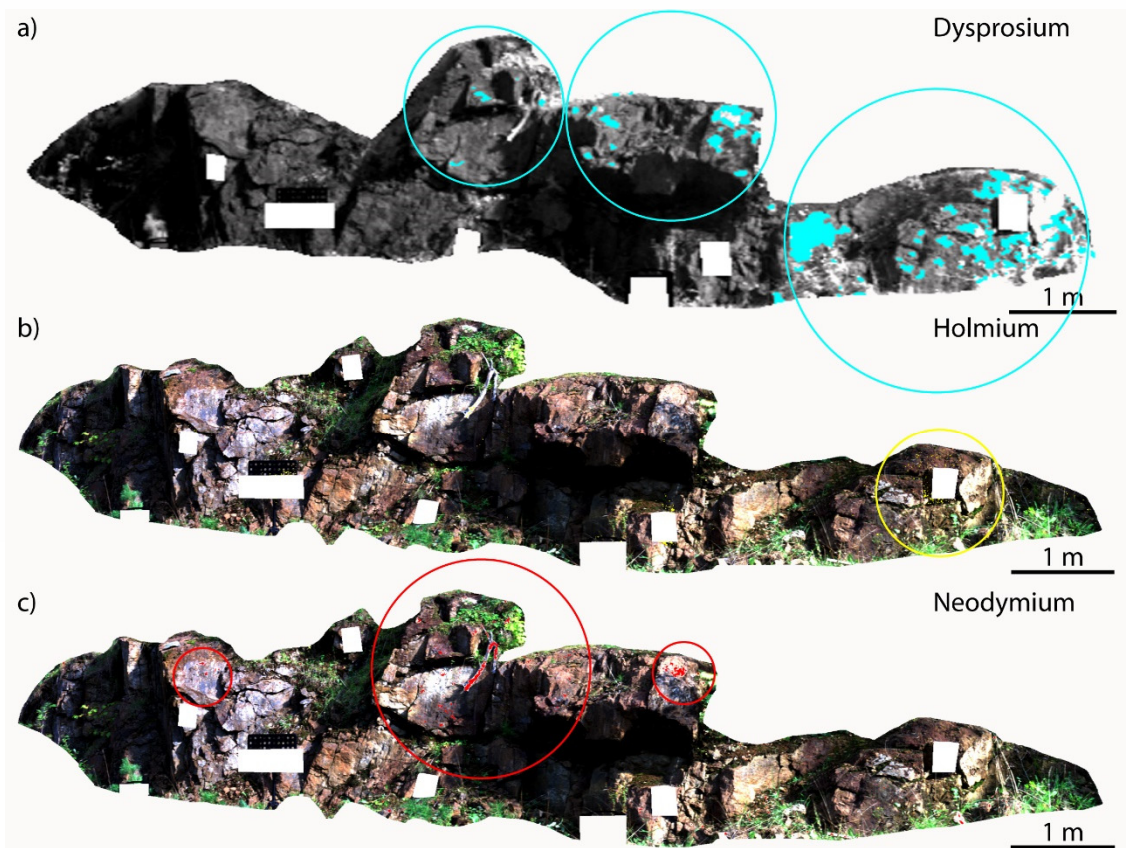


Figure 3.1.15: Thematic map of rare earth element distribution showing the rauhaugite outcrop. The classification was done using the proposed approach of this paper. a) shows the dysprosium distribution, b) shows the holmium distribution and c) shows the neodymium distribution.

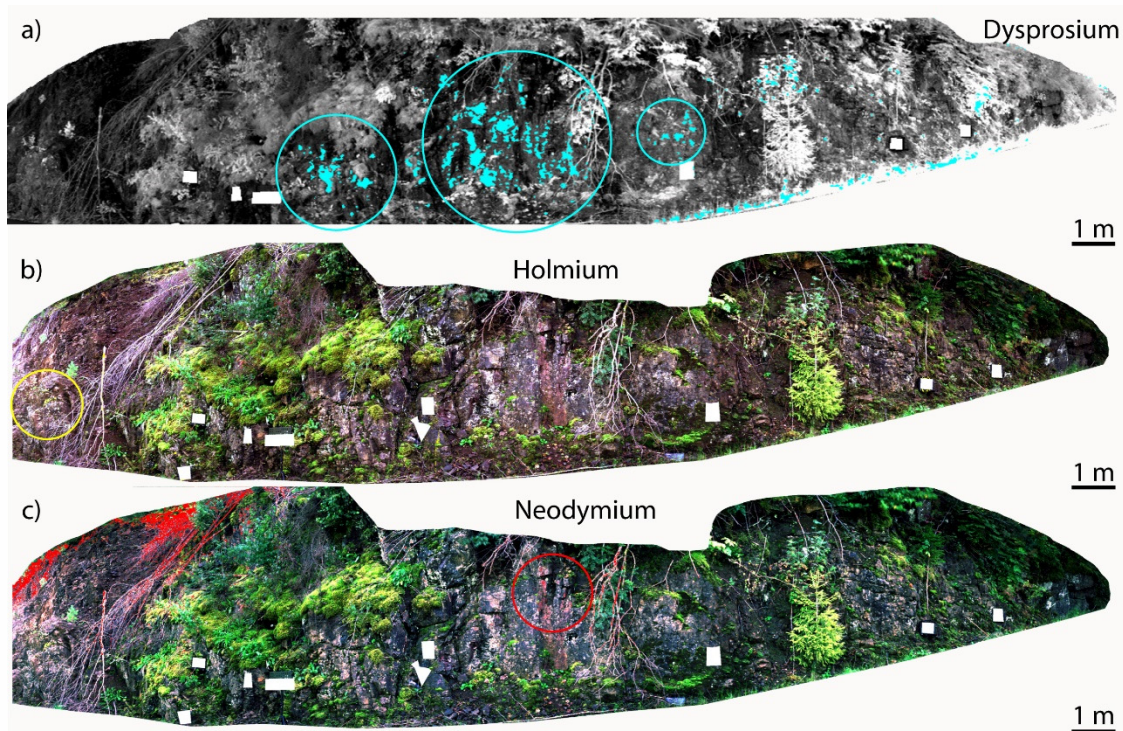


Figure 3.1.16: Thematic map of rare earth element distribution showing the rødbergite outcrop. The classification was done using the proposed approach of this paper. a) shows the dysprosium distribution, b) shows the holmium distribution and c) shows the neodymium distribution.

The resulting spectra of the artificial mixtures, that were produced to investigate the limiting factor of superimposing iron oxides, are shown in figure 3.1.17. Subplot 3.1.17a) and 3.1.17c) show the original retrieved reflectance spectra from the HySpex acquisitions. Subplot 3.1.17b) and 3.1.17d) show the same spectra after applying the Richardson Lucy deconvolution. In the subplots of the original HySpex-spectra there are two superimposing indentations perceptible, the broad iron oxide absorption and the narrow neodymium absorption. A determination of the neodymium-feature shoulders is hampered, because the neodymium feature is included in the left side of the iron oxide feature. Especially for the lower concentration (0.1% neodymium) shown in subplot 3.1.17a) image noise aggravates the discrimination of the neodymium feature. The figure 3.1.17 shows that the occurrence of iron oxide reduces the discrimination of the neodymium feature. If the Richardson Lucy deconvolution is applied, the maximum limit of iron concentration under which a neodymium discrimination is still possible appears to be about 5%. Without using the Richardson Lucy deconvolution a detection is not possible. The maximum limit of iron concentration for mixture 2 (0.5% neodymium) is 10% for both using the Richardson Lucy deconvolution and without using it. This is due to the incorporation of the iron feature whose chemical relation is limited by the low percentage saturation effect as assumed in Mielke et al., 2014.

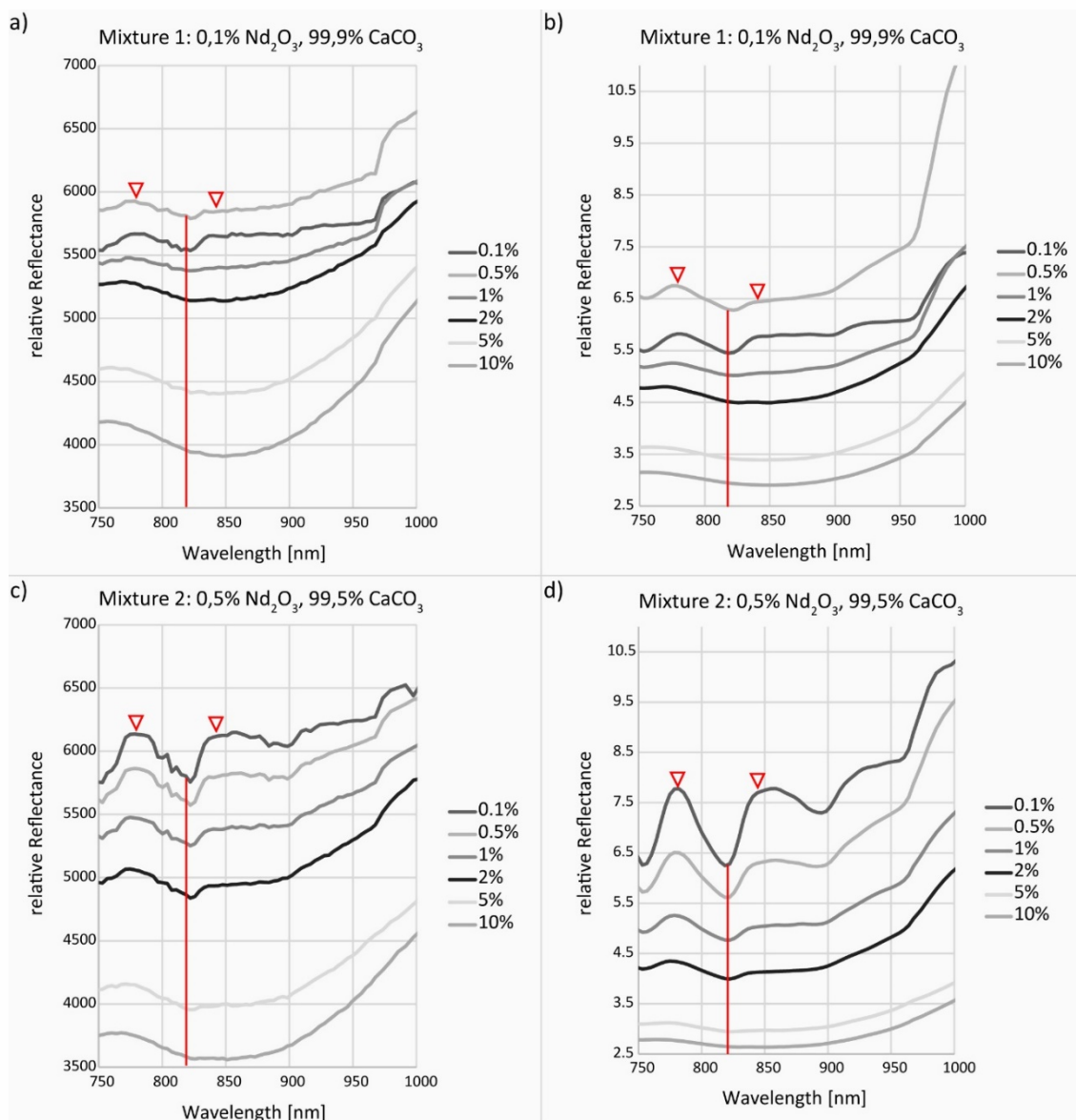


Figure 3.1.17: The spectra of the artificial mixtures. a) and b) represent the mixture one and c) and d) represent the mixture two. The left graphs show the original HySpex spectra. The right graphs show the spectra after applying the Richardson Lucy deconvolution.

3.1.4.2 The geochemical results

The mobile XRF results enable a comparison between all three outcrops. The major element composition shows that the main difference between all outcrops is 1) the occurrence of silicate rocks and 2) the distribution of iron and magnesium (table 3.1.7 and figure 3.1.18). Higher concentrations of potassium, silicon and aluminum (lithophile elements) were determined for the søvite outcrop. The rødbergites show higher values in iron and magnesium (siderophile elements). The rauhaugites do not show relative enrichments of neither lithophile nor siderophile elements. Trace element analyses show an increase of sulfur for the rauhaugite and søvite rock types, while uranium, thorium, yttrium and lead are comparatively lower for this rock types. The in situ XRF analyses of the light rare earth elements show the lowest concentrations for the søvite carbonatite rock, medium concentrations for the rauhaugite carbonatite rock and the highest values for the rødbergite carbonatite rock.

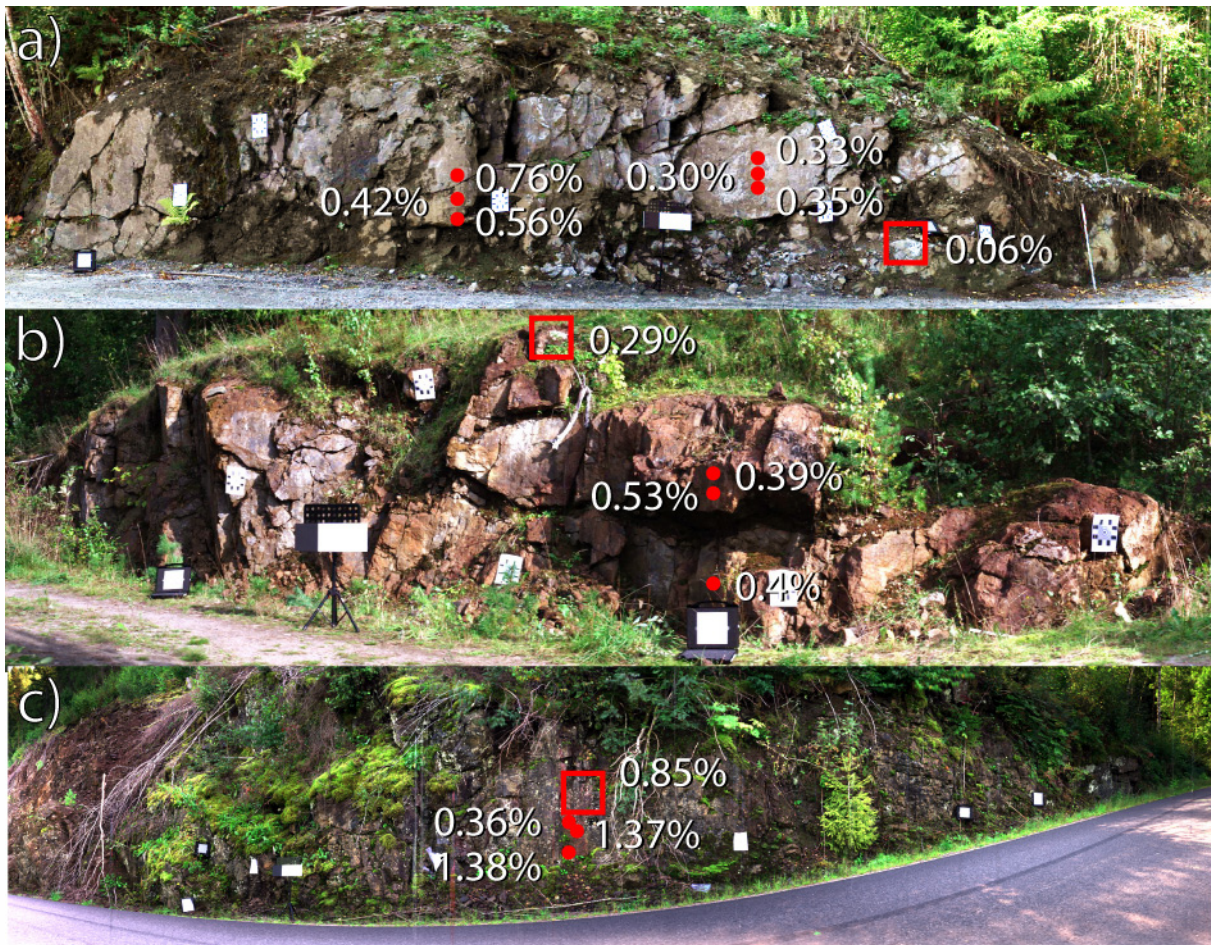


Figure 3.1.18: Visualization of the geochemical results for a total of all rare earth elements with their sampling locations at the outcrop. a) shows the søvite, b) shows the rauhaugite and c) shows the rødbergite. The underlying images were acquired with the HySpex imager (R, G, B color composite).

Table 3.1.6 shows the ICP-AES analyses for all rare earth elements. Few measurements are marked as NaN (Not-a-Number) values. Those measurements were problematic either due to spectral interferences between the single rare earth element spectra or other sample materials. Some samples were repeatedly measured to ensure reproducibility. In figure 3.1.19 one can see the rare earth distribution pattern for all three outcrops. Although all patterns show a carbonatite-typical distribution (chondrite normalized), there are differences between the three rock types visible. The søvites show a continuous decrease of the enrichment of lanthanum (La) to lutetium (Lu). Towards the HREE a plateau is visible. The enrichment of the LREE is low compared to previous studies of the Fen carbonatites (Boesche et al., 2015; Hornig-Kjarsgaard, 1998). The relatively low enrichment of the LREE is also causing a low $(La/Lu)_n$ ratio (≈ 100). The rauhaugites show a log-linear pattern with a continuous decrease from La to Lu. The determined $(La/Lu)_n$ ratio of 162 is the highest for all measured samples. The rødbergites have the highest rare earth element concentration and show a chondrite-normalized positive anomaly of cerium, praseodymium, neodymium, samarium (in respect to lanthanum and europium). This is probably due to the occurrence of cerium-, neodymium- and praseodymium-rich bastnaesite as the dominant rare earth element phase (Sieg, 2004). From europium to gadolinium a normal decrease of the chondrite-normalized concentration is perceptible. Hornig-Kjarsgaard, 1998, observed that the three-parted trend in rare earth element measurements of Fen minerals or rocks appears for most of the distribution pattern when silicate rocks associations are occurring.

Table 3.1.6: Results of the ICP-AES analysis in ppm.

	C1-chondrite	Søvite	Rauhaugite	Rødbergite
Y	1.57	44	276	301
La	0.237	125	565	1520
Ce	0.612	268	1070	3367
Pr	0.095	30	114	478
Nd	0.467	115	449	2140
Sm	0.153	20	115	377
Eu	0.058	6.3	41	77
Gd	0.2055	17	121	155
Tb	0.0374	2.5	18	20
Dy	0.254	11	86	75
Ho	0.0566	1.7	11	12
Er	0.1655	4.1	25	NaN
Tm	0.0255	NaN	3.1	NaN
Yb	0.17	3.1	14	19
Lu	0.0254	0.44	1.7	2.4

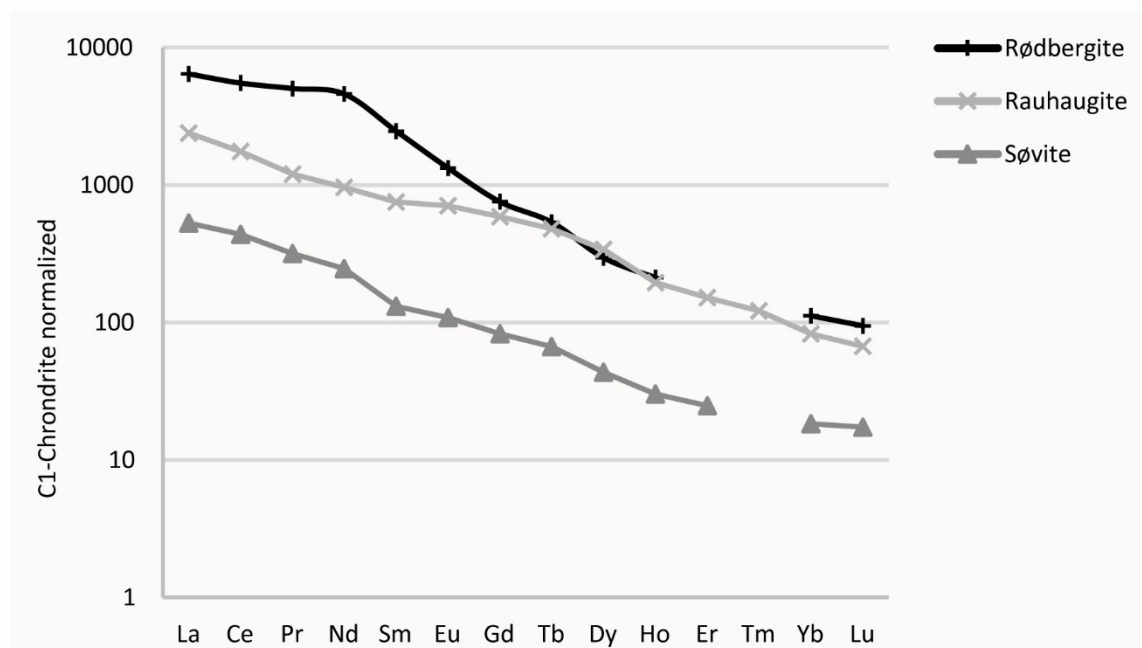


Figure 3.1.19: Rare earth element distribution pattern of the analyzed søvite, rauhaugite and rødbergite rock samples.

Table 3.1.7: Elements concentrations of the in situ rock analyses. LOD is the limit of detection. The relative concentrations between all rock samples are color coded from red (high concentrations) to green (low concentrations). A trend from the calcitic to the dolomitic and to the ankeritic carbonatites is perceptible. While calcitic carbonatites show higher concentrations for lithophile elements, ankeritic carbonatites show higher concentrations for siderophile elements. Those rocks are also relatively enriched in LREE.

	Unit	1	2	3	4	5	6	7	8	9	10a	10b	11	12	
Major Elements	SiO2	%	27	24	31	40	32	30	12	4	4	3	2	2	6
	Al2O3	%	8	6	7	4	4	3	3	1	1	1	1	1	1
	K2O	%	2	2	1	3	2	2	1	0	0	0	0	0	0
	P2O5	%	1	1	1	1	1	0	1	0	9	0	0	0	0
	Fe2O3	%	17	19	17	18	14	12	23	19	18	48	34	34	8
	FeO	%	15	17	15	16	13	11	21	17	16	44	31	31	8
	MnO	%	0	0	0	0	1	1	1	1	1	0	1	2	1
	CaO	%	3	3	5	7	16	15	16	21	25	7	21	28	35
Rare Earth Elements	MgO	%	1	<LOD	2	3	<LOD	4	3	<LOD	<LOD	<LOD	3	<LOD	
	Nd	ppm	2158	1641	1658	1525	1297	1237	1683	1653	1835	3150	5037	4910	1501
	Nd 2σ	ppm	155	143	146	141	139	130	154	164	168	231	238	237	123
	Pr	ppm	1016	840	904	831	699	656	877	704	809	1019	1384	1335	416
	Pr 2σ	ppm	96	91	93	90	89	84	98	104	106	134	125	125	75
	Ce	ppm	2648	964	1727	504	527	910	803	1804	869	2392	5285	5437	1168
	Ce 2σ	ppm	103	85	92	81	80	80	88	102	95	141	165	169	75
	La	ppm	1756	730	1280	446	446	673	544	1157	538	1020	2057	2028	498
	La 2σ	ppm	74	63	68	61	60	59	65	74	70	95	98	98	53
	Trace Elements	Nb	ppm	523	1678	449	303	166	46	710	654	488	3133	319	296
Nb 2σ		ppm	15	27	12	11	9	6	16	16	14	67	24	39	13
Y		ppm	92	78	47	102	94	67	64	85	404	724	725	1123	525
Y 2σ		ppm	7	7	5	6	6	5	5	6	11	24	20	31	12
U		ppm	<LOD	13	<LOD	45	16	28	11						
U 2σ		ppm	10	16	13	11	18	8	12	6	10	14	10	14	4
Th		ppm	<LOD	<LOD	<LOD	<LOD	<LOD	35	<LOD	<LOD	<LOD	1441	1296	4044	453
Th 2σ		ppm	449	447	414	338	503	4	403	625	365	835	648	1163	11
Pb		ppm	<LOD	61	26	<LOD	17	15	59	<LOD	<LOD	313	96	139	81
Pb 2σ		ppm	16	13	10	12	9	6	12	21	20	35	22	35	11
S		ppm	1559	5627	4026	4305	5137	3728	13263	9045	4125	2152	1575	1427	1171
S 2σ		ppm	203	282	188	172	196	166	430	371	213	268	158	171	160
Total		%	76	76	81	93	85	75	83	69	76	104	92	102	61

3.1.5 Discussion

3.1.5.1 Discussion of the proposed methodologies

Our results show that a proper preprocessing of the hyperspectral data cube is mandatory for an accurate geological classification of the images. This is particularly valid for insufficiently illuminated hyperspectral acquisitions that have been acquired using rotational scanning modes (spatial and spectral gradients may be introduced into the image). This is especially the case for usual outcrop scans that may have a rotational angles of 70 up to 150 degree. The application of the albedo normalization was therefore crucial to simulate similar illumination conditions for all scan lines.

The lithological classification could be accomplished by using the MICA, MIFD and rare earth element mapping. The MICA results are of high value for an overview of the lithological units and their distribution. The results are qualitative lithological maps. The limitation of this method is that every pixel can only be classified with one lithological unit. Local gradients within a unit are not detectable unless the whole material class is changed. The iron feature depth determination forms a very important basis for the analysis of outcrops bearing rare earth elements. It is necessary to qualitatively know the distribution of iron oxides at the surface of the outcrop to evaluate the detection feasibility of rare earth elements. Due to the exclusive analysis of VNIR data cube, the applicability of the 940 nm iron feature was limited. However, the 650 nm feature gives valuable information on the distribution of iron oxides and allows a semi-quantification of the abundancies. The detection of neodymium, dysprosium and holmium enables a qualitative and semi-quantitative mapping of the spatial distribution of light and heavy rare earth elements. The recalibration of the neodymium detection (Boesche et al., 2015) and the modification for dysprosium and holmium proposed in this work improve the performance and widens the applicability of the method. The example of the dysprosium mapping shows that due to its sharp absorption bands in the SWIR the method can be used for the SWIR detector as well.

In order to better understand the limitation of the algorithm when iron oxides are present, artificial mixtures were established and spectroscopically analyzed. Figure 3.1.17 shows that the diagnostic features can be better discriminated after the Richardson Lucy deconvolution even if iron is present. However, it also shows that the presence of iron reduces the feature depth and changes the reflectance of the absorption feature shoulders. The impacts of iron oxides and of Richardson Lucy deconvolution are shown in the four plots of figure 3.1.20. Subplot 20a) and 20c) show the classic neodymium feature depth estimation without and subplot 20 b) and d) with deconvolution. The functional relationship between abundance and absorption depth is preserved after applying the Richardson Lucy deconvolution as shown in the subplots for mixture 1 (1000 ppm neodymium). The preservation of the absorption depth was not necessary for the mixture 2 (5000 ppm neodymium). Moreover, the subplots for mixture 2 show that after the Richardson Lucy deconvolution a decorrelation of the iron content from the originally mixed image pixel could be achieved. This fact may enable semi-quantificational neodymium determination of samples in future. In summary, the analysis of the artificial mixtures proves that the detection of rare earth element in the presence of iron oxides is possible when using the deconvolution.

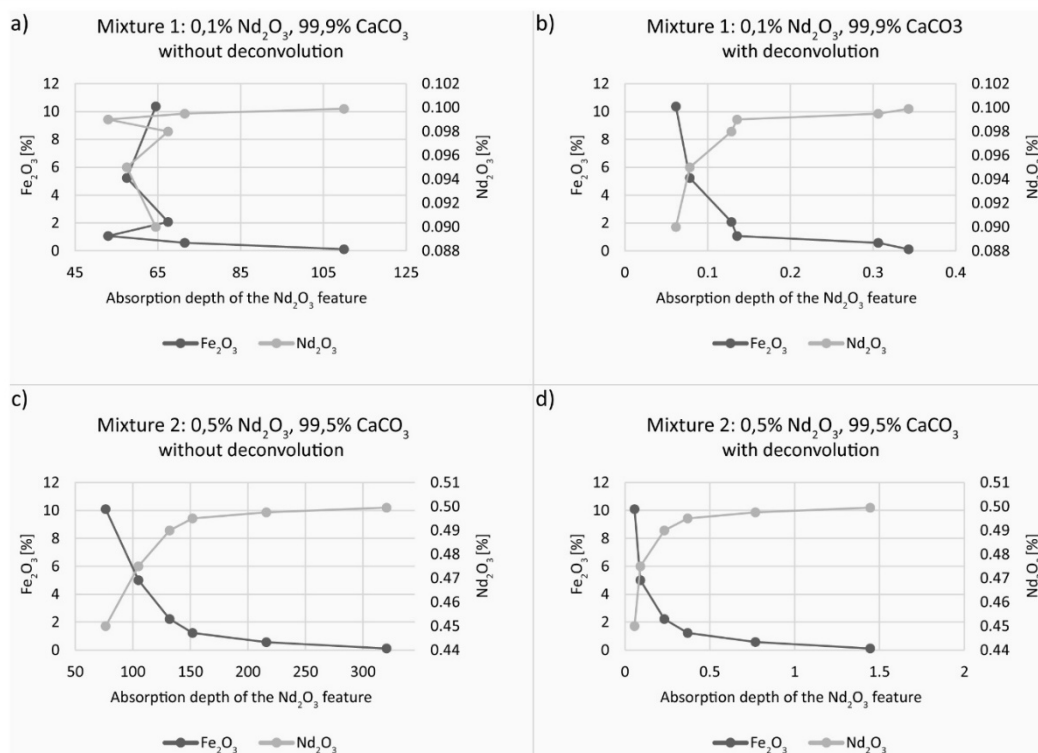


Figure 3.1.20: The absorption feature depth analyses of the spectra from the artificial mixtures. a) and b) represent the mixture one and c) and d) represent the mixture two. The left graphs show the feature depth determination on the original HySpex spectra. The right graphs show the feature depth determination on the spectra after applying the Richardson Lucy deconvolution. Especially for the mixture one a recovering of the functional relationship is visible after applying the Richardson Lucy deconvolution. For mixture two a delineation of the influence of iron oxides and neodymium oxide is occurring.

3.1.5.2 Discussion of the resulting outcrop maps and geological interpretation

The søvite outcrop is made of a homogeneous material and mainly consists of calcitic carbonatites. A gradient of rare earth element enrichment can be observed from left side of the outcrop (higher concentrations of rare earth element) to right side (lower concentrations of rare earth element). The rauhaugite outcrop is comprised of two lithological units: 1) dolomitic carbonatite and 2) ankeritic carbonatite. The ankeritic carbonatite is located to the right of the outcrop. It is sharply separated from the rest of the outcrop by a fault and it represents a homogeneous material. The dolomitic carbonatite is located to the left of the outcrop. This unit shows a material gradient from the top to the bottom. From the bottom, which is comprised of more calcitic-dolomitic material, to the top the rocks show increasing amounts of siderophile elements (Fe, Mg) and neodymium and dysprosium. The rødbergite outcrop bears the highest enriched material in the Fen Complex. This is confirmed by the geochemical analysis. Spectroscopically it is the most challenging outcrop of the Fen complex, because it bears also the highest amounts of iron oxides of up to 40% (table 3.1.7). The investigations at this outcrop demonstrated that the Richardson Lucy deconvolution was highly necessary to qualitatively map rare earth elements with the presence of iron. The resulting iron and rare earth elements maps show that at the center of the image there is a higher concentration of these elements. Additionally, vertical dykes are visible that bear the highest concentrations of iron and rare earth element (table 3.1.7). In summary this outcrop has a gradual increase of siderophile elements to the center of the image that surrounds the vertical dykes. It can therefore be assumed that the dykes intruded the surrounding rocks during the second intrusion event in the Fen complex and contemporarily altered the wall rocks.

3.1.6 Conclusion

A combination of state-of-the-art approaches for hyperspectral lithological classification and new or recently published methodologies are used for an integrative geological interpretation of three carbonatite outcrops at the Fen complex, Norway. Additionally, the influence of iron oxides, whose absorption spectra superimpose the rare earth elements characteristic absorption features, was quantified using artificial mixtures. The resulting lithological and mineralogical maps were validated using in-situ handheld X-ray fluorescence analyses and laboratory inductively coupled plasma atomic emission spectroscopy. The major findings of this study are:

1. The reflectance retrieval with prior albedo normalization is crucial for rotationally acquired images, or images that are acquired without nadir illumination conditions. The quality of the final lithological map highly depends on the quality of the preprocessing.
2. For a lithological classification of the outcrops the combination of the Material Identification and Characterization Algorithm (MICA) and the Modified Iron Feature Depth (MIFD) algorithm are beneficial. Especially for the detection of local gradients within the lithological units the MIFD was useful.
3. In order to map rare earth elements enriched zones within an outcrop, the advanced and modified approach first published by Boesche et al. (2015) was necessary. Especially for the delineation of the spectral signal of neodymium and iron oxides, the deconvolution method is recommended. The recalibration of the method for holmium and dysprosium widens the applicability of the algorithm and shows the potential to map narrow shaped features independent of the target material.
4. The presence of iron oxides directly hampers the detectability of neodymium and holmium. If the Richardson Lucy deconvolution is used to analyze the neodymium content, the detection of neodymium was limited to a maximum of 5% iron oxide content when having 1000 ppm neodymium in a mixture with carbonate. For the 5000 ppm neodymium in a mixture with carbonate, the detection limit was reached with 10% iron oxide content. For the second mixture (5000 ppm) the Richardson Lucy deconvolution improved the spatial delineation of iron oxides and neodymium.

In summary, the combination of traditional mineral mapping approaches and new element and element oxides (iron oxides and rare earth elements) based algorithm is a powerful methodology for the geological description of the carbonatite outcrops surface. It provides a full outcrop covering thematic map that is able to highlight enriched zones and gives valuable information on the local distribution of minerals and rocks. Every routine is physically based and independent of manual predefinitions or post-processing steps. The approach is suitable for carbonatite outcrops in general and can be applied within a time span of approx. 20-60 min (depending on illumination conditions that would increase the need for multiple acquisitions and the amount of rare earth elements that are supposed to be tested). Hence, the resulting thematic map can be generated directly in the field at any carbonatite outcrop and its full outcrop coverage links hyperspectral spatial qualitative information with chemical point analyses (XRF). The limitations of the methodology clearly are that it does not provide element concentrations directly and that the ore body can only be analyzed on the outcropping surface (penetration depth is wavelength dependent, but always less than 1 mm). Future studies may extend the current methodological calibration for the remaining rare earth elements. Moreover, we plan testing the rare earth element-detection method on larger scales, such as from the spaceborne EO-1 Hyperion satellite or the future EnMAP hyperspectral missions. Supplementary, the method could also be tested on smaller scales, such as microscopic hyperspectral images. Mineral size analyses of single grains may be then differentiated and the rock evolution may be spectroscopically investigated. For a better understanding of the surface reflection characteristics, such as roughness, fault zones, folds, etc., a 3-dimensional model of the outcrops would be beneficial for the preprocessing of the data cube and would therefore increase the robustness of the method.

3.1.7 Acknowledgements

The authors thank the German National EnMAP framework program (Department of Economics and Technology BMWi No. 50EE1256) and the GeoForschungsZentrum (GFZ) of the Helmholtz Foundation for the financial support. Many thanks are extended to BERGFALD Miljørådgivere for supporting this study and assisting with additional information about the Fen complex type locality. All our gratitude also goes to the editors and the reviewers for their valuable comments, which helped to improve the quality of this paper.

3.1.8 References

1. Agilent technologies ICP-OES Vista MPX axial [WWW Document] URL <http://www.chem.agilent.com/Library/applications/ICPES-01.pdf> (accessed 15.01.15)
2. Andersen, T., (1986). Magmatic fluids in the Fen carbonatite complex, S.E. Norway. *Contr. Mineral. and Petrol.* 93, 491–503. doi:10.1007/BF00371719
3. Andersen, T., (1988). Evolution of peralkaline calcite carbonatite magma in the Fen complex, southeast Norway. *Lithos* 22, 99–112. doi:10.1016/0024-4937(88)90019-9
4. Bedini, E., (2009). Mapping lithology of the Sarfartoq carbonatite complex, southern West Greenland, using HyMap imaging spectrometer data. *Remote Sensing of Environment* 113, 1208–1219. doi:10.1016/j.rse.2009.02.007
5. Ben-Dor, E., Chabrilat, S., Demattê, J.A.M., Taylor, G.R., Hill, J., Whiting, M.L., & Sommer, S., (2009). Using Imaging Spectroscopy to study soil properties. *Remote Sensing of Environment, Imaging Spectroscopy Special Issue* 113, Supplement 1, 38–55. doi:10.1016/j.rse.2008.09.019
6. Boesche, N. K., Rogass, C., Lubitz, C., Brell, M., Herrmann, S., Mielke, C., Tonn, S., Appelt, O., Altenberger, U., & Kaufmann, H., (in review). Hyperspectral REE (Rare Earth Element) Mapping of Outcrops — Application for Neodymium Detection. *Remote Sens.* 2015
7. Brøgger, W.C., (1894). Die Eruptivgesteine des Kristianiagebietes - IV. Den Fengebiet in Telemark, Norwegen. *Videnskapsselskapets Skrifter. I. Mat.-Naturv. Klasse* 1921 No.9. In commission bei J. Dybwad, Kristiania (chapter 2, 159-167, chapter 3 & 4, 231-276, chapter 7, 328-334)
8. Clark, R.N., & Swayze, G.A., (1995). Mapping minerals, amorphous materials, environmental materials, vegetation, water, ice, and snow, and other materials: The USGS Tricorder Algorithm, Summaries of the Fifth Annual JPL Airborne Earth Science Workshop. *JPL Publication*, 39–40.
9. Clark, R.N., Swayze, G.A., Livo, K.E., Kokaly, R.F., Sutley, S.J., Dalton, J.B., McDougal, R.R., & Gent, C.A., (2003). Imaging spectroscopy: Earth and planetary remote sensing with the USGS Tetracorder and expert systems. *Journal of Geophysical Research* 108, 5131.
10. Cloutis, E.A., (1996). Review Article Hyperspectral geological remote sensing: evaluation of analytical techniques. *International Journal of Remote Sensing* 17, 2215–2242. doi:10.1080/01431169608948770
11. Cocks, T., Jenssen, R., Stewart, A., Wilson, I., & Shields, T., (1998). The HyMap™ airborne hyperspectral sensor: the system, calibration and performance, 1st EARSEL Workshop on Imaging Spectroscopy, Zurich, Switzerland. 37–42.
12. FieldSpec3 Hi-Res (build in 2010). Documentation: [WWW Document], URL [http://www.sphereoptics.de/en/spectrometersdocs/Field Spec 3 HR 2010.pdf](http://www.sphereoptics.de/en/spectrometersdocs/Field%20Spec%203%20HR%202010.pdf) (accessed 13.8.14).
13. Hornig-Kjarsgaard, I.-K., (1998). Rare Earth Elements in Sövitic Carbonatites and their Mineral Phases. *J. Petrology* 39, 2105–2121. doi:10.1093/petroj/39.11-12.2105
14. HySpex VNIR 1600, HySpex SWIR 320-me. [WWW Document], URL main specifications: <http://www.hypex.no/hypex/> (accessed 28.01.15)
15. Julien, Y., Sobrino, J.A., Mattar, C., Ruescas, A.B., Jiménez-Muñoz, J.C., Sòria, G., Hidalgo, V., Atitar, M., Franch, B., & Cuenca, J., (2011). Temporal analysis of normalized difference vegetation index (NDVI) and land surface temperature (LST) parameters to detect changes in the Iberian land cover between 1981 and 2001. *International Journal of Remote Sensing* 32, 2057–2068. doi:10.1080/01431161003762363

16. Kokaly, R., (2011). Processing routines in IDL for spectroscopic measurements (installation manual and user's guide, version 1.0) [WWW Document]. URL <http://pubs.usgs.gov/of/2011/1155/pdf/ofr2011-1155-17oct2011.pdf> (accessed 24.10.14).
17. Lie, A., & Ostergaard, C., (2011). THE FEN CARBONATITE COMPLEX, ULEFOSS, SOUTH NORWAY. 21 st NORTH, Svendborg.
18. Mielke, C., Boesche, N.K., Rogass, C., Kaufmann, H., Gauert, C., & de Wit, M., (2014). Spaceborne Mine Waste Mineralogy Monitoring in South Africa, Applications for Modern Push-Broom Missions: Hyperion/OLI and EnMAP/Sentinel-2. *Remote Sensing* 6, 6790–6816. doi:10.3390/rs6086790
19. Mitchell, R.H., & Brunfelt, A.O., (1975). Rare earth element geochemistry of the Fen alkaline complex, Norway. *Contr. Mineral. and Petrol.* 52, 247–259. doi:10.1007/BF00401455
20. Rowan, L.C., Hook, S.J., Abrams, M.J., & Mars, J.C., (2003). Mapping hydrothermally altered rocks at Cuprite, Nevada, using the advanced spaceborne thermal emission and reflection radiometer (ASTER), a new satellite-imaging system. *Economic Geology* 98, 1019–1027.
21. Rowan, L.C., Kingston, M.J., & Crowley, J.K., (1986). Spectral reflectance of carbonatites and related alkalic igneous rocks; selected samples from four North American localities. *Economic Geology* 81, 857–871. doi:10.2113/gsecongeo.81.4.857
22. Sieg, L., (2014). Bachelorarbeit: SEE-Minerales des Fen-Karbonatit-Komplexes von Ulefoss in S.E.-Norwegen, Universität Potsdam
23. Sunshine, J.M., & Pieters, C.M., (1993). Estimating modal abundances from the spectra of natural and laboratory pyroxene mixtures using the modified Gaussian model. *Journal of Geophysical Research: Planets* 98, 9075–9087. doi:10.1029/93JE00677
24. Sun, S., & McDonough, W.F., (1989). Chemical and isotopic systematics of oceanic basalts: implications for mantle composition and processes. Geological Society, London, Special Publications 42, 313–345. doi:10.1144/GSL.SP.1989.042.01.19
25. Thermo Scientific Niton XRF Analyzer: Niton XL3t Documentation: [WWW Document]. URL [http://www.thermoscientific.com/content/dam/tfs/ATG/CAD/CAD_Documents/Catalogs_&Brochures/Elemental Analysis/XRF/D00194~.pdf](http://www.thermoscientific.com/content/dam/tfs/ATG/CAD/CAD_Documents/Catalogs_&Brochures/Elemental%20Analysis/XRF/D00194~.pdf) (accessed 28.01.15)
26. Townsend, T.E., (1987). Discrimination of iron alteration minerals in visible and near-infrared reflectance data. *Journal of Geophysical Research: Solid Earth* 92, 1441–1454. doi:10.1029/JB092iB02p01441
27. Van der Meer, F.D., van der Werff, H., van Ruitenbeek, F.J.A., Hecker, C.A., Bakker, W.H., Noomen, M.F., van der Meijde, M., Carranza, E.J.M., Smeth, J., & Woldai, T., (2012). Multi- and hyperspectral geologic remote sensing: A review. *International Journal of Applied Earth Observation and Geoinformation* 14, 112–128.
28. Yap, C.-W., 2015. China Ends Rare-Earth Minerals Export Quotas. *Wall Street Journal*.
29. Zuleger, E., & Erzinger, J., (1988). Determination of the REE and Y in silicate materials with ICP-AES. *Z. Anal. Chem.* 332, 140–143. doi:10.1007/BF00470631

3.2 Supplement: Proxy Minerals for Fenites

3.2.1 Materials and Methods

Besides re-calibration of the REE detection routine, Chapter 3.1 has so far discussed the mapping of proxy minerals in carbonatites. What is not covered, is a mapping of fenites. As described in Chapter 1.5 the fenites are metasomatized country rocks that surround the carbonatite igneous rocks. The fenitic zone is often several hundred meters or even kilometers wide and can therefore be mapped with hyperspectral sensors that have a ground sampling distance of 30 x 30 m. In general, the ground sampling distance must be seen as one limitation for the detection of REE deposits from space. Especially when the enriched zones occur as dyke swarms, meaning, they are a few meters wide and maybe several hundred meters long. In this case the spectral signal of the REEs would therefore be mixed with spectra of the surrounding material. Hence, being able to map the fenitic alteration of the country rock might be beneficial to finding the ore zone. In order to investigate the spectral characteristics of fenitic rocks nine field spectra at a fenite outcrop in Fen Complex (Norway) were collected. The fenites are located at a distance of around 3 km to the main intrusion of the carbonatites. The measurement spots were macroscopically determined from a team of field geologists as k-feldspar rich metasomatized gneisses and albitites. Moreover, Na-amphiboles, chlorites, epidotes, fluorites, pyrites, and chalkopyrites were found. Biotite, which is a usual mineral in gneisses, was not much available. The grainsizes of the minerals was up to 10 cm and some parts of the outcrops were monomineral rocks (1-2 m). The used instrument was the ASD Fieldspec 3 [28] (see specification in table 8.4 in the appendix). In order to test the applicability of a spectral detection of the fenite characteristic spectrum in hyperspectral image data the weathered albite b spectrum was used as the reference spectrum. A spectral feature fitting (ENVI software) was applied here. The spectral feature fitting was applied on a hyperspectral dataset from the EO-1 Hyperion, which covers the area of the second test site of this thesis, the Lofdal Complex, Namibia. The Lofdal Complex was chosen because the coverage of vegetation is low and several image acquisition exist from that area. The input dataset is the result of the multitemporal weighted averaging from 21 image scenes that was produced for the third paper (see: Chapter 4.1).

3.2.2 Results and Evaluation of the Results

The spectra of the fenites show two diagnostic absorption bands (at 2200 and 2330 nm). The 2200 nm absorption band is related to kaolinite, a weathering product of albite and k-feldspars. The 2330 nm absorption band is characteristic for calcite. Additionally, one spectrum of a fresh sample with a high amount of albites and of a small carbonatitic dyke (2 cm wide) was collected. This spectrum surprisingly shows the spectral signature of neodymium in the VNIR range. That means that even in the remote fenitic areas (3 km distance to the main intrusion) REE bearing carbonatites were exposed to the country rock. The peculiarity of fenites is the simultaneous presence of kaolinite and carbonates. In the spectrum the mixture of their characteristic absorptions is visible in the SWIR range as two neighboring absorption bands. Both absorption bands would appear with a high absorption depth, if their pure material is measured. Here both absorption bands show a medium high absorption depth. Although it is particular for fenites, these two medium strong absorptions can also occur in a subpixel sized layering in dipped sedimentary rocks. However, if the carbonatites intruded country rocks of granitic composition, the hyperspectral mapping of the alteration zone is possible.

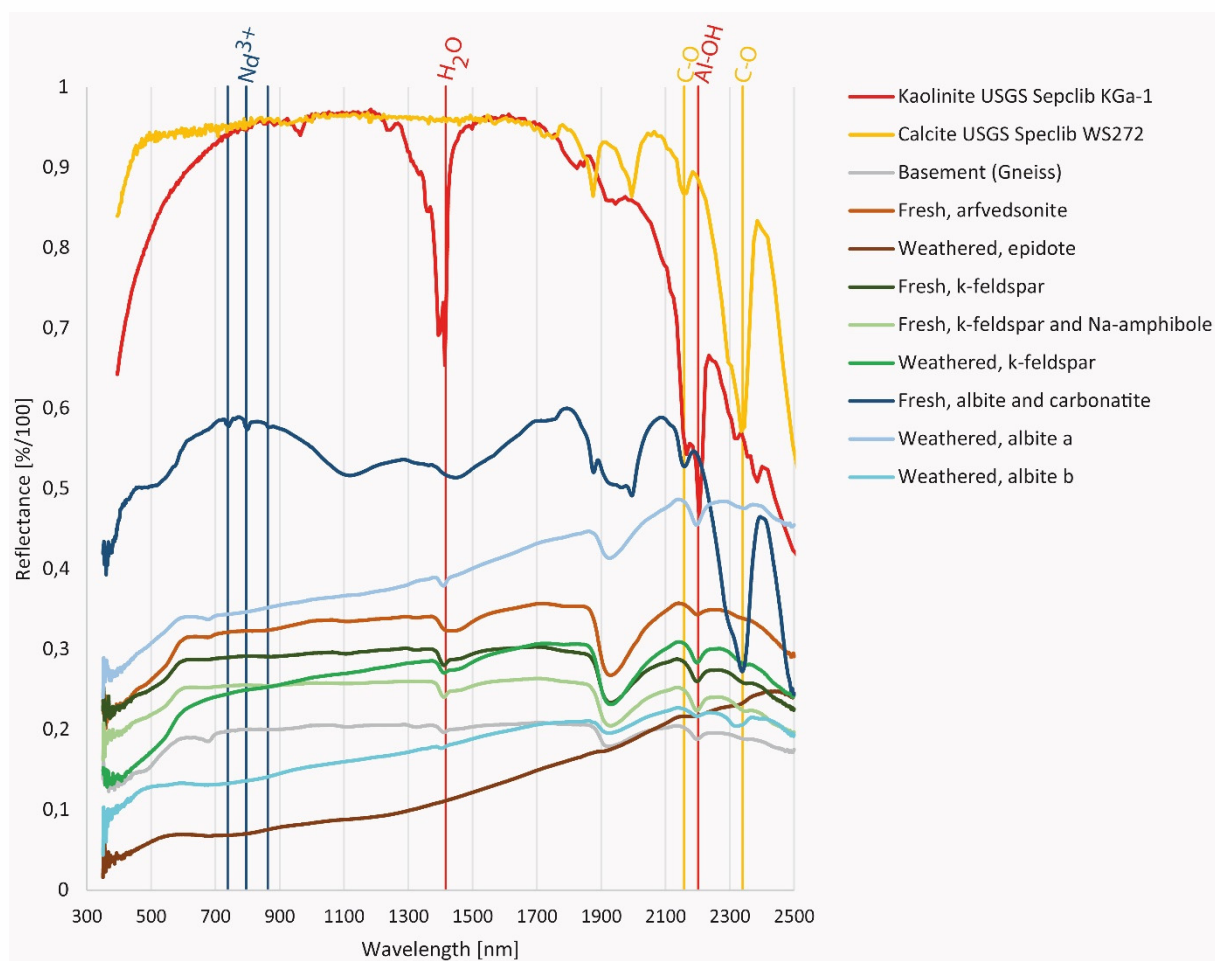


Figure 3.2.1: The spectra shown are related to the typical minerals that occur in fenite rocks. In comparison, the USGS speclib spectra of the main constituents of fenites are plotted (kaolinite as a weathering product of feldspars, and calcite) [2]. Note that the discriminative absorption bands of fenites are related to the Al-OH and C-O vibrations of kaolinite and calcite. Additionally, neodymium related absorptions can be observed in one sample.

The result of the fenite mapping using the spectral feature fitting is shown in Figure 3.2.2. It is shown in comparison to the geological map of Lofdal area, Namibia. The spectral feature fitting with the weathered albite bearing fenite spectrum highlights the alteration zones in green color, which are mapped in red in the geological map. Hence, this supplement investigation shows that a hyperspectral mapping of fenites is beneficial to locate alteration zones and, therefore, gives further insights in areas where REE mineralization might be expected.

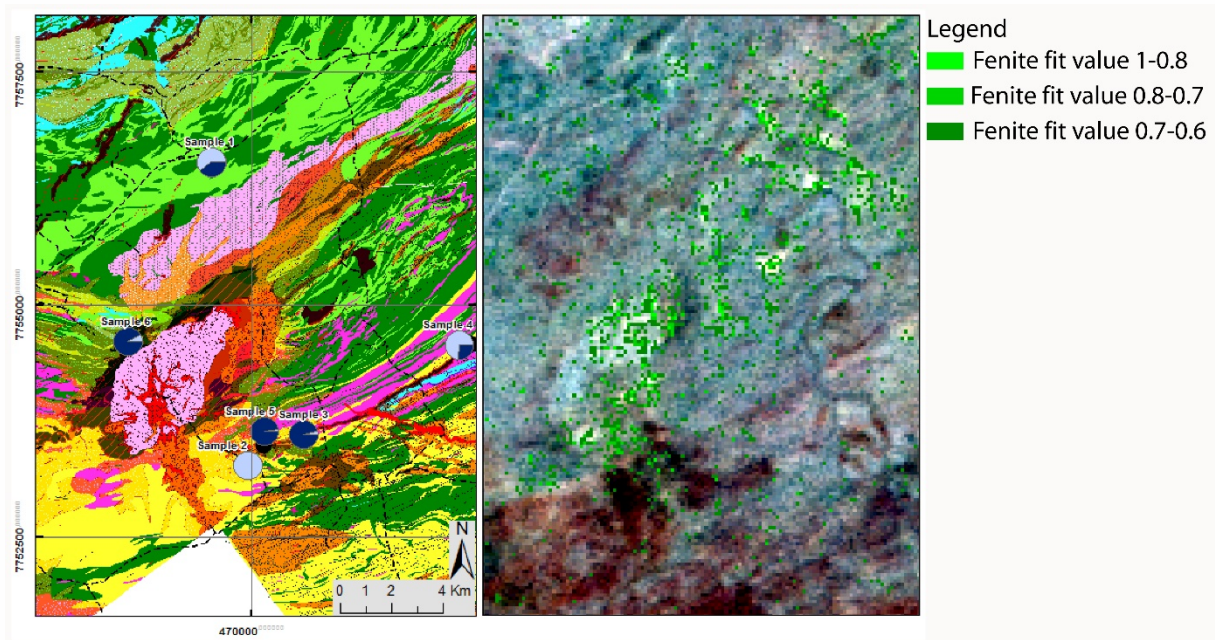


Figure 3.2.2: The mapping result of the fenitic zone is shown in comparison to the geological map of Lofdal Complex, Namibia. The red dykes in the geological map mark the carbonatite dykes. The remote sensing fenite mapping is based on a spectral feature fitting and is colored according to the fit values (green). The fenites could be observed in the field to surround the carbonatite dykes and as a part of the main intrusion area.

4. Chapter

Adaption of REEMAP on thulium and erbium and for satellite image data and investigation of the most important limiting factor (signal to noise ratio).

4.1 Spaceborne Rare Earth Element Mapping (Neodymium, Thulium and Erbium) - Capabilities and Limitations of Hyperspectral Imaging Sensors (EO-1 Hyperion and EnMAP) (submitted to mdpi, "The Environmental Mapping and Analysis Program (EnMAP) Mission: Preparing for Its Scientific Exploitation", in June 2015)

Nina K. Boesche ^{1,2,*}, Christian Rogass ¹, Karl Segl ¹, Sabine Tonn ¹, Maximilian Brell ¹, Christian Mielke ^{1,2}, Sabrina Herrmann ^{1,2}, Uwe Altenberger ² and Luis Guanter ¹

¹ GeoForschungsZentrum Potsdam, Helmholtz Zentrum, Telegrafenberg, 14473 Potsdam, Germany; E-Mails: rogass@gfz-potsdam.de (C.R.); segl@gfz-potsdam.de (K.S.); saherrma@gfz-potsdam.de (S.H.); sabine.tonn@gfz-potsdam.de (S.T.); luis.guanter@gfz-potsdam.de (L.G.)

² Universität Potsdam, Karl-Liebknecht Str. 24-25, 14476 Potsdam-Golm, Germany; E-Mail: altenber@uni-potsdam.de

* Author to whom correspondence should be addressed; E-Mail: nina.boesche@gfz-potsdam.de; Tel.: +49-331-288-28775; Fax: +49-331-288-1192.

Received: 12 June 2014

Abstract: Hyperspectral remote sensing surveys are more often used in geological exploration, in order to detect minerals directly. In this study, an existing method for the hyperspectral detection of rare earth elements on outcrops is adapted to spaceborne sensors (EO-1 Hyperion and the future EnMAP sensor). The adaption is comprised of (1) a sensor based preprocessing of the hyperspectral raw data, (2) setting up a new calibration of a spectral REE-feature sharpening algorithm for neodymium, erbium and thulium and (3) changing the REE detection methodology, from feature depth determination to a correlation with reference spectra. The test site is the Lofdal Carbonatite Complex in Namibia from which 25 overlapping the EO-1 Hyperion images are available. The EnMAP dataset was simulated from hyperspectral laboratory measurements from a synthetic mixture series, which represents natural and artificial concentrations of rare earth elements (REE) in carbonatites. The results show that state of the art and future hyperspectral satellite sensors are able to detect REE; the location of the enriched zones could be indicated with some positive findings. A mapping of the full extent of the enriched areas might be possible with improved hyperspectral sensors such as EnMAP, if image noise can be reduced and if the atmospheric correction does not obliterate the REE features.

Keywords: rare earth elements; imaging spectroscopy; neodymium; erbium; thulium; hyperspectral; EnMAP; EO-1 Hyperion

4.1.1. Introduction

Rare Earth Elements (REE) are important components of modern technological devices. Due to REE, new technical components are more efficient (e.g. batteries) and smaller (e.g. magnets), and REE form a basis for new technologies (optical components; REE nanophores, innovative luminescent substances). Industrial production of such new components is strongly dependent on delivery times and prices of REE. The economically most valuable REE-deposits are hosted by carbonatites, hence, this study concentrates on carbonatites. Over 90% of the worldwide supply of rare earth oxides (REO) origins from China. Because China ends the export quotas for REE recently, thus, the USA, Japan, Korea and the EU invest in the exploration for REE deposits [26]. Today, geological exploration techniques include hyperspectral surveys for a general geological overview in combination with field mapping. First studies on a direct detection of REEs and REOs using an optical spectral dataset were already published in 1970s [12,27]. Rowan et al. 1986 primarily found REE related absorption bands in carbonatites. Although today the characteristic optical behavior of REE is well known and widely utilized in optical components, the hyperspectral detection of the characteristic features from satellite images is proved to be difficult. The direct detection of REE related absorption features in a spaceborne hyperspectral dataset often fails due to a combination of the low concentration of REE in the ore body (few percent), a low signal-to-noise ratio (SNR) of actual sensors and a coarse spatial resolution. Hence, satellite instrument-based studies are primarily focused on mineral mapping of the ore rock types and alteration zones [15,28–32]. An additional hampering factor is the geological character of REE deposits. The distribution of the ore minerals is often highly heterogenic in ore bodies and so is the distribution of economically valuable areas. Recently, the optical reflectance spectra of REE bearing minerals and rocks from laboratory and field acquisitions were successfully analyzed directly for REEs/REOs [33–35]. Turner et al. 2014 detected REE related absorption features in REE bearing fluorocarbonates and Boesche et al. 2015 published a first direct REE mapping from near-field at a carbonatitic outcrop [34–36].

The methodology of Boesche et al. 2015 [33,34,36] was tested on outcrop images that were acquired with the HySpex imager (with a spectral resolution of around 4 nm in the VNIR and a spatial resolution of few centimeters) [20]. The main steps of the methodology are 1) a multi temporal characterization of the spectral uniformity of white, gray and black references that were placed in front of the outcrops, 2) a smoothing of the image spectra and a sharpening of the rare earth element related absorption bands using a Richardson Lucy Deconvolution with a Gaussian shaped filter function and 3) absorption depth retrieval using a continuum removal and the feature depth determination after [2,34]. The here presented study comprises the adaption of this hyperspectral analysis methodology to spaceborne hyperspectral images. Most of the modifications to this method are made in step one and three, step two is similar to the near field methodology of the presented HySpex-based technique [34]. Step one includes a multitemporal noise estimation from multiple scenes based on the homogeneity of white references that were placed in front of outcrops. However for satellite images, the noise estimation was achieved differently. The third step is an absorption depth determination that is used as a quantifying factor of the statistical probability of REE in the sample pixel. Unfortunately, the absorption depth parameter describes two independent spectroscopic interrelations: The concentration of the REE in the sample and the percentage of REE bearing material in a certain pixel. For outcrop scans with a pixel size of few centimeters the subpixel percentage is negligible, but not in satellite images. In order to adapt the REE detection from near-field to space analysis, the feature depth determination was replaced with a Pearson Correlation of a spectral library feature with every sharpened image feature.

The adaption of the rare earth element mapping methodology, presented here, is tested for two spaceborne imaging spectrometers: EO-1 Hyperion [37] and the future EnMAP sensor [38–40]. The specifications of the sensors are listed in Table 4.1.1. The images of the EO-1 Hyperion were chosen, because they include the short wave infrared region that include two additional investigated absorption bands [37,41]. Testing the methodology on a real dataset was important in order to investigate the capability of satellite based REE detection. The EnMAP sensor was chosen as a second satellite, because its sensor characteristics are published and a simulation of varying acquisitions could be achieved on different REE concentration level. In order to focus on the limitations of satellite REE detection, EnMAP-like image pixels with diverse REE concentrations in the ground and different illumination conditions were simulated. Unfortunately, no spaceborne acquired data

is available until 2018, when the EnMAP will be launched and thus, the detection of REE using EnMAP is discussed theoretically in this study.

Table 4.1.1: Sensor specifications of EO-1 Hyperion and EnMAP [37,39,41].

Sensor	EO-1 Hyperion	EnMAP
Spectral Range	0.4-2.5 μm	0.42-2.45 μm
Ground Sampling Distance	30 m	30 m
Swath Width	7.5 km	30 km
Mean Spectral Sampling Interval	10 nm	6.5 nm VNIR and 10 nm SWIR
Number of Bands	220	244
Target Revisit Time	16 days	27 days; 4 days (VZA 30°)
SNR	190:1 VNIR; 40:1 SWIR	400:1 VNIR; 150:1 SWIR

4.1.1.1 Geological Setting

The satellite images from the Hyperion sensor were acquired over the carbonatite-hosted rare earth deposit Lofdal. It is located in the northern part of Namibia (Lat/Long: S 20° 18' 31.70"/E 14° 43' 7.94", Alt: 974 m asl).

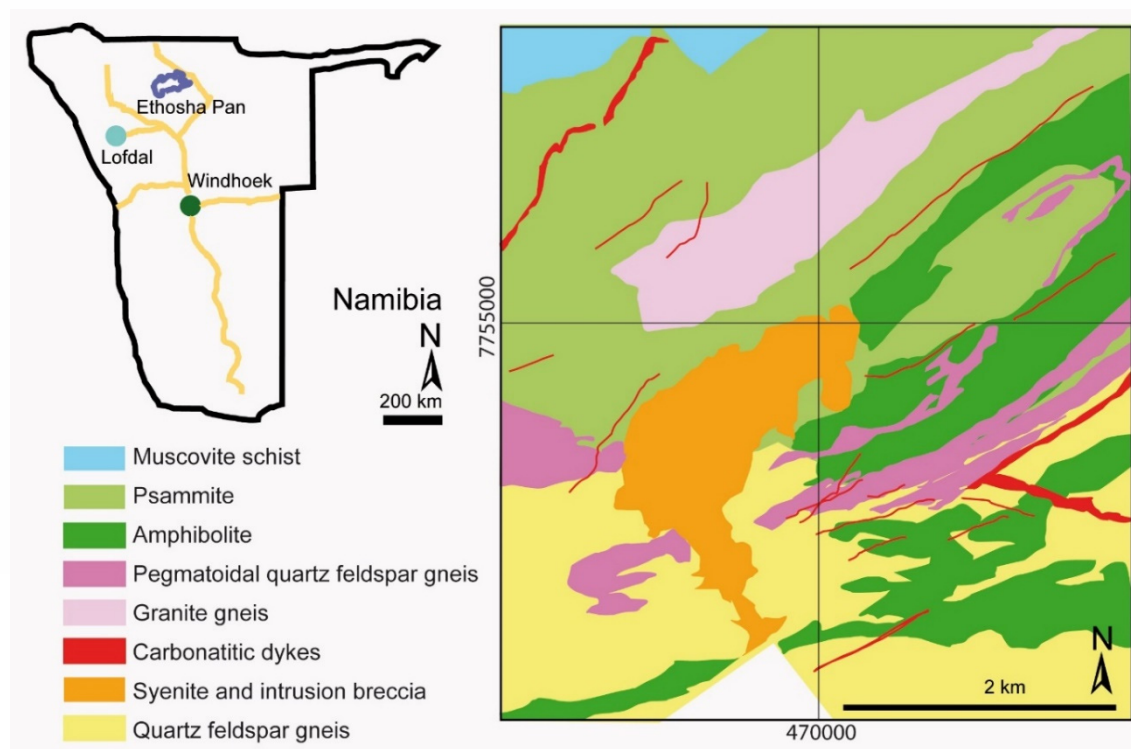


Figure 4.1.1: Geological sketch map of the study area: Lofdal, Namibia (simplified after Namibia Rare Earth Inc., / Remote Exploration Services (RES)). The map is a comprehensive work of intense geological field surveys, airborne hyperspectral remote sensing and geochemical investigations. It was iteratively improved over more than a decade.

The Lofdal complex is situated in the Welwitschia Inlier, which is part of the Huab Metamorphic Complex. The Huab Metamorphic Complex (green colored lithological units in Figure 4.1.1) is comprised of leucocratic granitic gneiss, banded paragneiss and quartzite, amphibolite, and mica/chlorite schists [42]. To the north and south the Huab Metamorphic Complex is overlain by the Damara Belt. The Damara belt is an orogen that is associated with metamorphosed clastic sediments to the North (blue colored lithological unit in Figure 4.1.1), and quartzite, arkose, conglomerate and subordinate calc-silicate and limestone to the South [42]. A series of

alkali silicate rocks and carbonatites intruded the Huab Metamorphic Complex at about 760 Ma BP [42]. The intrusion can be divided into two units: The main syenite-carbonatite intrusion and NE-trending swarms of carbonatite-phonolite dykes. The main intrusion (orange colored lithological unit in Figure 4.1.1) is a mixture of nepheline syenites and phonolites, and the Lofdal breccia (a coarse grained breccia that contains basement and syenitic rocks). The satellite intrusions originated later than the main intrusion [42]. Several hundreds of single dykes can be observed around the main intrusion. The dykes vary in their chemical composition. NE-SW trending dykes seem to carry REE ore minerals, such as xenotime, bastnaesite, parisite, synchesite and monazite. Most dykes are surrounded by metasomatized (fenitized) zones of potassium rich rocks (K-feldspar, epidote, allanite, fluorite, aegirin). Figure 4.1.2 shows a small carbonatite dyke, with fenites towards the outer rim of the dyke.

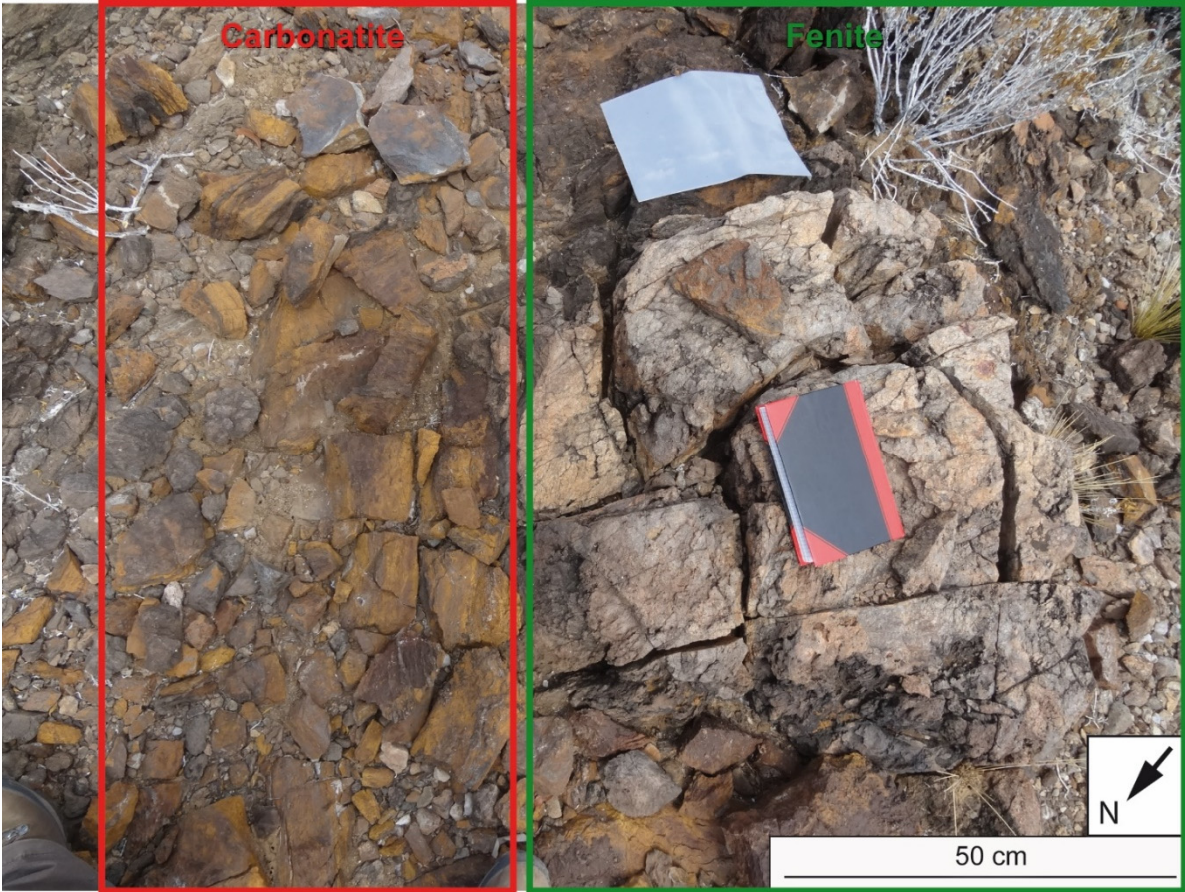


Figure 4.1.2: Photograph of a carbonatite dyke and its surrounding fenitized country rock.

4.1.2. Experimental Setup

4.1.2.1 Materials and production of hyperspectral datasets

4.1.2.1.1. EO-1 Hyperion dataset and preprocessing

The Hyperion sensor is on board of the EO-1 Satellite. It acquired 25 cloud-free image scenes between Sep 2013 and Jan 2015 that are suitable for a multi-temporal analysis (the EO-1 Hyperion dataset comprises all image scenes listed in Table 4.1 of the appendix). The multi-temporal analysis is based on the methodology from [34] and will be explained in more details towards the end of this chapter. Radiometrically corrected and geocoded EO-1 Hyperion scenes (L1R and L1T) were overlaid by an ASTER digital elevation model and transformed into at-surface reflectance images using the automated processing chain described in [43]. This methodology comprises the transformation to radiance, erroneous pixel reduction, column reduction, reduction of radiometric miscalibration, keystone reduction, and cloud masking. In the next step the images are georeferenced and co-registered using an automatic tie point detection approach combined with the ASTER DEM. Finally, a transformation from at-sensor radiance to at-surface reflectance is carried out considering an automated spectral smile estimation in the atmospheric correction process [44]. In order to overlay the images and to perform the multitemporal averaging, the scenes were manually georeferenced with a referencing error of around 1-2 pixels (relative error towards one predefined base image and the actual image). Two scenes showed an error of 4 pixels. However, they were decided to be useful in order to increase the detectability of areas with a greater extent of 4 pixels. Images with a higher relative referencing error of 4 pixel were not used. Therefore, 21 images were finally used for the production of the averaged image.

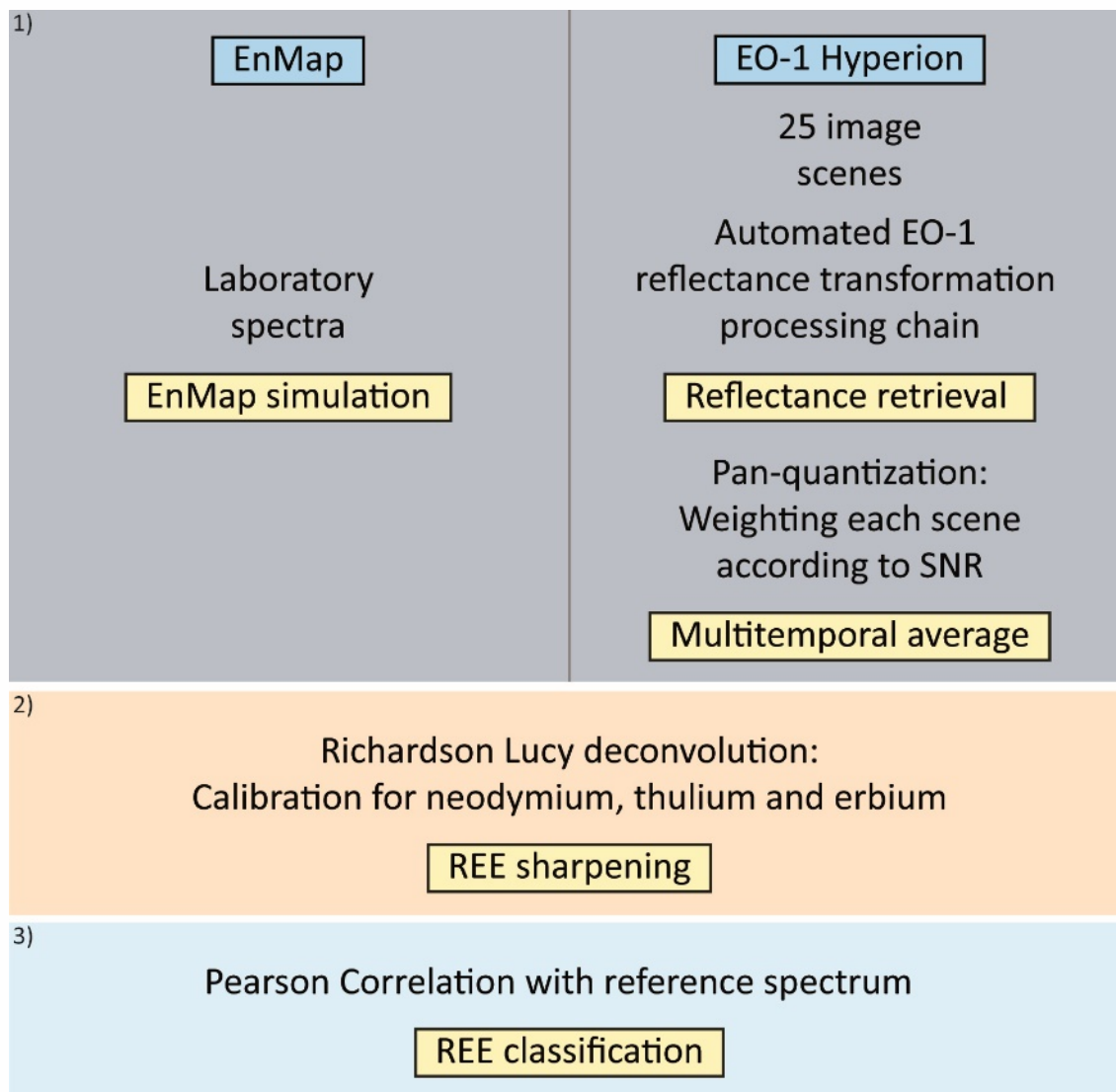


Figure 4.1.3: Flow chart showing the main processing steps of the REE detection algorithm.

The first step of the REE detection routine is an estimation of the noise of each image scene (Figure 4.1.3). The determination of the noise has the advantage that the images can be weighted according to their signal-to-noise ratio, when the average is calculated. For this purpose, a “pan-quantization” was developed and applied on every image scene. The fundamental objective of the pan-quantization is to extract a representative value for the noise on a certain spatial and spectral subset of the images. First, a spectral subset on a predefined spectral range that is known to be relevant for the REE absorption feature [34–36] is extracted. Therefore, the minimum and maximum wavelength of the spectral subset are equal to the wavelength positions of the absorption feature shoulders (Table 4.1.3). Next, the pan image is produced from this subset by calculating the total of each pixel along the wavelength axis. In order to produce the spatial subset, the pan image is quantized into 10 levels. Because the noise is highest in the lowest level of the 10 quantiles, the pixel of first level are used as the spatial subset ($Reflectance_{x,y}$). The subsets were then reduced in their size by subtracting one pixel in x- and one pixel in y-direction (spatial erosion). Outlier and small anomalies were therefore reduced and a spatial mask image produced. After having set up the spatial subset, one mean spectrum per image was produced (21 spectra in total). Therefore, all pixel that are located within the mask were selected and their mean image was extracted in the spectral range ($\lambda_{min}-\lambda_{max}$). The standard deviation (stdev) of the 21 mean spectra were then calculated. Finally, the standard deviation was used as a weighting parameter in the **multitemporal averaging** algorithm [34].

4.1.2.1.2. EnMAP dataset and preprocessing

Simulated EnMAP spectra were used for this study. The simulated spectra were produced using the EnMAP End-to-End Simulation Tool (EeteS) [40]. The basis for the simulations were hyperspectral laboratory measurements of powdered samples that consist of a mixture of rare earth elements and calcite powder. The rare earth element powder were provided from Alfa Aesar and belong to a series of rare earth metals (REacton). In this study three REE were chosen showing pronounced absorption features in the atmospheric windows of the solar reflective range of the electromagnetic light [12,27,35]. All rare earth oxide powders comprise at least 99.9 % of a specified rare earth element (Nd^{3+} : at least 99.99%, Er^{3+} : at least 99.9% and Tm^{3+} : at least 99.99%). The calcite powder (product number: 31208) was produced by the Riedel-de Haen AG, and were provided from Helmholtz Centre Potsdam - GFZ German Research Centre for Geosciences. The calcite powder was chosen as a representative of the carbonatitic host rock material. The REOs were provided as synthetically produces powders. Therefore, the calcitic material was chosen to have the same grain size. Natural carbonatitic REE deposits can also comprise dolomitic and ankeritic carbonate material, and some associated minerals such as iron and magnesium bearing silicates and oxides, epidotes or silica-undersaturated minerals. Except of iron bearing minerals, those associated minerals are spectroscopically homogeneous in the VNIR range. As a result, they would only have a feature depth reducing effect on the REE related absorptions that can representatively be simulated with calcite powder. Iron oxides play an important role for the detectability of REEs [34,45]. Therefore, pixels that show iron related absorption bands are masked in the proposed methodology. However, in order to produce synthetic mixtures that represent carbonatites, it is sufficient to use calcitic powders as the matrix material only. Per mixture series almost uniform concentrations were prepared and each series only contains one REO as the ore component and calcite as the matrix component. The proportions of REO powder that were admixed in the carbonate matrix is based on naturally occurring concentrations, as well as unrealistically high amounts in REO carbonate. The natural concentrations (1000, 5000, and 10,000 ppm) were determined based on published values of international occurring deposits [46]. Lower concentrations were not preparable, because a homogeneous distribution of the components is unrealistic and the measurement scale was not precise enough. The unrealistic high concentrations were prepared in order to analyze the full spectroscopic behavior of the REE characteristic absorption feature. The concentrations of the rare earth element powder and calcite powder per sample are listed in Table 4.1.2. Every mixture contains 12 different concentration levels, except of thulium. Thulium is so cost expensive that raw material for more than eight mixtures could not be purchased. The reflectance spectra were then measured with a Perkin Elmer Lambda 950 spectrometer [47]. This spectrometer was used, because its spectral resolution is settable to 1 nm. It is estimated that the concentration level are homogeneous within one EnMAP pixel (30 m x 30 m). Therefore, subpixel variations are not considered in the production of the sample mixtures.

Table 4.1.2: Concentrations and total amounts of REE that are in a synthetic mixture with calcium carbonate powder.

	REO in gr	REO in wt. %	CaCO ₃ in gr	Sum in gr
Neodymium	0.0011	0.11	1.0019	1.0030
	0.0054	0.54	0.9953	1.0007
	0.0118	1.18	0.9977	1.0095
	0.0203	2.03	0.9798	1.0001
	0.0503	5.03	0.9564	1.0067
	0.1088	10.88	0.8962	1.0050
	0.2017	20.17	0.8002	1.0019
	0.3010	30.10	0.7064	1.0074
	0.5025	50.25	0.5073	1.0098
	0.7055	70.55	0.2980	1.0035
	0.8028	80.28	0.2004	1.0032
	0.9558	95.58	0.0464	1.0022
Erbium	0.0014	0.14	1.0016	1.0030
	0.0051	0.51	0.9999	1.0050
	0.0127	1.27	0.9922	1.0049
	0.0223	2.23	0.9782	1.0005
	0.0505	5.05	0.9527	1.0032
	0.1008	10.08	0.9079	1.0087
	0.2014	20.14	0.8017	1.0031
	0.3036	30.36	0.7043	1.0079
	0.5003	50.03	0.5012	1.0015
	0.7130	71.30	0.2937	1.0067
	0.8091	80.91	0.2356	1.0447
	0.9647	96.47	0.0361	1.0008
Thulium	0.0021	0.21	1.0033	1.0054
	0.0056	0.56	1.0343	1.0399
	0.0122	1.22	1.0558	1.0680
	0.0205	2.05	0.9917	1.0122
	0.0558	5.58	0.9623	1.0181
	0.1060	10.60	0.9455	1.0013
	0.2023	20.23	0.8587	1.0610
	0.3269	32.69	0.6821	1.0090

The spectra were transformed into EnMAP characteristic spectra using the EnMAP End-to-End Simulation Tool (EeteS) [40]. Therefore, the laboratory spectral libraries were integrated into an empty grid that was based on a future EnMAP pushbroom image scene. The grid has thousand pixels per line (in Figure 4.1.4 the first 50 pixels per line are shown as an example). Every sampled line is filled with only one library spectrum, and therefore one concentration level of a specified mixture. In the first step of the EnMAP simulation process, this reflectance image is transformed into raw EnMAP data using a series of forward processing steps that model atmospheric conditions and account for spectral, and radiometric differences between the two detectors. A spatial simulation was not considered assuming a pixel size of already 30 m for the input data, because the concentration levels would be changed. The software then simulates the full EnMAP image processing chain, including onboard calibration and atmospheric correction to ultimately produce EnMAP-like at-surface reflectance. In order to analyze the limitations of REE detection on spaceborne acquired image

scenes, a second EnMAP dataset was generated. In this case the surface pixels were illuminated only with diffuse radiation in the atmospheric module, simulating spectra from shaded areas or effects from clouds causing a lower SNR. Finally, hyperspectral mapping of the simulated scene was done with the REE detection routine from Boesche et al. 2015 [34].

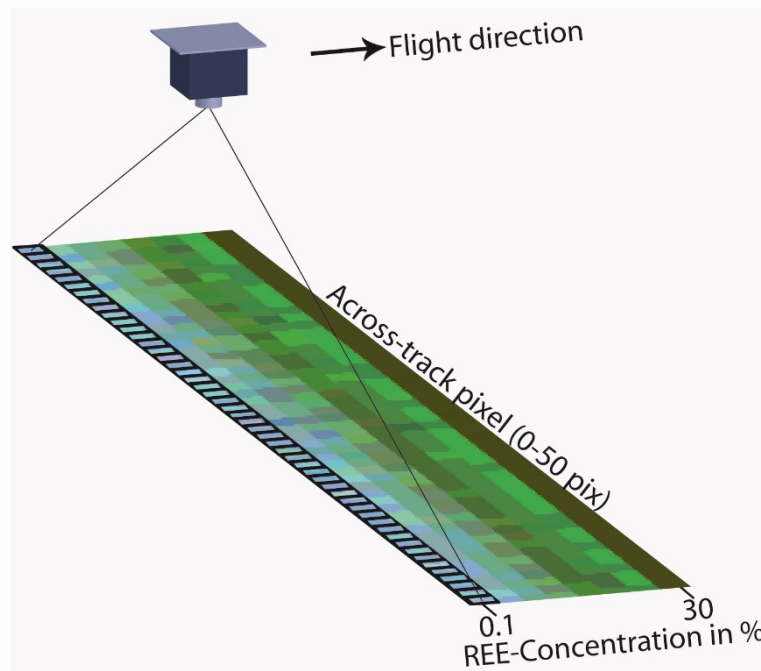


Figure 4.1.4: Sketch showing the spatial arrangement of laboratory spectra for the simulation of an EnMAP image. The first 50 of a total 1000 across-track pixels are depicted. Variations along each across-track line represent sensor characteristic noise.

4.1.2.2 Data analysis

Both sensors were analyzed with the same REE detection routine [33,34]. Besides the preprocessing of the data sets, the REE detection routine includes two more steps. The first step (step 2 in figure 4.1.3) is a sharpening of the relevant absorption features. Prior to this step, the peak wavelength positions and shoulder wavelength positions were manually determined at a resolution of 1 nm in the library spectra (see section 2.1.1). At the beginning of the sharpening routine, the 1-nm spectral resolution of the library spectra has to be adapted to the target sensor resolution. Therefore, the wavelength positions of the target REE related features are transformed into the corresponding spectral band position of the satellite image. The fundamental principle of the sharpening algorithm is a convolution of the image spectrum with a Gaussian shaped filter. Here, a **Richardson Lucy Deconvolution** is used. The filter function is dependent on the stdev of a Gaussian function, which is related to the shape of the target REE absorption feature. Feature parameters (peak and shoulder positions) and the stdev are listed in Table 4.1.3. The second step (step 3 in figure 4.1.3) comprises a **Pearson Correlation** of the spectral library feature with every sharpened image feature. In order to increase the comparability of both absorption features, the 1% REE concentration spectrum was used as the reference for the correlation. This decision has the benefit that the algorithm is trained for the detection of high natural REE concentration. The spectral library spectra were spatially attached to the image scene prior to the sharpening step, so that they are treated in step one as well. A visually determined correlation threshold of higher than 0.95 percent for neodymium and erbium and 0.99 percent for thulium could be used for the final image classification. Additionally, in the EO-1 Hyperion image analysis an iron feature depth determination [48] and the NDVI [49] were used as a filter mask on the results.

Table 4.1.3: Wavelength position in nm of the used absorption feature peaks and their shoulders. These parameters were used as a basis for the Gaussian filter determination of the Richardson Lucy Deconvolution. The stdev of the Gaussian filter is shown in the right column of the Table.

REE	Left shoulder [nm]	Peak position [nm]	Right shoulder [nm]	Stdev [nm]
Neodymium	559	579	609	4.17
	745	753	771	2.17
	785	822	836	4.25
Thulium	677	685	695	1.5
	1193	1204	1218	2.08
	1617	1634	1649	2.67
Erbium	515	523	531	1.33
	645	654	666	1.75
	1522	1534	1544	7.83

4.1.2.3 Geochemical Analysis

In order to validate the Hyperion results, six field samples were collected and geochemically analyzed. The used method is based on ion-exchange chromatography and atomic emission spectroscopy [50]. The field samples were ground to a powder of a particle size of <63 μm . The ore mineral fraction of the sample powder was then solved in a Na_2O_2 -sinter dissolution. In order to separate the REE from the solution, ion-exchange chromatography was applied. In the following step, the resulting REE are dispersed in an inductively coupled plasma and the characteristic electromagnetic signatures analyzed that are emitted by excited atoms and ions (Agilent technologies ICP-OES Vista MPX axial specifications). The resulting REE concentrations are provided in ppm units. In order to increase the comparability, all concentrations were normalized using the C1-chondrite factors from [46]. Compared to other geochemical methods (such as XRF) the method after [50] is a time consuming method that can be used for a small amount of samples. However, a very important advantage of this method is the high precision of resulting concentrations and, after all that heavy rare earth elements (HREE) can be determined.

4.1.3. Results and Discussion

4.1.3.1 Geochemical results and discussion

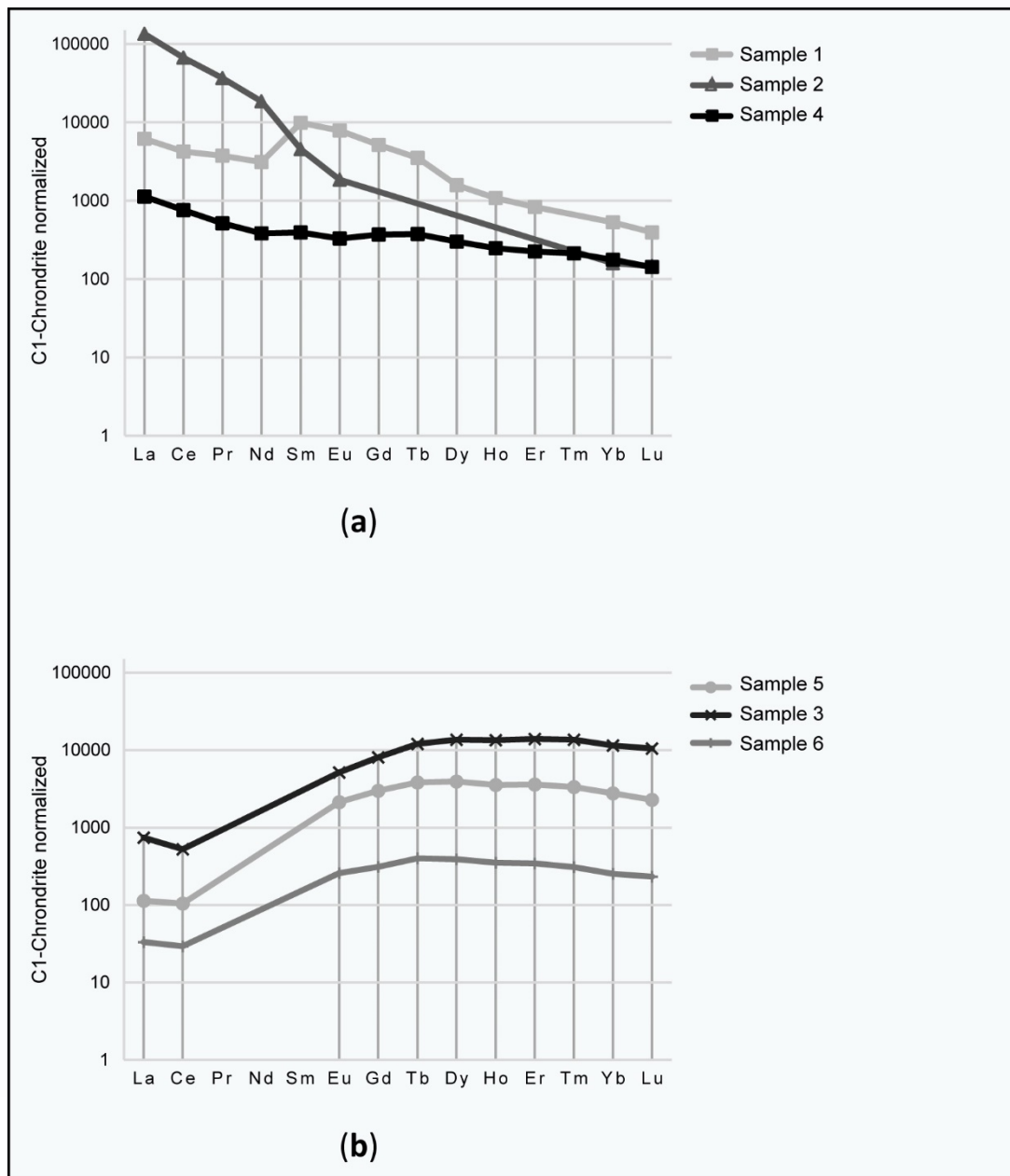


Figure 4.1.5: REE distribution pattern of six samples from Lofdal area, Namibia. The (a) graph shows the distribution pattern of samples that were collected from carbonatites of the early intrusion event. Those carbonatites show either no enrichment or an enrichment in light rare earth elements (LREE), which follows a normal trend for REE enriched carbonatite. The (b) graph shows an enrichment in heavy rare earth elements (HREE). The corresponding samples were collected from carbonatites that originated in the later carbonatite dykes. The rocks of the second type are believed to be hydrothermally altered to contain economically valuable concentrations of HREE [42].

In order to validate and interpret the findings of the hyperspectral analysis of the EO-1 Hyperion image, a fundamental knowledge of the Lofdal REE deposits is necessary. Therefore, six field samples were collected and geochemically analyzed and the results compared to the geological map of the Lofdal region. Particularly important for the evaluation is a decimeter to hundred meter wide dyke, which is located to the lower right of the main intrusion. It is marked as a red band on the geological map. The dyke is enriched in HREE. The concentration of HREE is increasing towards the central deposit and is decreasing towards the outer region

of the image extent. Two samples were collected along the HREE part of the dyke (Sample 3 and 5). Another HREE carbonatite intrusion is located towards the north of the main intrusion (Sample 6). It is moderately enriched in HREE but shows the same trend in the spider diagram as the samples from the main dyke. In the spider diagram of Figure 4.1.5, the trend of the C1-chondrite normalized REE concentration is shown. Siegfried and Hall 2012 [42] published that the HREE and LREE enriched carbonatites originate from two independent events. The dolomitic carbonatites at sample location 1 were collected at Dolomite Hill. They can be assigned to the earlier intrusion event of the LREE enriched carbonatites of sample 2 [42,51]. In Figure 4.1.5 those two samples show a trend, which supports the similarity between the LREE enriched carbonatites and the dolomitic carbonatites at Dolomite Hill. However, the LREE enriched carbonatites show extremely high concentrations of LREE (>85%) (Table 4.1.4, Figure 4.1.5). Sample 4 was collected at a carbonatitic dyke that was geochemically tested beforehand not to be enriched in REE.

Table 4.1.4: Concentrations of total LREE and HREE in the field samples. The concentrations are given in ppm.

Sample #	Total Light REE in ppm	Total Heavy REE in ppm
Sample 1	7359	2042
Sample 2	85641	107
Sample 3	498	5863
Sample 4	1018	185
Sample 5	91	1880
Sample 6	26	193

4.1.3.2 EO-1 Hyperion image classification results and discussion

Figure 4.1.6 shows the estimated SNR of every EO-1 Hyperion image. The SNR was estimated using the ratio of the mean and the standard deviation values of those pixels that were located in the spatial and spectral subset, which was determined using the pan-quantization. The spectral subset that was used in the pan-quantization includes the spectral range of the 1634 nm feature for Thulium. The spatial subset includes the eroded spatial extent of the first level quantization of the pan image. Hence, the calculated SNR values represent the SNR in the darkest pixels of the images, not of the whole image. The figure 4.1.6 highlights the increased SNR of the multitemporal averaged image (right data point in figure 4.1.6). Thus, a multitemporal averaging and therefore increased SNR will lead to a higher probability to detect REE related features.

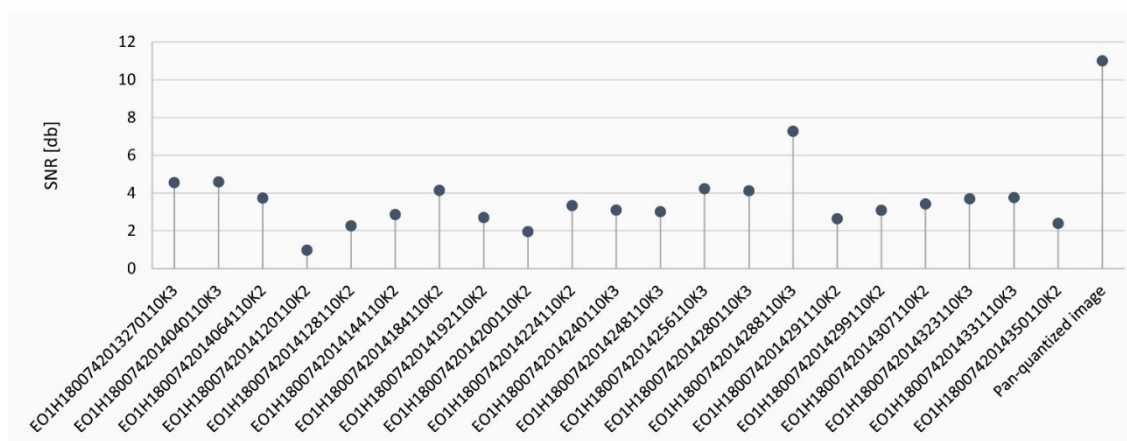


Figure 4.1.6: Estimated Signal-to-Noise Ratio for the EO-1 Hyperion images. The SNR were calculated as the ratio of mean and standard deviation for all pixel spectra (within the wavelength range of the Tm feature at 1634 nm) over a predefined neighborhood (level 1 of the pan-quantization). Note the SNR for the final pan-quantized image on right side of the graph that was used for further REE detection.

In Figure 4.1.7 the result of the hyperspectral REE mapping of the REE deposit in Namibia is visualized. It shows two examples of the mapping results that worked out best. Neodymium could not be detected in any analyzed image scene of the three absorption features within the 0.95 threshold of the Pearson correlation coefficient. This could be explained by the distribution of enriched material in the Lofdal region. It is mainly enriched in HREE (Figure 4.1.5), only a small region south of the main intrusion is enriched in LREE (Table 4.1.4). For erbium and thulium the features at 1534 nm and 1634 nm worked best. Both features are located in the infrared range of the electromagnetic spectrum, a part that is less affected atmospheric superimpositions. Every single positive identification of thulium and erbium cannot be validated with geochemical field analyzes, because field verification at this stage was focused on Neodymium detection. However, in order to compare the hyperspectral results with the geological map in Figure 4.1.7a), the positive identifications in Figure 4.1.7b) and c) can be evaluated for their probability of enrichment for that area in the geological map. Based on field work in the Lofdal area, an evaluation of some findings was achieved. The HREE enriched dyke to the east of the main intrusion can be identified in both REE maps with one pixel in the erbium map (Figure 4.1.7b) and two pixels in the thulium map (Figure 4.1.7c). The enrichment area to the north of the main intrusion could be identified in the thulium map (Figure 4.1.7c) but was not confirmed in the field evidence yet. Some findings are detectable in the strongly deformed amphibolites in the upper right quarter of the image extent. Those findings are not unrealistic, but cannot be ground-truthed in this study as well. However, the regions where field samples for the evaluation of the HREE were collected (Table 4.1.4; Figure 4.1.7) could be validated with the hyperspectral analyses.

The area of Dolomite Hill could not be identified, this zone was also not particularly highly enriched. False positive findings can be observed towards the south of the image. This area has a low albedo (equivalent to higher noise) and a high amount of iron (reddish colored pixel). Iron hampers the detectability of REE and a higher noise causes randomly occurring tiny features that might be identified as REE by the methodology [45,52]. The findings in this area are therefore not reliable. Additional limitations of the EO-1 Hyperion image classification for thulium and erbium are mainly correlated to the data quality of the raw data and the preprocessing quality of each scene. Particular important is an accurate atmospheric correction of the radiance data. Many absorption features of the REE are located close or at the positions of the atmospheric absorptions. Therefore, it is important to reduce the atmospheric effect with a most precise model instead interpolating the spectra at the wavelength ranges of the atmosphere. It should also be noted that the EO-1 Hyperion input data were 21 image scenes that were georeferenced to each other with an error of less than 2 pixels in average (maximum 4 pixels). Hence, a geospatial linkage of the positive identifications to the georeferenced geological map is not possible.

In the appendix of this paper, an example REE map is shown, that was produced with a lower correlation threshold (0.9). The map shows a higher number of positive findings. Although it can be clearly seen, that the HREE enriched dyke to the east of the main intrusion can be detected in a greater extent, the number of eventual false positive identifications increases. However, the proposed REE detection methodology is trained to be as robust as possible. Therefore, only pixels that show a very high correlation with the library spectrum are recommended to be flagged as positive.

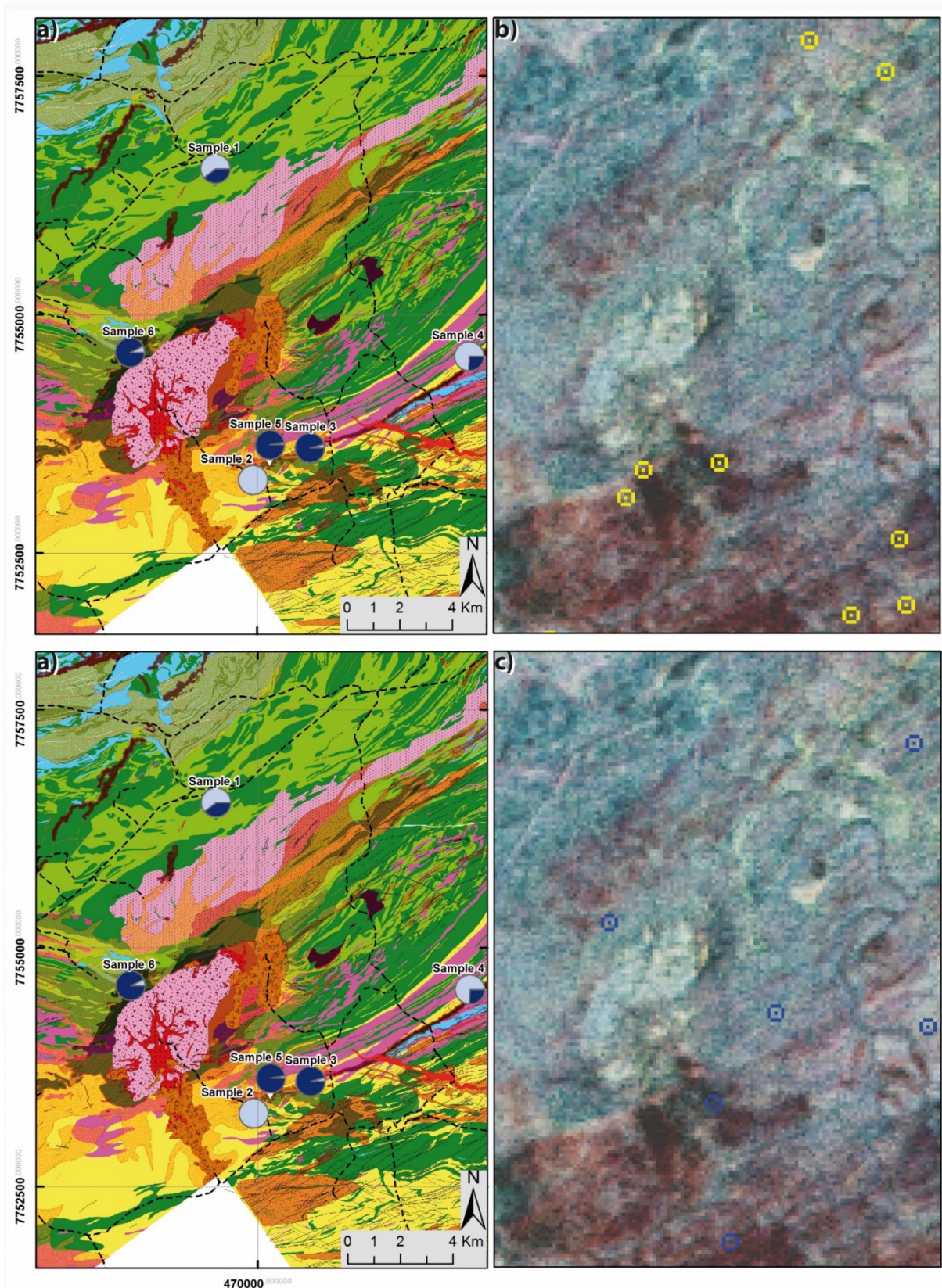


Figure 4.1.7: The results of the hyperspectral classification of erbium 7b) and thulium 7c) are shown in comparison to the detailed lithological map of Lofdal, Namibia 7a) after Namibia Rare Earth Inc., Namibia/ Remote Exploration Services (RES). The blue pie diagrams show the concentration of LREE in light blue and HREE in dark blue as part of total REE. The positive findings of erbium (yellow) and thulium (blue) have a spatial extent of one image pixel (30 m). In order to increase visibility of the findings a circle is drawn around the positively identified pixel.

4.1.3.3 EnMAP classification results and discussion

The results in Figure 4.1.8 show the detectability of different REE concentrations for the known EnMAP sensor characteristics [40]. Every subplotted map in Figure 4.1.8 shows a classification of the surface material that is based on the correlation coefficients between the reference library features with a REE feature of the image spectrum. The yellow result map represents erbium, green is neodymium and blue represents thulium. Image scenes that are illuminated with direct incoming sun radiation are plotted in the first row of subplots, simulated scenes with high noise (diffuse sun illumination) are plotted in the bottom row.

The best results are supposed to be visually determined on every third line from left, which is identified positive in Figure 4.1.8. This is based on the criterion that the simulated 1% mixture of the reference spectrum is located in the third line and hence, this line is to be found in any case. The 523 nm and 654 nm feature for erbium can therefore be determined in a robust manner. However, even the 1534 nm feature for erbium shows at least few positive identifications. Neodymium was found in all third lines of the image scenes for the analysis of the three features, wherein the feature at 822 and at 579 nm seem to work slightly better. In thulium only the 1634 nm feature produces a reliable detection result. As expected, in scenes with indirect sun illumination the detectability is significantly reduced. Here only the very high, unnatural concentrations are found (at 654 nm for erbium, all three features for neodymium, and at 1204 nm and 1634 nm for thulium). Taking the criterion that the 1% concentration pixel must be found, only correlations of erbium and thulium (at 1534nm and 1634 nm) can be considered to be useful in pixel with indirect sun illumination. However, positive identifications in the pixel with diffuse sun illumination are not necessarily distinctive, because the used methodology is still sensitive for extreme noise. In order to discuss the influence of non-optimal acquisition conditions, the spectral range of the thulium absorption band at is shown in figure 4.1.9. The comparison between pixel with direct and diffuse illumination conditions is shown in 4.1.9a) and 4.1.9b). Under optimal illumination conditions the absorption bands are visible at lowest concentration levels (0.1 % thulium). Under diffuse illumination conditions, the feature cannot be distinguished from noise (except of 30 % thulium). Figure 4.1.9c) and 4.1.9d) show the identical image spectra after applying the Richardson Lucy Deconvolution. Except of 2 % thulium, all REE-sharpened spectra show a pronounced absorption feature under diffuse illumination conditions. The plots show the two extremes of illumination conditions. Future acquired images will provide spectra whose signal to noise ratio is between these extremes. Therefore, we suggest for most cases to include a noise reduction (multitemporal averaging) in the preprocessing steps and the sharpening of the REE related absorption bands. Thereby, the REE detection in future hyperspectral images can be significantly improved. Nevertheless, there is a great potential that all three REE can be detected under good acquisition conditions.

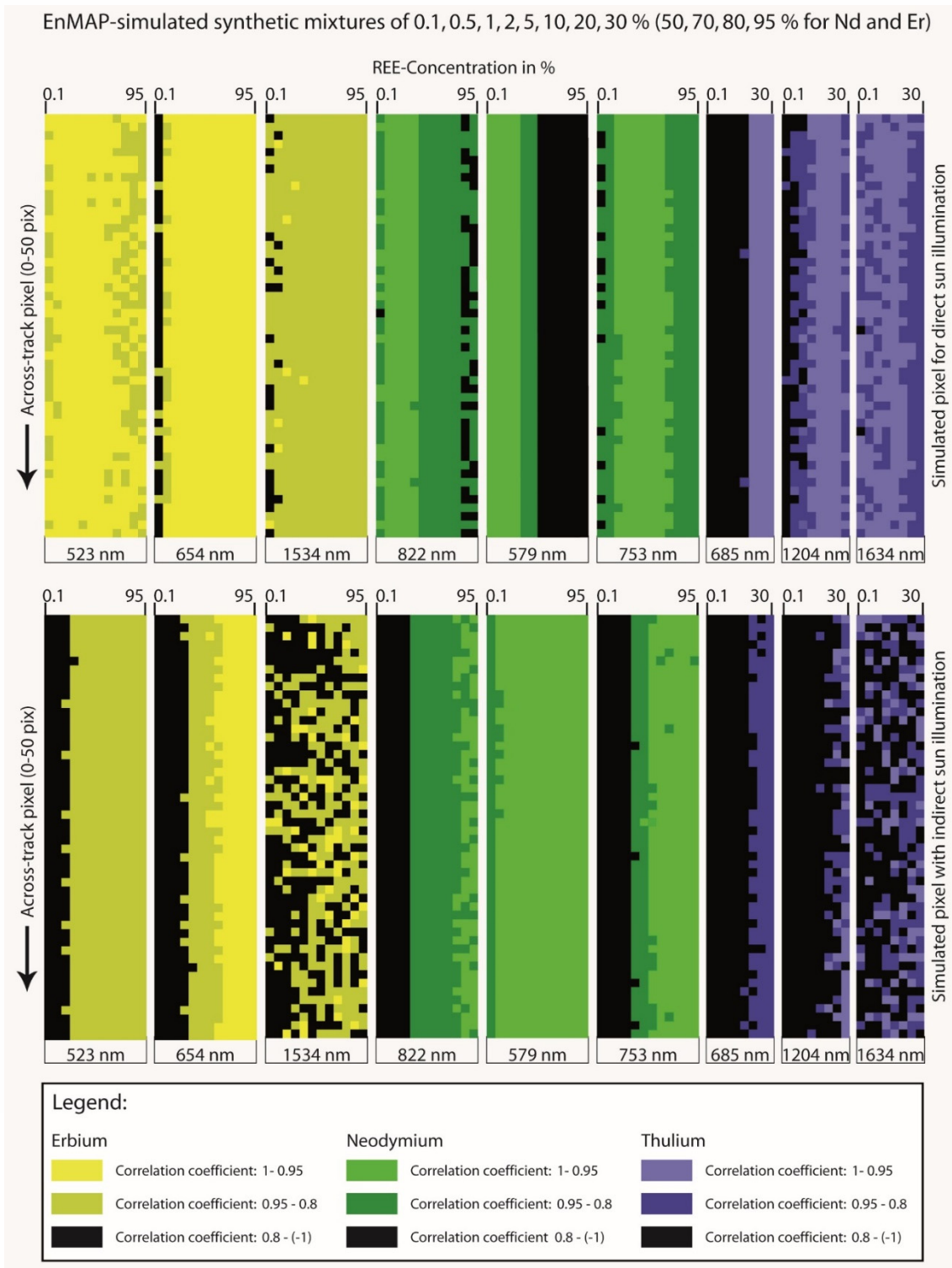


Figure 4.1.8: Result of the hyperspectral REE detection of simulated EnMAP image scenes [40]. The subplots in the top row represent an image simulation for direct sun illumination, the bottom row for pixel with indirect sun illumination (higher noise). The y-axis of every image represents the first 50 pixel of the across-track flight line that were simulated for certain concentrations of REE in a carbonate matrix. The x-axis of every image represents the concentrations of either erbium (yellow), neodymium (green) or thulium (blue). Every REE was analyzed for three different absorption features that were manually determined beforehand. The resulting images were classified using a Pearson correlation of a laboratory spectrum that represents a natural concentration level with every image pixel spectrum. Three classes of correlation were defined (1 to 0.95, 0.95 to 0.8 and 0.8 to (-1)). The class that represents the highest correlation is recommended by the authors to be used as a spatial REE detection.

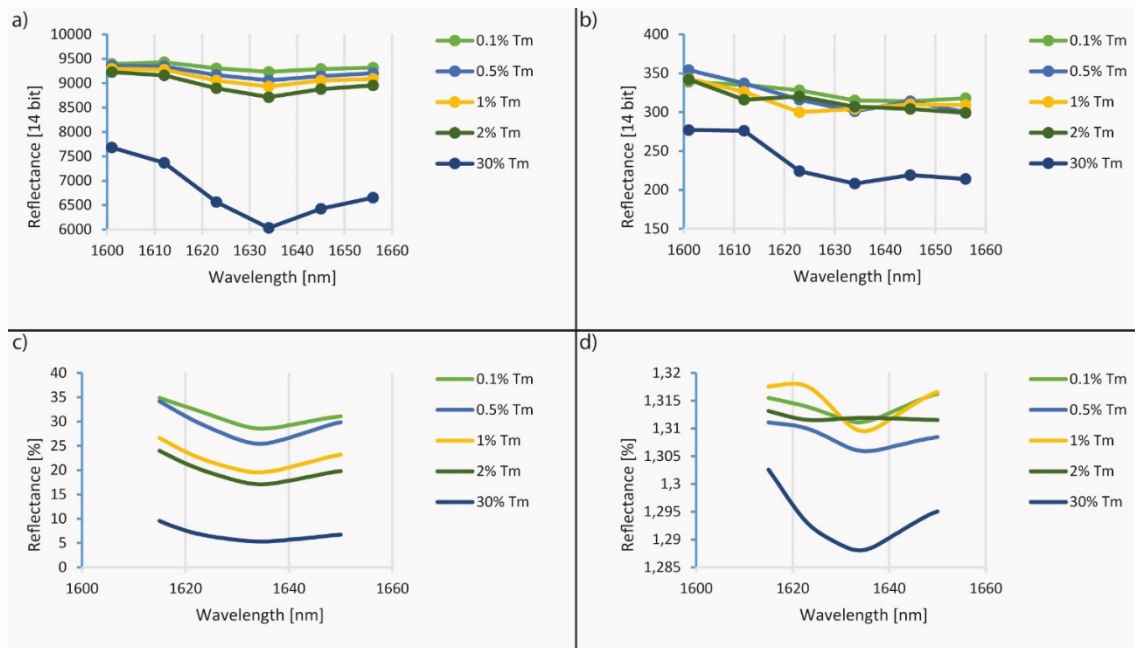


Figure 4.1.9: Comparison between image spectra that were simulated for direct 9a) and diffuse 9b) illumination conditions. 9c) and 9d) show the same spectra after applying the Richardson-Lucy Deconvolution (REE sharpening). The figure shows, that under good illumination conditions the absorption features are clearly visible. Under diffuse illumination conditions a sharpening of the absorption feature is necessary, in order to distinguish between noise and actual absorption.

4.1.4. Conclusions

This study shows that hyperspectral surveys have a great future potential to support REE exploration. The detection of the distinct shape and tiny absorption depths of the REE features in today's and near future satellite data is complex and a sharpening of the absorption features is beneficial. The results indicate that direct detection of the spectral signature of REE (neodymium, erbium and thulium) is possible if the concentration is high (~ 0.1 % or higher), the temporal coverage is high (21 scenes or higher) or the illumination conditions are good (direct incident radiation, no clouds, low atmospheric distortions, etc.). The best results can be expected if all three influencing factors are optimal.

The result for the REE detection in the EO-1 Hyperion image showed that the presented approach works best with the SWIR. Therefore, the features for erbium and thulium at **1534 nm** and **1634 nm** were producing the best results. In the resulting maps of the EO-1 Hyperion data the REE bearing dykes could not be mapped in their full extent but highlighted at several locations. With today's operating hyperspectral imager (like EO-1 Hyperion), the signal to noise ratio and the spatial resolution must be seen as a hampering factor for a full-extent mapping of REE. Anyway the proposed method is trained for a maximum reliability and therefore to keep false positive identifications as low as possible. The positive identifications should be ground truthed by a field team.

The result for the REE detection of natural REE concentrations in the EnMAP images showed, that under optimal illumination conditions the features at **523 nm** and **654 nm** worked out best for erbium and the **1534 nm** feature showed few positive erbium findings. For neodymium the features at **822 nm** and at **579 nm** worked particularly well. The best feature for thulium is the **1634 nm** feature. REE enriched pixel that were imaged under non optimal illumination conditions, could be detected best with the **1534 nm** and **1634 nm** for erbium and thulium. Therefore, the authors also recommend to use multiple coverage images for the REE detection with the future EnMAP, in order to cope with non-optimal illumination conditions. The relative spatial accuracy between different EnMAP L2a products from the same test area will be below 1 pixel and therefore optimal for a noise optimization.

In order to successfully map REE with remotely sensed imagery, future research should concentrate on the reduction of atmospheric effects with a most precise model instead of interpolating the spectra at atmospherically superimposed ranges. Additionally, a high number of accurately georeferenced overlapping scenes should be included in the processing steps. Moreover, a priori knowledge of the expected concentration is recommended for the calibration of the method.

4.1.5 Acknowledgments

The authors thank the Helmholtz Centre Potsdam - GFZ German Research Centre for Geosciences and the German National EnMAP framework program (Department of Economics and Technology BMWi No. 50EE1256) for the financial support. Special thanks go to Namibia Rare Earth Inc., namely Scott Swinden, Don Burton and Franck Bizouerne for supporting this study and assisting with additional information about the Lofdal complex. All our gratitude also goes to the editors of the EnMAP Special Issue and the reviewers for their helpful comments, which improved the quality of this paper.

4.1.6 Author Contributions

Nina Kristine Boesche carried out this study and wrote the manuscript. Karl Segl simulated the EnMAP dataset from hyperspectral laboratory measurements of synthetically produced mixtures. Christian Rogass transferred the EO-1 Hyperion radiance data into reflectance data. Sabine Tonn monitored the geochemical measurements on the field samples. Sabrina Herrmann produced the synthetic mixtures series and carried out the hyperspectral measurements on those mixtures. Karl Segl, Christian Mielke and Maximilian Brell helped with the fieldwork and gave valuable input for the manuscript. Uwe Altenberger and Luis Guanter supervised the geological/geochemical and remote sensing investigations and helped with the interpretation of the results.

4.1.7 Conflicts of Interest

The authors declare no conflict of interest.

4.1.8 References

1. Yap, C.-W. China Ends Rare-Earth Minerals Export Quotas. *Wall Str. J.* 2015.
2. Dieke, G. H.; Crosswhite, H. M. The Spectra of the Doubly and Triply Ionized Rare Earths. *Appl Opt* **1963**, *2*, 675–686.
3. White, W. B. Diffuse-Reflectance Spectra of Rare-Earth Oxides. *Appl Spectrosc* **1967**, *21*, 167–171.
4. Rowan, L. C.; Mars, J. C. Lithologic mapping in the Mountain Pass, California area using Advanced Spaceborne Thermal Emission and Reflection Radiometer (ASTER) data. *Remote Sens. Environ.* **2003**, *84*, 350–366.
5. Rowan, L. C.; Kingston, M. J.; Crowley, J. K. Spectral reflectance of carbonatites and related alkalic igneous rocks; selected samples from four North American localities. *Econ. Geol.* **1986**, *81*, 857–871.
6. Bedini, E.; Tukiainen, T. Using spectral mixture analysis of hyperspectral remote sensing data to map lithology of the Sarfartoq carbonatite complex, southern West Greenland. **2008**, *Geological Survey of Denmark and Greenland Bulletin*, 69–72.
7. Bedini, E. Mapping lithology of the Sarfartoq carbonatite complex, southern West Greenland, using HyMap imaging spectrometer data. *Remote Sens. Environ.* **2009**, *113*, 1208–1219.
8. Hernandez, E. A.; Filho, C. R. de S. Spectral reflectance and emissivity features of PO₄-bearing carbonatitic rocks from the Catalão I and Tapira complexes: New constraints for detection of igneous phosphates with remote sensing data. *An. XVI Simpósio Bras. Sensoriamento Remoto-SBSR Publ. Foz Iguaçu Bras.* **2013**.
9. Momose, A.; Miyatake, S.; Arvelyna, Y.; Nguno, A.; Mhopjeni, K.; Sibeso, M.; Muyongo, A.; Muvangua, E. Mapping pegmatite using HyMap data in southern Namibia. In *Geoscience and Remote Sensing Symposium (IGARSS), 2011 IEEE International*; 2011; pp. 2216–2217.
10. Boesche, N. K.; Rogaß, C.; Mielke, C.; Kaufmann, H. Hyperspectral digital image analysis and geochemical analysis of a rare earth elements mineralized intrusive complex (fen carbonatite complex in Telemark region, Norway). In *EARSel 34th Symposium Proceedings*; University of Warsaw, 2014.
11. Boesche, N. K.; Rogass, C.; Lubitz, C.; Brell, M.; Herrmann, S.; Mielke, C.; Tonn, S.; Appelt, O.; Altenberger, U.; Kaufmann, H. Hyperspectral REE (Rare Earth Element) Mapping of Outcrops—Applications for Neodymium Detection. *Remote Sens.* **2015**, *7*, 5160–5186.
12. Turner, D. J.; Rivard, B.; Groat, L. A. Visible and short-wave infrared reflectance spectroscopy of REE fluorocarbonates. *Am. Mineral.* **2014**, *99*, 1335–1346.
13. *Rare Earths Industry: Technological, Economic, and Environmental Implications*; Lima, I. B. D.; Filho, W. L., Eds.; 1 edition.; Elsevier, 2015.
14. Norsk Elektro Optikk HySpex VNIR 1600/SWIR320 m-e <http://www.sphereoptics.de/de/spektrometer/docs/HySpex-GenerellMail.pdf> (accessed Apr 1, 2015).
15. Clark, R. N.; Swayze, G. A. Mapping minerals, amorphous materials, environmental materials, vegetation, water, ice, and snow, and other materials: The USGS Tricorder Algorithm. In *Summaries of the Fifth Annual JPL Airborne Earth Science Workshop*; JPL Publication, 1995; Vol. 1, pp. 39–40.
16. Pearlman, J.; Carman, S.; Segal, C.; Jarecke, P.; Clancy, P.; Browne, W. Overview of the Hyperion Imaging Spectrometer for the NASA EO-1 mission. In *Geoscience and Remote Sensing Symposium, 2001. IGARSS '01. IEEE 2001 International*; 2001; Vol. 7, pp. 3036–3038 vol.7.
17. Guanter, L.; Segl, K.; Kaufmann, H. Simulation of optical remote-sensing scenes with application to the enmap hyperspectral mission. **2009**, *47*, 2340–2351.
18. Kaufmann, H.; Segl, K.; Guanter, L.; Hofer, S.; Foerster, K.-P.; Stuffer, T.; Mueller, A.; Richter, R.; Bach, H.; Hostert, P.; Chlebek, C. Environmental Mapping and Analysis Program (EnMAP) - Recent Advances and Status. In *Geoscience and Remote Sensing Symposium, 2008. IGARSS 2008. IEEE International*; 2008; Vol. 4, pp. IV–109–IV–112.
19. Segl, K.; Guanter, L.; Rogass, C.; Kuester, T.; Roessner, S.; Kaufmann, H.; Sang, B.; Mogulsky, V.; Hofer, S. EeteS - The EnMAP End-to-End Simulation Tool. *IEEE J. Sel. Top. Appl. Earth Obs. Remote Sens.* **2012**, *5*, 522–530.
20. Beck, R. EO-1 User Guide v. 2.3. *USGS Earth Resour. Obs. Syst. Data Cent. EDC* **2003**.

21. Siegfried, P.; Hall, M. NI 43-101 Technical Report and Mineral Resource Estimate for Area 4 of the Lofdal Rare Earth Element (REE) Project, Khorixas District, Republic of Namibia 2012.
22. Rogass, C.; Guanter, L.; Mielke, C.; Scheffler, D.; Boesche, N. K.; Lubitz, C.; Brell, M.; Spengler, D.; Segl, K. An automated processing chain for the retrieval of georeferenced reflectance data from hyperspectral EO-1 HYPERION acquisitions. In *EARSeL 34th Symposium Proceedings*; University of Warsaw, 2014.
23. Guanter, L.; Segl, K.; Sang, B.; Alonso, L.; Kaufmann, H.; Moreno, J. Scene-based spectral calibration assessment of high spectral resolution imaging spectrometers. **2009**, *17*, 11594–11606.
24. Townsend, T. E. Discrimination of iron alteration minerals in visible and near-infrared reflectance data. **1987**, *92*, 1441–1454.
25. Sun, S.-S.; McDonough, W. F. Chemical and isotopic systematics of oceanic basalts: implications for mantle composition and processes. *Geol. Soc. Lond. Spec. Publ.* **1989**, *42*, 313–345.
26. Perkin Elmer Applications and Use of Integrating Spheres With the LAMBDA 650 and 850 UV/Vis and LAMBDA 950 UV/Vis/NIR Spectrophotometers http://www.perkinelmer.com/CMSResources/Images/44-74191APP_LAMBDA650IntegratingSpheres.pdf (accessed May 6, 2015).
27. Mielke, C.; Boesche, N. K.; Rogass, C.; Kaufmann, H.; Gauert, C.; de Wit, M. Spaceborne Mine Waste Mineralogy Monitoring in South Africa, Applications for Modern Push-Broom Missions: Hyperion/OLI and EnMAP/Sentinel-2. *Remote Sens.* **2014**, *6*, 6790–6816.
28. Julien, Y.; Sobrino, J. A. Temporal analysis of NDVI and LST parameters to detect changes in the Iberian land cover between 1981 and 2001. *Int. J. Remote Sens.* **2011**, *32*, 2057–2068.
29. Zuleger, E.; Erzinger, J. Determination of the REE and Y in silicate materials with ICP-AES. *Fresenius Z. Für Anal. Chem.* **1988**, *332*, 140–143.
30. Gaudet, M. A. Mineralogical study of uranium and niobium mineralization at the main intrusion of the Lofdal carbonatite complex, Namibia, Africa. Bachelor of Science - Thesis, Dalhousie University: Halifax, Nova Scotia, 2013.
31. E. Ben-Dor, S. C. Using Imaging Spectroscopy to study soil properties. *Remote Sens. Environ.* **2009**.

© 2015 by the authors; licensee MDPI, Basel, Switzerland. This article is an open access article distributed under the terms and conditions of the Creative Commons Attribution license (<http://creativecommons.org/licenses/by/4.0/>).

4.1.9 Appendix

Table 4.1.9.1: Raw data information on the EO-1 Hyperion datasets that were used for the hyperspectral REE analysis.

#	Name of the EO-1 Hyperion image scene	Acquisition date
1	EO1H1800742015001110K3	01.01.2015
2	EO1H1800742014350110K2	16.12.2014
3	EO1H1800742014339110K3	05.12.2014
4	EO1H1800742014331110K3	27.11.2014
5	EO1H1800742014323110K3	19.11.2014
6	EO1H1800742014307110K2	03.11.2014
7	EO1H1800742014299110K2	26.10.2014
8	EO1H1800742014291110K2	18.10.2014
9	EO1H1800742014288110K3	15.10.2014
10	EO1H1800742014280110K3	07.10.2014
11	EO1H1800742014256110K3	13.09.2014
12	EO1H1800742014248110K3	05.09.2014
13	EO1H1800742014240110K3	28.08.2014
14	EO1H1800742014224110K2	12.08.2014
15	EO1H1800742014200110K2	19.07.2014
16	EO1H1800742014192110K2	11.07.2014
17	EO1H1800742014184110K2	03.07.2014
18	EO1H1800742014176110K2	25.06.2014
19	EO1H1800742014144110K2	24.05.2014
20	EO1H1800742014128110K2	08.05.2014
21	EO1H1800742014120110K2	30.04.2014
22	EO1H1800742014112110K2	22.04.2014
23	EO1H1800742014064110K2	05.03.2014
24	EO1H1800742014040110K3	09.02.2014
25	EO1H1800742013270110K3	27.09.2013

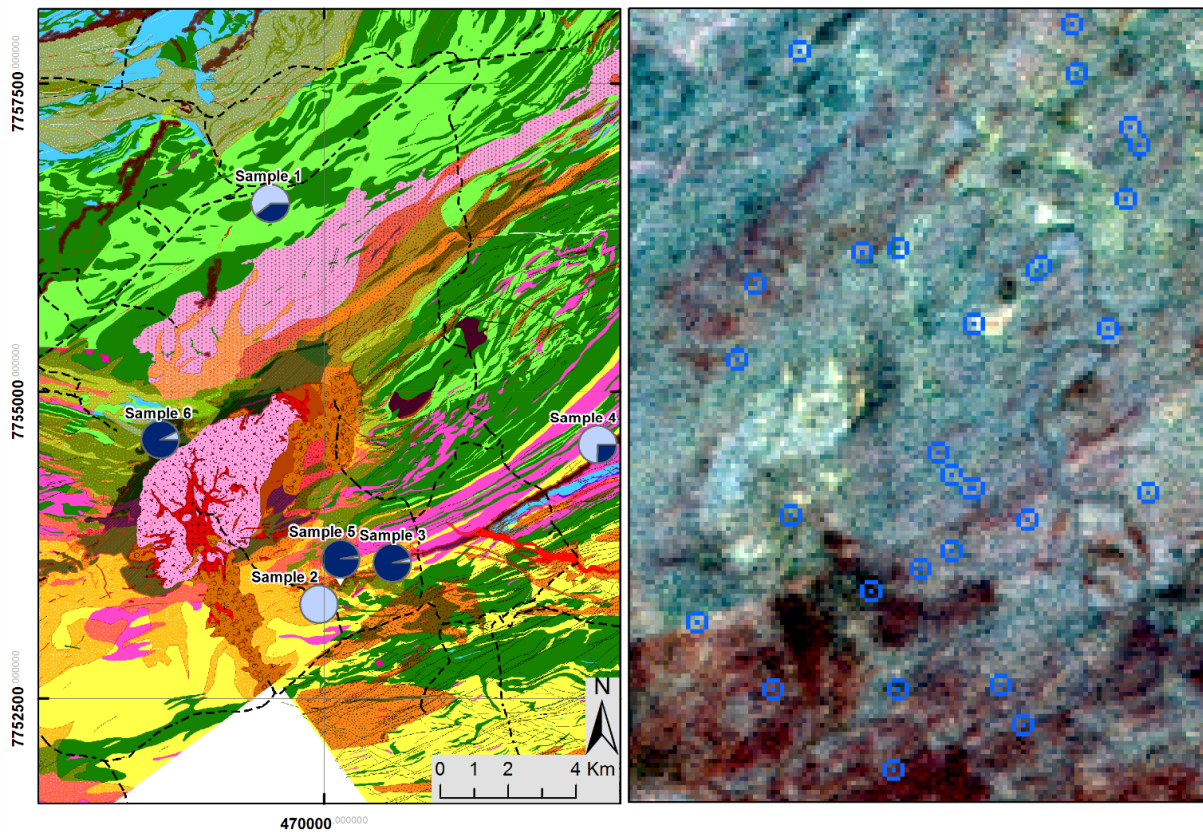


Figure 4.1.9.1: The results of the hyperspectral classification of thulium, for a lower correlation threshold of 0.9, is shown in comparison to the lithological map of Lofdal, Namibia. It is shown that a lower correlation threshold increases the amount of REE-positively indicated pixel. However, the amount of false negative classification would increase as well. Therefore, the authors recommend to use a considerably high threshold, in order to increase the robustness of the method. The lithological map was provided by Namibia Rare Earth Inc., Namibia, and produced by Remote Exploration Services (RES), South Africa, drafted by A. Johnson in 2013.

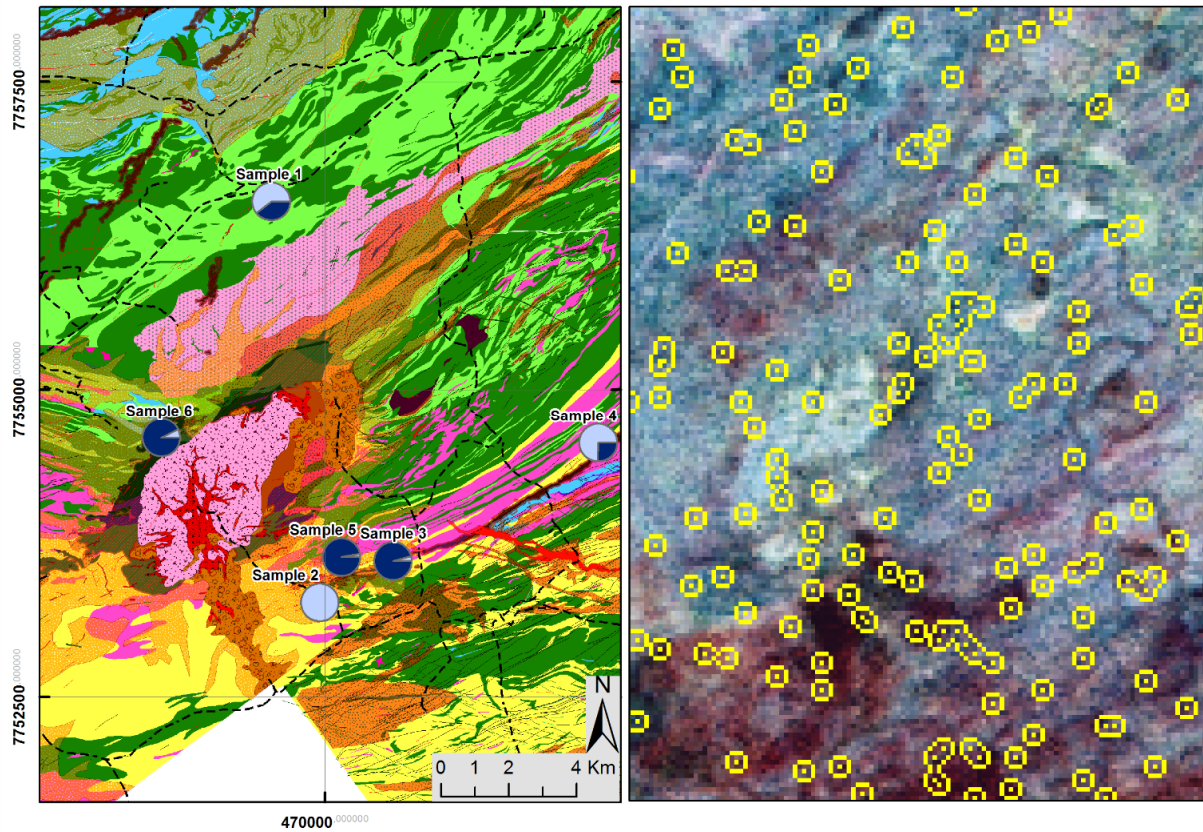


Figure 4.1.9.2: The results of the hyperspectral classification of erbium, for a lower correlation threshold of 0.9, is shown in comparison to the lithological map of Lofdal, Namibia. The amount of false positive classifications is very high if a low correlation threshold is used (0.9). Therefore, the authors recommend to use the threshold of at least 0.95, in order to increase the robustness of the method. The lithological map was provided by Namibia Rare Earth Inc., Namibia, and produced by Remote Exploration Services (RES), South Africa, drafted by A. Johnson in 2013.

5. Chapter

Discussion and Conclusion

5.1 Discussion of the Results

5.1.1 REE Related Spectra and their Special Optical Characteristics

This doctoral thesis shows that REE related spectra show a high number of absorption bands in 9 of the measured REOs (see: Table 8.1 appendix). Because some absorption bands are determined to probably occur due the vibrational motion in water, it can be assumed that at least 8 REOs are robustly detectable in a related reflectance spectrum. The mathematical description of the absorption bands turned out to be more difficult. Therefore, the following section will discuss the observed special optical behavior of REEs. All spectroscopic measurements performed on different REE bearing samples lead to the assumption that the REE absorption bands are sensitive to several influencing factors. When analyzing the spectra of the REMs, only neodymium and europium showed their characteristic absorptions. Due to the theory of the crystal field transition absorptions, it was expected that the remaining six REE also absorb electromagnetic light. However, that is not the case in the measurements presented in Chapter 2.2. Hence, it can be assumed that the bond of the REEs to another ion may enable the absorption of electromagnetic light or that the instruments are not sensible enough to measure the absorptions. Anyhow, the fact that neodymium and europium do absorb, when occurring as metals, might be explainable with the hypersensitive transitions (see: Chapter 1.4.3) that are published for those two elements. Meaning, that bonds to other ions are not required for neodymium and europium to absorb the electromagnetic light at the energy levels for the hypersensitive transitions. Nevertheless, even in these spectra not all known absorptions are visible. Only absorption bands related to hypersensitive transitions can be observed in the spectra of the metals.

When the 8 mentioned REEs are bound to neighboring ions, several absorptions occur. In all element oxides (except of neodymium) the absorptions can be located at distinct wavelength positions. Therefore, these element oxides can be classified to show robustly detectable features. The hypersensitive transitions that are published for neodymium are known to produce a shift of the peak position inversely proportional to the 4f and 5d energy differences [6]. For example, fluorine (a typical ion in the bastnaesite-parisite solid solution series) shows the greatest impact on those shifts. The shifts could not be observed for europium because it is usually not incorporated to a high amount in the bastnaesite-parisite solid solution series. However, since europium is known to have hypersensitive transitions, a shift can be expected [29, 30]. Another finding of this study is the sensitivity of neodymium to varying illuminations or other sensor characteristics. This sensitivity can also be observed in a shift of the peak position of the absorption band. This finding has a special importance for spectroscopy. In this study the impact of the measurement mode on the wavelength position could not be examined in full detail. However, when using a library spectrum or a look-up-table of peak positions, in order to detect the absorption feature, a spectral library built with the same illumination/sensor conditions is required. Whether this would also be valid for changing illumination conditions, using the sun as a light source, could not be answered in this work. However, it must be assumed that differing peak positions along the wavelength axis are also a function of varying direct and diffuse illuminations of the sun. Another sensitivity of neodymium, that could be observed, is a changing depth of several absorption bands. The changes often occur in individual absorption bands that make up a multiple absorption feature. Moreover, it seems that the area at the range of the multiple absorption bands does not change significantly. Therefore, it is recommended to compare the area with a look-up-table for those features or a cross correlation approach with a freely moving but REE limited spectral lag, rather than extracting the peak position or perform a Pearson-correlation. This finding has a great impact on spectroscopy, because through changing absorption depths the subjective shift of the highest absorption depth can vary for more than 20 nm (for example at the 800 and 870 nm feature). Although neodymium turned out to show a complicated spectroscopic behavior, thus it is strongly recommended for hyperspectral LREE detection. Especially, when working with mineral analysis the neodymium absorption bands are the best visible absorptions in the spectrum. Samarium also shows distinct and doubtless more robust absorptions, but it occurs in a lower concentration in natural deposits, which makes a recognition in the spectrum more difficult. For the detection of HREE deposits,

working with holmium, erbium, dysprosium, and samarium is also recommended, because their absorption bands are robustly detectable in the spectrum of the HREE ore xenotime. Generally, HREE deposits show varying concentrations in the individual element's distributions. Therefore, from the geological perspective, no REE should be preferred for the detection of HREE deposits. However, dysprosium, samarium, erbium, thulium, europium, and ytterbium should be preferred for the SWIR range and erbium, holmium, and thulium for the VNIR range.

Even though this thesis indicates a mathematical dependency of a second polynomial degree between the absorption depth and REE concentration, a quantification using today's hyperspectral techniques for a concentration determination in samples is not recommended and requires more basic research. This recommendation relates the fact that the sensitivities of REEs on electromagnetic light [6, 29, 30] and the influence of associated materials are not fully understood so far and might be additionally aggravated by the abundance of mixed pixels (especially on satellite images).

5.1.2 REEMAP Methodology

A new approach has been developed that detects REEs in hyperspectral data in the wavelength range of the VNIR and SWIR. The new approach basically delineates the spectral information of REEs and other spectral signals. Besides preprocessing of data, the basic steps include a multitemporal weighted averaging of images that cover the area to be mapped and a sharpening of the spectral signature of the target REE.

In detail the preprocessing includes several steps that need to be chosen differently, depending on the sensor and measurement mode. For outcrops scans, where white reference panels could be placed in front of the outcrop, the image can straightforwardly be transformed into reflectance data using panel radiance measurements. Besides this, it is recommended to also perform an albedo normalization to reduce varying illumination and shadowing impacts on the succeeding analyses. This is also valid for images acquired by rotational scan modes. The reference panels can also serve for the image noise estimation that is used as a weighting factor in the multi-temporal averaging within the REEMAP procedure. For spaceborne images adequate white references are not available. In this case the reflectance transformation must be performed based on radiative transfer modeling, using either commercial or in-house developed software, such as ATCOR, FLAASH, ACT, EeteS, etc. For the noise estimation homogeneous targets of low SNR have to be determined. The REEMAP routine uses a newly developed "pan-quantization" to detect these targets. Pan-quantization involves an artificial panchromatic image within the spectral range of the target feature to extract a spatial subset. The subset that marks the target area is defined as the eroded spatial extent of the first quantization level of the panchromatic image.

The next step is the multi-temporal weighted averaging. It is performed to reduce noise in the spectra. This processing step requires a high relative geometric accuracy, because each image pixel will be spatially connected to its corresponding pixel of the spatially overlaying scenes. In Chapter 2.1 it was tested how many overlaying scenes are required for a first REE mapping of outcrops and how many scenes are necessary to detect low-enriched zones. In this context weather, instrument characteristics and calibration, multiple reflections of surrounding objects (trees, buildings, cars, lakes, etc.) might be listed as parameters that influence the image quality and the analysis. However, the image data used in Chapter 2.1 was not optimal, due to dark target materials, shadowed outcrops and low sun elevation angles. For those conditions seven scenes were found to be the minimum number of scenes that should be used for a multi-temporal averaging. In Chapter 4.1 the multi-temporal averaging was performed on 21 image scenes. This number of scenes produced a good quality average image, which could further successfully be used in the feature sharpening routine. Further investigations, testing lower number of images, were not performed. As a general rule it can be stated, that the higher the amount of scenes the smoother the resulting image spectrum. Nevertheless, when the multi-temporal procedure is applied on satellite images the geospatial coverage of the same area in every pixel must be as good as possible - and that can be problematic. Therefore, noise estimation - based on pan-quantization - on every scene is recommended. Finally, it is also recommended to only use those scenes for the multitemporal averaging, which are firstly, reasonably rectifiable and secondly, show a high SNR in the first pan-level.

The final step of the REEMAP method is the sharpening of the image spectra and the detection of the REE related absorption band. Firstly, the spectrum of every image pixel is smoothed using a convolution with a Gaussian function and transformed into relative absorption. Then a Richardson-Lucy Deconvolution was conducted on every spectrum, in order to sharpen only those absorption bands that are related to REEs. The resulting spectrum differs only by higher depths of rare earth related absorption bands coevally improving the detectability and succeeding mathematically modeling. The fundamental principle of the deconvolution is, firstly, that absorption bands can be best modelled by Gaussian functions. Based on physics, this goes back to the assumption that regardless of the type of absorption (electronic field transitions or molecular motions) absorption bands represent a probability distribution [4, 5]. The second fundamental principle is based on the convolution theorem: A point-wise multiplication (Hadamard product) of two signals in one domain equals a convolution in the other domain [32]. The convolution theorem is usually applied in signal processing, where the convolution in the time domain equals a Hadamard multiplication in the frequency domain. Here it is used in the sampling theorem (also known as Nyquist–Shannon sampling theorem), which utilizes the convolution of a lowpass filter to achieve highpass filtering [32]. The Fourier-transformed spectrum is multiplied with a filter function (Gaussian function with a certain standard deviation). This goes back to the principle, that the sampling theorem can be applied to a Fourier-transformed signal that is defined in a certain interval in the local domain [32]. In order to respect the anti-aliasing-filter condition (Wiener-Khinchin-Einstein Theorem) the frequency band of the Gaussian bell-shaped filter must be defined with a standard deviation of half the standard deviation of the Gaussian curve that represents the target REE-related absorption [32]. Following this half-width filter condition the best filter result for the absorption band sharpening can be expected. If the half-width filter condition is not respected, an overlap in the sampling signal is producing a blurred filter result. Finally, the spectrum is exponentially transformed back to reflectance. After the spectrum has been sharpened, the absorption band has to be mathematically described. For outcrop images the determination of the absorption depth is used (feature based continuum removal for absorption depth determination). For spaceborne images the correlation of the image spectrum with a library spectrum is used to flag the pixel into enriched and non-enriched pixels. The library spectrum is transformed into the spectral sampling intervals of the satellite image and the spectral sharpening was performed prior to the correlation calculation.

In the discussions of Chapter 2.1, 3.1, and 4.1 the REEMAP method was evaluated for four outcrop scans and two satellite images. In all investigations the REEMAP method improved the detectability of REE related signals in the spectra. Different investigations were performed in those chapters to evaluate the method. The discussion in Chapter 2.1 states that the REEMAP method is especially valuable if transition zones between the REE bearing dykes and the alteration wall should be mapped. Additionally, it is mentioned that the amount of enriched pixels increases after the REEMAP method is applied. The discussion in Chapter 3.1 relates to spectral superimposing associated ferro-minerals. As a result it can be assumed, if applying REEMAP on the 800 nm neodymium-feature, that neodymium at a natural concentration level (1000 ppm) can be detected up to an iron oxides concentration of 5% in the sample. At high concentrations (5000 ppm) the iron concentration can increase up to 10% until neodymium is not detectable with REEMAP anymore. The discussion in Chapter 4.1 shows that, if thulium is searched with the REEMAP method on a simulated EnMAP image, thulium is detectable even under diffuse illumination conditions. All three investigations on the evaluation of the REEMAP method found a better delineation of the REE enriched zones in the images. All these evaluations give a comprehensive evaluation of the method, but cannot be seen as a 100% validation. In order to produce a statistically comprehensive dataset hundreds of field samples (geochemically analyzed) would have been required. Due to processing time of the geochemical analyses, such a ground truthing could not be accomplished. Although handheld XRF would provide fast field analysis (at least for cerium, lanthanum, neodymium, and for outcrop scans), there is a lack of information between geochemical analysis on field samples and hyperspectral analyses, because it is not fully understood if REEs are enriched or depleted in the surface of the imaged rocks. A diploma thesis investigation (supervised by Uwe Altenberger and Nina Bösch) on this topic is currently performed to better understand the weathering of carbonatite rocks and the concentration distribution of REEs from the surface to the fresh rock part. Besides handheld XRF analyzer, extensive geochemical analyses on field samples are commonly used for concentration determination and field validation. Although those geochemical methods can be counted as fundamental and important for

exploration, one small advantage of the REEMAP method must be mentioned as well. It is the lack of thulium detection for either handheld X-ray fluorescence (XRF) devices or the commonly used geochemical technique called inductively coupled plasma atomic emission spectroscopy. The handheld XRF devices utilize too little excitation energy to detect the HREE. In the spectrum of the inductively coupled plasma atomic emission spectroscopy an overlapping of the thulium peak and other REE related peaks often hampers a concentration determination for thulium. In contrast, thulium shows several peaks in hyperspectral spectroscopy that can be identified qualitatively.

The presented evaluations of the REEMAP method in Chapters 2.1, 3.1, and 4.1 give a good overview on how such a method can be evaluated and contemporaneously show the need for a more valid evaluation technique for hyperspectral surveys in the field of geology.

5.1.3 Capabilities and Limitations of the REE Detection Using Spectroscopy

The first limitation factor is the noise in the image spectra. In order to distinguish the spectral signal from noise the absorption depth must be higher than 99.7 % (3σ) of the standard deviation of the distribution of the noise. For the following estimation of the detectability at different sensor SNR the spectra of the 1000 ppm mixtures are used. When having an albedo of 20% and a SNR of 400:1 (like the average VNIR range of EnMAP) the 3σ value is 0.15. That means the absorption depth must be higher than 0.15% reflectance. The other extreme would be the SWIR range of the EO1-Hyperion. With a SNR of 40:1 and an albedo of 20% the 3σ value is 1.5. Therefore, the absorption bands must have a higher depth than 1.5% reflectance. In order to define a minimum image SNR value that is needed for the detection of REE absorptions, the following experiment was performed. The spectra, on which the experiment is based on, were measured with the Hypspx imager. Firstly, the Hypspx spectra were re-sampled to a spectral resolution of 1 nm using bicubic splines, in order to avoid aliasing in the succeeding spectral convolution. Afterwards, those spectra were resampled to the spectral resolution of the EnMAP and Hyperion sensor. The measured samples are the 1000 ppm mixtures of neodymium or erbium with calcite powder (see: Chapter 2.2). One example feature for the detection of neodymium and one for the detection of erbium were chosen. Those features are the 822 nm feature of neodymium (51 nm spectral distance between the two shoulders) and the 654 feature of erbium (77 nm spectral distance between the two shoulders). These features were selected because they were defined as robustly detectable, they are not positioned at detector sensitivity boundaries, and they represent a narrow and a medium wide typical REE absorption. The feature based continuum removal was calculated for every spectrum as a representative for the albedo. Additionally, the absolute feature depth was determined. These two parameters were then used to calculate the minimum image SNR, which would be necessary to classify the feature as detectable – following the 3σ criterion. Figure 5.1.1 shows a plot of this calculated minimum image SNR value that would be necessary to detect the 1000 ppm related REE features in the spectrum. Dependent on the feature width, depth, and shape different image SNR were determined as a minimum value for the detectability for every sensor. However, as this work shows, for the EnMAP sensor an image SNR below 400:1 is required for the detection of wider absorptions and absorption bands of lower depths, such as erbium. For more distinctive features, like the neodymium feature, an image SNR of at least 200:1 is required. In consequence, the minimum image SNR for Hypspx acquisitions is in this case lower (around 200:1 for both REEs) and the minimum image SNR for Hyperion acquisitions in this case is higher than the required image SNR for EnMAP acquisitions. The fact that with the Hyperion sensor the minimum required image SNR is not significantly increased for the erbium feature is explainable with the shape of the feature. The detectability improves if the peak and shoulder positions are directly covered with one channel of the sensor. This is the case for the Hyperion sensor and the erbium feature at 654 nm.

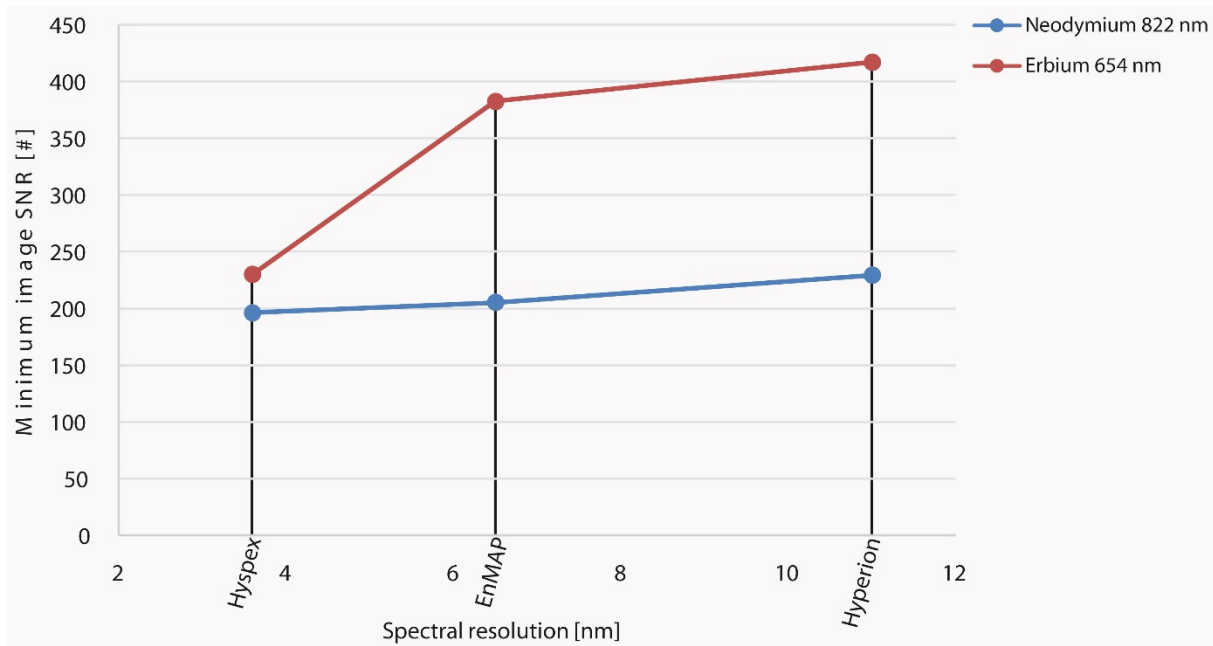


Figure 5.1.1: The minimum image SNR required in order to detect 1000 ppm neodymium oxide and erbium oxide with the spectral resolution of the used sensors in this thesis. The features were chosen as an example, because they represent the bulk of the determined absorption bands for REEs are shown. Depending on the spectral width of the REOs different minimum image SNR are required. In general the figure shows that for all sensors an image SNR of 400:1 should be present in order to detect 1000 ppm of most absorption features.

However, considering only the image SNR is not sufficient to characterize the detectability. Another important limitation factor is the spectral resolution. The image SNR and the spectral resolution should be considered together, as they both strongly impact the detectability.

The following section is based on the assumption that at least 5 channels are required to cover the range of the target absorption band to identify the absorption band with a feature based continuum removal and absorption depth determination. Thus, for narrow features, such as of thulium and erbium (e.g. around 20 nm spectral width at 515 and 677 nm), the spectral resolution should be at least 5 nm. For wider features (e.g. around 50 nm spectral width at 559 nm for neodymium) the spectral resolution of 12 nm at minimum is required, respectively. To visualize the amount of features that can be detected with certain spectral resolutions the absolute absorption depth was determined, based on the peak and shoulder positions of all features that are listed as robust in Table 8.1 in the appendix. Absorption bands located at the edge of the sensor were excluded from this estimation. The absolute absorption depth determination was performed on the same spectra as for the image SNR estimation in the previous section. Here, all features that showed a higher absorption depth than 3σ of a predefined image SNR were classified as detectable and were summed up for every element and sensor (Figure 5.1.2). The predefined image SNR was oriented on the value of the previous section (200:1) and it was applied on the spectral range from 350 to 2500 nm. Note: The chosen image SNR is higher than the provided sensor SNR of the Hyperion sensor. Most of the absorption bands would therefore probably not be detectable.

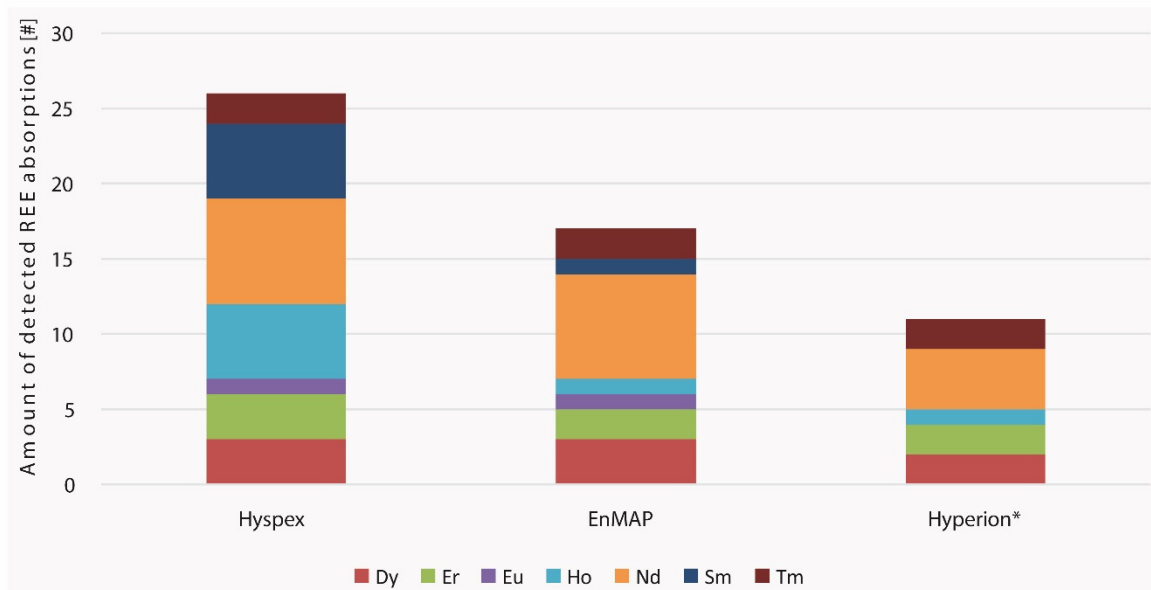


Figure 5.1.2: The amount of absorptions bands that are detectable in the spectra of a 1000 ppm mixture of REOs and calcite with different sensors. The detectability is defined with a 3σ criterion of the image SNR (here an image SNR of 200:1 is used). * The image SNR of 200:1 is lower than the sensor SNR of the Hyperion sensor, therefore the amount of detectable features is probably lower than presented here.

Finally, it can be assumed that the image SNR, the spectral resolution, and the position of the channel must be considered together to evaluate the theoretical detectability of REEs. The SNR and spectral resolution of sensors may depend on each other in a way that the optimization of one factor leads to a degradation of the other. To summarize, a spectral resolution of at least 10 nm is recommended to be able to utilize several absorption bands as representatives for the LREE and HREE deposits. When having a full width half maximum of 10 nm per channel, a spectral resampling to 1 nm is recommended to be able to perform a spectral sharpening of narrow target REE related absorption bands as well.

Chapter 3.1 showed that the associated minerals bearing iron oxides and vegetation have the most influence on the hyperspectral REE detection. Therefore, it was necessary to filter the images for vegetation pixel using the NDVI (>0.3 was flagged as vegetation) and for iron oxides using the MIFD (>0.9 was flagged as iron containing pixel) [33, 34]. Those two materials have a particularly large influence on the spectrum. Vegetation (and lichen), if it covers the outcrop, would make REE detection impossible. Even if it covers only a part of the pixel, it would change the spectrum in a way (red edge in the VNIR and wide water absorptions in the SWIR) that most of the narrow REE absorptions would not be visible anymore. Additionally, iron oxides are known to inhibit any reflection in the VNIR region. After Ben-Dor et al., 2009, thin coatings of iron oxides already hamper the detection of the underlying material significantly [35]. Other associated minerals - like calcites, feldspars, clay minerals, pyroxenes, and amphiboles or epidotes - mainly absorb in the SWIR range of the spectrum and would therefore not influence the REE detection between 350 and 1400 nm. Absorptions in REE related spectra that occur in the range where water absorbs should be excluded from the diagnostic bands, as long as the spectroscopy is not applied in the laboratory.

Moreover, Chapter 3.1 and 3.2 has shown that a hyperspectral mapping of the alteration zone and associating minerals is beneficial, especially to understand the distribution of different rock bodies in the deposit. Here, calcites, iron oxides, sulfates, phosphates, and kaolinite may be mentioned to be important as proxy minerals for an alteration mapping. Calcites (calcite, dolomite, ankerite), as host rocks, play the most important role in the detection of the ore hosting body. Secondly, the mapping of apatites and iron sulfates (pyrite and chalcopyrite) [3] can give additional information on melt fractionation processes that can lead to a local enrichment within the ore rock body. When applying the REE detection on satellite images a mapping of the

fenites gives important information on the alteration zone (see: Chapter 3.2). Especially, when the carbonatites occur in dykes of small spatial extent it is beneficial to map the fenites. Fenites often occur in a wider spatial extent around the ore rocks. To map the fenites a combination of the kaolinite and calcite absorptions can be mapped (see: Chapter 3.2).

The fourth limiting factor is especially valid for satellite images: the ground sampling distance. As explained in Chapter 1.5 carbonatite deposits are very heterogeneous. That means the enriched zones can be several meters to several hundred meters wide. Usually, the economical valuable zone is outcropping with a spatial extent that is rather smaller than 100 m across the dyke direction. For satellite images, like EnMAP, this means that for the mapping of the dyke almost every pixel must be flagged as REE-enriched in the resulting image (30 m ground sampling distance, width of the point spread function 32 m). Considering all the other limiting factors as well, a continuous dyke mapping becomes unlikely. However, to find possible deposits some positive findings might be valuable for a field team of geologists, so that they can explore the extent with field exploration techniques.

The fifth limiting factor is the rectification of the satellite images. This is valid for the EO-1 Hyperion sensor and the EnMAP sensor (especially when acquisitions with a great look angle are used). For the multi-temporal averaging step of the REEMAP method it is important to have a most precise pixel overlapping. Therefore, I would recommend to use images with nadir look direction, perform a geo-rectification (may be also incorporate a digital elevation model in order to better delineate the altitude effects), and choose only those scenes that show the lowest rectification error. As described in Chapter 5.1.2 the scenes with best rectification should further be evaluated for their image SNR and integrated in the REEMAP method.

The sixth limiting factor is the atmospheric correction of the satellite images. Some of the REE related absorptions are located in the same ranges where atmospheric absorptions occur. In detail the 760 nm water and oxygen molecule absorption overlaps the 744 nm dysprosium, the 756 nm holmium, and the 751 nm neodymium absorption. The 942 nm water absorption overlies the 967 nm erbium and the 954 nm samarium feature. The 1135 nm water absorption superimposes the 1132 nm holmium absorption. The 1454 nm water absorption overlaps the 1419 nm lanthanum, the 1421 nm neodymium, and the 1402 samarium absorption. And finally, the broad 1875 nm water absorption covers the 1937 nm holmium and 1966 nm samarium absorption. Although some of these REE absorptions do not fully overlap the atmospheric absorptions, they would be affected by the atmospheric corrections. Many common correction software use interpolation at the wavelength range, where atmospheric absorptions occur. Those corrections can sometimes cause a little step in the spectrum. This step is often identified as a false positive identification in REE detection. Another effect of the interpolation is that it also causes offsets of the REE related absorptions. Hence, I recommend excluding these features from the list of robustly detectable absorptions (Table 8.1). Moreover, I recommend excluding those absorption bands from the list, which are located at the wavelength ranges of the sensor edges (usually at 350 to 400 nm, 900 to 1100 nm, and 2400 to 2500 nm). This includes the absorption bands at 351 nm of dysprosium, at 258, 380 and 976 nm of erbium, at 363 nm of holmium, at 895 and 823 nm of neodymium, 976 nm of ytterbium, and 357, 360 and 954nm of samarium.

5.2 Summarizing Remarks and Outlook

REE spectra This thesis addresses the special characteristics of REEs. In conclusion at least seven rare earth oxides (REOs) show diagnostic absorption bands in the visible to near infrared and short wave infrared region. Most of the absorption bands are very small and form multiple features. Several absorption bands of REO related spectra were identified to be robustly detectable, because they are not overlapped by other absorption bands, they are not located at the spectral limits of the detectors, they have a higher absorption depth than 3σ of the standard deviation of the noise of operating and future sensors at natural concentrations, they can be resolved with a spectral resolution of 10 nm (five-point criterion), and they are not sensitive to neighboring ions or illumination conditions. Neodymium, the eighth detectable element, fulfills all these mentioned criteria, except of the sensitivity to neighboring ions and illumination conditions.

REEMAP This thesis introduced a new rare earth element detection method, named REEMAP. Basically it is applied to delineate the REE related signal from other signals (noise, other absorptions). The output is a sharpened absorption band that can be mathematically analyzed. Its fundamental principle is a highpass filtering that is calibrated for the target absorption bands. It is calibrated for features of neodymium as a representative of LREEs and the robust features of dysprosium, holmium, erbium, and thulium as a representative of HREEs. The lowest detectable concentration for each listed REEs are below 1000 ppm, if the image SNR is, e.g., higher than 400:1 for erbium and 200:1 for neodymium. It uses a pre-filtering for vegetation and iron oxides to minimize false positive identifications. The method is applicable from space to near-field. The minimum spectral resolution for REE detection is defined as, e.g., 10 nm for the detection of thulium, neodymium and erbium. For detection of a higher number of different REEs a spectral resolution of 6.5 (EnMAP) or 3.6 (Hypex) is necessary. It is a fast method that can be applied to the images directly in the field. The processing time, incl. image acquisition, is 20 – 60 min using a standard mobile workstation. The processing steps are:

1. Image acquisition, reflectance retrieval
2. Setting the parameters for the REEMAP method (target absorption band, acquisition mode (rotational, translational/push-broom), distance to target area, spectral resolution)
3. Perform the REEMAP method
4. Classify the image using the feature depth determination, area comparison with library or Pearson correlation
5. Validate the results in the field

Remote Sensing in REE exploration Among other physical and chemical methods, hyperspectral image analysis represents a powerful tool to support geological exploration for carbonatite deposits. As described in Chapter 1.6, hyperspectral surveys provide an important contribution to field exploration, especially when a first classification of an unknown area is required. If hyperspectral surveys are applied a basic idea of the deposit type usually already exists. At this stage, when a mapping of alkaline complexes is aspired, a mapping of the fenites and the typical host minerals can be performed. Afterwards, a possible REE enrichment might be highlighted using the REEMAP method. In the second stage of exploration (resource evaluation) the REEMAP method can be applied to analyze hyperspectral drill core scans, leading to a continuous classification of the core surface. When ore processing is performed, hyperspectral outcrop scans can be used to estimate the distribution of REE in the outcrop walls. This can give valuable information on the extension and continuity of the ore body. However, hyperspectral techniques must be seen as an additional tool in the exploration and mining process because quantitative information cannot be released yet.

EnMAP The EnMAP hyperspectral sensor, with its actual sensor specifications (June 2015), can be used to detect some of the robustly detectable REE absorption bands. In order to summarize the amount of absorption bands that may be found with the EnMAP satellite, the calculations of the minimum required image SNR from

section 5.1.3 are more specifically performed with the EnMAP specific SNR. If only the image SNR (here I chose the minimum image SNR equal to the 3-fold value of the representative sensor SNR of the VNIR and SWIR of EnMAP >400:1 at 495 nm / >180:1 at 2200 nm) and the spectral sampling distance are considered, the EnMAP satellite will be able to detect 10 absorption bands in the VNIR range (for erbium, dysprosium, holmium, neodymium, and europium, thulium). Moreover, three absorption bands in the SWIR can be detected (for samarium, thulium, erbium). These estimations have to be considered as theoretical numbers that can be used as a rough orientation, because (as discussed in section 5.1.3) the spectral resolution and the image SNR will influence the actual quality of REE detection interdependently and the exact position of the channel is directly related to detectability as well. Considering the ground sampling distance, EnMAP based REE detection will be able to delineate some positive findings if the deposit is larger than 30 x 30 m. For subpixel analysis, concentration levels of below 1000 ppm or images with a high noise a higher detection probability can be achieved if the REEMAP method is applied. The multi-temporal averaging can be highly seen as especially beneficial, because the EnMAP geometric accuracy is around 0.1 pixels.

Future perspectives Future investigations should focus on understanding the optical behavior of neodymium oxide and europium oxide. The shift of the peak positions and the absorption depth variations that are due to the measurement technique, illumination and neighboring ions must be quantized to set up the filter in REEMAP. Moreover, 3-dimensional REE-mapping of open pit outcrop walls can give important information on the spatial extension and continuity of the ore zone. In the second stage of geological exploration microscopic hyperspectral REE-investigations might be of a high interest for field geologists. The detectability in other REE deposits should also be investigated. Further studies may also concentrate on hyperspectral quantitative estimation of REEs. The concentration variations between fresh rock material and the surface of the outcrops should be studied further to gain a comprehensive knowledge on how weathering of carbonatites develops. Moreover, the pre-processing of the raw images should be investigated. It is recommended to incorporate 3-dimensional photogrammetric techniques or laser altitude/morphology measurements to perform the image rectification and reflectance transformation. The better the quality of the input images, the more robust the REE detection will be. Finally, a closer collaboration between experts in atmospheric correction, experts in noise reduction, and geological remote sensing experts might lead to a highly robust approach for the conservation of REE-related features during preprocessing of the raw data and atmospheric correction.

5.3 Conclusion

Hyperspectral remote sensing techniques can be used in order to detect REE deposits from near-field to space. That means, several REE related signals in a reflectance spectrum can be delineated from other signals and a REE mapping can be applied in a spatially wide range. The main findings of this doctoral thesis are:

1. Out of all REOs, eight REOs turned out to show robust absorption bands that can be used for detection routines.
2. A newly developed REE detection approach can be used, which uses a spectral sharpening of the REE related absorption bands to increase the REE detection probability (REEMAP). Especially for images with a higher noise, e.g., near-field images that were acquired under non-optimal illumination conditions and spaceborne acquired images, the REEMAP approach turned out to improve REE mapping.
3. Proxy mineral mappings (iron oxides, iron-bearing sulfates, calcite and kaolinite) help to detect metasomatic alteration zones. This is particularly important if the ore body is smaller than the ground sampling distance.
4. The limitations of REE detection were outlined. The most important limitations are the interdependent image SNR and spectral resolution. Image acquisition conditions, such as overlying materials (iron coatings or vegetation), a high influence of atmospheric effects, non-optimal illumination conditions are additional factors that influence the detectability of REEs.
5. The future hyperspectral EnMAP satellite (with its currently published specifications, June 2015) will be capable to detect several absorption bands of erbium, dysprosium, holmium, neodymium and europium, thulium and samarium. However, it should be noted that good image acquisition conditions, e.g., under direct sun illumination, and either a high REE concentration level or a wide spatial extent of the target deposit are beneficial.
6. Future investigations should concentrate on the characterization of the spectral behavior of the robust absorption bands of neodymium and europium. Other REE deposits types, such as REE clays or pegmatites, should be studied. New ways in the reduction of noise (e.g. accurate pre-processing of the data) should be investigated.

In consequence, a hyperspectral methodology named REEMAP was developed and proposed that enables spatially wide and rapid mapping of REEs using current and future hyperspectral instruments (HysepX, EnMAP, EO-1 Hyperion) to meet the rising demand for remotely sensed, environmentally compatible, resource-efficient and economical geological exploration.

6. References

1. Brüning, C.; Böhmer, H. *Seltene Erden - Der wichtigste Rohstoff des 21. Jahrhunderts*; 1st ed.; Börsenbuchverlag, 2011.
2. Clark, R. N.; Swayze, G. A. Mapping minerals, amorphous materials, environmental materials, vegetation, water, ice, and snow, and other materials: The USGS Tricorder Algorithm. In *Summaries of the Fifth Annual JPL Airborne Earth Science Workshop*; JPL Publication, 1995; Vol. 1, pp. 39–40.
3. Hunt, G., R. Spectral signatures of particulate minerals in the visible and near infrared. *Geophysics* **1977**, *42*, 501–513.
4. Sunshine, J. M.; Pieters, C. M.; Pratt, S. F. Deconvolution of mineral absorption bands: An improved approach. *J. Geophys. Res. Solid Earth* **1990**, *95*, 6955–6966.
5. Sunshine, J. M.; Pieters, C. M. Estimating modal abundances from the spectra of natural and laboratory pyroxene mixtures using the modified Gaussian model. *J. Geophys. Res. Planets* **1993**, *98*, 9075–9087.
6. Kumar, G. A.; Riman, R. E.; Diaz Torres, L. A.; Banerjee, S.; Romanelli, M. D.; Emge, T. J.; Brennan, J. G. Near-infrared optical characteristics of chalcogenide-bound Nd³⁺ molecules and clusters. **2007**, *19*, 2937 – 2946.
7. Misra, S. N.; Mehta, S. B.; Balar, B. M.; John, K. Absorption Difference and Comparative Absorption Spectrophotometry of Neodymium(III) Haloacetates in Non-Aqueous Media and in Crystalline State. *Synth. React. Inorg. Met.-Org. Chem.* **2006**, *22:6*, 729–757.
8. Laznicka, P. *Giant Metallic Deposits*; Springer Berlin Heidelberg: Berlin, Heidelberg, 2010.
9. Pirajno, F. *Hydrothermal Mineral Deposits*; Springer Berlin Heidelberg: Berlin, Heidelberg, 1992.
10. Casillas, R.; Demény, A.; Nagy, G.; Ahijado, A.; Fernández, C. Metacarbonatites in the Basal Complex of Fuerteventura (Canary Islands). The role of fluid/rock interactions during contact metamorphism and anatexis. *Lithos* **2011**, *125*, 503–520.
11. Mineralogy Database <http://webmineral.com/> (accessed Jun 19, 2015).
12. Guanter, L.; Kaufmann, C.; Segl, K.; Foerster, S.; Rogass, C.; Chabrillat, S.; Kuester, T.; Hollstein, A.; Roessner, S.; Chlebek, C.; Straif, C.; Fischer, S.; Schrader, S.; Storch, T.; Haiden, U.; Müller, A.; Bachmann, M.; Mühle, H.; Müller, R.; Habermayer, M.; Ohndorf, A.; Hill, J.; Buddenbaum, H.; Hostert, P.; van der Linden, S.; Leitão, P.; Rabe, A.; Doerffer, R.; Krasemann, H.; Xie, H.; Mauser, W.; Hank, T.; Locherer, M.; Rast, M.; Staenz, K.; Sang, B. The Environmental Mapping and Analysis Program (EnMAP) spaceborne imaging spectroscopy mission for Earth observation. *Remote Sens.* **2015**, *submitted*.
13. Dieke, G. H.; Crosswhite, H. M. The Spectra of the Doubly and Triply Ionized Rare Earths. *Appl Opt* **1963**, *2*, 675–686.
14. Jassie, L., B. Diffuse reflectance spectra of ten rare earths. *Spectrochim. Acta* **1964**, *20*, 169–177.
15. White, W. B. Diffuse-Reflectance Spectra of Rare-Earth Oxides. *Appl Spectrosc* **1967**, *21*, 167–171.
16. Rowan, L. C.; Kingston, M. J.; Crowley, J. K. Spectral reflectance of carbonatites and related alkalic igneous rocks; selected samples from four North American localities. *Econ. Geol.* **1986**, *81*, 857–871.
17. Rowan, L. C.; Bowers, T. L.; Crowley, J. K.; Anton-Pacheco, C.; Gumiel, P.; Kingston, M. J. Analysis of airborne visible-infrared imaging spectrometer (AVIRIS) data of the Iron Hill, Colorado, carbonatite-alkalic igneous complex. *Econ. Geol.* **1995**, *90*, 1966–1982.
18. Bedini, E.; Tukiainen, T. Using spectral mixture analysis of hyperspectral remote sensing data to map lithology of the Sarfartoq carbonatite complex, southern West Greenland. **2008**, *Geological Survey of Denmark and Greenland Bulletin*, 69–72.
19. Bedini, E. Mapping lithology of the Sarfartoq carbonatite complex, southern West Greenland, using HyMap imaging spectrometer data. *Remote Sens. Environ.* **2009**, *113*, 1208–1219.
20. Momose, A.; Miyatake, S.; Arvelyna, Y.; Nguno, A.; Mhopjeni, K.; Sibeso, M.; Muyongo, A.; Muvangua, E. Mapping pegmatite using HyMap data in southern Namibia. In *Geoscience and Remote Sensing Symposium (IGARSS), 2011 IEEE International*; 2011; pp. 2216–2217.
21. Hernandez, E. A.; Filho, C. R. de S. Spectral reflectance and emissivity features of PO₄-bearing carbonatitic rocks from the Catalão I and Tapira complexes: New constraints for detection of igneous phosphates

- with remote sensing data. In *Anais XVI Simpósio Brasileiro de Sensoriamento Remoto - SBSR*; Foz do Iguaçu, PR, Brasil, 2013.
22. Dai, J.; Wang, D.; Wang, R.; Chen, Z. Quantitative estimation of concentrations of dissolved rare earth elements using reflectance spectroscopy. *J. Appl. Remote Sens.* **2013**, *7*, 073513–073513.
 23. Turner, D. J.; Rivard, B.; Groat, L. A. Visible and short-wave infrared reflectance spectroscopy of REE fluorocarbonates. *Am. Mineral.* **2014**, *99*, 1335–1346.
 24. Herrmann, S. Capacity of imaging spectroscopy for the characterisation of REO, REE bearing minerals & primary REE-deposits 2015.
 25. Williams, M. L.; Jercinovic, M. J.; Harlov, D. E.; Budzyń, B.; Hetherington, C. J. Resetting monazite ages during fluid-related alteration. *Chem. Geol.* **2011**, *283*, 218–225.
 26. Norsk Elektro Optik HySpex VNIR 1600/SWIR320 m-e
<http://www.sphereoptics.de/de/spektrometer/docs/HySpex-GenerellMail.pdf> (accessed Apr 1, 2015).
 27. Perkin Elmer http://www.perkinelmer.com/CMSResources/Images/44-74191APP_LAMBDA650IntegratingSpheres.pdf (accessed May 6, 2015).
 28. ASD inc. Field Spec 3 HR (build in 2010)
<http://www.sphereoptics.de/en/spectrometers/docs/Field%20Spec%203%20HR%202010.pdf> (accessed Apr 1, 2015).
 29. Holzer, C.; Wernbacher, A. M.; Senekowitsch, J. M.; Gatterer, K.; Kelterer, A.-M. A Theoretical Study on Trivalent Europium: From the Free Ion to the Water Complex. *J. Phys. Chem. A* **2014**, *118*, 11499–11511.
 30. Taboada, S.; de Andrés, A.; Muñoz Santiuste, J. E.; Prieto, C.; Martínez, J. L.; Criado, A. Optical phonons, crystal-field transitions, and europium luminescence-excitation processes in Eu₂BaCoO₅: Experiment and theory. *Phys. Rev. B* **1994**, *50*, 9157–9168.
 31. Ryan, J. L.; Jørgensen, C. K. Absorption Spectra of Octahedral Lanthanide Hexahalides. *J. Phys. Chem.* **1966**, *70*, 2845–2857.
 32. Beyerer, P. D.-I. habil J.; León, P. D.-I. F. P.; Frese, D.-I. C. Bildsignale. In *Automatische Sichtprüfung*; Springer Berlin Heidelberg, 2012; pp. 435–545.
 33. Mielke, C.; Boesche, N. K.; Rogass, C.; Kaufmann, H.; Gauert, C.; de Wit, M. Spaceborne Mine Waste Mineralogy Monitoring in South Africa, Applications for Modern Push-Broom Missions: Hyperion/OLI and EnMAP/Sentinel-2. *Remote Sens.* **2014**, *6*, 6790–6816.
 34. Julien, Y.; Sobrino, J. A. Temporal analysis of NDVI and LST parameters to detect changes in the Iberian land cover between 1981 and 2001. *Int. J. Remote Sens.* **2011**, *32*, 2057–2068.
 35. E. Ben-Dor, S. C. Using Imaging Spectroscopy to study soil properties. *Remote Sens. Environ.* **2009**.

7. Acknowledgments

The time I spent researching and writing my doctoral thesis was very exciting. I will always remember these influential years of my life. I learned a lot of new things, met a lot of amazing people and found close friends during the last three years. Therefore, I take this opportunity to thank the people who supported me on this journey and have occupied a piece of my heart.

First, I would like to thank Charly (Hermann Kaufmann), who trusted in me and my work all the time. With his fascination for remote sensing and his ambitious nature he is one of the most impressive persons I ever met. Charly, thank you for your new ideas and unconventional thinking, for supporting and fighting for me during hard times, and for becoming more than just a supervisor!

A word of thanks also goes to Uwe Altenberger, who gave rise to my passion for mineralogy and never left a question unanswered. His open heart for students and his warm and supportive nature gave me the motivation to become a grown scientist and gave me the energy to supervise my BSc, MSc and Dipl. students. Uwe, thank you for the amazing time we had in Norway and for all the new research interests that you introduced to me!

Special thanks to Christian Rogaß, who gave all his passion into the supervision of my work. He taught me IDL programming and how to write scientific papers. He is always full of new ideas and never gives up on a topic until he fully understands it. He inspired me to think as a remote sensing scientist and always supported me when I tried to adapt other scientific disciplines to reflectance spectra. Chris, thank you for your unstinting help (at any time of the day or night) and for becoming a good friend!

I would like to thank Christian Mielke, for being a wonderful company in the field. His spontaneous humor and passion for geology made it possible for us to become a perfect field-team. Christian, thank you for all the nice moments we had in Spain and Namibia and for keeping me safe in any situation!

Christin Lubitz and Max Brell, thank you, not only for being inspiring and wonderful scientists, but for becoming friends on the way. Christin, thank you for all the wonderful girl-conversations during all our fieldtrips! Max, thank you that I could share all my thoughts with you and that you would never be fed up listening!

My BSc, MSc, and Dipl. students (Lisa Sieg, Sabrina Herrmann, Nicolle Köllner), I would like to thank for a lot of wonderful and funny situations in the field, for assisting in the field and the help to set up the huge amount of data we could work on.

Further, I would like to thank the section 1.4 of the Helmholtz Centre-GeoForschungsZentrum for being supportive colleagues and friends.

A remote sensing study requires validation in the field. My doctoral work took me to two wonderful places in the world – Norway and Namibia. In Norway I had the great honor to be supported by BERGFALD Miljørådgivere. They provided me with geological background material and gave me permission to work in the field. Special thanks go to Paloma Magistrati and Bård Bergfald for the support of this work. In Namibia my research was connected to the ongoing field work of Namibia Rare Earth Inc. I am especially grateful that all colleagues of NRE and RES (Remote Exploration Services, South Africa) made me feel to be part of the team and introduced me to the area. Special thanks go to Rainer Ellmies and Scott Swinden for the fieldtrips we made together. Don Burton and Franck Bizouerne are thanked for the general and financial support.

The Helmholtz Centre Potsdam - GFZ German Research Centre for Geosciences and the German National EnMAP framework program (Department of Economics and Technology BMWi No. 50EE1256) are thanked for providing the infrastructure and for the funding of my doctoral work.

Von ganzem Herzen möchte ich mich bei meiner Familie bedanken. Meinen Eltern möchte ich danken, dass sie mich zur Person gemacht haben die ich bin. Mama und Papa, ein warmes und herzliches Zuhause und Einflüsse aus der ganzen Welt habe ich Euch zu verdanken. Meiner Schwester möchte ich danken, dass sie nicht nur Schwester sondern auch beste Freundin ist. Boris möchte ich danken, dass er zur wichtigsten Person meines Lebens geworden ist und einfach immer für mich da ist.

Appendix

8.1 Appendix of the supplementary Chapter 2.1 and 3.1

Table 8.1: List of all observed absorption bands in the rare earth oxide related spectra. Bold numbers represent the absorption bands that were classified as robust. Absorptions, that were published as f-transitions in literature before [6,30,31] are marked '+'. The wavelength position was identified as 'published before' if the wavelength was within a range of ± 5 nm.

Wvl [nm]		Wvl [nm]		Wvl [nm]		Wvl [nm]		Wvl [nm]		Wvl [nm]		Wvl [nm]		Wvl [nm]		Wvl [nm]	
275	Dy	258	Er	321	Eu	336	Ho	1385	La	298	Nd	281	Sm	278	Tm	907	Yb
296	Dy	275	Er	364	Eu	349	Ho	1419	La	310	Nd	293	Sm	289	Tm	944	Yb
325	Dy	290	Er	383	Eu	363	Ho+			339	Nd	308	Sm	360	Tm	976	Yb
351	Dy	295	Er	395	Eu	383	Ho+			360	Nd+	320	Sm	465	Tm	1030	Yb
364	Dy	307	Er	403	Eu	387	Ho			366	Nd	335	Sm	476	Tm+	1078	Yb
387	Dy	319	Er	417	Eu	393	Ho+			389	Nd	349	Sm	488	Tm	1387	Yb
424	Dy	359	Er	428	Eu	416	Ho			424	Nd	367	Sm	658	Tm	1415	Yb
447	Dy	368	Er	467	Eu	420	Ho+			438	Nd+	381	Sm	668	Tm	1932	Yb
455	Dy	380	Er+	479	Eu	449	Ho			470	Nd	393	Sm	685	Tm	2107	Yb
727	Dy	409	Er+	489	Eu	457	Ho+			484	Nd	410	Sm+	697	Tm+	2216	Yb
744	Dy	446	Er	527	Eu	464	Ho			521	Nd+	423	Sm+	723	Tm		
758	Dy	454	Er+	535	Eu	475	Ho			537	Nd+	443	Sm	745	Tm		
765	Dy	491	Er+	553	Eu	486	Ho+			590	Nd+	446	Sm	767	Tm		
777	Dy	512	Er	569	Eu	528	Ho			600	Nd	469	Sm+	776	Tm		
790	Dy	523	Er+	581	Eu+	538	Ho+			609	Nd	482	Sm+	796	Tm+		
795	Dy	538	Er	593	Eu+	550	Ho			618	Nd	493	Sm+	812	Tm		
800	Dy	548	Er+	612	Eu+	624	Ho			632	Nd	506	Sm	1123	Tm		
811	Dy+	563	Er	1386	Eu	638	Ho			639	Nd	533	Sm+	1150	Tm		
819	Dy	654	Er+	1425	Eu	643	Ho			694	Nd	558	Sm	1180	Tm		
846	Dy	660	Er	1787	Eu	649	Ho+			703	Nd	568	Sm+	1204	Tm		
859	Dy	676	Er	1847	Eu	660	Ho			751	Nd+	954	Sm	1246	Tm		
887	Dy+	684	Er	1904	Eu	667	Ho			762	Nd	1059	Sm	1279	Tm		
1066	Dy	776	Er	1999	Eu	739	Ho			798	Nd+	1091	Sm+	1319	Tm		
1096	Dy	795	Er	2033	Eu	751	Ho			809	Nd+	1188	Sm	1482	Tm		
1131	Dy+	800	Er	2081	Eu	756	Ho			817	Nd	1209	Sm	1527	Tm		
1194	Dy	804	Er	2188	Eu	768	Ho			823	Nd	1251	Sm+	1577	Tm		
1214	Dy	811	Er	2349	Eu	777	Ho			895	Nd+	1325	Sm	1633	Tm		
1231	Dy	815	Er			856	Ho			1387	Nd	1352	Sm	1671	Tm		
1261	Dy+	823	Er			886	Ho			1421	Nd	1402	Sm	1728	Tm		
1321	Dy	828	Er			913	Ho			1606	Nd	1425	Sm+	1765	Tm		
1336	Dy	839	Er			1058	Ho			1670	Nd	1507	Sm	1802	Tm		
1377	Dy	846	Er			1086	Ho			1731	Nd	1537	Sm	1856	Tm		
1613	Dy	936	Er			1132	Ho			1754	Nd	1567	Sm	1936	Tm		
1640	Dy	976	Er			1149	Ho			1809	Nd	1966	Sm	2061	Tm		

Table 8.1: continued from page 137.

Wvl [nm]		Wvl [nm]		Wvl [nm]		Wvl [nm]		Wvl [nm]		Wvl [nm]			
1681	Dy	1008	Er		1189	Ho		1902	Nd	2215	Sm	2216	Tm
1717	Dy	1028	Er		1203	Ho		2105	Nd	2314	Sm		
1758	Dy	1394	Er		1348	Ho		2219	Nd	2392	Sm		
1789	Dy	1461	Er		1754	Ho		2417	Nd	2456	Sm		
1831	Dy	1475	Er		1850	Ho		2469	Nd				
1929	Dy	1497	Er		1881	Ho							
2105	Dy	1515	Er		1937	Ho							
2218	Dy	1535	Er		1973	Ho							
		1551	Er		2009	Ho							
		1574	Er		2086	Ho							
		1599	Er		2218	Ho							
		1643	Er										
		1659	Er										
		1940	Er										
		2216	Er										

Table 8.2: Hypsax settings for laboratory measurements of the REM, REO and REE-bearing minerals.

Hypsax settings		
Lamp arrangement	45 °	
Distance, sample to sensor	1m	
Sensor arrangement head to head	eq on	
Wavelength range	350 to 2500 nm	
Sampling interval	VNIR	SWIR
	3.7	6
Radiometric resolution	12 bit	14 bit
Lightsource	2 x 1000 W	
	VNIR (1600px)	SWIR (320px)
Frames	variable	variable
Integration time [µs]	30 000	5 000
Frameperiod [µs]	31 000	123 506

Table 8.3: Perkin Elmer settings for laboratory measurements of the REM, REO and REE-bearing minerals.

Perkin Elmer settings		
Lamp	Deuterium- and Tungston Lamp	
Lamp change	319.2 nm	
Wavelength range	175 to 2500 nm	
Sampling interval	1 nm	
Monochromator - detector change	860.8 nm	
Detector (settings)	Gain	Response
PMT	Auto	0.2
Pbs	2.0	0.2

Table 8.4: Analytical Spectral Device Fieldspec 3 settings for laboratory measurements of the REM, REO and REE-bearing minerals.

Analytical spectral device settings	
Wavelength range	350 to 2500 nm
Sampling interval	1 nm
Distance, sample to sensor	2-3 cm
Measurement mode	Contact probe
Sample count	200
Integrationtime	68 ms

Table 8.5: Description of the minerals that were spectroscopically analyzed in chapter 2.2.

Monazite $\varnothing < 1,5$ mm	Cleveland County, North Carolina/USA
Bastnaesite-(Ce)	3 x 1.3 cm Zagi Mountain, Warzal Dam, North-West Frontier Prov./Pakistan
Parisite-(Nd) incl. in Parasite-(Ce)	2.6 x 1.6 cm Mountain Pass Mine, Ivanpah Mts., San Bernardino Co., California/USA
Synchysite-(Y)	1.5 x 2.5 cm White Cloud Pegmatite, South Platte, Jefferson Co., Colorado/USA
Xenotime-(Y)	0.7 x 0.3 cm Novo Horizonte, Ibitiara, Bahia/Brazil
Xenotime (Y)	1.2 x 0.4 cm Novo Horizonte, Ibitiara, Bahia/Brazil

Table 8.6: Weight and weight percent of REEs and calcite amounts in the synthetic mixtures, used for the spectroscopic measurements in Chapter 2.2, after [24].

	REE in gr	REE in %	CaCO ₃ in gr	Sum in gr
Lanthanum	0,0015	0,15	1,0098	1,0073
	0,0046	0,46	1,0081	1,0127
	0,0112	1,12	0,9966	1,0078
	0,02	2	0,9942	1,0142
	0,0503	5,03	0,9667	1,013
	0,1028	10,28	0,9139	1,0167
	0,1997	19,97	0,8139	1,0136
	0,294	29,4	0,7169	1,0109
	0,5074	50,74	0,518	1,0362
	0,69	69	0,3225	1,0125
	0,8208	82,08	0,1896	1,0104
	0,9451	94,51	0,0644	1,0095
	Cerium	0,0013	0,13	1,001
0,0048		0,48	0,998	1,0028
0,011		1,1	0,9913	1,0023
0,0267		2,67	0,9733	1
0,0511		5,11	0,9595	1,0106
0,101		10,1	0,9043	1,0053
0,2093		20,93	0,7941	1,0034
0,305		30,5	0,7018	1,0068
0,5051		50,51	0,4972	1,0023
0,7023		70,23	0,3213	1,0254
0,8378		83,78	0,19	1,0278
0,9567		95,67	0,0453	1,005
Neodymium		0,0011	0,11	1,0019
	0,0054	0,54	0,9953	1,0007
	0,0118	1,18	0,9977	1,0095
	0,0203	2,03	0,9798	1,0001
	0,0503	5,03	0,9564	1,0067
	0,1088	10,88	0,8962	1,005
	0,2017	20,17	0,8002	1,0019
	0,301	30,1	0,7064	1,0074
	0,5025	50,25	0,5073	1,0098
	0,7055	70,55	0,298	1,0035
	0,8028	80,28	0,2004	1,0032
	0,9558	95,58	0,0464	1,0022

	REE in gr	REE in %	CaCO ₃ in gr	Sum in gr
Samarium	0,0011	0,11	1,001	1,0021
	0,0056	0,56	0,997	1,0026
	0,0122	1,22	0,9898	1,002
	0,0243	2,43	0,9796	1,0039
	0,0522	5,22	0,9509	1,0031
	0,1002	10,02	0,9086	1,0088
	0,2025	20,25	0,8094	1,0119
	0,3016	30,16	0,7026	1,0043
	0,5042	50,42	0,5006	1,0078
	0,7015	70,15	0,3005	1,0022
	0,8001	80,01	0,2093	1,0094
	0,9514	95,14	0,0516	1,0003
	Europium	0,0016	0,16	1,0025
0,0065		0,65	0,9941	1,0006
0,011		1,1	1,0121	1,0231
0,0218		2,18	0,9822	1,004
0,0507		5,07	0,9501	1,0008
0,1031		10,31	0,9055	1,0086
0,2011		20,11	0,8108	1,0119
0,3019		30,19	0,6992	1,0011
0,5025		50,25	0,5017	1,0042
0,7007		70,07	0,3229	1,0236
0,8025		80,25	0,199	1,0015
0,9524		95,24	0,476	1
Gadolinium		0,0012	0,12	1,0251
	0,0057	0,57	1,0057	1,0114
	0,0137	1,37	1,0078	1,0215
	0,0208	2,08	0,9804	1,0012
	0,0549	5,49	0,9523	1,0072
	0,1008	10,08	0,9054	1,0062
	0,2272	22,72	0,8286	1,0958
	0,3004	30,04	0,79	1,0004
	0,5043	50,43	0,5017	1,006
	0,7008	70,08	0,3176	1,0184
	0,8142	81,42	0,1972	1,0114
	0,9484	94,84	0,0596	1,008

	REE in gr	REE in %	CaCO ₃ in gr	Sum in gr
Terbium	0,0009	0,09	1,0157	1,0166
	0,0068	0,68	1,0183	1,0251
	0,0136	1,36	1,0176	1,0312
	0,0197	1,97	1,0616	1,0818
	0,0514	5,14	0,949	1,0004
	0,1155	11,55	0,8905	1,006
	0,2275	22,75	0,777	1,0054
	0,3086	30,86	0,6936	1,0022
	0,5097	50,97	0,4975	1,0054
	0,7049	70,49	0,2973	1,0022
	0,8073	80,73	0,2036	1,001
Dysprosium	0,0017	0,17	1,0175	1,0192
	0,0068	0,68	0,9989	1,0057
	0,0125	1,25	0,9888	1,0013
	0,0268	2,68	0,9843	1,0111
	0,055	5,5	0,9652	1,0202
	0,1137	11,37	0,9018	1,0155
	0,208	20,8	0,7943	1,0023
	0,3003	30,03	0,7163	1,0166
	0,5225	52,25	0,5108	1,0333
	0,6999	69,99	0,3138	1,0137
	0,8045	80,45	0,2388	1,0433
0,9568	95,68	0,049	1,0098	
Holmium	0,0009	0,09	1,0029	1,0038
	0,0058	0,58	0,9945	1,0003
	0,0116	1,16	0,9938	1,0054
	0,0205	2,05	0,9831	1,0036
	0,0526	5,26	0,9487	1,0013
	0,1012	10,12	0,9082	1,0094
	0,1994	19,94	0,8051	1,0045
	0,2985	29,85	0,7024	1,0009
	0,5014	50,14	0,501	1,0024
	0,6994	69,94	0,3206	1,02
	0,8032	80,32	0,1984	1,0016
0,9491	94,91	0,0669	1,016	

	REE in gr	REE in %	CaCO ₃ in gr	Sum in gr
Erbium	0,0014	0,14	1,0016	1,003
	0,0051	0,51	0,9999	1,005
	0,0127	1,27	0,9922	1,0049
	0,0223	2,23	0,9782	1,0005
	0,0505	5,05	0,9527	1,0032
	0,1008	10,08	0,9079	1,0087
	0,2014	20,14	0,8017	1,0031
	0,3036	30,36	0,7043	1,0079
	0,5003	50,03	0,5012	1,0015
	0,713	71,3	0,2937	1,0067
	0,8091	80,91	0,2356	1,0447
	0,9647	96,47	0,0361	1,0008
	Thulium	0,0021	0,21	1,0033
0,0056		0,56	1,0343	1,0399
0,0122		1,22	1,0558	1,068
0,0205		2,05	0,9917	1,0122
0,0558		5,58	0,9623	1,0181
0,106		10,6	0,9455	1,0013
0,2023		20,23	0,8587	1,061
0,3269		32,69	0,6821	1,009
Ytterbium	0,0009	0,09	1,009	1,0093
	0,005	0,5	0,9998	1,0048
	0,0102	1,02	0,9915	1,0017
	0,0212	2,12	0,9803	1,0015
	0,0544	5,44	0,9628	1,0172
	0,1031	10,31	0,902	1,0051
	0,2157	21,57	0,7895	1,0052
	0,3111	31,11	0,6962	1,0073
	0,4998	49,98	0,5097	1,0086
	0,7023	70,23	0,3163	1,0186
Lutetium	0,8142	81,42	0,1858	1
	0,9616	96,16	0,389	1,0005
	0,0011	0,11	1,0149	1,016
	0,0064	0,64	0,997	1,0034
	0,011	1,1	0,9927	1,0037
	0,0228	2,28	0,9883	1,0111
	0,0517	5,17	1,0765	1,1282
	0,1048	10,48	0,9096	1,0144
	0,2077	20,77	0,8315	1,0392
	0,3054	30,54	0,695	1,0004

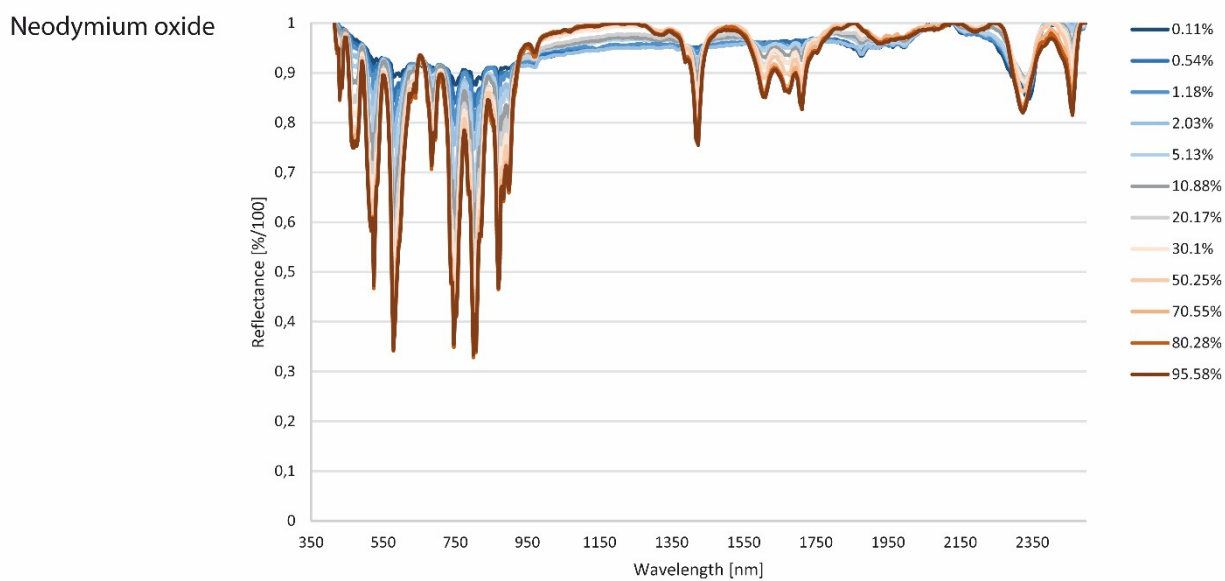
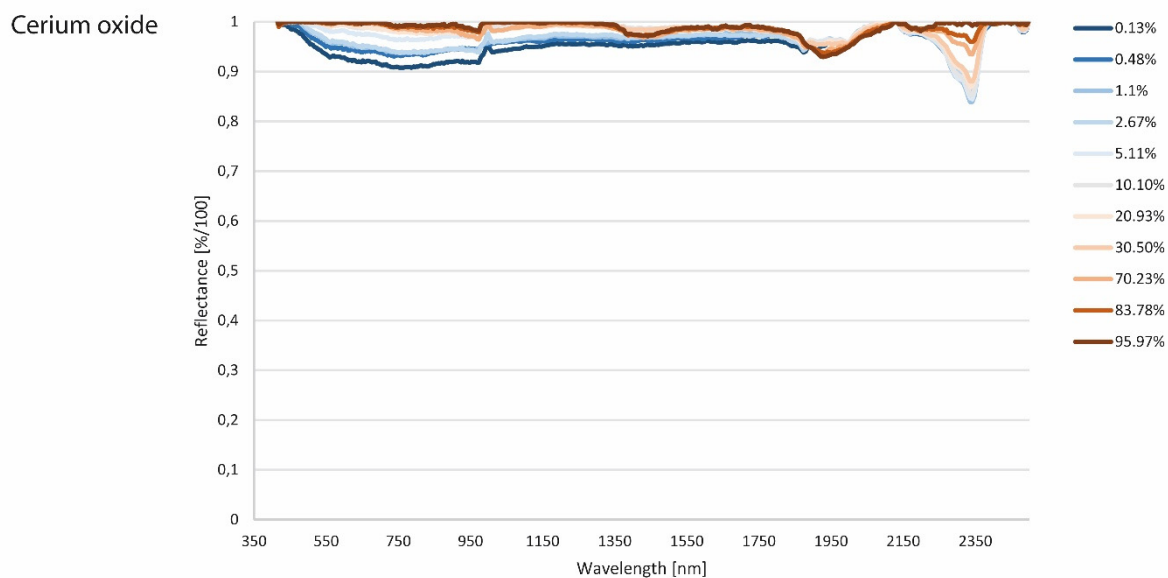
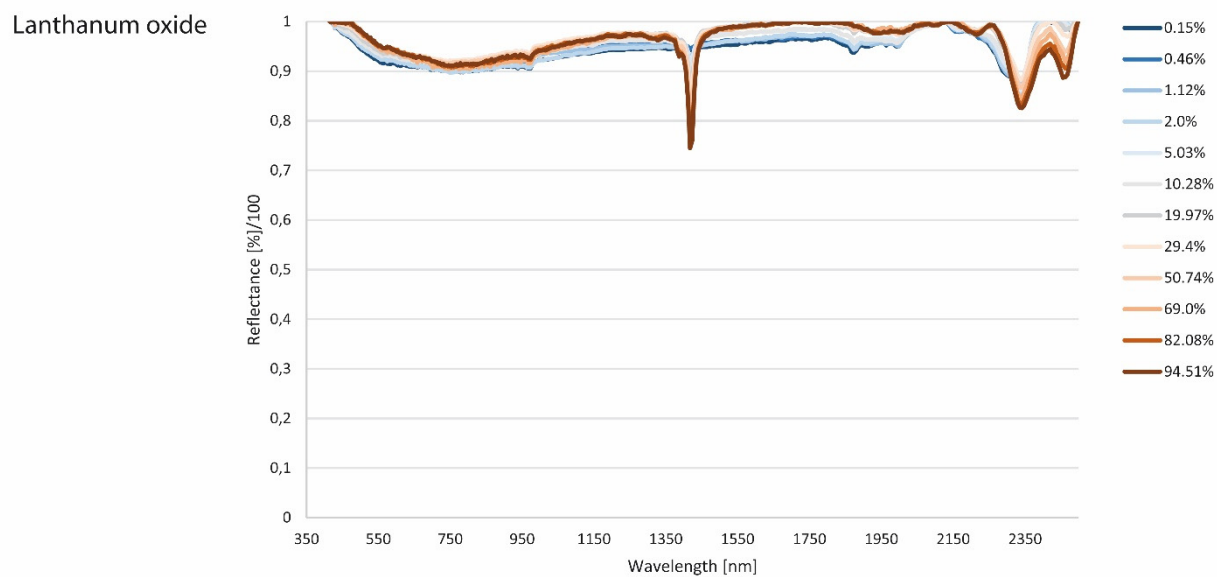
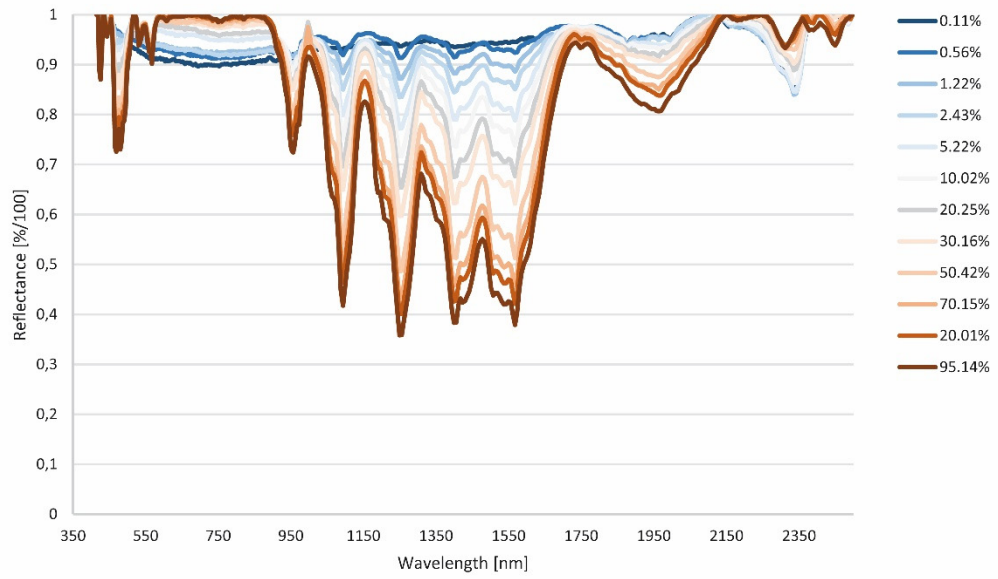
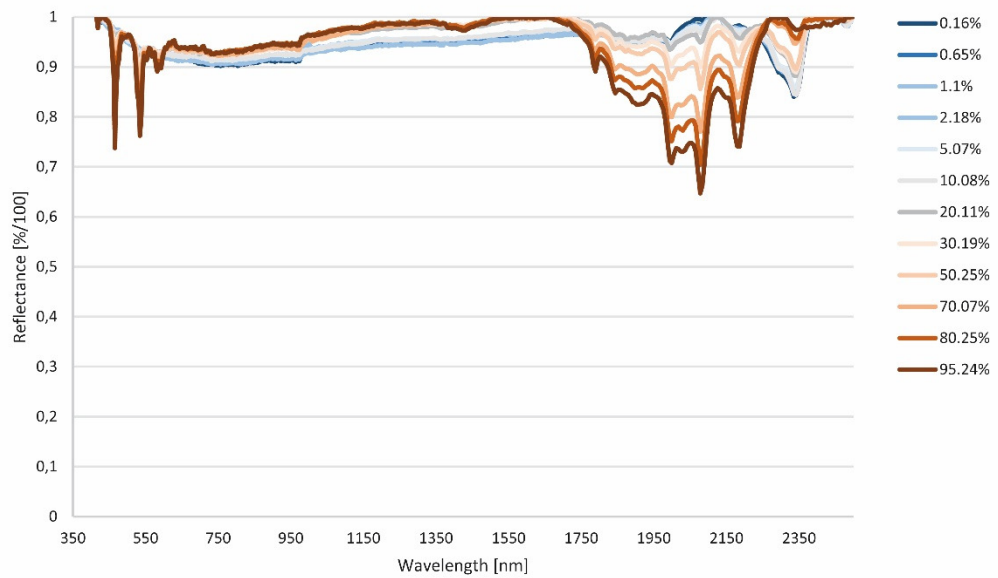


Figure 8.1: Reflectance spectra of the REE-calcite mixtures. The legend represents the amount of a certain REE in the mixture.

Samarium oxide



Europium oxide



Gadolinium oxide

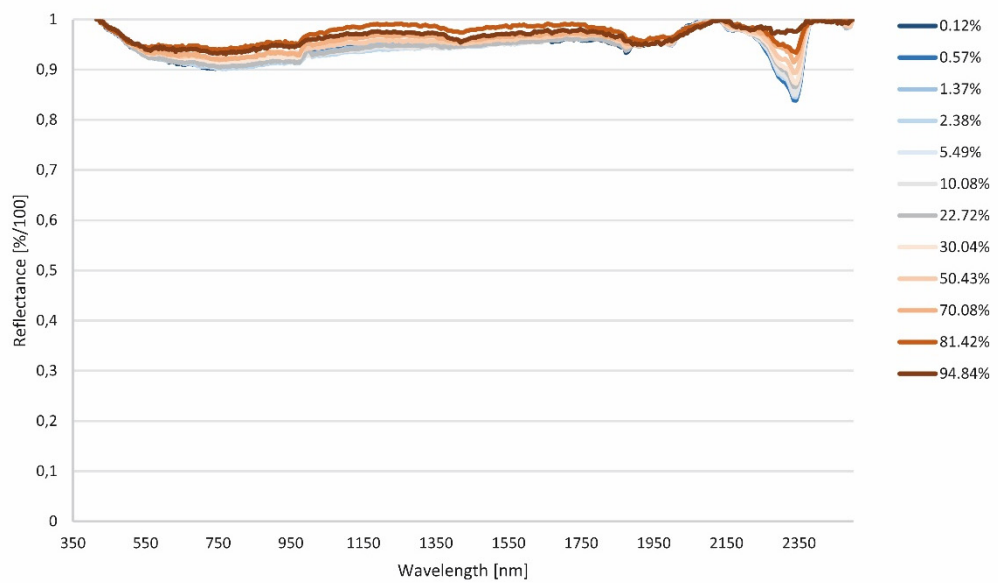
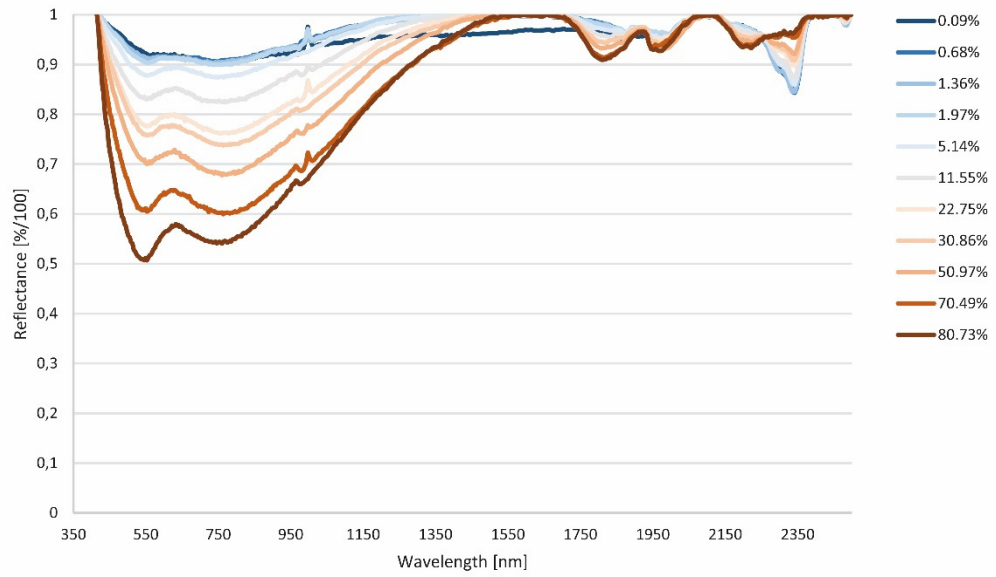
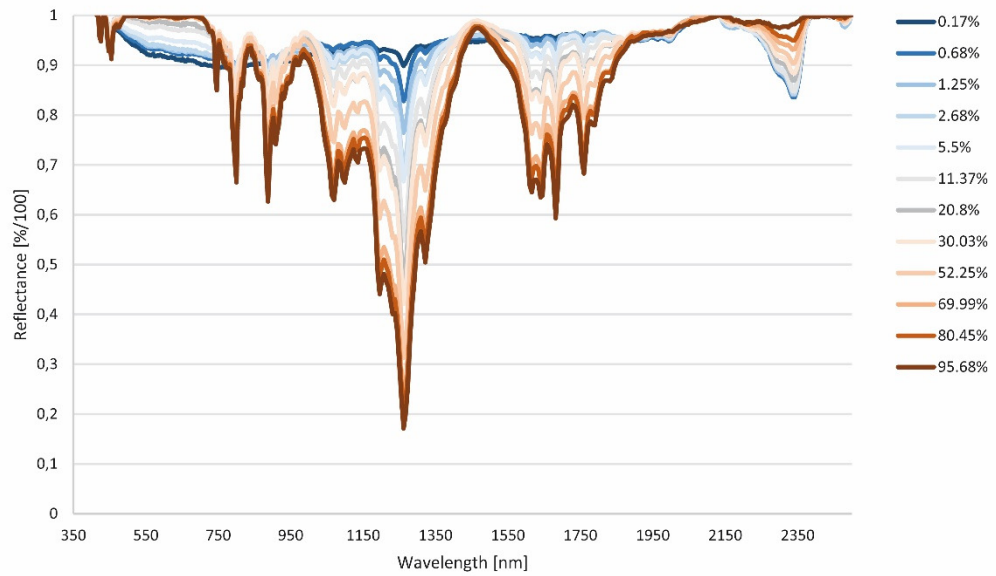


Figure 8.2: Reflectance spectra of the REE-calcite mixtures. The legend represents the amount of a certain REE in the mixture.

Terbium oxide



Dysprosium oxide



Holmium oxide

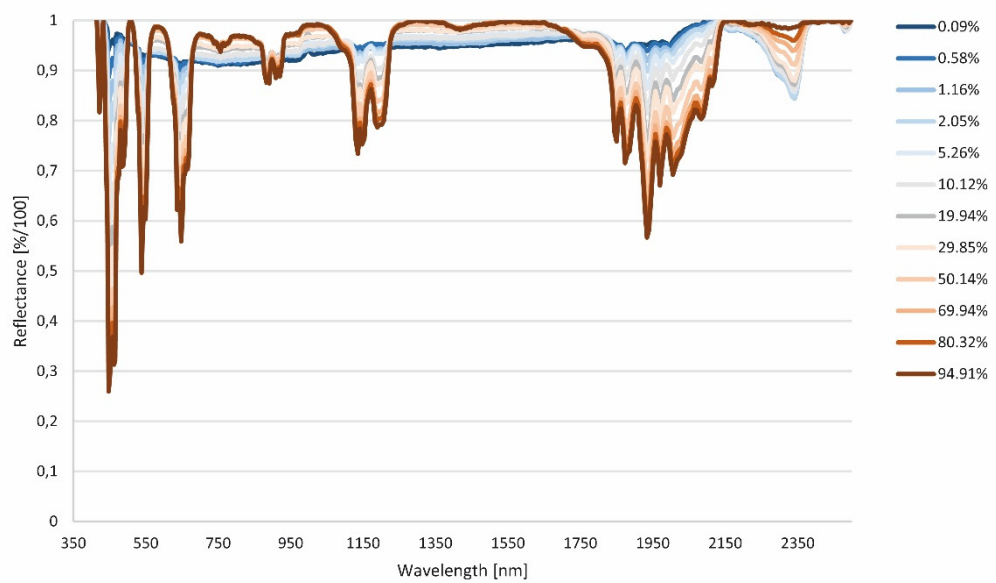
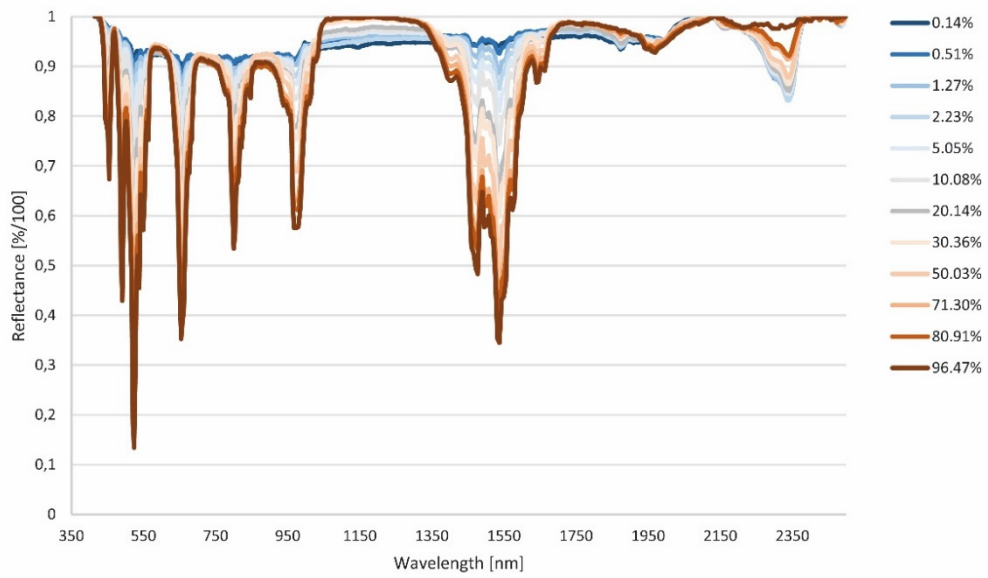
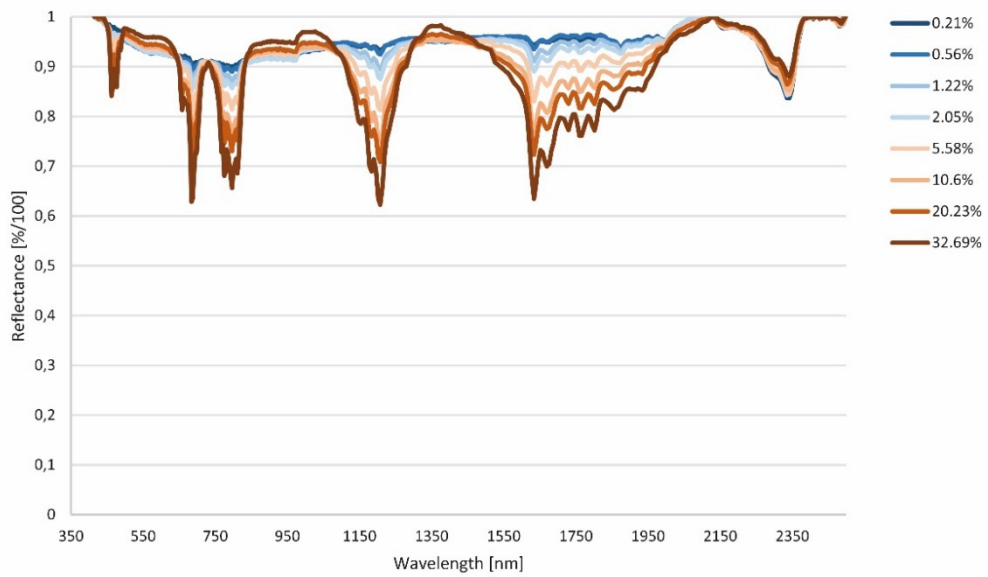


Figure 8.3: Reflectance spectra of the REE-calcite mixtures. The legend represents the amount of a certain REE in the mixture.

Erbium oxide



Thulium oxide



Ytterbium oxide

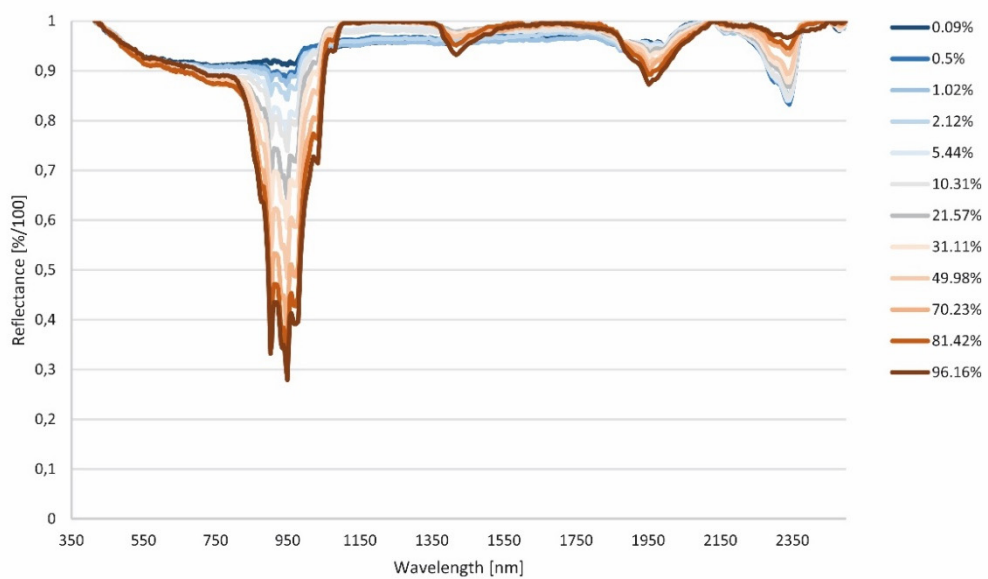


Figure 8.4: Reflectance spectra of the REE-calcite mixtures. The legend represents the amount of a certain REE in the mixture.

Lutetium oxide

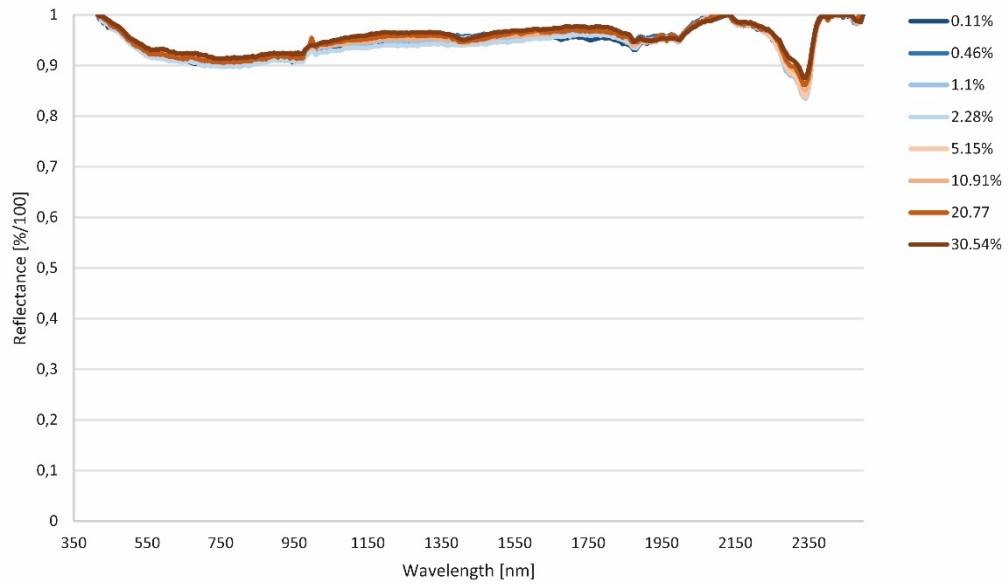


Figure 8.5: Reflectance spectra of the REE-calcite mixtures. The legend represents the amount of a certain REE in the mixture.

Spell- and Grammar check by WennText Eszter Molnár Nedlitzer Str. 23 14469·Potsdam
Cover design and typo by Detlef Bösche, Grafikdesigner (cover template after www.freepik.com)